National Library
of Canada

Acquisitions and
Bibliographic Services Branch

395 Wellington Street
Ottawa, Ontario
K1A 0N4

Bibliothèque nationale
du Canada

Direction des acquisitions et
des services bibliographiques

395, rue Wellington
Ottawa (Ontario)
K1A 0N4

Your file Votre référence

Our file Notre référence

NOTICE

The quality of this microform is heavily dependent upon the quality of the original thesis submitted for microfilming. Every effort has been made to ensure the highest quality of reproduction possible.

If pages are missing, contact the university which granted the degree.

Some pages may have indistinct print especially if the original pages were typed with a poor typewriter ribbon or if the university sent us an inferior photocopy.

Reproduction in full or in part of this microform is governed by the Canadian Copyright Act, R.S.C. 1970, c. C-30, and subsequent amendments.

AVIS

La qualité de cette microforme dépend grandement de la qualité de la thèse soumise au microfilmage. Nous avons tout fait pour assurer une qualité supérieure de reproduction.

S'il manque des pages, veuillez communiquer avec l'université qui a conféré le grade.

La qualité d'impression de certaines pages peut laisser à désirer, surtout si les pages originales ont été dactylographiées à l'aide d'un ruban usé ou si l'université nous a fait parvenir une photocopie de qualité inférieure.

La reproduction, même partielle, de cette microforme est soumise à la Loi canadienne sur le droit d'auteur, SRC 1970, c. C-30, et ses amendements subséquents.

Canada

UNIVERSITY OF ALBERTA

SHIP ICING AND STABILITY

BY

Victor Kwok Keung Chung ©

A thesis submitted to the Faculty of Graduate Studies and Research in partial fulfilment of the requirements for the degree of **DOCTOR OF PHILOSOPHY IN METEOROLOGY.**

DEPARTMENT OF GEOGRAPHY

Edmonton, Alberta

FALL, 1995

National Library
of Canada

Acquisitions and
Bibliographic Services Branch

395 Wellington Street
Ottawa, Ontario
K1A 0N4

Bibliothèque nationale
du Canada

Direction des acquisitions et
des services bibliographiques

395, rue Wellington
Ottawa (Ontario)
K1A 0N4

Your file Votre référence

Our file Notre référence

THE AUTHOR HAS GRANTED AN IRREVOCABLE NON-EXCLUSIVE LICENCE ALLOWING THE NATIONAL LIBRARY OF CANADA TO REPRODUCE, LOAN, DISTRIBUTE OR SELL COPIES OF HIS/HER THESIS BY ANY MEANS AND IN ANY FORM OR FORMAT, MAKING THIS THESIS AVAILABLE TO INTERESTED PERSONS.

L'AUTEUR A ACCORDE UNE LICENCE IRREVOCABLE ET NON EXCLUSIVE PERMETTANT A LA BIBLIOTHEQUE NATIONALE DU CANADA DE REPRODUIRE, PRETER, DISTRIBUER OU VENDRE DES COPIES DE SA THESE DE QUELQUE MANIERE ET SOUS QUELQUE FORME QUE CE SOIT POUR METTRE DES EXEMPLAIRES DE CETTE THESE A LA DISPOSITION DES PERSONNE INTERESSEES.

THE AUTHOR RETAINS OWNERSHIP OF THE COPYRIGHT IN HIS/HER THESIS. NEITHER THE THESIS NOR SUBSTANTIAL EXTRACTS FROM IT MAY BE PRINTED OR OTHERWISE REPRODUCED WITHOUT HIS/HER PERMISSION.

L'AUTEUR CONSERVE LA PROPRIETE DU DROIT D'AUTEUR QUI PROTEGE SA THESE. NI LA THESE NI DES EXTRAITS SUBSTANTIELS DE CELLE-CI NE DOIVENT ETRE IMPRIMES OU AUTREMENT REPRODUITS SANS SON AUTORISATION.

ISBN 0-612-06193-0

Canada

UNIVERSITY OF ALBERTA

RELEASE FORM

NAME OF AUTHOR: Victor Kwok Keung Chung

TITLE OF THESIS: Ship Icing and Stability

DEGREE: Doctor of Philosophy

YEAR THIS DEGREE GRANTED: 1995

Permission is hereby granted to the University of Alberta Library to reproduce single copies of this thesis and to lend or sell such copies for private, scholarly or scientific research purposes only.

The author reserves all other publication and other rights in association with the copyright in the thesis, and except as hereinbefore provided neither the thesis nor any substantial portion thereof may be printed or otherwise reproduced in any material form whatever without the author's prior written permission.

Kwok Keung. Chung

7th Floor, Flat G,
Wah Tai Building,
220 Chai Wan Road, Chai Wan,
Hong Kong

August 1, 1995

You rule over the powerful sea;
you calm its angry waves.

Bible (Psalms 89:9)

...Then Jesus got up and ordered the winds and the waves to stop, and there was a great calm. Everyone was amazed. "What kind of man is this?" they said. "Even the winds and the waves obey him!"

Bible (Matthew 8:26-27)

UNIVERSITY OF ALBERTA

FACULTY OF GRADUATE STUDIES AND RESEARCH

The undersigned certify that they have read, and recommend to the Faculty of Graduate Studies and Research for acceptance, a thesis entitled **SHIP ICING AND STABILITY** submitted by **(Victor) Kwok Keung Chung** in partial fulfilment of the requirements for the degree of **DOCTOR OF PHILOSOPHY IN METEOROLOGY.**

Edward Lozow

E. P. Lozowski, Supervisor

R Baddour

R. E. Baddour, External Examiner

T. W. Forest

G W Reuter

G. W. Reuter

JD Wilson

J. D. Wilson

July 28 1995

DEDICATION

In remembrance of the crews who lost their lives in the "Blue Mist II" tragedy which happened on February 18, 1966.

ABSTRACT

The objective of this research is to investigate the effect of spray icing on a ship's static and dynamic stability. To do this, a three-dimensional ship icing model has been developed for the stern trawler MT Zandberg. A grid cell mesh is superimposed on the surface of the Zandberg so that the ice load distribution as well as the total ice load can be calculated. The numerical icing model consists of two sub-programs. The first is a spraying model which is based on data from scale-model spraying experiments. This spraying model calculates the local spray flux to each grid cell. Spraying model studies suggest that the total amount of spray generated during a ship/wave collision depends on the ship speed (V_s) and significant wave height ($H_{1/3}$) according to $V_s^3 H^7_{1/3}$. The wind acts to re-distribute this spray mass. The second sub-program has three modules: a spray thermodynamics module, a brine film dynamics module, and an icing module. These work together to calculate the ice growth rate on each grid cell.

The icing model predictions depend in a significant way on all the atmospheric and oceanographic parameters included in the model except for air pressure. The disappearance of the side trawler "Blue Mist II" is used as a case study to demonstrate the performance of the icing model. The model evaluation suggests that using a heat transfer coefficient double that for a surface yields results which are more consistent with observations. Using such values for the deck and wheelhouse, the model's predictions agree reasonably well with both the NOAA and Soviet icing data.

Using the "Blue Mist II" scenario, the effect of icing on the ship's static and dynamic stability is also studied. Of the three wind directions considered (0°, 15°, 45°), it is found that the ice load with a wind direction of 15° has the most dramatic effect on the static and dynamic stability. The asymmetrical ice distribution in this case causes the ship to trim and list significantly and become statically unstable within 10 hours. A ship dynamics analysis indicates that the asymmetrical ice distribution induces a large roll motion which causes the ship to capsize with three hours of spray ice loading. Based on this new method for combined ship icing and stability analysis, some suggestions on navigation safety are presented.

ACKNOWLEDGMENTS

I would like to express my sincere gratitude to Professor Edward P. Lozowski for his supervision in this project. Without his guidance, kindly support, invaluable suggestions, and encouragement, the completion of this interdisplinary project would have been impossible.

My thesis research have been a collaborative project with the Institute for Marine Dynamics, National Research Council of Canada, St. John's, Newfoundland (IMD/NRC). First I thank the Institute for granting me the privilege of using the ship dynamics model developed by Dr. Jacek S. Pawlowski. Thanks especially go out to Dr. Pawlowski for his kindness and tutelage in helping me to prepare the digitization of the ship hull. Without his help, this project would not have been completed. I also thank Dr. Q. Xu (from the same Institute) for his help in running the ship dynamics model.

The spraying experiments were performed by Dr. Paul W. Zakrzewski, Dr. R. Gagnon, and Mr. Terry Thompson. I would like to express my gratitude for their efforts. The use of the towing tank facilities at the IMD/NRC is also gratefully acknowledged.

I express my thanks to the supervisory committee members, Professor Tom W. Forest and Dr. Gerhard Reuter, for their invaluable suggestions and comments on my thesis. I especially appreciate Dr. R.E. Baddour for being the external examiner. Professor John D Wilson is also gratefully acknowledged for serving as an examiner. Comments from all these examiners on my thesis have been very helpful.

Special thanks go out to Mr. Ryan Z. Blackmore and Mr. Russell D. Sampson for their kindness in editing several chapters of my thesis. My thanks also go to Mrs. Laura Smith for her help in preparing some of the graphs and drawings.

I am especially grateful for the award of a University of Alberta Ph.D scholarship and for financial support from an NESERC Strategic Grant. Without these awards, this project could not have been completed.

Finally, I would like to extend my thanks to all of the staffs and graduate students in the department for their support and companionship.

TABLE OF CONTENTS

CHAPTER PAGE

1. INTRODUCTION..1
   1.1 Definition and Nature of the Problem...........1
   1.2 Geographical Distribution of Marine Icing and Environmental Conditions.........................2
   1.3 The Effect of Icing on Ship Stability..........6
   1.4 Literature Review..............................7
      1.4a Ship Icing.................................7
      1.4b Ship Dynamics.............................14
   1.5 A New Three-Dimensional Time-Dependent Ship Icing Model.......................................17

2. SPRAYING DATA ANALYSIS.............................20
   2.1 Data Analysis.................................23
   2.2 Empirical Equation for the Longitudinal Mass Distribution...................................26
   2.3 Full-Scale Spray Flux Equation................36
   2.4 Discussion of the Full-Scale Spray Flux Equation.......................................41
   2.5 Concluding Remarks on Model Spraying Experiments....................................43

3. SPRAYING MODEL.....................................45
   3.1 The Architecture of the MT Zandberg and the Formulation of a Grid Cell Network.............47
   3.2 Spray Droplet Trajectories and Conservation of Spray Mass.................................50
   3.3 Spraying Model Implementation.................54
   3.4 Sensitivity Tests.............................60
      3.4I Effect of Atmospheric/Oceanographic Conditions on the Total Spray Mass.......61
      3.4II Effect of Droplet Size on the Total Spray Mass and the Spray Flux Distribution.....67

CHAPTER PAGE

3.5 Results and Discussion....................77
    3.5I Total Spray Mass on the Entire Vessel....83
    3.5II Spray Flux Distribution....................83
3.6 Concluding Remarks on the Spraying Model.......96

4. A NOVEL SHIP ICING MODEL....................99
4.1 Seaway Condition....................99
4.2 Thermodynamic Properties of Brine and Saline Ice....................104
4.3 Temperature of the Impinging Spray Droplets....113
4.4 Physics of Brine Flow....................117
    4.4a Vertically Falling Liquid Film............117
    4.4b Horizontal Liquid Film....................122
4.5 Physics of Ice Accretion....................129
4.6 Model Implementation....................139
4.7 Sensitivity Tests....................141
4.8 Results and Discussion....................158
    4.8I A Case Study - "Blue Mist II"............158
    4.8II Model Evaluation....................174
4.9 Concluding Remarks on the Ship Icing Model.....182

5. EFFECT OF ICING ON SHIP STABILITY....................185
5.1 Centre of Mass and Moments of Inertia..........187
5.2 Hydrostatic Particulars....................194
5.3 List, Stability Curves, Energetics of Static Stability and Trim....................200

6. RESULTS AND DISCUSSION....................214
6.1 Summary of the Icing Results....................214
6.2 Centre of Mass and Moments of Inertia..........217
6.3 Hydrostatic Particulars....................220
6.4 Stability Curves, Trim, and List...............222
6.5 Implementation of the Ship Dynamics Analysis...232
6.6 The Effect of Icing on Ship Dynamics...........237

CHAPTER PAGE

6.7 Statistical Analysis of the Computed Ship Motion....240
6.7a Distributions of the extrema....240
6.7b Ship Motions Statistics....249
6.7c Wilcoxon Signed-Rank Test....253
6.8 Spectral Analysis of the Ship Motion....254
6.9 Comments on Navigation Safety under Icing Conditions....262

7. SUMMARY, CONCLUSIONS and RECOMMENDATIONS....265
7.1 Summary and Concluding Remarks on Spray Generation....265
7.2 Summary and Concluding Remarks on the Ship Icing Model....266
7.3 Summary and Concluding Remarks on the Effect of Icing on the Ship's Static and Dynamic Stability....268
7.4 Recommendations....270

BIBLIOGRAPHY....274

APPENDIX 1A: Total Spray Mass (g) Collected on the Deck of the Model-Scale Zandberg in Each of the 23 Gauges During the Course of an Entire Experimental Run....284

APPENDIX 1B: Derivation of a Relation Describing the Spray Mass Distribution over the Deck....292

APPENDIX 1C: Normalized Collected Spray Mass (M_{ij}/M_{Gk}) along the Lines y = 0 and y = ±15.4 cm....296

APPENDIX 1D: Normalized Collected Spray Mass (M_{ij}/M_{Gk}) along the Lines y = ±7.8 cm....301

APPENDIX 2A: Calculation of the Spray Flux onto the Ship 306

APPENDIX 2B: Spray Flux Distributions over Various Components of the Zandberg for the Two Cases Studies..327

APPENDIX 3A: A Comparison between Predictions of the Zandberg Icing Model and Those of the Comiskey Icing Nomogram..................................342

Appendix 3B: NOAA Icing Data Collected in Alaskan Waters...346

Appendix 3C: Soviet Icing Data Collected by Soviet Fishing Vessels................................347

Appendix 4: Listing of Programs.........................349

LIST OF FIGURES

FIGURE PAGE

1.1.1 The physical processes of spray icing due to ship/wave collision....3

1.2.1 The locations of icing events on Soviet ships....4

2.1 Distribution of the spray collecting gauges over the deck of the scale-model Zandberg....22

2.1.1 A schematic diagram showing the convention of ship heading....25

2.2.1 The normalized mass distribution as a function of x measured from the perimeter of the hull along different longitudinal lines....27

2.2.2 Variation of the total spray mass collected per minute with wave height and ship speed....32

2.2.3 Variation of the total spray mass collected per minute with $v_s^3 h_{1/3}^7$....34

2.4.1 The spray flux distribution along different longitudinal lines for $V_s = 3$ ms^{-1} and $H_{1/3} = 4.5$ m....42

2.4.2 The spray flux distribution along $y_P = 0$ for different ship speeds and wave heights....42

3.1 A schematic diagram showing the effect of wind drag on the spray receiving zone....46

3.1.1 The general configuration and dimensions of the idealized MT Zandberg Trawler....48

3.1.2 Digitization of the stern trawler "MT Zandberg" 49

3.2.1 Spray droplet trajectories in a situation in which the ship speed is V_s and there is (a) no air drag (b) air drag and a wind speed of U in a direction opposite to the ship's course....53

3.2.2 A schematic diagram showing the convention of wind direction....55

FIGURE PAGE

3.3.1 The effect of the time step on the final destination of a droplet trajectory.............57

3.3.2 Possible destinations of a trajectory beginning at S with initial vertical velocity (a) lower than V_{zo} and (b) higher than V_{zo}.................59

3.4.1 Sensitivity test of the spraying models..........63

3.4.2 Droplet trajectories for four different droplet diameters.......................................69

3.4.3 Effect of droplet sizes on the spray flux distribution over the foredeck...................71

3.4.4 Variation of the longitudinal dimension of the spray tube Δx′ for two different droplet sizes...73

3.4.5 Effect of different droplet sizes on the vertical spray flux distribution over the front of the wheelhouse.....................................75

3.4.6 Effect of different droplet sizes on the longitudinal spray flux distribution over the top of the wheelhouse..........................78

3.4.7 Effect of different droplet sizes on the vertical spray flux distribution over the mast............80

3.5.1 Spray flux distribution over various components under standard conditions for a wind direction of 0°...85

3.5.2 Spray flux distribution over various components under standard conditions for a wind direction of 10°..88

3.5.3 Spray flux distribution over various components under standard conditions for a wind direction of 45°..93

3.5.4 Spray flux distribution over various components under standard conditions for a wind direction of 90°..97

4.1.1 Variation of total icing load with spraying duration......................................103

FIGURE PAGE

4.1.2 Ice thickness distribution along the column y = 0.5 m over the deck as a function of spraying duration....103

4.2.1 Spray icing on a vertical surface....106

4.3.1 A droplet trajectory and its temperature evolution....118

4.4.1 (a) Liquid film of uniform thickness on a vertical grid cell. (b) Vertical velocity profile within the liquid film....120

4.4.2 Maximum laminar brine film thickness and the corresponding maximum mean vertical velocity vs kinematic viscosity....123

4.4.3 Cross-section of a circular pool of liquid at rest on a horizontal surface....125

4.5.1 A grid cell located on a vertical surface....131

4.5.2 A comparison of the Nusselt numbers as a function of Reynolds number under a turbulent flow regime for a cylinder, a flat plate, and a sphere....134

4.6.1 Periods of spraying during two spray cycles....142

4.7.1 A sensitivity test of the icing model....148

4.7.2 Scattergram of observed air temperature and sea-surface temperature from Soviet icing data....155

4.8.1 One hour total ice load accumulated on the Zandberg for different wind directions....160

4.8.2 One hour ice thickness distribution over various components for a wind direction of 0°....161

4.8.3 One hour ice thickness distribution over various components for a wind direction of 15°....166

4.8.4 One hour ice thickness distribution over various components for a wind direction of 45°....171

4.8.5 One hour ice thickness distribution over various components for a wind direction of 90°....173

4.8.6 A comparison between the model predictions and NOAA icing data....177

FIGURE PAGE

4.8.7 A comparison between the model predictions and Soviet observations....179

4.8.8 A comparison between the model predicted icing rates (with a doubled Nusselt number) and NOAA and Soviet icing data....183

5.1 A schematic diagram showing the frame of reference used and the dimensions of the stern trawler MT Zandberg....186

5.1.1 The frame of reference used in the calculation of the coordinates of the new centre of mass of the ship with ice accretion....188

5.1.2 The rotational axes and centres of mass of a ship under conditions with and without ice accretion....192

5.2.1 A schematic front view diagram of a ship showing how the transverse metacentre is defined....196

5.2.2 A schematic diagram showing the centre of flotation of a ship....198

5.3.1 The righting arm (G_1Z_1) of an iced ship with its centre of mass G_1 located on the centreplane....202

5.3.2 The righting arm (G_2Z_2) of an iced ship with its centre of mass G_2 located off the centreplane....202

5.3.3 Changes in metacentric height (GM) for various locations of a ship's centre of mass....205

5.3.4 Stability curves for various locations of a ship's centre of mass....206

5.3.5 Relationship between stability curves and work required to heel a ship....208

5.3.6 Schematic diagrams showing the trimming of a ship....211

6.1.1 Final one hour ice load distribution for the stern trawler Zandberg under the conditions encountered by "Blue Mist II" for three different wind directions....215

FIGURE PAGE

6.4.1 Stability curves for the Zandberg under the different ice loading conditions given in Table 6.1.1 for three different wind directions 226

6.5.1 The original line drawings (reduced) for the stern trawler Zandberg....234

6.5.2 Digitization of the Zandberg's hull into panels 235

6.5.3 Stability curves (GZ) for Zandberg at 0 hours (no ice) and 3 hours (with ice)....238

6.6.1 Time series of the computed motion of the Zandberg at 0 hours....239

6.6.2 Time series of the computed motion of the Zandberg at 3 hours....241

6.7.1 Local peaks of a time series of ship motion....244

6.7.2 Histograms of heave extrema without ice and with ice....245

6.7.3 Histograms of pitch extrema without ice and with ice....247

6.7.4 Histograms of roll extrema with ice....250

6.8.1 Normalized power spectrum of the modelled wave train....257

6.8.2 Normalized power spectra of heave motion....258

6.8.3 Normalized power spectra of pitch motion....260

6.8.4 Normalized power spectrum of roll....261

1B.1 Data set along different longitudinal lines....294

2A.1.1 Determination of the minimum and maximum injection velocities....307

2A.1.2 Spray droplet trajectories, with the effect of wind drag, to various components under the situation with wind speed U, wind direction 0°, and ship speed V,....309

2A.2.1 Ship hull perimeter segments used to determine spray source locations....315

FIGURE PAGE

2A.2.2 Determination of the spray source point using the bisection method....................................317

2A.2.3 Spray droplet trajectories (with wind drag) to various components, for wind speed U, wind direction θ°, and ship speed V_s....................319

2B.1.1 Spray flux distribution over various components of the Zandberg under low conditions for a wind direction of 0°....................................327

2B.1.2 Spray flux distribution over various components of the Zandberg under low conditions for a wind direction of 10°....................................329

2B.1.3 Spray flux distribution over various components of the Zandberg under low conditions for a wind direction of 45°....................................332

2B.1.4 Spray flux distribution over various components of the Zandberg under low conditions for a wind direction of 90°....................................333

2B.2.1 Spray flux distribution over various components of the Zandberg under extreme conditions for a wind direction of 0°....................................334

2B.2.2 Spray flux distribution over various components of the Zandberg under extreme conditions for a wind direction of 10°....................................336

2B.2.3 Spray flux distribution over various components of the Zandberg under extreme conditions for a wind direction of 45°....................................339

2B.2.4 Spray flux distribution over various components of the Zandberg under extreme conditions for a wind direction of 90°....................................341

3A.1 The modified version of Wise and Comiskey's nomogram (1980)...343

3A.2 A comparison between the model's results and the modified nomogram's prediction...................345

FIGURE PAGE

4A.1 Four simplified flowcharts showing the processing flow of the computer programs developed to study ship icing and stability....351

LIST OF TABLES

TABLE PAGE

1.2.1 The duration of the icing season, and the frequency of icing on ships in different regions..5

2.1.1 The total mass collected in the 23 gauages under different experimental conditions................24

2.2.1 Values of α and β corresponding to y.............30

3.4.1 Total spray mass per minute impinging on the entire vessel under different atmospheric/oceanographic conditions.............61

3.4.2 Total spray mass per minute with different droplets sizes..................................67

3.5.1 Total spray mass per minute impinging on the entire vessel for different conditions...........82

4.4.1 Variation of γ_b/ρ_b and δ_h with salinity at a brine temperature of 0 °C........................129

4.7.1 Effect of atmospheric and oceanographic conditions on the total ice accumulation over the entire vessel in 1 hour.................................144

4.8.1 Icing rates corresponding to different fractions of q_s for different sea-surface temperature......180

4.8.2 Icing rates corresponding to different fractions of q_s for different air temperatures with a constant sea-surface temperature of 5 °C.........181

5.2.1 Hydrostatic particulars for the stern trawler MT Zandberg....................................199

5.2.2 The hydrostatic particulars for the stern trawler Zandberg under loading condition no. 4 with a draught of 5.39 m..................................197

5.3.1 K'N data for the stern trawler Zandberg under different loading conditions....................203

TABLE PAGE

6.1.1 Absolute and relative icing load as a function of time for the stern trawler Zandberg under the conditions encountered by "Blue Mist II".........217

6.2.1 The centre of mass of the Zandberg at various times under the three ice loading conditions given in Table 6.1.1 and illustrated in Figure 6.1.1......................................218

6.2.2 The moments of inertia of the ship after different icing periods under the three ice loading conditions described in Table 6.1.1 and Figure 6.1.1......................................221

6.3.1 The hydrostatic particulars of the Zandberg after different icing periods under the three ice loading conditions given in Table 6.1.1..........223

6.4.1 The trimming conditions of the ship at different icing periods under the three ice loading conditions given in Table 6.1.1..................230

6.4.2 The listing angle of the ship after different icing periods under the three ice loading conditions given in Table 6.1.1..................232

6.5.1 Icing load, centre of mass, moments of inertia, and various hydrostatic particulars of the Zandberg after 3 hours of ice accretion..........236

6.7.1 Heave statistics with and without ice based on the model-simulated data.........................251

6.7.2 Pitch statistics with and without ice based on the model-simulated data.........................251

6.7.3 Roll statistics with ice based on the model-simulated data.............................267

NOMENCLATURE

a,b,c,d, e, f	coefficients of polynomial equations 2.3.15 and 2.3.16.
A	cross-sectional area of the cylindrical gauge (cm^2).
$A_{(j,k)}$	surface area of grid cell (j,k) (m^2)
A_1,A_2,B_1,B_2	constants of Equations 4.1.1 and 4.1.2.
C	proportionality constant of Equation 2.3.23 ($kgs^3min^{-1}m^{-10}$).
C_D	drag coefficient of air.
C_b	specific heat capacity of a spray brine droplet ($Jkg^{-1}K^{-1}$).
$C_{b(j,k)}$	specific heat capacity of the brine remaining on grid cell (j,k) after spongy ice formation ($Jkg^{-1}K^{-1}$).
$C_{bt(j,k)}$	specific heat capacity of the total brine flux to (j,k) ($Jkg^{-1}K^{-1}$).
C_{sea}	specific heat capacity of the sea-surface brine ($Jkg^{-1}K^{-1}$).
C_w	specific heat capacity of pure water ($Jkg^{-1}K^{-1}$).
C_p	specific heat capacity of air at constant pressure ($Jkg^{-1}K^{-1}$).
d	diameter of a spray brine droplet (m).
D	mean diameter of the ship mast (m).
$e(T_{s(j,k)})$	equilibrium vapor pressure over a plane surface of pure water at temperature $T_{s(j,k)}$ (mb).
$e(T_a)$	equilibrium vapor pressure over a plane surface of pure water at the air temperature T_a (mb).
$e_s(T_{s(j,k)})$	equilibrium vapor pressure over the brine surface on grid cell (j,k) at temperature $T_{s(j,k)}$ (mb).
$e_s(T_d)$	equilibrium vapor pressure over the surface of a brine droplet at the droplet temperature T_d (mb).
f_{la}	liquid-air interface force (Nm^{-1}).

f_{sl}	solid-liquid interface force (Nm^{-1}).
f_{sa}	solid-air interface force (Nm^{-1}).
f_n	Fourier frequency (s^{-1}).
F	fetch (m).
Fr	Froude number.
F_m	normalized mass.
F_r	accretion fraction.
F_{spg}	frequency of spray generation (min^{-1}).
g	acceleration due to gravity (ms^{-2}).
GZ	right lever about the point G (m).
G_1G_2	distance between G_1 and G_2 (m).
G_1Z_1	righting lever about the point G_1 (m).
G_2Z_2	righting lever about the point G_2 (m).
$h_{(j,k)}$	heat transfer coefficient for the grid cell (j,k) ($Wm^{-2}K^{-1}$).
h_d	heat transfer coefficient for a spherical droplet of diameter d ($Wm^{-2}K^{-1}$).
h_k	data series expressed in time domain.
$h_{1/3}$	model-scale significant wave height (m).
h^*_i	ice thickness on grid cell i (m).
$h^*_{(j,k)}$	ice thickness on grid cell (J,K) after a single spraying event (m).
$h^*(t_n)$	spongy ice thickness on a grid cell at time t_n (m).
$H_{1/3}$	full-scale significant wave height (m).
$H(f_n)$	data series expressed in frequency domain.
$H^*(f_n)$	complex conjugate of $H(f_n)$.

$H^{*}_{(j,k)}$	total ice thickness on grid cell (J,K) after N hours (m).
i	complex number $(-1)^{1/2}$.
$I_{(j,k)}$	spongy ice growth rate ($kgm^{-2}s^{-1}$).
I_{xx}	moment of inertia of the ship without ice about the axis of rotation xx (kgm^{2}).
I'_{xx}	moment of inertia of the ship with ice load about the axis of rotation xx (kgm^{2}).
$I'_{xx'}$	moment of inertia of the ship with ice load about the axis of rotation xx' (kgm^{2}).
I_{yy}	moment of inertia of the ship without ice about the axis of rotation yy (kgm^{2}).
I'_{yy}	moment of inertia of the ship with ice load about the axis of rotation yy (kgm^{2}).
$I'_{yy'}$	moment of inertia of the ship with ice load about the axis of rotation yy' (kgm^{2}).
I_{zz}	moment of inertia of the ship without ice about the axis of rotation zz (kgm^{2}).
I'_{zz}	moment of inertia of the ship with ice load about the axis of rotation zz (kgm^{2}).
$I'_{zz'}$	moment of inertia of the ship with ice load about the axis of rotation zz' (kgm^{2}).
k	proportionality constant of Equation 3.1 ($kgs^{3}min^{-1}m^{-12}$).
k	an integer ranging from 0 to N - 1.

k_a	conductivity of air ($Wm^{-1}K^{-1}$).
$K'G$	distance between K' and G (m)
$K'G_1$	distance between K' and G_1 (m).
$K'N$	righting lever about the point K' (m).
l	model-scale ship length at the waterline (m).
l	distance between centre of flotation and aft perpendicular (m).
l_{xx}	perpendicular distance between the parallel axes xx' and xx (m).
l_{yy}	perpendicular distance between the parallel axes yy' and yy (m).
l_{zz}	perpendicular distance between the parallel axes zz' and zz (m).
L	full-scale ship length at the waterline (m)
L	characteristic length for heat transfer (m).
L_1, L_2	lengths of two adjacent sides of a parallelogram (m).
L_1, L_2, L_3, L_4	lengths of the four sides of a rhombus (m).
L_v	specific latent heat of vaporization of pure water ($2.5 x 10^6\ Jkg^{-1}$).
L_f	specific latent heat of fusion of pure water (Jkg^{-1}).
L_{fs}	specific latent heat of fusion of a spongy ice accretion (Jkg^{-1}).
$m(x,y)$	spray mass flux at (x,y) without wind drag ($kgm^{-2}min^{-1}$).
$m(x,y,z)$	spray mass flux at (x,y,z) without wind drag ($kgm^{-2}min^{-1}$).
$m(x,y,z)_A$	spray mass flux to A without wind drag ($kgm^{-2}min^{-1}$).
$m(x,y,z)_B$	spray mass flux to B without wind drag ($kgm^{-2}min^{-1}$).
$m(x',y)$	spray mass flux at (x',y) with wind drag ($kgm^{-2}min^{-1}$).
$m(x',y',z')$	spray mass flux at (x',y',z') with wind drag ($kgm^{-2}min^{-1}$).

$m_{EF}(x',y',z')$	spray mass flux to the plate characterized by the line EF and with centre at (x',y',z') with wind drag ($kgm^{-2}min^{-1}$).
$m_{GH}(x',y',z')$	spray mass flux to the plate characterized by the line GH and with centre at (x',y',z') with wind drag ($kgm^{-2}min^{-1}$).
$m_{GH}(x',y',z')_{cyl}$	spray mass flux to the arc surface GH with wind drag ($kgm^{-2}min^{-1}$).
m_1,m_2	constants of Equations 4.1.1 and 4.1.2.
$m_{bt(j,k)}$	total brine flux to the grid cell (j,k) ($kgm^{-2}s^{-1}$).
m_{sf}	instantaneous spray flux ($kgm^{-2}s^{-1}$).
$m_{sf(j,k)}$	instantaneous spray flux to the grid cell (j,k) ($kgm^{-2}s^{-1}$).
$m_{F0},m_{F1},m_{F2},m_{F-1}$	spray mass density collected in gauges located in the F^{th} row, and columns 0, 1, 2, and -1 (gcm^{-2}).
m_{ij}	spray mass density in a gauge located at position (i,j) of the model-scale ship (gcm^{-2}).
m_{ijF}	spray mass density at positon (i,j) on the deck of the full-scale ship (kgm^{-2}).
m'_{ij}	spray mass flux density at position (i,j) of the model-scale ship ($gcm^{-2}min^{-1}$).
m'_{ijF}	spray mass flux density at position (i,j) on the deck of the full-scale ship ($kgm^{-2}min^{-1}$).
$m_{I(j,k)}$	ice load on a grid cell (j,k) after a single spray icing event (kg).
$m_I(t_n)$	ice load on a grid cell (j,k) at time t_n (kg).

M	total mass of impinging spray at model-scale (kg).
M_F	total mass of impinging spray at full-scale (kg).
$M(y)$	transverse mass distribution over the model-scale ship deck (g).
$M_{f(j,k+1)}$	total mass of brine flowing into grid cell (j,k) from cell (j,k+1) in one second (kg).
$M_{l(j,k)}$	brine mass remaining on grid cell (j,k) after run off (kg).
M_{Gk}	total water mass collected in all the gauges in the kth model spraying experiment (g).
M_{ij}	mass of spray collected in the gauge located at position ij in one model spraying experiment (g).
M_{ijF}	spray mass collected at position (i,j) on the deck of the full-scale ship (kg).
$M_{I(j,k)}$	total ice load on grid cell (j,k) after N hours (kg).
M_{Itot}	total ice load over the entire vessel (kg).
M_{ship}	the mass of the ship (kg).
n	an integer from 0 to N/2 - 1.
N	total number of data points.
N	number of hours.
Nu	Nusselt number.
P	sum of the four sides of a rhombus divided by 2 (m).
P, P_0, P_2	coefficients of parabolic Equations 1B.1, 1B,2, and 1B.3.
PE	change in gravitational potential energy during spreading of a liquid (J).
P_a	air pressure (mb).
P_{en}	ship/wave encounter period (s).

P_o	significant wave period (s).
$P(f_n)$	power spectrum of a time series (m^2Hz^{-1}).
$P_N(f_n)$	normalized power spectrum of a time series (m^2Hz^{-1}).
Pr	Prandtl number.
P_{sp}	period of direct spraying (s).
P_{spg}	time interval between successive spray events (s).
$q_{c(j,k)}$	heat flux due to forced convection from the icing surface on grid cell (j,k) (Wm^{-2}).
$q_{e(j,k)}$	evaporative heat flux from the icing surface on grid cell (j,k) (Wm^{-2}).
$q_{f(j,k)}$	heat flux due to the release of latent heat of freezing from the icing surface on grid cell (j,k) (Wm^{-2}).
$q_{r(j,k)}$	heat flux due to net longwave radiative heat transfer away from the icing surface on grid cell (j,k) (Wm^{-2}).
$q_{s(j,k)}$	heat flux associated with cooling of the total incoming brine flux to its equilibrium freezing temperature on the icing surface on grid cell (j,k) (Wm^{-2}).
Q_c	heat flux from the surface of a brine droplet due to convection (Wm^{-2}).
Q_E	evaporative heat flux of a brine droplet (Wm^{-2}).
Q_R	net heat flux from the surface of a brine droplet due to longwave radiation (Wm^{-2}).
$\vec{r}_G$	the position vector of the centre of mass of the uniced ship (m).
$\vec{r}'_G$	the position vector of the centre of mass of the ship with ice accretion (m).

$\overline{r}_i$	the position vector of the centre of mass of the ice accretion on a grid cell (m).
R	radius of a pool of liquid lying on a horizontal surface (m).
Re	Reynolds number.
RH	relative humidity.
S	surface area of the liquid-air interface (m^2).
S'	surface area of the liquid-solid interface (m^2).
Sc	Schmidt number.
S_m	scaling factor of the model-scale Zandberg.
S(y)	non-dimensional transverse mass distribution over the model-scale ship deck.
$S_B(y)$	non-dimensional transverse mass distribution along row B over the model-scale ship deck.
$S_{b(j,k)}$	salinity of the brine remaining on the grid cell (j,k) after spongy ice formation.
$S_{bt(j,k)}$	salinity of the total brine flux to the grid cell (j,k).
S_{sea}	salinity of sea water.
$S_{I(j,k)}$	salinity of the spongy ice accretion on grid cell (j,k).
t	total change of trim (cm).
t_{Af}	draught at the aft perpendicular (m)
t_{Ff}	draught at the forward perpendicular (m).
Δt_{Af}	change of draught at the after perpendicular (m).
Δt_{Ff}	change of draught at the forward perpendicular (m).

t_k	time at the end of the k^{th} time step (s).
Δt	data sampling interval (s).
Δt	duration of spraying (min).
Δt_F	full-scale time duration (min).
Δt_k	duration of experiment #k (min).
T_a	air temperature (°C).
T_{ak}	air temperature (K).
T_d	temperature of a brine droplet (°C).
$T_{im(j,k)}$	temperature of a brine droplet when impinging on grid cell (j,k) (°C).
$T_{mean(j,k)}$	mean temperature of the total brine flux to the grid cell (j,k) (°C).
$T_{s(j,k)}$	equilibrium freezing temperature of the total brine flux to the cell (j,k) (°C).
$T_{sk(j,k)}$	equilibrium freezing temperature of the total brine flux to the cell (j,k) (K).
U	upstream wind speed at the 10 meter reference level (ms^{-1}).
$\overline{U}$:	upstream wind vector (ms^{-1}).
U_{bz}	vertical flow speed of brine film (ms^{-1}).
$<U_{bz(j,k)}>$	average vertical velocity of the brine film on grid cell (j,k) (ms^{-1}).
v_s	model-scale ship speed (ms^{-1}).
V	volume of an incompressible fluid.
$\overline{V}_d$:	velocity vector of the brine droplet (ms^{-1}).
V_p	significant wave phase speed (ms^{-1}).

V_{rw}	speed of the ship relative to the oncoming waves (ms^{-1}).
V_s	full-scale ship speed (ms^{-1}).
V_x	x-component of the velocity of a spray droplet upon hitting the point O' (ms^{-1}).
V_y	y-component of the velocity of a spray droplet upon hitting the point O' (ms^{-1}).
V_{zl}	vertical injection velocity of the lower bound trajectory (ms^{-1}).
V_{zo}	vertical injection velocity of the trajectory which hits the target (ms^{-1}).
V_{zu}	vertical injection velocity of the upper bound trajectory (ms^{-1}).
ΔV_z	increment in the vertical injection velocity (ms^{-1}).
w	mass load on ship (kg).
W	displacement of the ship (kg).
W_a	work required to heel a ship to angle ϕ_a (J).
W_b	work required to heel a ship to angle ϕ_b (J).
W_{la}	surface energy of the pool of liquid for the liquid-air interface portion of the surface (J).
W_{ls}	work done by surface tension along the perimeter of the liquid-solid boundary (J).
x	horizontal distance normal to the plane of the liquid film (m).
x	model-scale longitudinal distance measured from the perimeter of the hull (cm).
x'	longitudinal distance measured from the bow (m).
x'	x-coordinate of the centre of mass of the total ice mass (m).

Δx	length of grid cell centred at O (m).
$\Delta x'$	length of grid cell centred at O' (m).
x_{hull}	x-coordinate of a point on the perimeter of the hull measured from the bow (m).
x_d	distance over which the mass load is shifted (m).
x_F	full-scale longitudinal distance measured from the perimeter of the hull (m).
x_i	x-coordinate of the centroid of a grid cell (m).
x'_i	x-coordinate of the centre of mass of the ice accretion on a grid cell relative to the centre of mass of the uniced ship (m).
X_1, X_2	dummy variables of Equation (4.2.5).
x_G	x-coordinate of the centre of mass of the uniced ship (m).
x'_G	x-coordinate of the centre of mass of the ship with ice load (m).
y	model-scale transverse distance measured from the centreline (positive to the starboard) (cm).
y_F	full-scale transverse distance measured from the centreline (positive to the starboard) (m).
y'	y-coordinate of the centre of mass of the total ice mass (m).
y_G	y-coordinate of the centre of mass of the uniced ship (m).
y'_G	y-coordinate of the centre of mass of the ship with ice load (m).
y_i	y-coordinate of the centroid of a grid cell (m).
y'_i	y-coordinate of the centre of mass of the ice accretion on a grid cell relative to the centre of mass of the uniced ship (m).

Δy	width of a grid cell (m).
z'	z-coordinate of the centre of mass of the total ice mass (m).
z_G	z-coordinate of the centre of mass of the uniced ship (m).
z'_G	z-coordinate of the centre of mass of the ship with ice load (m).
z_i	z-coordinate of the centroid of a grid cell (m).
z'_i	z-coordinate of the centre of mass of the ice accretion on a grid cell relative to the centre of mass of the uniced ship (m).
Δz	height of the grid cell (m).
$\Delta z'$	height of the grid cell (m).
α	model-scale polynomial expressions for spray mass distribution (Equation 2.2.3).
α_F	full-scale polynomial expressions for spray mass distribution (Equation 2.3.17).
β	model-scale polynomial expressions for spray mass distribution (Equation 2.2.4) (m^{-1}).
β_F	full-scale polynomial expressions for spray mass distribution (Equation 2.3.18) (m^{-1}).
ρ_a	air density (kgm^{-3}).
ρ_b	density of brine droplet (kgm^{-3}).
$\rho_{b(j,k)}$	density of the brine remaining on the grid cell (j,k) after spongy ice formation (kgm^{-3}).
ρ_w	density of pure water (kgm^{-3}).
$\rho_{ac(j,k)}$	density of the spongy ice accretion on grid cell (j,k) (kgm^{-3}).

ρ_i	density of pure ice (kgm^{-3}).
υ	kinematic viscosity of air (m^2s^{-1}).
υ_b	kinematic viscosity of brine (m^2s^{-1}).
λ	wavelength of significant wave (m).
λ	liquid fraction of the ice matrix.
δ	thickness of brine film (m).
$\delta_{b(j,k)}$	thickness of the brine remaining on grid cell (j,k) after spongy ice formation (m).
δ_h	equilibrium thickness of a pool of liquid lying on a horizontal surface (m).
δ_L	the thickness of a laminar layer (m).
μ_b	dynamic viscosity of brine at the equilibrium freezing temperature ($kgm^{-1}s^{-1}$).
μ_{bo}	dynamic viscosity of brine at 0 °C ($kgm^{-1}s^{-1}$).
$\in$	ratio of the molecular weight of water vapor to dry air.
σ	Stefan-Boltzmann constant ($5.67x10^{-8}$ $Wm^{-2}K^{-4}$).
η	non-dimensional distance parameter at the liquid surface.
γ	trim angle (°).
γ_b	surface tension of the brine film (Nm^{-1}).
γ_{bo}	surface tension of the brine film at 0 °C (Nm^{-1}).
ϕ	sum of the opposite angles of a rhombus divided by 2 (°).
ϕ	angle of heel (°).
ϕ_a	angle of heel (°).
ϕ_b	angle of heel (°).

θ_{12}	angle between line L_1 and line L_2 (°).
θ_{34}	angle between line L_3 and line L_4 (°).
β	wetting angle of a pool of liquid lying horizontally (°).
β	droplet impact angle relative to the centreline of the ship (°).

CHAPTER 1 INTRODUCTION

1.1 Definition and Nature of the Problem

The objective of this research is to investigate the effect of spray icing on a ship's static stability and its dynamic performance. In order to do this, a new ship icing model for the stern trawler MT Zandberg has been developed. With the icing data computed from the icing model, the changes in the ship's hydrostatic and static stability conditions can be calculated. Then, the ship's hydrostatic conditions with ice loading are fed into the ship dynamics model of Pawlowski and Bass (1991), so that the relation between icing and ship dynamics can be studied.

Ship spray icing, which often occurs throughout the North Atlantic and Pacific and their adjoining seas during winter (Zakrzewski and Lozowski, 1989), is a result of the impingement and freezing of sea spray. When the ship hull slams an oncoming wave, a spray cloud, which consists of numerous spray droplets, is generated, usually along the forward perimeter of the hull. Due to the relative motion of the vessel and the effects of wind drag and gravity, the spray droplets travel through the air and eventually impinge on the ship's deck and superstructure. At the same time, cooling also takes place as the droplets fly through the air. Hence, the temperature of the impinging droplets is lower than their initial temperature, which is the sea-surface temperature. The impinging spray droplets spread out and form a brine film on the surface of the deck and superstructure. Under favourable conditions in which the heat lost from the brine film to the air is large enough, part of the brine film will be frozen to form a spongy accretion. After a sufficiently long time, many tonnes of spongy ice can accumulate over the entire vessel. According to Zakrzewski's (1987) recent studies on collision-generated spray, the spray flux and the temperature of the impinging droplets are different on different parts of the ship's surface. The heat fluxes from the various ship components may also be different. Consequently, the ice growth rate can be expected to vary over the ship's surface . The ice load and its distribution can drastically change the ship's hydrostatic conditions and hence adversely affect its motion and stability. Figure 1.1.1 illustrates the physical processes of spray icing due to ship/wave collision generated spray.

1.2 Geographical Distribution of Marine Icing and Environmental Conditions

The locations of icing events on Soviet ships world-wide is illustrated in Figure 1.2.1, according to Panov (1976). Clearly the ship positions where icing took place are concentrated in the main fishing areas. The duration of the icing season, and the frequency of ship icing during the icing season over different regions is summarized in Table 1.2.1, according to Borisenkov and Pchelko (1975).

The environmental conditions favourable to icing on ships are as follows:

(1) Air temperature: Based on Soviet icing data, icing of ships occurs at air temperatures from 0 °C to -26 °C (Borisenkov and Panov, 1972).

(2) Wind speed: Spray icing on ships usually takes place at high wind speed under favourable air and sea temperatures. But sometimes it can also occur at low wind speed in the presence of swell. The wind speed range over which icing has been observed is 0 to 55 ms^{-1} (Panov, 1976).

(3) Sea-surface temperature: According to Borisenkov and Panov (1972), spray icing occurs at sea-surface temperatures from -1.8 °C to +6 °C. The lower limit is a result of sea ice formation below -1.8 °C. Sea ice formation can suppress spray generation and thus prevent spray icing. When the sea water temperature becomes too warm (> +6 °C), the temperature of the impinging spray droplets may be too high to allow immediate ice formation. However, under very low air temperatures, the brine film remaining on the vessel's surface may cool to its equilibrium freezing temperature during the interval between sprays. In this case, part of the brine film may freeze. Therefore, it is possible that the upper limit for sea-surface temperature may be even higher than +6 °C (Shekhtman, 1967).

Besides the environmental conditions, the ship operating parameters also play an important role in the occurrence of spray icing. For example, the severity of spray icing

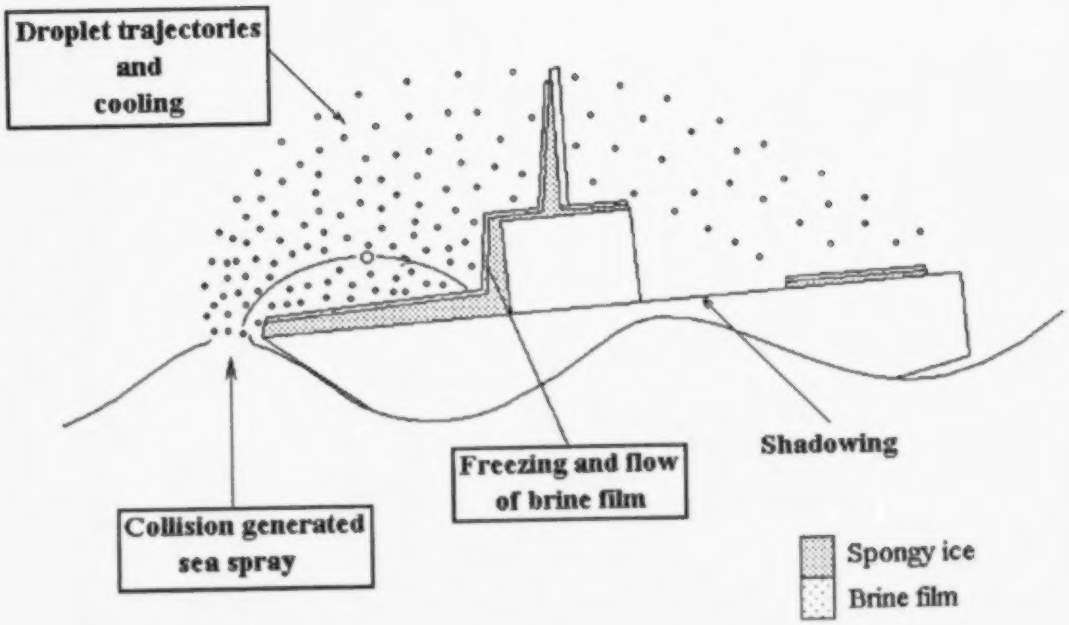
Droplet trajectories and cooling
Collision generated sea spray
Freezing and flow of brine film
Shadowing
Spongy ice
Brine film

Figure 1.1.1: The physical processes of spray icing due to ship/wave collision.

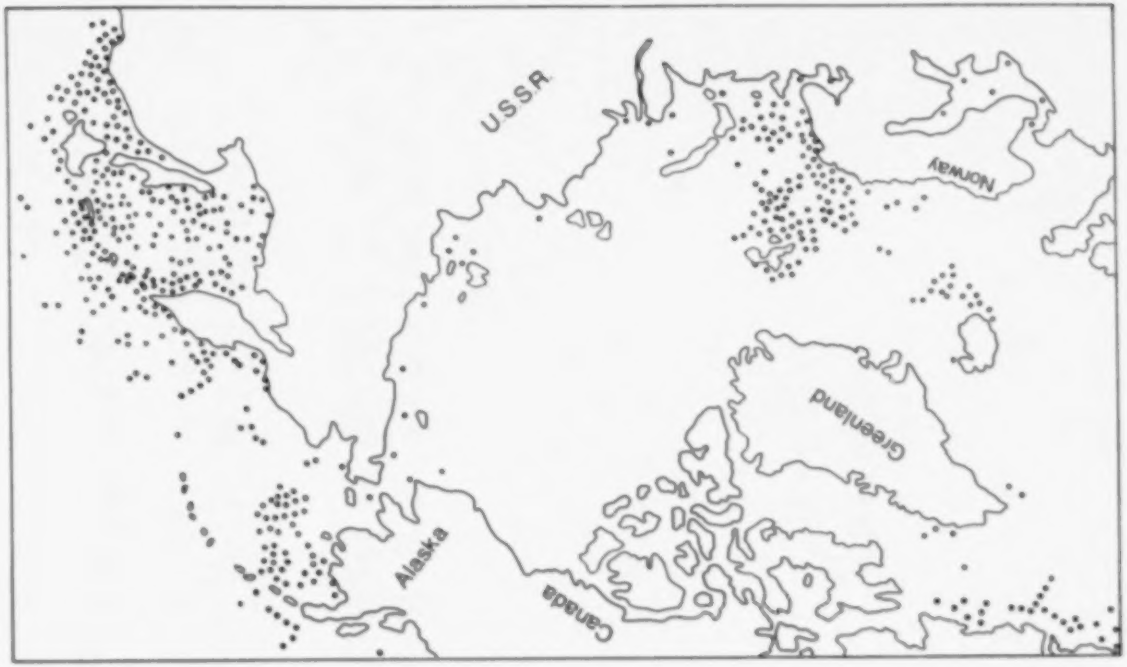
U.S.S.R.
Norway
Greenland
Alaska
Canada

Figure 1.2.1: The locations of icing events on Soviet ships (after Panov, 1979).

Region	No. of cases	Icing season	Frequency (%)
NW Atlantic	85	15 Dec - 15 Mar	92
Norwegian and Greenland seas	109	15 Dec - 31 Mar	77
North Atlantic	63	15 Dec - 15 Mar	92
Barents Sea	390	1 Jan - 15 Mar	78
Baltic Sea	21	15 Dec - 29 Feb	85
Newfoundland Region	15	1 Jan - 15 Mar	79
Bering Sea	185	1 Dec - 31 Mar	70
Sea of Okhotsk	337	1 Dec - 31 Mar	70
Sea of Japan	226	1 Dec - 29 Feb	85
NW Pacific	183	15 Dec - 31 Mar	79
Arctic Seas (Kara, Laptev, East Siberian, and Chukchi)	71	15 June - 15 Nov	100

Table 1.2.1: The duration of the icing season, and the frequency of icing on ships in different regions (Borisenkov and Pchelko, 1975).

is reduced if the vessel travels at low speeds or downwind. In these situations, spray generation is greatly reduced.

1.3 The Effect of Icing on Ship Stability

Icing on ships is a hazard for several reasons, but especially because it can result in a loss of ship stability. Normally a ship travels with designated hydrostatic conditions. The draught is fixed, the loading is distributed evenly over the vessel and the centre of mass must be below the metacentric height and along the centreline plane. However, when ice accumulates on the topside of the vessel, the extra ice load and its uneven distribution causes the centre of mass of the vessel to shift away from its original position. Thus, apart from the fact that the ship now travels with a deeper draught, it may list and have a larger angle of trim as well. Topside icing always raises the centre of mass. When the centre of mass is higher than the metacentric height, the ship becomes unstable and may capsize. In general, ship motion possesses six degrees of freedom: surge, sway, heave, pitch, roll, and yaw (Pawlowski and Bass, 1991). Observations indicate that an extra load due to icing can seriously affect the dynamic performance of a ship and reduce its stability, especially under severe icing conditions and heavy seas.

Knowing that icing is a menace to shipping and fisheries, mariners have put much effort into minimizing the ship icing hazard by (i) better ship design, (ii) improved regulation, (iii) better icing forecasts, (iv) prudent ship operation, and (v) the use of de-icing equipment (Makkonen, 1984). However, despite the above effort, numerous ship icing disasters still occur. Recent examples include:

1) On January 31, 1993, the side-trawler Cape Aspy sank off the southwestern tip of Nova Scotia with the loss of five lives. It was found that spray icing was one of the causes of this disaster (Transportation Safety of Canada, 1994).

2) On December 8, 1989, the 300-foot bulk carrier "Johanna B" and the 420-foot container ship "Capitan Torres" capsized due to icing in the Gulf of St Lawrence with 39 casualties (Zakrzewski and Lozowski, 1991).

3) On January 19, 1989, a modern, large fishing vessel "Fjord West" was lost due to

icing in the Bering sea (Zakrzewski and Lozowski, 1991).

4) In February, 1988, a medium-sized trawler under the Phillipino flag capsized due to icing in the cold waters off Newfoundland. Only one survivor was rescued from the ocean (Zakrzewski and Lozowski, 1991).

Based on the above discussion, the hypothesis of this research is that icing on ships can influence ship dynamics and at some point may cause the ship to capsize. Despite the considerable literature which has been published in the fields of spray icing and ship dynamics, the amount of ice accumulation on a ship which will cause it to capsize is still not known. Hence, the objective of this research is to link these two fields of knowledge together so that the relation between spray icing and ship dynamics can be investigated. With this new understanding, useful suggestions for navigation safety and ship design as they relate to severe icing conditions can be proposed. In order to do this, a new three-dimensional ship icing model is developed and the output from this icing model is input to the ship dynamics model developed by Pawlowski and Bass (1991). Using the two models together, the resulting ship-wave interaction under icing conditions is analyzed.

1.4 Literature Review

(a) Ship Icing

Although spray icing frequently occurs over the North Atlantic and Pacific oceans, very few data sets on ice growth on sea-going ships have been published by western researchers. There are two well-known data sets available in western countries (Stallabrass, 1980; Pease and Comiskey, 1985).

Based on the analysis of ship icing reports collected during the period 1970/71 - 1978/79 (exclusive of the season 1972/73), Stallabrass (1980) documented 39 cases of ship icing for which the icing rate had been estimated. In this data set, the air and sea temperatures, relative humidity, and ocean salinity were also included. However, Stallabrass' data set has a shortcoming. The reported ice thickness was not measured but rather estimated visually. Thus, there is a large uncertainty in the reported values of "average ice thickness". Since the ice load distribution may exhibit great variability over a ship (Zakrzewski et al., 1988), the "average ice thickness" given in these report may be somewhat misleading.

A total of 85 icing observations were collected by Pease and Comisky (1985) in Alaskan waters for vessels ranging from 20 - 115 meters in length during the period 1979 to 1983. In this data set, the icing rate and the air sea parameters were determined based on ship icing reports. Again, the major shortcoming of this data set is that the ice thicknesses were simply estimated visually.

Perhaps, the most detailed and comprehensive ship icing data have been published in the former Soviet Union. Following several ship icing disasters during the 1950s and 1960s, a comprehensive research program was launched by Soviet scientists in 1966 and was carried out until 1973. The publications of Soviet scientists on ship icing during the above period cover many aspects of the icing phenomenon including the following:

(i) Spray generation, zone of spraying a vessel, frequency of spraying, and spray cloud parameters.

(ii) Geographical distribution of icing events, environmental conditions favourable to icing on ships, the period of potential ship icing, and the frequency of icing at sea.

(iii) Ice growth rates, and ice distribution on different ship components.

(iv) Physical properties of ice accretion on ships.

A detailed review of these Soviet icing data has been published by Zakrzewski and Lozowski (1989).

In addition to the icing data discussed above, a lot of research has been done on the modelling of ice accretion on ships. There are basically two types of models - statistical and physical. Statistical ship icing models are based on empirical relationships between air-sea parameters and observed icing rates. These models generally do not take into account all of the meteorological and oceanographic parameters which have proved to be crucial in determining the ice load and its distribution. In addition, this type of model is not ship specific and thus the variation of ice load from ship to ship is not considered. Many statistical models have been developed and some of them are described below.

Based on an analysis of the variation of the icing rate on Japanese patrol and fishing vessels in the Bering sea with air temperature and wind speed, Sawata (1966) developed a nomogram to estimate the icing intensity qualitatively. In this nomogram, the icing intensity was classified into three categories: light, moderate, and heavy. Sea-surface temperature was not taken into account in the nomogram because of a lack of field data.

Vasil'ieva (1966) correlated 'severe' icing of ships operating in the Bering sea with wind speeds greater than 20 ms^{-1} and air temperatures less than -15 °C. However, this correlation does not provide any information on icing rates. Thus, this correlation is rather qualitative. He also suggested a threshold condition, with wind speeds greater than 5 ms^{-1} and air temperature less than 0 °C, for which sea spray icing occurs.

Mertins (1968) examined several hundred ship icing reports from vessels operating in the North Sea and, with this information, developed a simple empirical nomogram which relates air and sea-surface temperatures and wind speed to icing rates. Mertins (1968) classified the icing rates into four categories: light icing (1 - 3 cm/day), moderate (4 - 6 cm/day), heavy (7 - 14 cm/day), and very heavy (> 15 cm/day). Mertins' nomogram was revised by Wise and Comisky (1980) to correlate the icing rates on ships operating in the Bering sea and the Gulf of Alaska with air and sea-surface temperatures, and wind speed.

Comiskey et al. (1984) performed a linear, multiple and stepwise regression analysis on eighty-five recorded cases of ship icing. Predictive equations for icing rate for the lee (in the shadow of an island), open water, and downwind (following seas) icing cases were developed and compared with the icing expressions derived by Stallabrass (1980). The icing nomogram originated by Wise and Comisky (1980) was modified by doubling the icing rate associated with each icing class, in order to be more consistent with the observed icing rates.

The most detailed empirical model is the one developed by Overland et al. (1986). They used the 85 icing observations collected by Pease and Comisky (1985), and from them, selected 58 cases with open-ocean, non-downwind conditions for analysis. Then, they applied a categorical forecasting procedure to relate icing potential to wind speed, and to air and sea-surface temperatures. This categorical forecasting procedure is based on the determination of a predictor which is a function of wind speed, the freezing point of the brine, and the air and sea-surface temperatures.

Physical ship icing models are based on physical laws and equations which govern the processes of spraying and icing. They allow the calculation of icing rate given an input of the appropriate physical and meteorological/oceanographic parameters. Since many aspects of spray dynamics and icing are still not well understood, certain assumptions and the neglect of some not-so-important parameters are inevitable in developing a physical/numerical ship icing model. Consequently, this type of model may sometimes give rise to large errors. Fortunately, potentially large errors that may arise in physical models can readily be detected through comparison with field observations and with the predictions of tested empirical models.

The first physical ship icing model was developed in the USSR (Zakrzewski et al. 1988). Borisenkov (1969) suggested a formula which relates the icing rate to the heat transfer coefficient and other atmospheric parameters. This formula was recommended for the prediction of the icing rate for both atmospheric and spray icing (Borisenkov et al., 1971; Panov, 1976). However, some inconsistencies exist in this formula, particularly in as much as liquid water content and the wind speed are not considered. These two parameters are found to be important in determining the icing rate (Zakrzewski et al., 1988). Nevertheless, Borisenkov's formula gave a first approximation to the average icing rate on a ship.

Borisenkov's formula was subsequently modified by Panov (1971, 1976). Panov (1971) added a term representing the local aerodynamic heating to Borisenkov's formula. Another modification by Panov (1976) was the incorporation of the kinetic energy of the impinging spray into the heat balance equation used for the derivation of the icing rate equation (Zakrzewski et al., 1988). However, these two modifications have only a minor effect on the icing rate, since the effects of aerodynamic heating and the kinetic energy of the impinging spray droplets are almost negligible in marine icing (Zakrzewski et al., 1988).

Kachurin et al. (1974) devised a model to calculate the ice growth rate on a circular cylinder in a cross flow. They then correlated the model prediction with the overall ice load under the same environmental conditions on an entire vessel, by using field data. In this model, the growth of ice was assumed to occur in the wet regime and the spray flux was assumed to be continuous. It was also suggested that the liquid water content in the spray cloud is linearly proportional to the wave height (Kachurin et al., 1974). However, the proportionality constant is not well known, and ship speed and heading, which are found to be crucial for spray generation (Zakrzewski, 1987), are not included in the formula. On the positive side, the model is based on a heat balance equation for an icing surface that includes the sensible heat flux associated with the spray. Kachurin et al. (1974) suggested that only 20 - 30 % of the impinging spray participates in the sensible heat exchange with the icing surface. This suggested fraction requires further verification, since it would seem that the fraction of the impinging spray directly involved in the heat exchange process should also depend on the magnitude of the spray flux and on the atmospheric conditions as well. Based on the correlation between the icing rate on a cylinder and a vessel, Kachurin et al. (1974) produced a nomogram to predict vessel icing rates. The required input parameters in this nomogram includes the air and sea-surface temperatures, wind speed, significant wave height, and sea-surface salinity.

Stallabrass (1980) calculated the icing rate using a heat balance equation at the surface of various ship components, under a continuous steady spray assumption. The collection efficiency for spray droplets was assumed to be unity. Stallabrass (1980) found that the model performed better against Canadian data if the liquid water content in the spray cloud was one-sixth of that given by the Kachurin et al. (1974) equation. The model of Stallabrass seems to perform well compared with the previously described models when tested against Canadian data. However, his model also suffers from several shortcomings. The model does not include the sensible heat flux of the rundown water shed from more elevated locations (Zakrzewski et al., 1988). In addition, the liquid water content used in the model depends on the wave height only. This wave height dependence seems too simple because ship speed and heading are known to affect the spray cloud parameters as well (Zakrzewski, 1987). The Stallabrass model was calibrated using icing reports from ships operating in the waters east of Canada during the icing seasons of 1977/78 and 1978/79.

Zakrzewski et al. (1983 and 1988) have developed a three- dimensional, time dependent ship icing model for a Coast Guard Cutter and a Navy Destroyer. This model basically consists of two modules, one for spraying and one for icing. In the spraying module, a vertical spray jet is assumed to be ejected around the forward perimeter of the hull. The liquid water content in the spray cloud is expressed as a function of wave height, ship speed relative to the moving waves, and height above deck. The topside of the ship is divided into components and a network of grid cells is superimposed on each component. The spray flux to each grid cell in each component is determined through a backward trajectory calculation. Also included in the spraying module are the dimensions of the spray cloud, the residence time of the spray cloud over the vessel, the frequency of spray cloud generation, and the extent of the spraying zone on the ship. In the icing module, the droplet impingement temperature is first calculated using the trajectory and heat conservation equations. Then, the icing rate on each grid cell is calculated using a heat balance equation. Unlike the model of Stallabrass (1980), the net heat flux due to shed water, and the heat flux due to radiation are also included in the model. In addition, water and salt transport down vertical walls, and the sponginess of the ice accretion are all included in this model. The model of Zakrzewski et al. (1988) was basically the only one of its kind until the present work. The authors suggested the following improvements to the model:

(1) The duration of water film residence on the icing surface is time-dependent and this should be incorporated into the model (Zakrzewski et al., 1988).

(2) Field tests are necessary in order to determine the convective heat transfer coefficient for full-scale ship components in a turbulent flow (Zakrzewski et al., 1988).

(3) The spraying module is based on field data collected on Soviet trawlers. Thus, for modern Canadian trawlers, some modification may be needed in the spraying module.

Several other shortcomings of the model of Zakrzewski et al. (1988) were not mentioned by the authors. In the spraying module, it was assumed that the liquid water content in the spray cloud varies only vertically and not laterally. But, according to model-scale spraying experiments performed at the Institute for Marine Dynamics, St. John's, Newfoundland, it was found that the amount of spray water impinging on the ship's deck varies both longitudinally and laterally (Chung et al., 1993). This implies that the liquid water content in the spray cloud should vary laterally as well. Although a trajectory equation is used in the model of Zakrzewski et al. (1988) to calculate the spray flux to different grid cells, any shadowing effect (see Figure 1.1.1) is ignored. Due to blocking of the spray droplets by the superstructure, some parts of the vessel may not receive spray. Neglecting this effect may result in an overestimation of the ice load.

An innovative approach has been used by Blackmore and Lozowski (1994) to develop an heuristic model of vessel icing. This model, though simple in physics, includes essentially all the relevant atmospheric and oceanographic parameters as input. This model can be used to predict the overall icing rate for different sizes of ships as long as their length, beam, and freeboard are known. The authors envisage the vessel to be enveloped in a continuous spray cloud. They further assume that dynamic and thermodynamic equilibrium are complete by the time the spray impinges on the vessel. Thus, the spray droplets and the air parcel have the same temperature and velocity at the moment of impingement. Therefore, the convective heat loss from various components on the vessel is neglected. In other words, for the purposes of this model, the supercooling of the spray droplets is taken to be the major heat sink for ice growth. The spray/air heat balance is applied under one of two assumptions. The first is that the spray supercools, and the second, that the spray is nucleated. It was found that the nucleated spray model gives icing rates up to 400 % greater than the supercooled version (Blackmore et al., 1994). The nucleated process needs further verification, especially in determining what kinds of environmental conditions can lead to such a process. Nevertheless, both the supercooled and nucleated version of the heuristic model perform well against data and other icing models (Blackmore et al., 1994). Although the heuristic model of Blackmore et al. (1994) is simple and universal, it predicts only the overall icing rate for the entire vessel. It does not predict the variation in ice growth on different parts of the vessel. In Section 1.5, a new ship icing model specifically designed to achieve this purpose will be presented.

(b) Ship Dynamics

Considerable research on ship dynamics has been published and many advances have been made in this field in recent years. Before the invention of computers, the performance of a ship could only be tested using a model-scale ship running in a towing tank. In this way, the ship resistance, ship stability and motion could be evaluated and the results projected to the full-scale ship through the "Froude law of comparison" (Todd, 1967). One way to calculate the ship-wave interaction was based on "strip theory" (Lewis, 1967) in which the hull was assumed to be made up of a number of transverse strips or segments. The hydrodynamic load and moment are calculated on each strip and then summed. With the recent advances in computer technology, the study of ship dynamics has now shifted to the numerical modelling of non-linear ship motion in arbitrary seas. Numerical modelling of ship motion has made a substantial contribution to the evaluation of ship performance and ship design. Model-scale experiments always encounter certain limitations which are not constraints in numerical modelling. However, towing tank experiments are still very valuable because they can be used to establish the validity and performance of numerical models. To date, towing tank experiments are still widely used in the evaluation of a ship's performance.

The earliest work on ship dynamics is that of Krylov (1898). He calculated the hydrodynamic loads and ship motions in waves, based on the simple assumption that the presence of the ship does not change the pressure distribution in the propagating wave. This assumption is called the Froude-Krylov hypothesis. Since then, progress in the modelling of ship interaction with waves has consisted chiefly in the development of techniques for computing the very disturbances discarded by the Froude-Krylov hypothesis (Pawlowski and Bass, 1991). Reviews of this progress can be found in Newman (1983) and Hutchison (1990). Despite recent progress, knowledge of these disturbances is still constrained by the necessary assumption of small wave amplitudes, small ship motions, and small disturbances induced by the ship in the oncoming wave field (Pawlowski et al., 1991).

Neglecting fluid viscosity, the disturbance discarded by the Froude-Krylov hypothesis can be decomposed into radiation and diffraction disturbances (Pawlowski et al., 1991). The radiation disturbance is the disturbance induced in calm water by a hull oscillating about a stationary or a steadily advancing mean position. The diffraction disturbance is the disturbance induced in the wave field by a stationary or a steadily advancing hull (Pawlowski and Bass, 1991). These two components can be solved for separately either in the frequency domain (Faltinsen and Michelsen, 1974, Hogben and Standing, 1974, Chang, 1977, and Inglis and Price, 1982) or in the time domain (Liapis, 1986, Beck and Liapis, 1987, and King, 1987), using panel methods. The solutions can be expressed in terms of Green's functions which satisfy appropriate linear free surface conditions (Pawlowski et al., 1991).

For solutions in the frequency domain, the disturbance problems can be solved by considering only the linear frequency domain and assuming a zero forward ship speed (Newman and Sclavounos, 1988). Methods aimed at the inclusion of non-linear effects in the frequency domain solution with zero forward ship speed have also been considered by Ogilvie (1983), Lee, Newman, Kim and Yue (1991) and Pawlowski (1991).

The advantage of time domain methods is that they allow arbitrary motion of the hull, and thus the assumption of zero forward ship speed (or small ship motions) can be discarded. In addition, the distinction between cases with and without forward speed can also be eliminated (Pawlowski et al., 1991). However, the assumption of small oncoming and disturbance wave amplitudes has to be retained (Lin and Yue, 1990, and Magee, 1991).

A novel ship dynamics model has been developed by Pawlowski and Bass (1991). Since this model will be used together with a new ship icing model (described later) to investigate the effect of icing on ship stability, it is worthwhile to describe relevant features of their model here. More details can be found in the original paper.

The model of Pawlowski and Bass (1991) assumes that the oncoming wave is steep and high, and that the motions of the ship caused by the wave are also large, of a magnitude proportional to the wave height. In this way, the Froude-Krylov hypothesis is abandoned. A new hypothesis, called the weak scatterer hypothesis is introduced instead. The key assumption of this hypothesis is that the disturbance induced by the moving ship in the wave field is considered to be of a smaller order of magnitude than the wave flow quantities which are proportional to the wave height, but at least of the same order of magnitude as the wave flow quantities which are proportional to the square of the wave height. The weak scatterer hypothesis applies when the ship moves compliantly with steep waves of a length and height comparable to the ship's dimensions.

The weak scatterer assumption has been used before by Newman (1970) to investigate the hydrodynamic loads on submerged bodies, and also by Salvesen (1974) to simplify expressions for steady, second-order hydrodynamic loads induced on conventional surface ships. There is a fundamental difference between their weak scatterer assumption and that of Pawlowski and Bass (1991), however. The former is based on "strip theory" which can be justified only for slender ships operating at normal speeds in head and bow waves (Salvesen, Tuck and Faltinsen, 1970), while the latter is not limited in this respect, but depends only on the compliant motion of the ship. Thus it is applicable to the modelling of large ship motions.

Using the weak scatterer hypothesis, the weak scattering potential (which must satisfy Laplace's equation, the impermeability condition on the hull, the free surface condition, and appropriate initial conditions) can be solved for using the modal potentials method (Pawlowski, 1982; Pawlowski et al., 1988). The flow disturbance is expressed by a finite number of modal velocity potentials with unknown time-dependent amplitudes which are evaluated in the course of a time domain simulation. The modal amplitudes determine the corresponding modal potentials using an appropriately defined, pre-selected potential influence function. One of the advantages of the modal potentials method is that the distinction between the radiation and diffraction disturbance is immaterial. The flow disturbance is simply represented by a single scattering velocity potential which is obtained by summing the modal potentials.

In the model of Pawlowski and Bass (1991), the effect of viscosity is included in the calculation of the roll damping, and the lift and drag contribution to the sway force and yaw moment is included using appropriately known semi-empirical expressions (Himeno, 1981, Crane, Eda, and Landsburg, 1989). Finally, using Bernoulli's equation, the unsteady resultant hydrodynamic force and the moment generated on the instantaneous wetted surface of the hull can be calculated.

Comparison of the model simulation with experimental data has confirmed the validity of the weak-scatterer hypothesis for steep wave conditions, and the efficiency of the modal potentials method (Pawlowski and Bass, 1991).

1.5 A New Three-Dimensional Time-Dependent Ship Icing Model

The objective of this dissertation is to study the effect of spray icing on ship stability. Thus, determination of the ice load distribution over the ship is required in order to calculate the hydrostatic and dynamic conditions under the ice load. These new hydrostatic conditions are required as input to the dynamics model of Pawlowski and Bass (1991). The icing model of Zakrzewski et al. (1988) is not entirely suitable in this respect since their model output gives the total ice load on each ship component and not the variation within a given component. The type of ship that is modelled in the present research is also different from that used in the model of Zakrzewski et al. (1988). In addition, new spraying data are now available which were not available to Zakrzewski et al. (1988).

Hence, an essentially new ship icing model for the stern trawler MT Zandberg has been developed. This model calculates the total ice accumulation and the ice load distribution over different parts of the topside of the ship. For a different ship, the present icing model may need to be modified. But, using the currently available icing statistics, the total ice load on a different type of ship can be estimated by correlating the predicted total ice load for the Zandberg and the observed total ice loads for that ship. The present ship icing model is different from that of Zakrzewski et al. (1988) in various ways. Improvements have been made to rectify several shortcomings of their model. The principal differences are the following:

(a) The entire topside of the vessel, including the deck, wheelhouse, and mast, is superimposed with a well organized grid cell network. As a result of this simplified design, the ice load distribution can be more accurately represented.

(b) The spray generation and the spray flux algorithm used in the new icing model is based on experimental data obtained from a scale-model spraying experiment.

(c) The new ship icing model takes into account brine flow on vertical surfaces and the residual brine film on horizontal surfaces.

(d) The shielding (shadowing) effect on spray droplet trajectories is also included in this new ship icing model.

The new ship icing model consists of four parts:

(1) The spraying module which is based on the results of scale-model experiments undertaken in the 200 meter wave tank at the Institute for Marine Dynamics (IMD), St. John's, Newfoundland. Using statistical analysis, Froude scaling, trajectory modelling, and continuity of spray mass, a full-scale flux equation has been derived.

(2) The spray thermodynamics module is based on droplet trajectory and heat conservation equations. Using this, the temperature of the droplets impinging on the superstructure can be determined.

(3) The impinging droplets form a brine film on the surface of the superstructure. The brine flow rate is crucial in determining the ice accretion rate. In the brine film dynamics module, the film is assumed to flow downwards on all vertical surfaces and Nusselt's equation is used to calculate the flow rate. On horizontal surfaces, no brine flow is considered.

(4) The ice accretion rate on the superstructure, due to the freezing of the brine film, is calculated based on a heat flux balance equation. In the icing module, the heat transfer coefficients for smooth flat plates under a turbulent flow regime or for cross flow over a cylinder in a turbulent flow regime are used as is appropriate.

In Chapter 2, model spraying experiments and the data analysis, which allow for the development of a model-scale empirical equation for the spray mass distribution over the deck of the MT Zandberg model, are discussed. Froude number scaling is used to transform this model-scale equation into a full-scale spray flux equation. This equation is used in Chapter 3 to develop a new three-dimensional spraying model to calculate the spray flux onto the components of the ship superstructure taking into account the effect of wind and air drag on the trajectory of spray droplets and conservation of spray mass. A novel ship icing model is developed in Chapter 4. This is done with a thorough analysis of the thermodynamic properties of brine and saline ice, and the physics of brine flow and ice accretion. In Chapter 5, a theoretical study of the effect of icing on the ship's static stability is presented. In Chapter 6, quantitative results on the effect of icing on the ship's static stability and its dynamic performance are presented and discussed. Some suggestions on navigation safety under severe icing conditions are also presented in this chapter. Finally, summary, conclusions and recommendations are given in Chapter 7.

CHAPTER 2 : SPRAYING DATA ANALYSIS

People living close to the sea are probably familiar with ship/wave collision-generated spray. This phenomenon is caused by the slamming of a ship's hull into oncoming waves. A large spray cloud consisting of numerous water droplets is generated around part of the perimeter of the hull. Due to the effect of wind drag and the forward motion of the ship, the spray droplets may impact the ship's surface. Ship/wave collision is similar in nature to waves slamming a vertical wall. The main difference between these two processes is that the former involves a moving boundary (the ship hull) while the latter involves a fixed boundary (the vertical wall). Kirby (1985) studied the problem of spray overtopping caused by the interaction of the waves with the vertical walls of the Tarsiut Island in the Canadian Beaufort Sea.

Collision-generated spray is particularly dangerous for ships travelling in cold regions. In this environment, the impinging spray droplets freeze on the superstructure and the entire vessel may accumulate many tonnes of ice in only a few hours. According to Zakrzewski and Lozowski (1988), collision-generated spray is the most common cause of ship icing (Shekhtman, 1967, 1968; Panov, 1976). Therefore, it is important to know how much spray can be produced during a ship/wave collision under given conditions in order to determine the icing rate.

There are two possible ways to collect spraying data. The first is by direct measurement of the spray mass on a full-scale ship. Zakrzewski and Blackmore have tried to collect the spray mass by putting buckets on the foredeck of the full-scale stern trawler MT "Zandberg". However, their efforts were unsuccessful due to various technical problems (personal communications with Zakrzewski and Blackmore). In addition, the captain also did not allow them to work on the foredeck because it was too dangereous.

Another way to obtain spraying data is through scale-model experiments in a wave tank. The experimental data is transformed into full-scale data using an appropriate scaling method. This type of experiment can easily be carried out whenever the required facilities are available, and personal safety is not a problem. Familiarity with the ship icing literature suggests that scale-model spraying experiments have not been done before. Therefore, we decided to investigate this physical phenomenon and to use the spraying data to formulate a full-scale spray flux equation.

In order to simulate the collision-generated spray phenomenon, a 1 to 13.43 scale ship model (with length 3.83 m and beam 0.86 m) of the stern trawler MT "Zandberg" was deployed in the clear water wave tank at the Institute for Marine Dynamics (IMD), National Research Council, St John's, Newfoundland. Twenty-three collecting gauges were installed over the deck of the model ship in order to collect spray drops (see Figure 2.1). These gauges protrude 5 cm above the deck to protect the collectors from "green" water that may flood the deck. Ship/wave collision produces ejected water which may consists of three components: "green" water, airborne water which has not been broken into droplets, and airborne spray droplets. In the spraying experiments, only the latter two components and any "green' water with thickness greater than 5 cm were collected. During the experiments, it was found that the model superstructure was likely to hit the carriage for runs requiring wave heights greater than 0.2 metres. Therefore, it was decided to remove the wheelhouse from the scale model.

The ship model was ballasted into its appropriate draft corresponding to the full-scale value and placed under the carriage in the water tank. The model was powered with a single propeller and was only allowed to move freely in pitch, heave, and surge. The wave spectrum (for fully developed irregular seas) was generated by an electric wave maker. The model had to be controlled in such a way as to keep it moving with the carriage at constant speed. The wave tank is about 200 metres long and for this reason only runs with a model speed of 0.5 ms^{-1} or lower would allow coverage of the entire wave spectrum during a single carriage trip down the length of the tank. Therefore, it sometimes requires several passes down the tank in order to cover the entire wave spectrum, depending on the model ship's speed. In this case, after each pass, spray water in each gauge was weighed and recorded before the next pass started.

Wind was also included in the spraying experiments. An air flow above the model's deck in a direction opposite to the ship motion was produced using a wind-

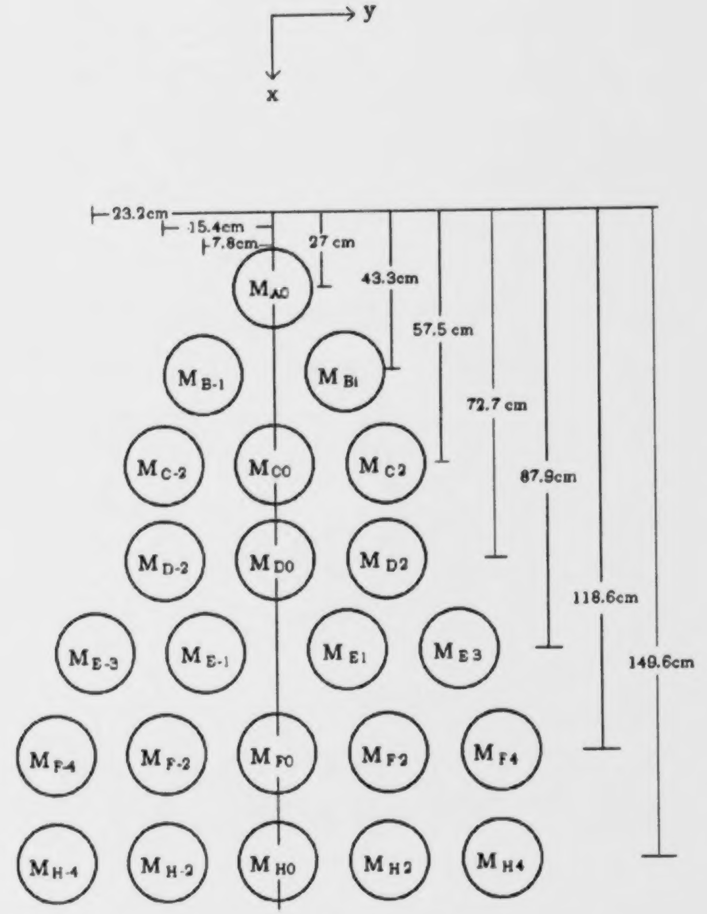
y
x
23.2cm
15.4cm
7.8cm
27 cm
43.3cm
57.5 cm
72.7 cm
87.9cm
118.6cm
149.6cm
M_{A0}
M_{B-1}
M_{B1}
M_{C-2}
M_{C0}
M_{C2}
M_{D-2}
M_{D0}
M_{D2}
M_{E-3}
M_{E-1}
M_{E1}
M_{E3}
M_{F-4}
M_{F-2}
M_{F0}
M_{F2}
M_{F4}
M_{H-4}
M_{H-2}
M_{H0}
M_{H2}
M_{H4}

Figure 2.1: Distribution of the spray collecting gauges over the deck of the scale-model of MT Zandberg (without the wheelhouse). Each collecting gauge has a diameter of 10.17 cm.

generating system which was installed under the carriage. A more detailed description of the spraying experiment and the wind system is given in Lozowski and Zakrzewski (1991 and 1992).

In the following discussion, an analysis of the spraying data is presented and an empirical equation, at model-scale, for the water mass distribution over the ship's deck is derived. This model-scale equation is then transformed into a full-scale equation using Froude scaling.

2.1 Data Analysis

Twenty-two ship spraying experiments under various conditions were performed successfully. The experimental conditions are given in Table 2.1.1. The ship heading was 180°, i.e. directly into the waves (see Figure 2.1.1) , and therefore, ideally, the water mass distribution over the deck should be symmetrical about the x-axis (the longitudinal centreline, see Figure 2.1). However, the experimental results showed that the water mass distribution over the deck was not perfectly symmetrical about the x-axis. This asymmetry may be attributable to the stochastic nature of collision-generated spray. Thus, more model-scale experiments are recommended for future investigation. The mass distributions (raw data) for the 22 experiments are given in Appendix 1A. The experimental results reveal two distinct characteristics. The first is that, generally, the mass collected decreases with increasing longitudinal distance from the perimeter of the hull. The second is that, for each of rows A, B, C, D, and E, the maximum mass collected is usually located on the centreline, and the mass decreases as the transverse distance from the centreline increases. However, there are a few exceptional cases in which the minimum mass occurs on the centreline. Table 2.1.1 gives a summary of the results for each experiment. In order to derive a relation describing the spray mass distribution over the deck, we interpolate linearly or parabolically between the observed data points using a procedure outlined in Appendix 1B.

By following this procedure, we obtain an interpolated symmetrical mass distribution for each experiment. The corresponding mass density distribution is obtained by dividing the mass in each gauge by its cross-sectional area. Since the experiments were undertaken under different conditions and over different durations, we obtained an

Expt#	M_{Gk} (g)	Δt_k (min)	$M_{Gk}/\Delta t_k$ (g/min)	v_s (m/s)	$h_{1/3}$ (m)	u_{10} (m/s)
1	1886.1	4.22	477.29	2.05	0.34	6.8
	469.3	5.37	87.45	2.05	0.26	6.8
3	294.7	4.20	70.17	2.05	0.22	6.8
4	1441.8	4.88	295.25	1.37	0.34	6.8
5	206.1	5.10	40.41	0.68	0.34	6.8
6	-	6.10	-	0.27	0.34	6.8
7	3111.3	5.33	583.37	1.71	0.34	6.8
8	86.9	4.40	19.75	2.05	0.19	6.8
9	4222.9	4.35	970.78	2.05	0.34	7.5
10	1182.5	4.27	277.15	2.05	0.34	6.0
11	2496.7	4.35	573.95	2.05	0.34	3.5
12	2220.1	4.43	500.78	2.05	0.34	0.0
13	94.8	6.55	14.47	0.68	0.34	6.8
14	41.0	4.47	9.18	2.05	0.19	6.8
15	2919.7	4.35	671.20	2.05	0.34	7.5
16	4061.3	4.35	933.63	2.05	0.34	6.0
17	367.4	4.33	84.79	2.05	0.26	6.8
18	5189.8	4.30	1206.93	2.05	0.34	6.8
19	744.7	4.93	150.95	1.37	0.34	6.8
20	2322.6	4.30	540.14	2.05	0.30	6.8
21	5316.2	4.28	1241.15	2.05	0.37	6.8
22	2160.3	3.98	542.34	2.20	0.34	6.8
23	3172.6	4.22	752.39	2.05	0.34	6.8

Table 2.1.1: Total mass collected in the 23 gauges M_{Gk}, total duration of the experiment Δt_k, and air/sea conditions for each experiment. v_s and $h_{1/3}$ are respectively the model-scale ship speed and significant wave height. u_{10} is the wind speed.

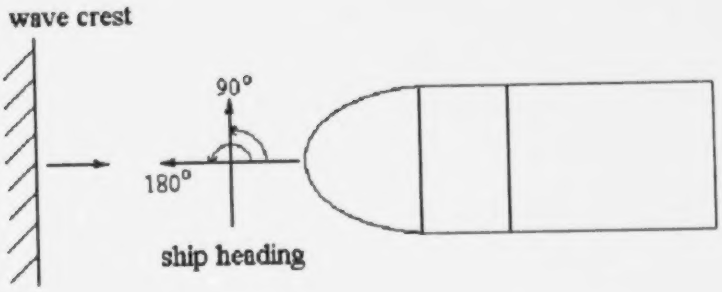
wave crest
90°
180°
ship heading

Figure 2.1.1: A schematic diagram showing the convention of ship heading. A ship heading of 180° means head seas while 90° means beam seas.

empirical formula describing the longitudinal mass distribution, by normalizing the data with respect to the total mass collected in each experiment. Thus, the normalized mass in each collecting gauge is given by:

$$F_m = \frac{m_{ij}A}{M_{Gk}} = \frac{M_{ij}}{M_{Gk}} \tag{2.1.1}$$

where

F_m : normalized mass.

A : cross-sectional area of the cylindrical gauge (A=81.23 cm^2).

m_{ij} : mass density in the gauge located in the i^{th} row and j^{th} column (gcm^{-2}).

M_{Gk} : total mass collected in all the gauges in the k^{th} run (g).

M_{ij} : mass collected in the gauge located in the i^{th} row and j^{th} column (g).

The normalized data sets are given in Appendices 1C and 1D.

2.2 Empirical Equation for the Longitudinal Mass Distribution

The normalized masses for columns y=0, y=±7.8 cm, and y=±15.4 cm are plotted semi-logarithmically in Figures 2.2.1a to 2.2.1c. Three experiments, #8, #13, and #14, have been discarded and not plotted, because very little spray (<100 g) was collected. Due to the stochastic variability of ship generated spray, which is prominent with low masses, incorporating these data into the analysis seems inappropriate.

We can see from these three plots that the normalized mass F_m appears to decrease exponentially with increasing longitudinal distance (measured from the perimeter of the hull). A linear regresion method was used to find the three best fit lines to these data. The result is an expression for the normalized mass F_m as a function of the longitudinal distance x at a particular y:

$$\ln(F_m) = \alpha + \beta x \tag{2.2.1}$$

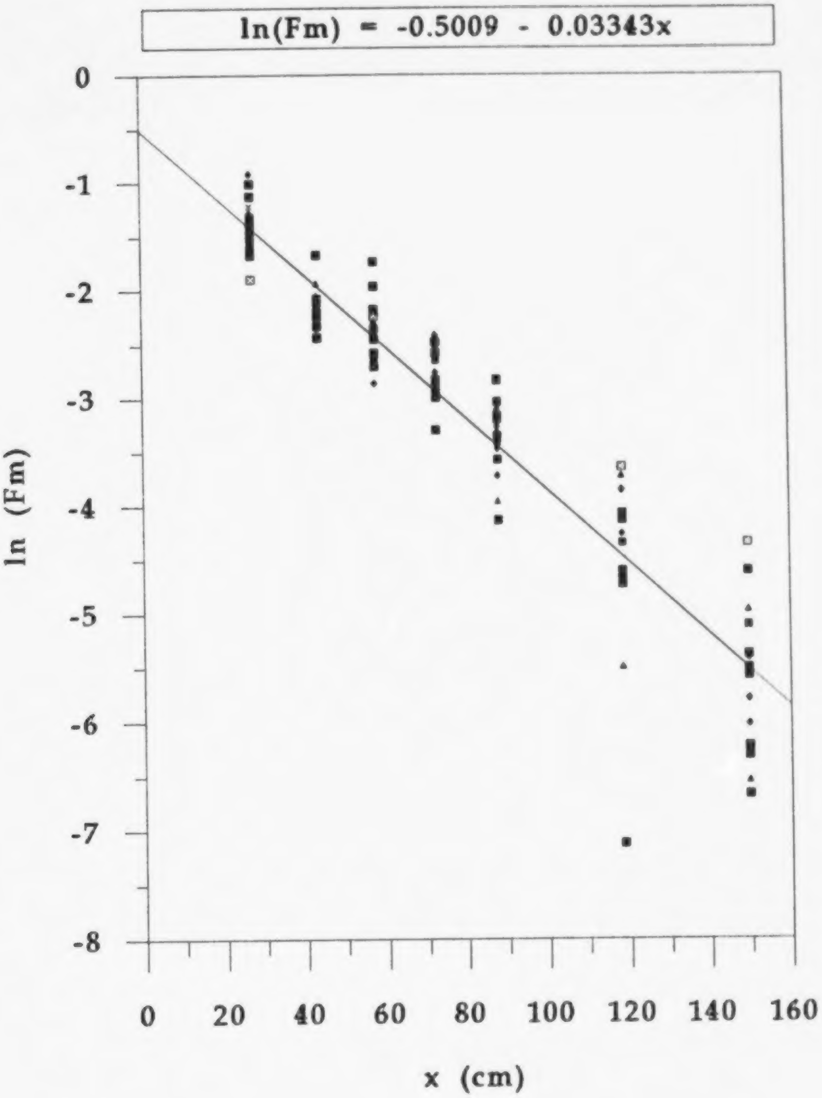

(a)

Figure 2.2.1: The normalized mass distribution as a function of x measured from the perimeter of the hull along the longitudinal lines: (a) y = 0 cm, (b) y = ± 7.8 cm, and (c) y = ± 15.4 cm. There are 22 symbols in each graph representing 22 spraying experiments. These symbols scatter around the best fit line.

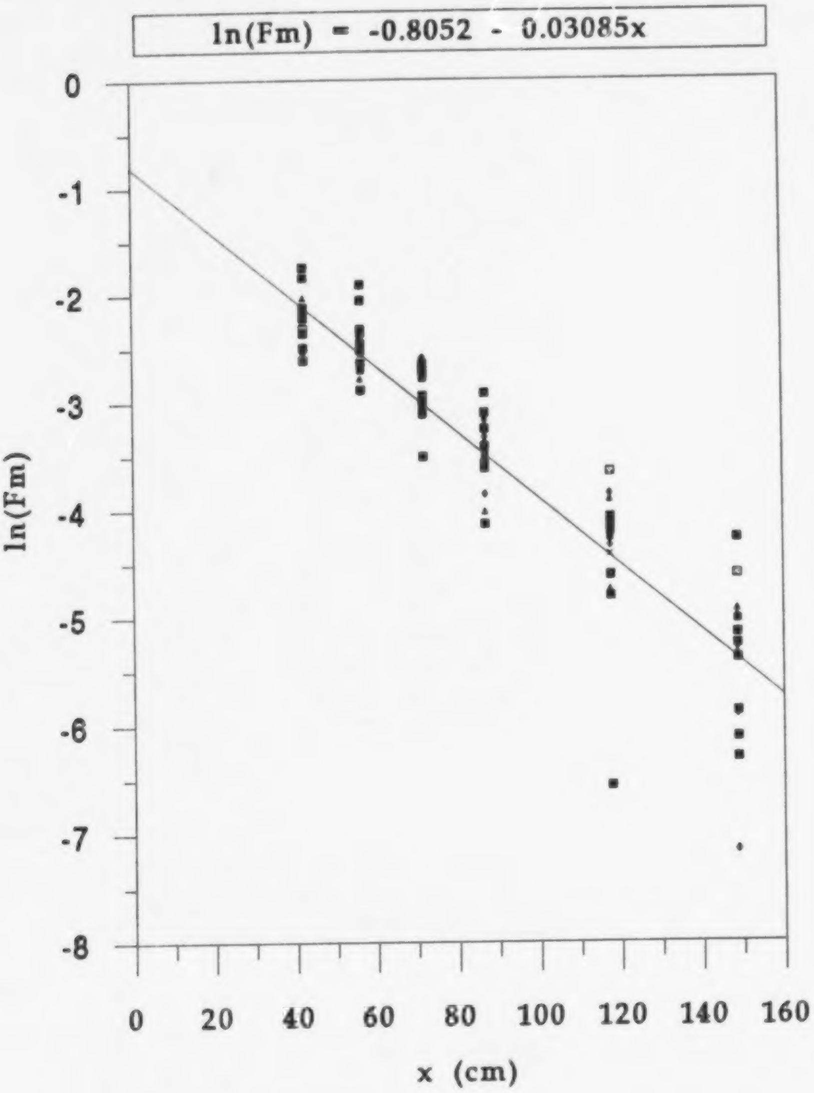
ln(Fm) = -0.8052 - 0.03085x
0
-1
-2
-3
-4
-5
-6
-7
-8
ln(Fm)
0
20
40
60
80
100
120
140
160
x (cm)

(b)

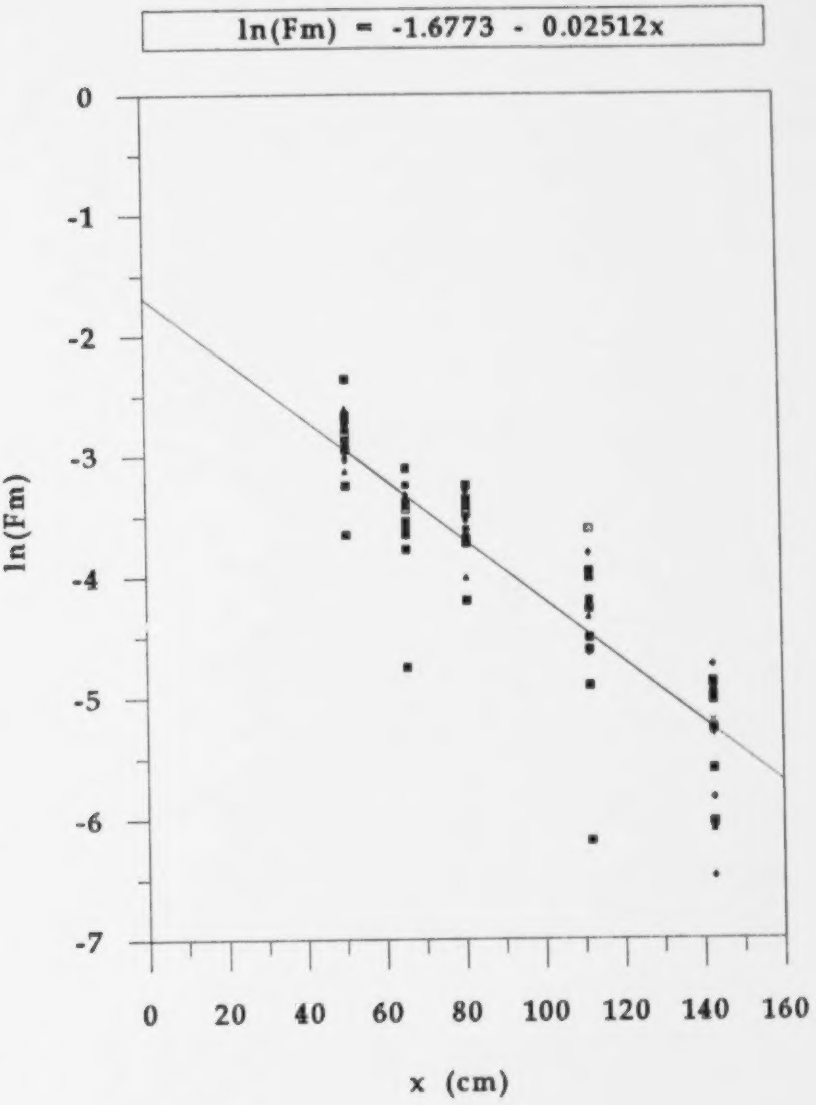
ln(Fm) = -1.6773 - 0.02512x
0
-1
-2
-3
-4
-5
-6
-7
ln(Fm)
0
20
40
60
80
100
120
140
160
x (cm)

(c)

where α and β are functions of the transverse distance y. Three values of α and β corresponding to y = 0, 7.8 cm, and 15.4 cm are listed in Table 2.2.1. Only positive values of y are considered because of symmetry. Using Equation 2.1.1, Equation 2.2.1 may be written in a mass flux density form:

$$m'_{ij} = \frac{M_{ij}}{A\Delta t_k} = \frac{M_{Gk}}{A\Delta t_k} e^{\alpha+\beta x} \qquad (2.2.2)$$

where

m'_{ij}: the mass flux density at the position ij.

Δt_k: the duration of experiment #k.

y (cm)	α	β
0	-0.5009	-0.03343
7.8	-0.8052	-0.03085
15.4	-1.6773	-0.02512

Table 2.2.1: Values of α and β in Equation 2.2.1 corresponding to particular values of y.

Since the values of α and β in Equation 2.2.2 are different at different transverse distances (y), it is necessary to determine how α and β vary with y.

It has been found that the values of α and β in Table 2.2.1 may be fitted by cubic polynominal equations. Using the required conditions that α is maximum at y = 0 (i.e $(d\alpha/dy)_{y=0} = 0$), β is minimum at y = 0 (i.e $(d\beta/dy)_{y=0} = 0$), and the data given in Table 2.2.1, two polynomial equations for α and β have been derived:

$$\alpha = -0.5009 - 5.0440x10^{-3}y^2 + 5.4315x10^{-6}y^3 \qquad (2.2.3)$$

$$\beta = -0.03343 + 4.9967x10^{-5}y^2 - 9.6930x10^{-7}y^3 \qquad (2.2.4)$$

The empirical equation for the spray mass distribution given in Equation 2.2.1 can be rewritten as:

$$M_{ij}=M_{Gk}e^{\alpha+\beta x} \tag{2.2.5}$$

In this equation, M_{Gk} is the total water mass collected in all 23 gauges installed on the ship's deck in experiment k. The amount of spray generated, and hence the total spray mass that actually splashes onto the entire deck, is affected by wave height, ship speed, ship heading, and wind speed. Therefore, it is appropriate to relate the total spray mass collected in all 23 gauges to the above four parameters.

In our experiment, the ship heading is fixed at 180°, i.e. directly into the waves. The experimental data show that at the model-scale the wind speed has no clear effect on the total water mass (see Table 2.1.1, cases 9, 10, 11, 12, 15, and 16). The reason is that the total amount of spray generated during ship/wave collision should only be affected by the momentum transfer between the hull and the wave. This momentum transfer merely depends on ship speed and wave height, but not on wind speed. Therefore, using Table 2.1.1, the total collected water mass can be expressed as a function of significant wave height ($h_{1/3}$) and ship speed (v_s). Figures 2.2.2a and 2.2.2b show how $M_{Gk}/\Delta t$ varies with $h_{1/3}$ and v_s. Best fit straight lines to the data on these figures are shown at the top. Thus, it appears that $M_{Gk}/\Delta t$ is approximately proportional to $h_{1/3}^7$ and v_s^3. Figure 2.2.3 shows how $M_{Gk}/\Delta t$ varies with $v_s^3 h_{1/3}^7$. The results (Table 2.1.1) from the model spraying experiments indicate that both the ship speed and wave height must exceed certain thresholds in order to produce a measurable amount of spray water (see also Figures 3.4.1a and 3.4.1c). The thresholds for the model-scale ship speed and wave height are approximately 0.27 ms^{-1} and 0.19 m respectively. Since the thresholds are small, we have assumed for simplicity that the spray generation function passes through $v_s = 0$ and $h_{1/3} = 0$. Then, $M_{Gk}/\Delta t$, when expressed in (kg/min), is given by:

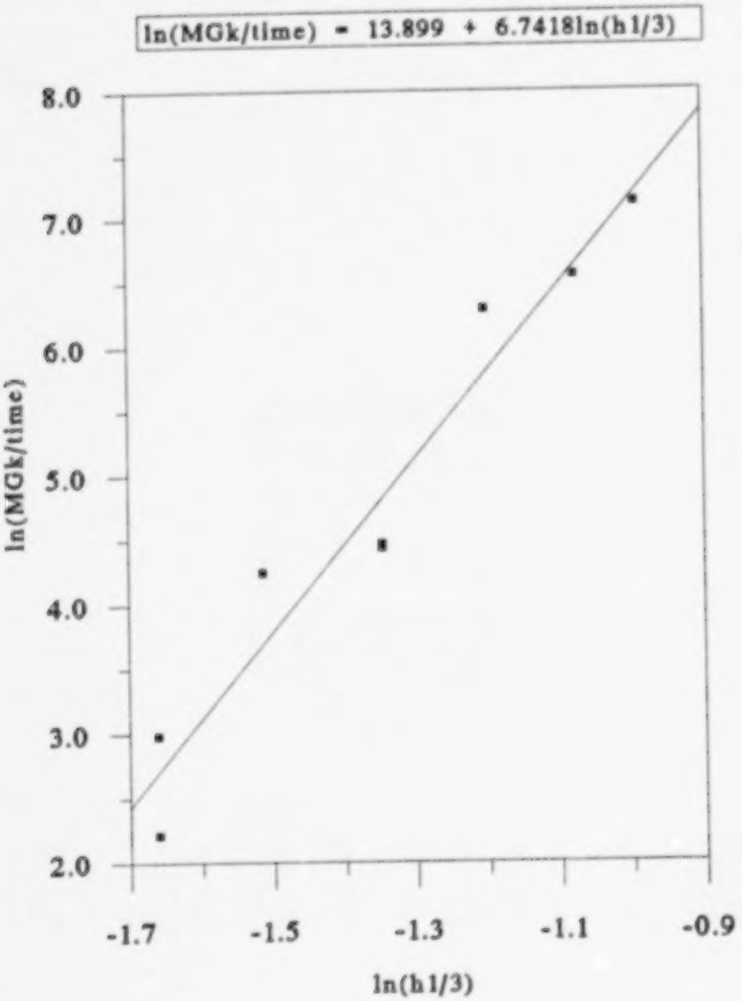

(a)

Figure 2.2.2: Variation of the total spray mass collected per minute with (a) significant wave height, (b) ship speed. Experiments # 1, 9, 10, 11, 12, 15, 16, 18, and 23 are averaged together as a single data value (see Table 2.1).

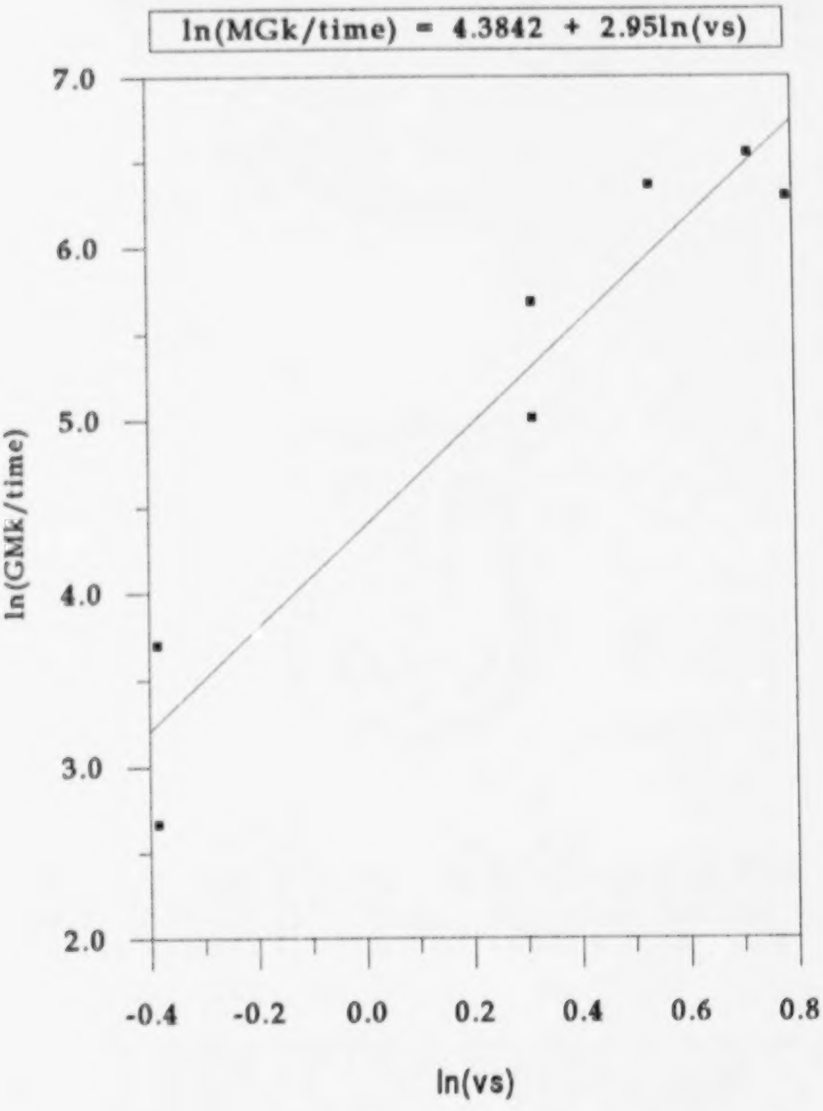
ln(MGk/time) = 4.3842 + 2.95ln(vs)
7.0
6.0
5.0
4.0
3.0
2.0
ln(GMk/time)
-0.4
-0.2
0.0
0.2
0.4
0.6
0.8
ln(vs)

(b)

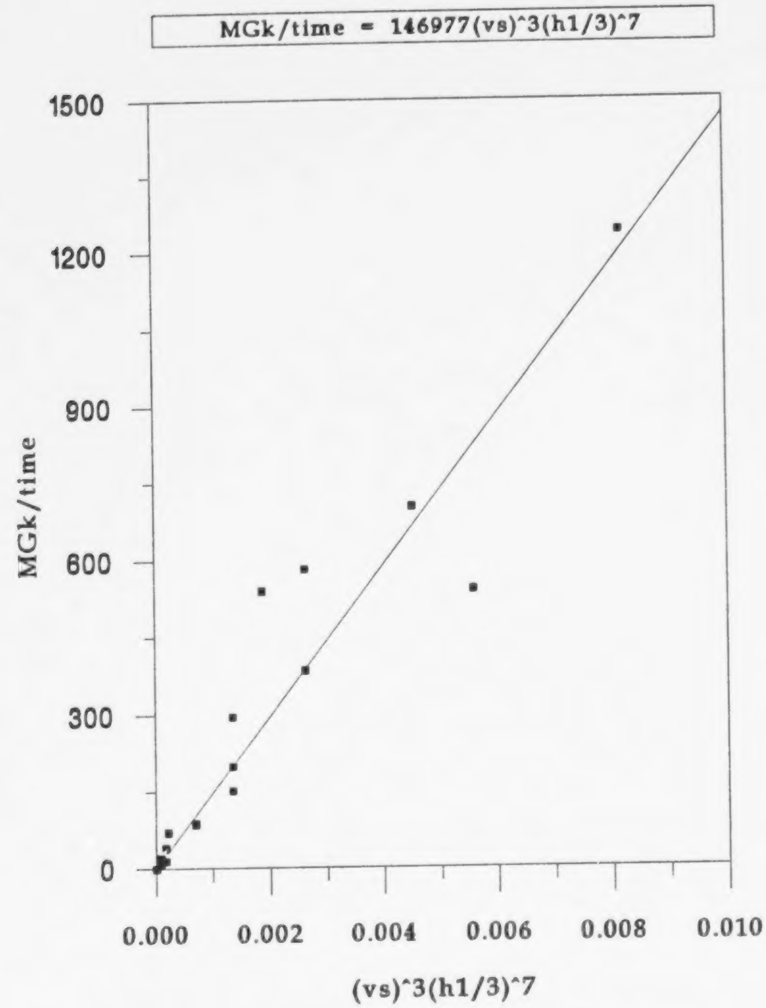

Figure 2.2.3: Variation of the total spray mass collected per minute with $v_s^3h_{1/3}^7$. Experiments 1, 9, 10, 11, 12, 15, 16, 18, and 23 are averaged together as a single data value (see Table 2.1.1).

$$\frac{M_{Gk}}{\Delta t}=Cv_s^3h_{1/3}^7 \qquad (2.2.6)$$

where C = $1.47\text{x}10^2$ $\text{kgs}^3\text{min}^{-1}\text{m}^{-10}$.

In the experiments, $h_{1/3}$ varies by a factor of about two and v_s by a factor of about 3. Before this equation is applied too broadly, it should be verified over a larger range of these parameters. Substituting Equation 2.2.6 into 2.2.5 and using Equation 2.1.1, the spray mass density distribution with all the parameters in S.I. units (except Δt which is in minutes) can be calculated by the following equation:

$$m_{ij}=\frac{C\Delta t v_s^3 h_{1/3}^7}{A}e^{\alpha+\beta x} \qquad (2.2.7)$$

where

m_{ij} : spray mass density in the gauge located in the i^{th} row and j^{th} column (kgm^{-2}).

$\alpha = -0.5009 - 50.440y^2 + 5.4315y^3$.

$\beta = -3.343 + 49.967y^2 - 96.93y^3$ (m^{-1}).

C = $1.47\text{x}10^2$ ($\text{kgs}^3\text{min}^{-1}\text{m}^{-10}$).

A : cross sectional area of the collecting gauge

($8.123\text{x}10^{-3}\text{m}^2$).

Δt : duration of a single run of spraying experiment (min).

v_s : model ship speed (ms^{-1}).

$h_{1/3}$: significant wave height at the model-scale (m).

x : longitudinal distance measured from the perimeter of the hull (m).

y : transverse distance measured from the centreline (m).

2.3 Full-Scale Spray Flux Equation

Thus far, we have obtained a model-scale empirical equation for the spray mass distribution over the deck of the MT Zandberg model. In this section, we use Froude number scaling (Schmitke, 1979) to transform Equation 2.2.7 into a full-scale empirical equation. The Froude number is defined as the ratio of inertial to gravitational forces. If the Froude number for a model-scale ship is the same as that for a full-scale ship, there should be a geometrically similiar ship-wave pattern (Lighthill, 1978). Thus, the model-scale ship speed, ship length, and wave height can all be transformed into full-scale using Froude scaling. The spray droplet trajectories and hence the spray mass distribution for a full-scale ship should also follow this same law of comparison. This is true as long as the wind drag is neglected. In this case, droplets trajectories are only controlled by the inertial and gravitational forces and thus satisfy the Froude number definition. The Froude number is given by:

$$Fr = \frac{v_s}{\sqrt{gl}} \tag{2.3.1}$$

where v_s: the model-scale ship speed (m/s).

g: the acceleration due to gravity (ms^{-2}).

l: the model-scale ship length at the waterline (m).

Froude scaling requires that the Froude number be the same for both the full-scale and model-scale ship. That is:

$$Fr = \frac{v_s}{\sqrt{gl}} = \frac{V_s}{\sqrt{gL}} \tag{2.3.2}$$

where

V_s : full-scale ship speed (m/s).

L : full-scale ship length at the waterline (m).

Thus, we obtain the following ratio:

$$\frac{V_s}{v_s} = \sqrt{\frac{L}{l}} = \sqrt{S_m} \tag{2.3.3}$$

where S_m is the geometrical scaling factor.

Lozowski and Zakrzewski (1992) state that the length ratio of the full- scale MT Zandberg to the model-scale MT Zandberg, S_m, is 13.43. Thus, the parameters below can be scaled to full-scale as follows (parameters with subscript F are at full-scale):

(i) Ship length

$$L = S_m l \tag{2.3.4}$$

(ii) Ship velocity

$$V_s = \sqrt{S_m} v_s \tag{2.3.5}$$

(iii) Distance

$$x_F = S_m x \quad , \quad y_F = S_m y \tag{2.3.6}$$

(iv) Wave height

$$H_{1/3} = S_m h_{1/3} \tag{2.3.7}$$

where

$H_{1/3}$: the full-scale significant wave height (m).

$h_{1/3}$: the model-scale significant wave height (m).

(v) Time

$$\Delta t_F = \sqrt{S_m}\Delta t \qquad (2.3.8)$$

(vi) Mass of water collected

Since the density of water at the model-scale is the same as that at full-scale, and volume V $\propto$ L^3, we have:

$$M_F = S_m^3 M \qquad (2.3.9)$$

Using these six relations, we can now derive a full-scale empirical equation for the spray mass distribution over the deck. We begin with the model-scale empirical Equation 2.2.5 in the form:

$$\ln(\frac{M_{ij}}{M_{Gk}}) = \alpha+\beta x \qquad (2.3.10)$$

The full-scale form of this equation is:

$$\ln(\frac{M_{ijF}}{M_{GkF}}) = \alpha_F+\beta_F x_F \qquad (2.3.11)$$

It is obvious that:

$$\frac{M_{ij}}{M_{Gk}} = \frac{M_{ijF}}{M_{GkF}} \qquad (2.3.12)$$

From Equations 2.3.10, 2.3.11, 2.3.12, and 2.3.6, we obtain the following two relations:

$$\alpha_F = \alpha \tag{2.3.13}$$

$$\beta_F = \frac{\beta}{S_m} \tag{2.3.14}$$

The model-scale expressions for α and β are given by Equation 2.2.7. The full-scale expressions for α_F and β_F have similar forms:

$$\alpha_F = a + by_F^2 + cy_F^3 \tag{2.3.15}$$

$$\beta_F = d + ey_F^2 + fy_F^3 \tag{2.3.16}$$

Using Equations 2.3.13, 2.3.14, 2.3.6, 2.3.15, 2.3.16 and the equations for α and β in Equation 2.2.7, α_F and β_F can therefore be written:

$$\alpha_F = -0.5009 - \frac{50.44}{S_m^2}y_F^2 + \frac{5.4315}{S_m^3}y_F^3 \tag{2.3.17}$$

$$\beta_F = -\frac{3.343}{S_m} + \frac{49.967}{S_m^3}y_F^2 - \frac{96.93}{S_m^4}y_F^3 \tag{2.3.18}$$

Therefore Equation 2.3.11, may be rewritten as:

$$M_{ijF} = M_{GkF}e^{\alpha_F+\beta_F x_F} \tag{2.3.19}$$

Starting with Equation 2.2.6, the full-scale equivalent total spray mass (M_{GkF}) may be expressed in a similar form:

$$M_{GkF} = C_F \Delta t_F V_s^3 H_{1/3}^7 \qquad (2.3.20)$$

Dividing Equation 2.3.20 by Equation 2.2.6, and using Equations 2.3.5, 2.3.7, 2.3.8, and 2.3.9, C_F is related to C by:

$$C_F = \frac{C}{S_m^6} \qquad (2.3.21)$$

Using Equations 2.3.21, 2.3.20, and 2.3.19, the spray mass distribution over the deck for the full-scale ship may then be expressed as:

$$M_{ijF} = \frac{C}{S_m^6} \Delta t_F V_s^3 H_{1/3}^7 e^{\alpha_F + \beta_F x_F} \qquad (2.3.22)$$

Using the fact that the cross-sectional area of an equivalent collecting gauge in full-scale is $A_F = S_m^2 A$, the full-scale spray flux at position i,j may finally be written as:

$$m'_{ijF} = \frac{m_{ijF}}{\Delta t_F} = \frac{C}{S_m^8 A} V_s^3 H_{1/3}^7 e^{\alpha_F + \beta_F x_F} \qquad (2.3.23)$$

where

$\alpha_F = -0.5009 - (50.44/S_m^2)y_F^2 + (5.4315/S_m^3)y_F^3$.

$\beta_F = -3.343/S_m + (49.967/S_m^3)y_F^2 - (96.93/S_m^4)y_F^3$ (m^{-1}).

$C = 1.47 \times 10^2$ ($kgs^3 min^{-1} m^{-10}$).

$A = 8.123 \times 10^{-3}$ (m^2).

$S_m = 13.43$.

Δt_F : full-scale time duration (min).

V_s : full-scale ship speed (ms^{-1}).

$H_{1/3}$: full-scale significant wave height (m).

x_F : full-scale longitudinal distance measured from the perimeter of the hull (m).
y_F : full-scale transverse distance measured from the centreline (x-axis) (m).
m_{ijF} : spray mass density at position ij on the deck of the full-scale ship (kgm^{-2}).
m'_{ijF}: spray flux density at position ij on the deck of the full-scale ship ($kgm^{-2}min^{-1}$).

2.4 Discussion of the Full-Scale Spray Flux Equation

Using Equation 2.3.23, the spray flux along the three longitudinal lines corresponding to $y_F = 0$, 2, and 4 m is calculated for $V_s = 3\ ms^{-1}$ and $H_{1/3} = 4.5$ m. The result is shown in Figure 2.4.1. It is clear that the spray flux decreases exponentially as x_F increases. This distribution pattern is similar to that suggested by Borisenkov et al. (1975). The spray flux decreases transversely as well. For $y_F = 4$ m, very little spray water is received along the entire longitudinal line. This behavior is the result of the dependence of α_F and β_F on y_F in Equation 2.3.23.

Figure 2.4.2 shows the spray flux distribution along $y_F = 0$ for different ship speeds and wave heights. This figure shows that when the results are plotted semi-logarithmically, the spray flux distributions have the same slope but different magnitudes depending on the ship speeds and wave heights (Figure 2.4.2). This means that the spray flux distributions for different ship speeds and wave heights have a similar form determined by the exponential function in Equation 2.3.23, but with different magnitudes determined by $V_F^3 H_{1/3}^7$.

Results from the model experiments indicate that the spray flux distribution is ambiguously affected by wind speed, at least within the range of wind speed applied during the experiment. However, this is unlikely to be the case at full-scale. In the experiments, the wind speed was scaled down according to Froude scaling, but the generated spray droplet sizes could not be scaled down. In the natural environment, the spray droplets generated by ship/wave collision are around the same size as or smaller than those generated in the laboratory, due to a stronger ship/wave impact and higher wind speeds which can break the spray droplets into smaller sizes. Consequently the

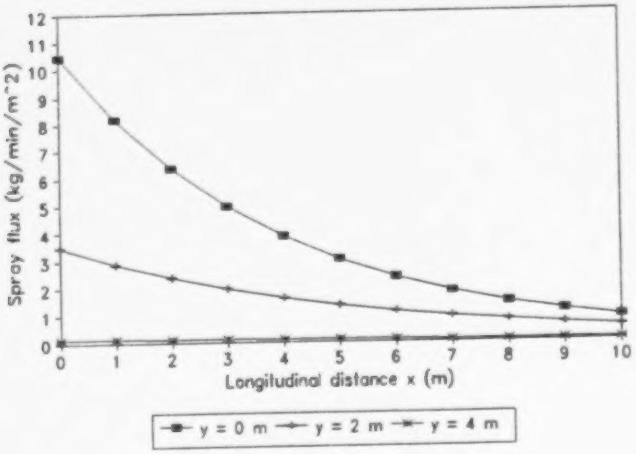

Figure 2.4.1: The spray flux distribution along the longitudinal lines $y_F = 0$, 2, and 4 m for $V_s = 3\ \mathrm{ms}^{-1}$ and $H_{1/3} = 4.5$ m. The longitudinal distance x_F is measured from the perimeter of the hull.

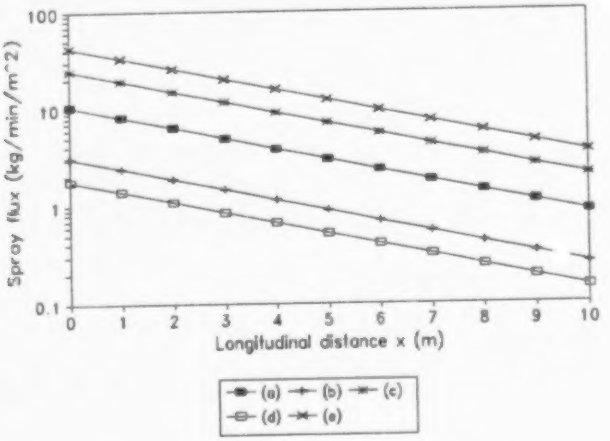

Figure 2.4.2: The spray flux distribution along $y_F = 0$ for: (a) $V_s = 3\ \mathrm{ms}^{-1}$, $H_{1/3} = 4.5$ m, (b) $V_s = 2\ \mathrm{ms}^{-1}$, $H_{1/3} = 4.5$ m, (c) $V_s = 4\ \mathrm{ms}^{-1}$, $H_{1/3} = 4.5$ m, (d) $V_s = 3\ \mathrm{ms}^{-1}$, $H_{1/3} = 3.5$ m, (e) $V_s = 3\ \mathrm{ms}^{-1}$, $H_{1/3} = 5.5$ m.

spray droplets are more prone to the effect of wind drag in the natural environment. Thus, it can be concluded that Equation 2.3.23 has been derived under conditions in which there is effectively "no wind" (i.e no wind drag) and the spray transport onto the deck occurs merely by the relative forward motion of the ship.

In order to make Equation 2.3.23 applicable at full-scale, the effect of wind drag has to be incorporated. As discussed earlier, the total amount of spray generated is determined by ship speed and wave height only. This is also assumed to be true for full-scale. Thus, the effect of wind drag is simply to transport the spray droplets farther downstream. This important concept makes it possible to calculate the spray flux distribution during a full-scale ship/wave collision using the empirical Equation 2.3.23, but with suitable modification for wind effect as described in Chapter 3.

2.5 Concluding Remarks on the Model Spraying Experiments

A model-scale spray flux equation has been derived based on twenty-two spraying experiments performed in the IMD wave tank. Using a Froude number scaling method, the model-scale equation has been transformed into a full-scale spray flux distribution equation. Since the experimental results indicate that the spray distribution is not greatly affected by the wind speed over the scale-model of MT Zandberg, it can be concluded that this full-scale spray flux equation is valid for conditions in which there is effectively "no wind". This full-scale equation, which indicates that the spray flux distribution decreases exponentially along the x-axis, is consistent with the formula proposed by Borisenkov et al. (1975):

$$w = 2.36x10^{-5}e^{-0.55h'} \qquad (2.5.1)$$

where

w: liquid water content (cm^3 cm^{-3}).

h': elevation above the deck (m).

The formula of Borisenkov et al. suggests that the spray mass decreases exponentially with height. It could be expected that with a wind and gravity such a vertical exponential distribution might translate into a horizontal exponential distribution. However, our equation also takes into account the lateral variation of spray flux while Borisenkov's formula does not. The experimental results indicate that the total mass of spray is determined only by the ship speed and wave height according to $V_s^3 H_{1/3}^7$. The effect of wind drag is merely to re-distribute the spray further downstream. This concept allows us to calculate the spray flux distribution during a full-scale ship/wave collision in a natural environment where the effect of wind drag becomes important. This will be discussed in more detail in Chapter 3.

CHAPTER 3 SPRAYING MODEL

Ship-wave collision generated sea spray is one of the most important physical phenomena that must be understood in order to calculate the icing on a ship. The amount of ice accreted on the ship's decks and superstructure depends on how much spray is blown onto the ship, as well as on the heat transfer. More brine impinging on the ship does not necessarily mean that more ice will be accreted. The explicit dependence of ice accretion on the spray flux and the heat transfer will be discussed in Chapter 4. In this chapter, the calculation of the spray flux onto various components of the full-scale trawler MT Zandberg, under high wind and heavy sea conditions, will be discussed.

In Chapter 2, a two-dimensional empirical equation for the spray flux to the deck of the full-scale Zandberg was derived. In this equation, the longitudinal distance is measured from perimeter of the hull. If we define a coordinate system with the origin located at the bow, Equation 2.3.23 should be rewritten as:

$$m(x,y) = kV_s^3 H_{1/3}^7 e^{\alpha+\beta(x-x_{hull})} \tag{3.1}$$

where x and y are full-scale longitudinal and transverse distances from the bow. x_{hull} is the x-coordinate of a point located on the hull perimeter at a transverse distance y. Equation 3.1 was derived under the specific assumption that there is no wind and no air drag acting on the spray and for full-scale ship speed V_s and significant wave height $H_{1/3}$ in the range (2.5, 8.0) ms^{-1} and (2.6, 5.0) m, respectively. In this chapter a mathematical method is developed, starting with Equation 3.1, to compute the spray flux onto various components, allowing for the effects of wind and air drag. This method is derived based on the effect of wind drag on changing the droplet trajectory. Figure 3.1 shows that, under a situation without wind drag, a given amount of spray droplets will fall onto box A over a given period of time. The boundary of the box denotes the destination of the droplet trajectories. When the effect of wind drag is taken into account, the same amount of spray droplets will now fall onto box B (with the same period of time), where the

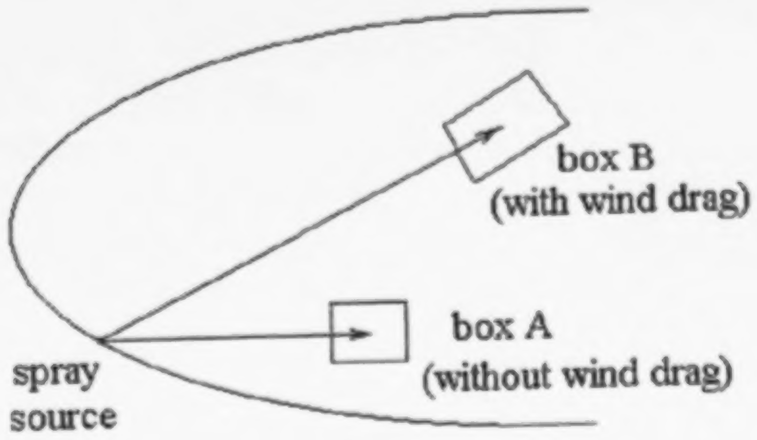
box B
(with wind drag)
box A
(without wind drag)
spray
source

Figure 3.1: A schematic diagram showing the effect of wind drag on the spray receiving zone. Without wind drag, the spray receiving zone is box A. With wind drag, the spray receiving zone transforms to box B.

location, shape and size of box B will be different from box A because wind drag has changed the droplet trajectories.

We will begin with a discussion of the ship's architecture and the development of an appropriate grid cell network. Next, we will discuss the details of the computation of the spray flux onto the ship's foredeck, wheel house, and mast. Finally, a discussion of the spray flux results will be presented.

3.1 The Architecture of the MT Zandberg and the Formulation of a Grid Cell Network

It is impractical at this stage to include every detail of the structure of the MT Zandberg in the spraying model. For simplicity, we include only the ship's foredeck, wheelhouse, the deck behind the wheelhouse, and the mast. The basic configuration and dimensions of this idealized ship are shown in Figure 3.1.1. Behind the wheelhouse, there is a large region of the deck used for fishing (shaded region in Figure 3.1.1). Spraying and icing are assumed not to occur in this area of the ship. A three-dimensional grid cell network is superimposed on the ship (see Figure 3.1.2).

Equation 3.1 is a two-dimensional equation which is a function only of the longitudinal distance x and the transverse distance y along the deck. But the spray flux to a given grid cell will also depend on its vertical distance above the deck. The main objective of this chapter, then, is to develop a numerical model to calculate the spray flux onto any grid cell whose geometric centre is located at a particular Cartesian coordinate (x, y, z). The origin of this Cartesian coordinate system is located at the bow. All the grid cells are designed to be either triangles, squares, or trapezoids, except for the mast which consists of cylindrical grid cells. Certain grid cells have one side bounded by the hull. These grid cells have one curved boundary. However, in order to calculate the geometrical centre and the surface area of these grid cells, the curved boundaries are approximated by straight lines. In order to achieve a reasonable spatial precision, the area of each grid cell is not allowed to exceed 1 m^2. The mast is divided into nine cylindrical sections each with a length of 1 m. The surface area of each section exceeds 1 m^2.

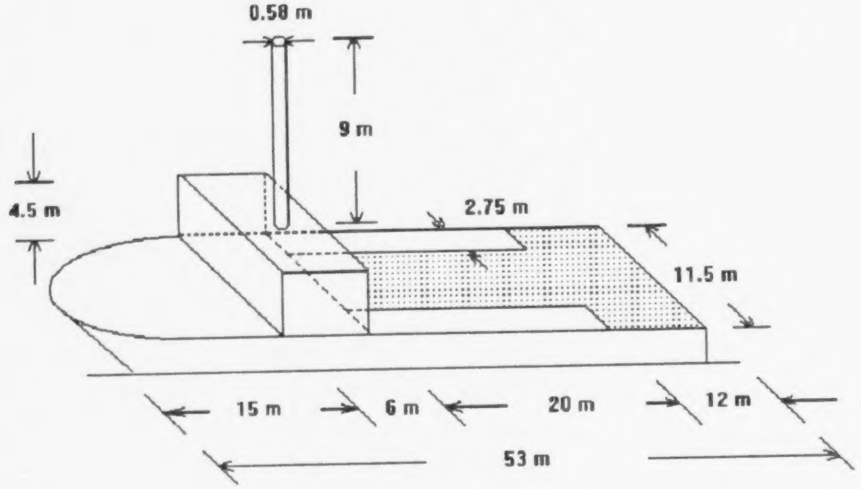
0.58 m
9 m
4.5 m
2.75 m
11.5 m
15 m
6 m
20 m
12 m
53 m

Figure 3.1.1: The general configuration and dimensions of the idealized MT Zandberg Trawler.

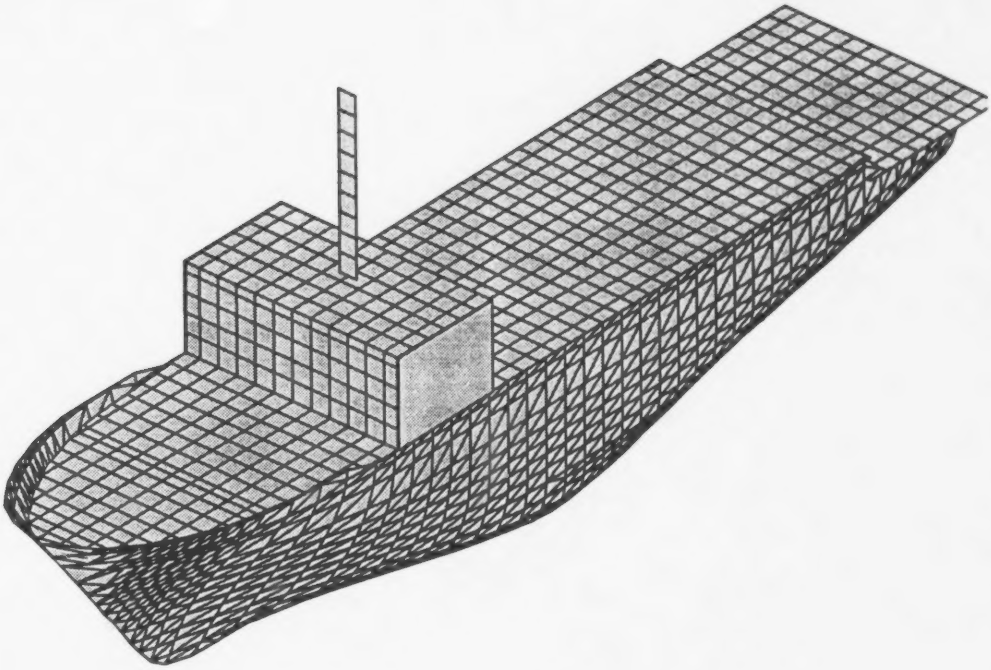

Figure 3.1.2: Digitization of the stern trawler "MT Zandberg". The largest square cells on the superstructure are 1m x 1m. Spray flux and icing rate are computed on each grid cell on the surface of the ship. In the ship dynamics model, the hydrodynamic load is computed on each panel on the hull surface (a more detailed discussion is given in Chapter 7).

However, since only the windward facing surface is prone to icing, the 'effective' icing area is less than 1 m^2. The coordinates of the perimeter of the hull, geometrical centre, unit normal vector and the area of each grid cell are calculated and stored in a file which may be accessed by the spraying program. This file is listed in Appendix 4. The geometrical centre of each cylindrical grid cell on the mast is taken to be along the axis of the mast. In calculating the spray flux onto the surface of the mast, the target point is shifted to the surface by adding the radius of the mast to the coordinates of the geometrical centre (i.e, x,y,z is shifted to x-D/2,y,z).

3.2 Spray Droplet Trajectories and Conservation of Spray Mass

(a) Spray Droplet Trajectories

We suppose a single spherical droplet to be injected vertically upward with a speed V_{zo} in an environment with a uniform and horizontal wind speed of U. Assuming that the mass of the droplet does not change with time due to evaporation and that there is no internal circulation or distortion of the droplet, then the motion of the droplet can be described by (Langmuir and Blodgett, 1946):

$$\frac{d\vec{V}_d}{dt} = -\frac{3C_D\rho_a}{4d\rho_d}|\vec{V}_d - \vec{U}|(\vec{V}_d - \vec{U}) + \vec{g} \qquad (3.2.1)$$

where

C_D: the drag coefficient of the droplet.

d: the diameter of the droplet (m).

ρ_a: the air density (kgm^{-3}).

ρ_d: the density of the droplet (kgm^{-3}).

$\overline{V}_d$: the velocity of the droplet (ms^{-1}).

$\overline{U}$: the wind velocity (ms^{-1}).

Neglecting any internal circulation or distortion of the droplet, the drag coefficient C_D can be approximated by that of a solid sphere (Langmuir and Blodgett, 1946):

$$C_D = \frac{24.0}{Re} + \frac{4.73}{Re^{0.37}} + 6.24x10^{-3}Re^{0.38} \qquad (3.2.2)$$

where the Reynolds number Re is defined by:

$$Re = \frac{|\vec{V}_d - \vec{U}|d}{\nu} \qquad (3.2.3)$$

and υ is the kinematic viscosity of the air (m^2s^{-1}). For Re > 10^5, Equation 3.2.2 does not hold because the boundary layer over the surface of the droplet becomes turbulent. However, in the present case, the Reynolds number for a droplet with a diameter 1.75 mm is usually less than 10^5.

Equation 3.2.1 is a non-linear differential equation which is solved using the Euler forward difference method (Press et al., 1992):

$$\vec{V}_d(t+\Delta t) = \vec{V}_d(t) + \frac{d\vec{V}_d(t)}{dt}\Delta t \qquad (3.2.4)$$

where Δt is the time step which is 0.001 seconds.

Ship-wave collisions generate a spray cloud with a wide droplet spectrum (Zakrzewski and Lozowski, 1989; Itagaki and Ryerson, 1993; Ryerson, 1993). Nevertheless, a monodisperse spray droplet spectrum is assumed here. According to Zakrezwski (1990), an average droplet diameter of 1.75 mm is appropriate.

Brine droplets in the spray cloud may interact with the wind and thus reduce the wind velocity. However, this complicated interaction is ignored here. On the other hand, effects of wind variation with height and due to disturbance in the flow around the ship, and airstream turbulence are also ignored. With the use of the droplet trajectory equation and the two-dimensional spray flux Equation 3.1, together with the concept of conservation of spray mass and an assumed injection velocity independent of wind speed, the calculation of the spray flux to any grid cell on the ship becomes possible.

(b) Conservation of Spray Mass

Let us begin with Equation 3.1. The physical meaning of this equation is as follows. Suppose that a spray cloud is generated by the hull near the bow under a condition in which the air drag is zero. The ship velocity is V_s in a direction perpendicular to the oncoming waves, and the significant wave height is $H_{1/3}$. Then the spray flux to a grid cell, located on the ship's deck, centred at (x,y), with dimensions $\Delta x \Delta y$, can be directly calculated by substituting (x,y) into Equation 3.1. It is assumed that the spray flux is the same everywhere within the grid cell and is equal to the spray flux (m) at the point (x,y) (Figure 3.2.1a). Then the impinging spray mass per unit time is $m\Delta x\Delta y$. In order that the spray droplets can impinge onto this grid cell, they must follow particular trajectories. In Figure 3.2.1a, three trajectories in the frame of reference of the ship are shown. All of these trajectories begin at S at the hull-deck boundary. The first trajectory, with vertical injection velocity $V_{zo} - \Delta V_z$, hits the forward boundary of the grid cell at point A. The second, with vertical injection velocity V_{zo}, hits the centre of the grid cell at point O. The third, with vertical injection velocity $V_{zo} + \Delta V_z$, hits the rear boundary of the grid cell at point B. These three trajectories terminating at A, O, and B respectively characterize the spray zone which covers the grid cell. It should be noted that a frame of reference fixed to the bow is used, and in this case the droplets travel across the deck only because the ship moves forward into the spray with a speed V_s.

Now, let us suppose that there is a uniform wind of speed U blowing horizontally in a direction opposite to the ship's course, and air drag on the droplets is imposed in this situation. The wind is taken to be vertically homogeneous. As a result, the three trajectories ending at A, O, and B will be influenced by the wind drag, and hence transported further downstream. In addition, the trajectories will be stretched farther apart by the wind and thereby cover a larger area (Figure 3.2.1b). In other words, A is translated to A', O to O', and B to B'. We assume that the vertical injection velocities for the three trajectories remain the same since the vertical injection force should be independent of the wind. Hence, it may be concluded that, for a given time interval Δt, the spray mass received by the grid area centred at O without wind would be equal to

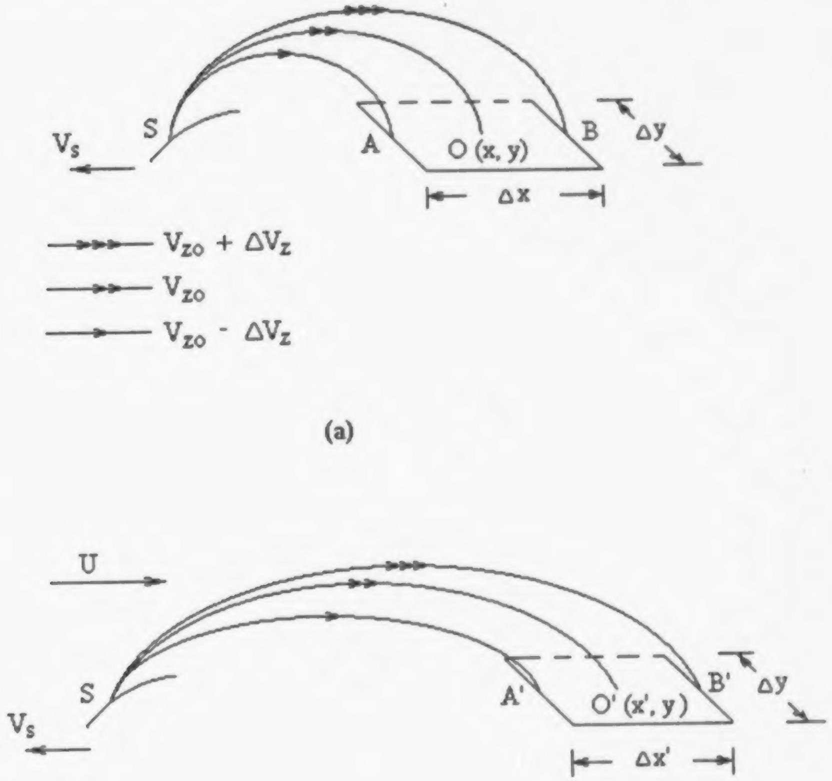
S
V_s
A
O (x, y)
B
Δy
Δx
$V_{zo} + \Delta V_z$
V_{zo}
$V_{zo} - \Delta V_z$
U
S
V_s
A'
O' (x', y)
B'
Δy
$\Delta x'$

(a)

(b)

Figure 3.2.1: Spray droplet trajectories in a situation in which the ship speed is V_s and there is (a) no air drag (b) air drag and a wind speed of U in a direction opposite to the ship's course.

that received by the grid area centred at O' with the effect of wind included in the model. Therefore,

$$m(x,y)\,\Delta x\Delta y\Delta t = m(x',y)\,\Delta x'\Delta y\Delta t \qquad (3.2.5)$$

Thus, the spray flux at O' can be calculated by :

$$m(x',y) = m(x,y)\,\frac{\Delta x}{\Delta x'} \qquad (3.2.6)$$

By combining Equations 3.2.1, 3.1, and 3.2.5, the spray flux to any grid cell on the deck can be readily calculated for a horizontally oriented grid cell. The trajectory theory and the mass conservation concept presented in this section can be extended and modified so that they can be applied to compute the spray flux to different ship components for various wind directions ranging from $0° \leq \theta \leq 90°$. The wind direction is defined in such a way that 0° means head wind whereas 90° means beam wind. The wind angle is measured from the centreline towards the starboard (see Figure 3.2.2). The details of the calculations of spray flux for different wind directions are presented in Appendix 2A.

3.3 Spraying Model Implementation

Two computer models, based on trajectory modelling and the semi-empirical spraying formulae discussed in Section 3.2, have been developed to simulate the ship/wave collision generated spray process. The first model is designed for the case with a wind direction of $\theta = 0°$, and the second model is designed for $0° < \theta \leq 90°$. The computer code is written in Fortran 77, and is listed in Appendix 4.

The input file for the spraying model includes the coordinates of the perimeter of the hull, the coordinates (x, y, z) of the geometrical centre of each grid cell, the grid cell surface area, and its unit outward normal vector (N_x, N_y, N_z).

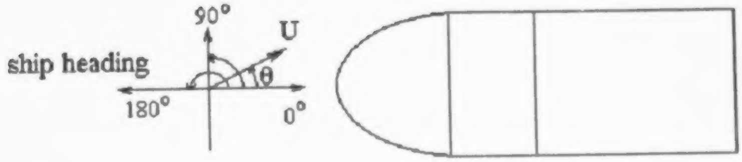
90°
U
ship heading
θ
180°
0°

Figure 3.2.2: A schematic diagram showing the convention of wind direction. A wind direction of 0° means head wind while 90° means beam wind.

With a wind direction of $\theta = 0°$, the geometrical centre of a given grid cell and its corresponding spray source point lie along the same longitudinal line. In these cases, a bisection method (see Appendix 2A) is used to search for the initial vertical velocity which allows the spray droplets to arrive at the target point. The accuracy of the "hit" is specified to be ± 0.01 m. Figure 3.3.1 shows the effect of different time steps on the destination of a droplet at the point of impingement. The curve approaches an asymptotic limit. This figure suggests that beyond $\Delta t = 0.001$s, the effect of a reduced time step on improving the accuracy of the trajectory is negligible. Therefore, a time step of 0.001 s is chosen in the model for calculating droplet trajectories. To calculate the spray flux to the ship's deck, three trajectories are required. The first, with initial vertical velocity V_{zo}, hits the centre of the grid (i.e. the target point). The other two, with initial vertical velocities of $V_{zo} \pm \Delta V_z$ respectively, give rise to the trajectories whose end points bound the target cell which encloses the centre of the grid. The choice of ΔV_z is made so that if V_{zo} is less than 1.0 ms^{-1}, ΔV_z is $0.2V_{zo}$. Otherwise, ΔV_z is 0.2 ms^{-1}. These magnitudes of ΔV_z are small enough so that the length of the spray tube intercepting the target cell does not exceed the grid cell size.

In cases with a wind direction other than 0°, the spray source point and the corresponding target point do not lie on the same longitudinal line. Therefore, it is necessary to search for the appropriate spray source point (located on the perimeter of the hull) for a particular target. The search method is described in detail in Appendix 2A.

The criterion for a successful search for the spray source origin of the trajectory to the grid cell centre O' (see Figures 3.3.2a and 3.3.2b) is that the end point of the termination of the trajectory should lie within a certain range from the centre of the cell. This means that the target point O' is bounded by a resolution box of sides Δx and Δy (the Δx and Δy shown in Figure 3.2.1a are the size of a grid cell and are different from the Δx and Δy defined here). If the end point of the trajectory lies within the box $\Delta x \Delta y$, the search is said to be successful. The resolutions used are as follows:

(i) Deck: $\Delta y = \pm 0.002$ m.
$\Delta x = \pm 0.04$ m.

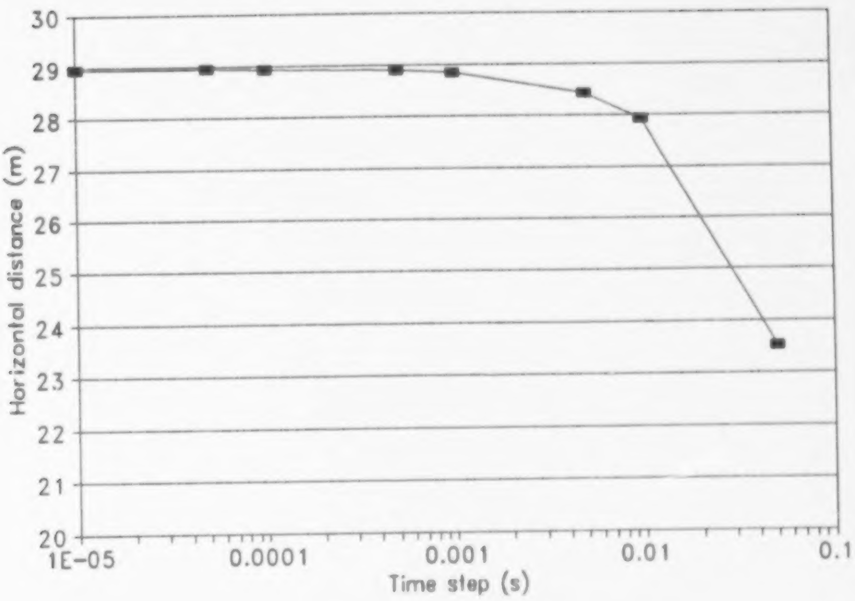

Figure 3.3.1: The effect of the time step on the final destination of a droplet trajectory. The conditions are: T_a = -10 °C, P_a = 1000 mb, RH = 75 %, U = 15 ms^{-1}, and a vertical injection velocity of V_{zo} = 30 ms^{-1}.

(ii) Front of the wheelhouse :

$\Delta z = \pm 0.002$ m.
$\Delta y = \pm 0.04$ m.

(iii) Top of the wheelhouse:

$\Delta z = \pm 0.002$ m.
$\Delta y = \pm 0.04$ m.

(iv) Mast: $\Delta z = \pm 0.002$ m.
$\Delta y = \pm 0.04$ m.

The reason for using a different resolution along different axes is illustrated in Figures 3.3.2a and 3.3.2b. Let us suppose that, for a small wind angle ($\theta \approx 10°$), S is the true spray source point from which a spray droplet is injected with initial vertical velocity V_{z0} and impinges on the deck within the resolution box. But, since the wind angle is small, a lower or higher initial vertical velocity may cause the trajectory to end within the range Δy but beyond the range Δx (Figures 3.3.2a and 3.3.2b). In the spraying model, the search is treated as unsuccessful if either Δx or Δy is exceeded (see Appendix 2A). In such a case, the bisection search starts to look for other spray source points, and the correct one is missed. In order to overcome this problem, we use a value for Δy which is rather smaller than Δx. A similar situation prevails with respect to Δy and Δz on vertically oriented surfaces. The model has been tested in many different ways and it has been concluded that the above resolution is appropriate. However, the model can still generate errors in situations where the wind direction is less than 10° because of the above resolution problem. This limitation can be overcome but only at the expense of much greater computation time. Consequently, the smallest wind angle that the model can handle without serious error is 10°. For wind angles less than 10°, the 0° model is used.

The time step for the calculation of these trajectories is again $\Delta t = 0.001$ s. As mentioned in Appendix 2A, a spray source interval characterized by $S_1(x-\Delta x, y+\Delta y, 0)$, $S(x, y, 0)$, and $S_2(x+\Delta x, y-\Delta y, 0)$ is required. Here a value of 0.1 m is chosen for Δy so that the source interval becomes $S_1(f(y+0.1), y+0.1, 0)$, $S(x, y, 0)$, and $S_2(f(y-0.1), y-0.1, 0)$. Where f is the piecewise equation for the hull perimeter (see Appendix 2A).

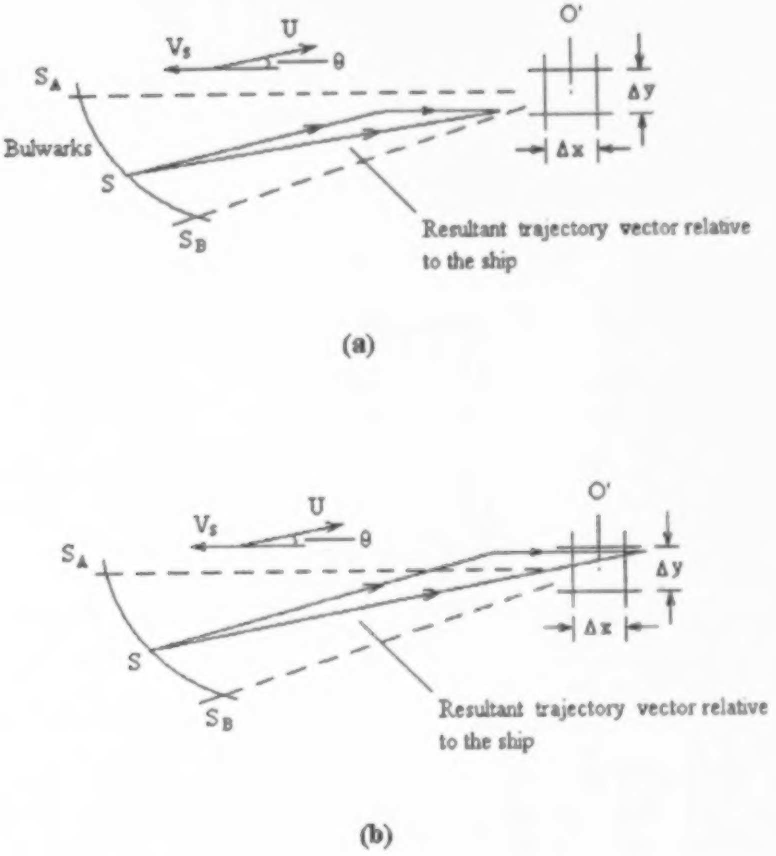
O'
U
V_s
θ
S_A
Δy
Bulwarks
Δx
S
S_B
Resultant trajectory vector relative to the ship
O'
U
V_s
θ
S_A
Δy
Δx
S
S_B
Resultant trajectory vector relative to the ship

(a)

(b)

Figure 3.3.2: Possible destinations of a trajectory beginning at S with initial vertical velocity (a) lower than V_{zo}, (b) higher than V_{zo}.

Five trajectories are initiated at these three points. One begins at S(x, y, 0), with an initial vertical velocity V_{z0}, and hits the point O'. The other four begin at S_1(f(y+0.1), y+0.1, 0) and S_2(f(y-0.1), y-0.1, 0), with initial vertical velocities $V_{z0} \pm \Delta V_z$. When these four trajectories arrive at the surface, they determine the vertices of the target cell (see Figure 2A.2.3a in Appendix 2A). The choice of ΔV_z is the same as that for $\theta = 0°$. The results show that the area formed by these four points is generally smaller than the grid cell size. Some grid cells lying on the top of the wheelhouse, behind the wheelhouse, and on the mast, may not receive spray because of the blocking of droplet trajectories by the superstructure. We call this blocking of trajectories the "shadowing effect". The shadowing effects caused by the wheelhouse and the mast are taken into account in the spraying models. Thus, if a droplet trajectory has to pass through the wheelhouse, which is bounded by $15 \le x \le 21$, $-5.75 \le y \le 5.75$, $z \le 4.5$, or the mast, which is bounded by $(x - 18.5)^2 + y^2 = 0.58^2$, $4.5 \le z \le 13.5$, before hitting its target, the spray flux is set to zero on this target.

3.4 Sensitivity Tests

Sensitivity tests have been performed to show the effect of different atmospheric/oceanographic conditions on the total spray mass, and the effect of different spray droplet sizes on the total spray mass and the spray flux distribution. The standard conditions are: air temperature T_a = -10 °C, air pressure P_a = 1000 mb, relative humidity RH = 75 %, ship speed $V_s = 3$ ms^{-1}, significant wave height $H_{1/3} = 4$ m, wind speed U = 15 ms^{-1}, and wind direction $\theta = 0°$. The standard droplet diameter is D = 1.75 mm. It is not necessary to include all the above parameters in the sensitivity test. Since the effects of T_a, P_a, and RH on the spraying process are negligible, these three parameters are always maintained at their standard values. The effect of V_s, $H_{1/3}$, U, and θ on the total spray mass will be discussed first. Then, the effect of different droplet sizes on the total spray mass and the spray flux distribution will be discussed as well.

I. Effect of Atmospheric/Oceanographic Conditions on the Total Spray Mass

Table 3.4.1 summarizes the total spray mass received on the entire vessel under various conditions. In the spraying experiments performed at IMD, the maximum full-scale ship speed and significant wave height were 8 ms^{-1} and 5 m,

V_s (ms^{-1})	$H_{1/3}$ (m)	U (ms^{-1})	θ (°)	Total spray mass per minute (kg)
3.0	4.0	15.0	0	68.9
1.0	4.0	15.0	0	2.1
2.0	4.0	15.0	0	19.7
5.0	4.0	15.0	0	325.3
8.0	4.0	15.0	0	1344.8
3.0	1.5	15.0	0	0.07
3.0	3.0	15.0	0	9.2
3.0	5.0	15.0	0	328.6
3.0	6.0	15.0	0	1177.4
3.0	4.0	5.0	0	70.6
3.0	4.0	10.0	0	70.0
3.0	4.0	20.0	0	68.4
3.0	4.0	25.0	0	68.4
3.0	4.0	15.0	10.0	69.5
3.0	4.0	15.0	30.0	54.3
3.0	4.0	15.0	45.0	38.9
3.0	4.0	15.0	60.0	30.6
3.0	4.0	15.0	90.0	18.4

Table 3.4.1 : Total spray mass per minute impinging on the entire vessel under different atmospheric/oceanographic conditions with T_a = -10 °C, P_a = 1000 mb, and RH = 75 %.

respectively. Thus, in the present spraying model, it is inappropriate to set these two parameters too far beyond these upper limits. Hence, we have set the upper limit for ship speed and significant wave height at 8 ms^{-1} and 6 m respectively. Figure 3.4.1a shows how the total spray mass varies with ship speed. For a ship speed less than 1 ms^{-1}, the total spray mass is very close to zero. This implies that there exists a threshold ship speed below which there is essentially no spray and above which the spray mass increases rapidly. For the present case, the threshold ship speed is around 1 ms^{-1}. As shown in Figure 3.4.1b, the total spray mass is proportional to ship speed to the power 3.1. This is a slightly greater power than in the empirical Equation 3.1 which has a power of 3. This small discrepancy may be due to the combined effect of vessel motion and wind speed on the trajectory. Despite the small discrepancy, this result shows (as it should) that the spraying model is consistent with the experiments.

The effect of significant wave height on the total spray mass received on the entire vessel is illustrated in Figure 3.4.1c. The threshold wave height is around 1.5 m after which the total spray mass increases rapidly as the seventh power of the wave height (see Figure 3.4.1d). Once again, this shows the consistency between the spraying model and the experiments.

The total spray mass is largely insensitive to wind speed variation as indicated in Figure 3.4.1e. As discussed in Chapter 2, the effect of wind is simply to re-distribute the spray onto different parts of the ship. It has no direct effect on the total spray mass. However, Figure 3.4.1e does show a small decrease in the total spray mass with increasing wind speed. This occurs because higher wind speeds cause some of the spray droplets to pass over the superstructure and return directly to the ocean.

Changing the wind direction from head winds to beam winds reduces the total spray mass received because fewer grid cells lie within the spraying zone. Figure 3.4.1f illustrates this situation. One apparent contradiction is that the total spray mass received at $\theta = 10°$ is slightly higher than that at $\theta = 0°$. The explanation is that the spraying models for $\theta = 0°$ and $0° < \theta \leq 90°$ are different. This small error (~ 1 %) is a result of the different methods of calculation used in the two models.

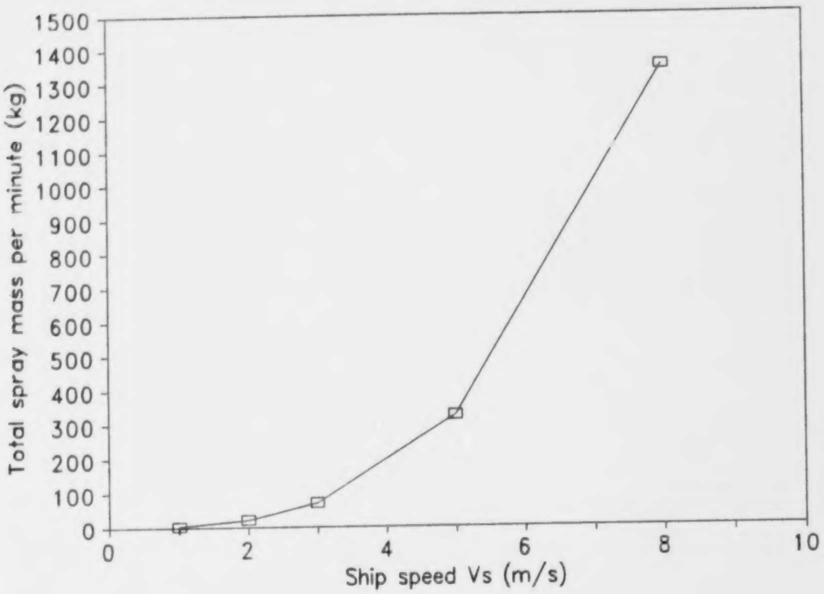

(a)

Figure 3.4.1: Sensitivity test of the spraying models.
a) Total spray mass per minute vs ship speed.
b) Same as (a) but plotted logarithmically.
c) Total spray mass per minute vs significant wave height.
d) Same as (c) but plotted logarithmically.
e) Total spray mass per minute vs wind speed.
f) Total spray mass per minute vs wind direction.
The standard conditions are: air temperature $T_a = -10$ °C, air pressure $P_a = 1000$ mb, relative humidity RH = 75 %, wind speed $U = 15\ ms^{-1}$, ship speed $V_s = 3\ ms^{-1}$, significant wave height $H_{1/3} = 4$ m, and wind direction $\theta = 0°$.

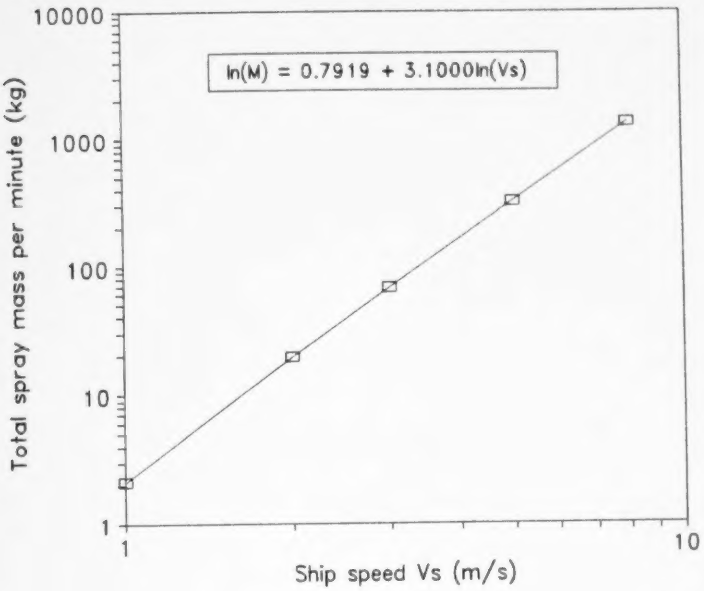

ln(M) = 0.7919 + 3.1000ln(Vs)
10000
1000
100
10
1
Total spray mass per minute (kg)
1
10
Ship speed Vs (m/s)

(b)

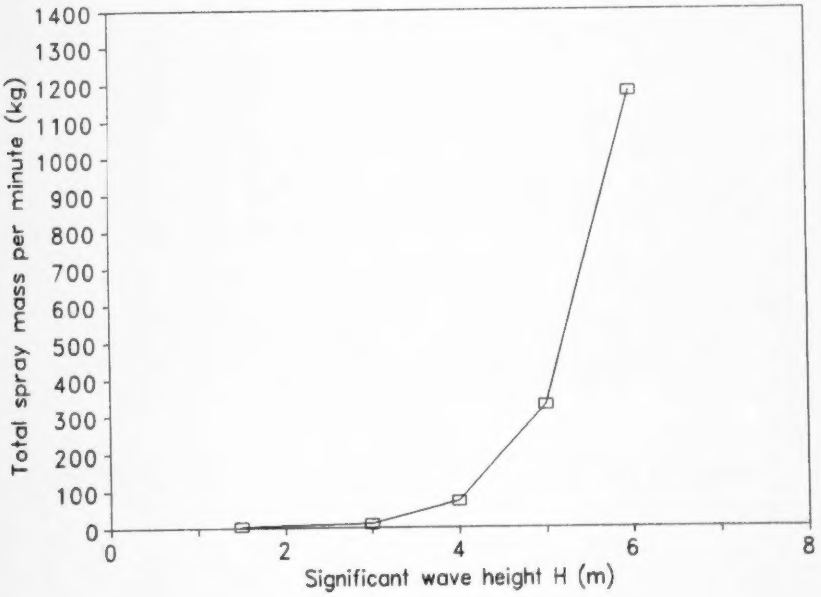

1400
1300
1200
1100
1000
900
800
700
600
500
400
300
200
100
0
Total spray mass per minute (kg)
0
2
4
6
8
Significant wave height H (m)

(c)

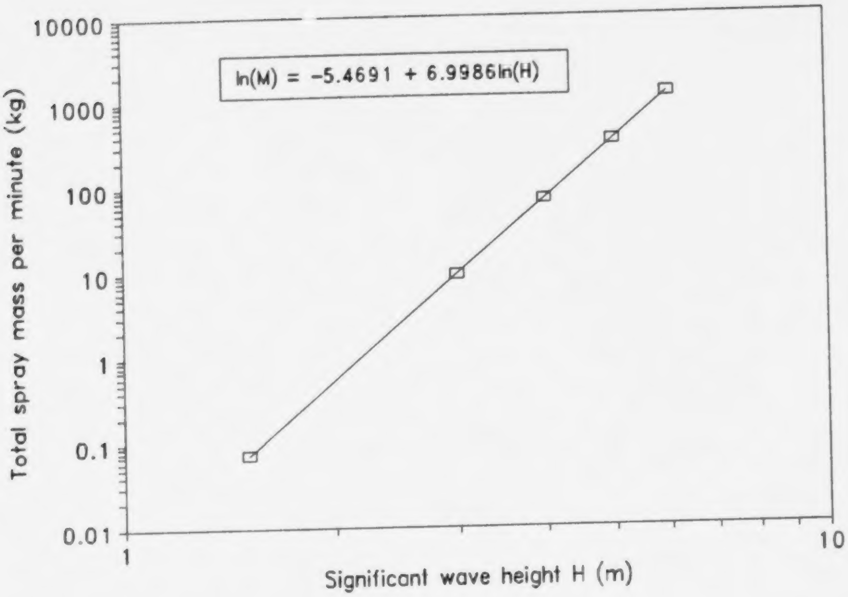
ln(M) = −5.4691 + 6.9986ln(H)
Total spray mass per minute (kg)
10000
1000
100
10
1
0.1
0.01
1
10
Significant wave height H (m)

(d)

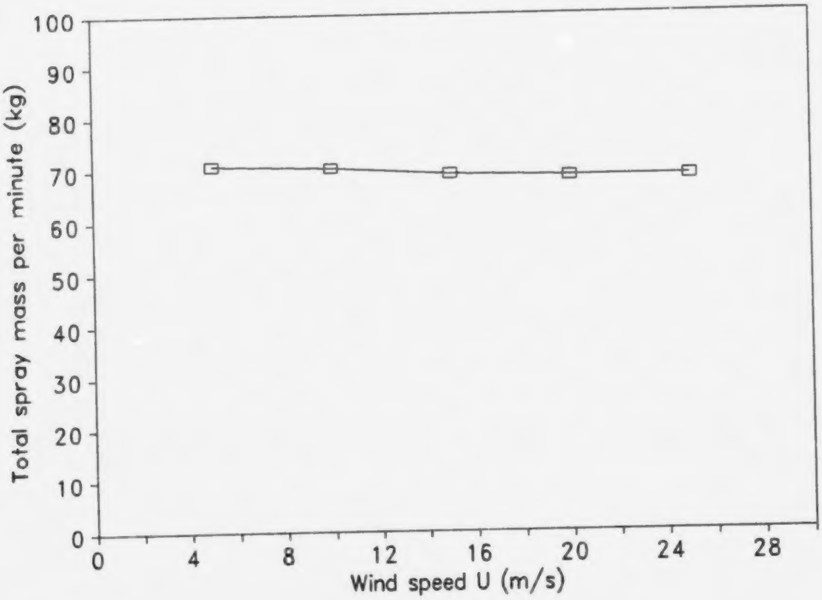
Total spray mass per minute (kg)
100
90
80
70
60
50
40
30
20
10
0
0
4
8
12
16
20
24
28
Wind speed U (m/s)

(e)

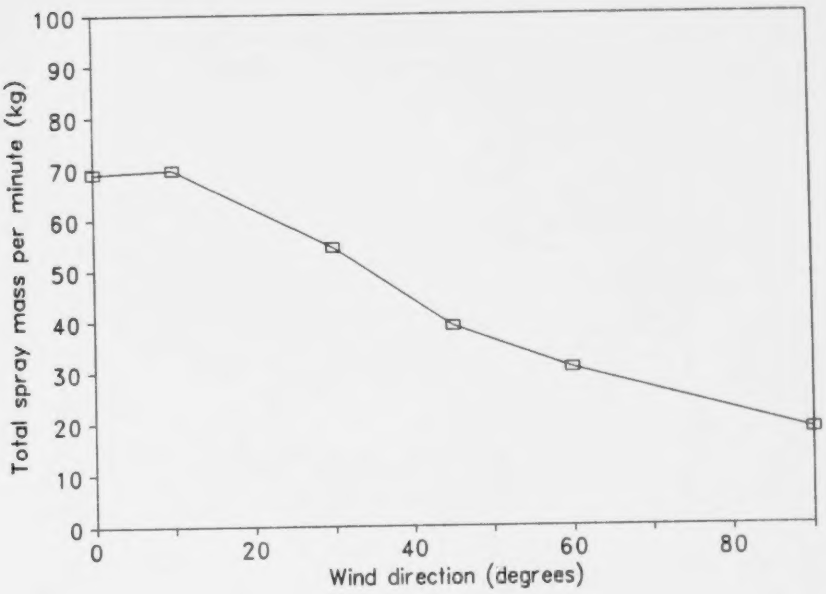

Total spray mass per minute (kg)
100
90
80
70
60
50
40
30
20
10
0
0
20
40
60
80
Wind direction (degrees)

(f)

II Effect of Droplet Size on the Total Spray Mass and the Spray Flux Distribution

Different spray droplet sizes give rise to different trajectories and hence affect the spray flux distribution. Table 3.4.2 shows that, according to our model, the total spray mass does not change significantly ($< 7\%$) as the droplet diameter increases from 0.1 mm to 3 mm. Except for the case with a droplet diameter of 0.1 mm, the model produces a smaller total spray mass with larger droplet sizes. This occurs because larger droplets have a smaller drag coefficient and so can reach a higher altitude than smaller droplets (Equations 3.2.1 to 3.2.3). Thus, the trajectories of some of the spray droplets can pass over the superstructure and these droplets are lost to the spray-free zone behind the wheelhouse or to the ocean. Smaller droplets are confined to a lower altitude due to the stronger vertical component of drag and thus fewer spray droplets are lost. For a droplet diameter of 0.1 mm, however, the total spray mass is 2.8 % less than that for a diameter of 1 mm. The reason for this effect is not obvious. It may arise because such small droplets have very low trajectories (see Figure 3.4.2a). Most of the spray droplets impinging on the front of the wheelhouse are thus confined to a very low altitude (less than 0.5 meters). Because of the finite grid cell discretization, much of this spray mass is ignored by the model.

Diameter (m)	Total spray mass (kgmin^{-1})
$1.0\text{x}10^{-4}$	69.2
$1.0\text{x}10^{-3}$	71.1
$1.75\text{x}10^{-3}$	68.9
$3.0\text{x}10^{-3}$	66.4

Table 3.4.2 : Total spray mass per minute with different droplets diameters. The atmospheric/oceanographic conditions are the standard ones.

The spray model results show that different droplet sizes can alter the spray flux distribution over the ship in a complex way. From Equation 2A.1.1 in Appendix 2A, it can be seen that the spray flux to a grid cell centred at (x',y',z') including the effect of wind drag, depends on m(x,y,z), the spray flux to its "equivalent target" without wind drag, and $\Delta x/\Delta x'$, the ratio of the lengths of the spray envelope at impact for the case without wind drag to that with wind drag. Different droplet sizes have different trajectories. Thus, the value of m(x,y,z), the ratio $\Delta x/\Delta x'$, and hence the spray flux to a given grid cell, are also different for different sizes of droplet. Figures 3.4.2a to 3.4.2d show the trajectories for four different droplet diameters. For each droplet diameter, eight trajectories are launched with initial vertical velocities of 1, 3, 5, 7, 9, 11, 13, and 15 ms^{-1}. The conditions are: $T_a = -10$ °C, $U = 15$ ms^{-1}, $V_a = 3$ ms^{-1}. The spray flux distribution for the foredeck, the wheelhouse, and the mast shall now be discussed. The spray flux to the grid cells located behind the wheelhouse is negligibly small and thus is not considered here. Nevertheless, it is included in the calculation of the total spray mass to the ship.

(a) The foredeck

The effect of droplet size on the spray flux distribution over the foredeck is illustrated in Figures 3.4.3a to 3.4.3d. The distribution pattern is directly correlated with the trajectories shown from Figures 3.4.2a to 3.4.2d. The spray flux distribution for a droplet diameter of 0.1 mm is distinctly different from the other three droplet sizes (Figures 3.4.3a to 3.4.3d). The reason is that droplets with a diameter of 0.1 mm experience a very large drag force (Equations 3.2.2 and 3.2.3). Thus, their trajectories are confined to a very low altitude (< 10 cm) (Figure 3.4.2a). As a result, a very high spray flux is found on the deck and no spray impinges on the wheelhouse and mast (Figure 3.4.3a). The local spray flux maximum found in Figure 3.4.3a is a result of the combined effect of the ratio $\Delta x/\Delta x'$ and the "no wind drag" spray flux m(x,y,z). Figure 3.4.4 shows the variation of the length of a spray tube, $\Delta x'$, for two droplet sizes, 0.1 mm and 1 mm. It is apparent that, for a droplet diameter of 0.1 mm, the ratio $\Delta x/\Delta x'$(Δx is constant which is the length of the spray tube without wind drag) increases

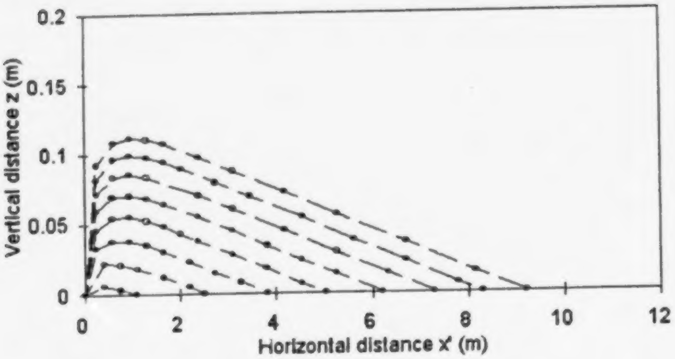

(a)

Figure 3.4.2: Droplet trajectories for four different droplet diameters. (a) 0.1 mm, (b) 1.0 mm, (c) 1.75 mm, and (d) 3.0 mm. The origin is at the bulwarks where 8 trajectories with initial vertical velocities 1, 3, 5, 7, 9, 11, 13, and 15 ms^{-1} are injected.

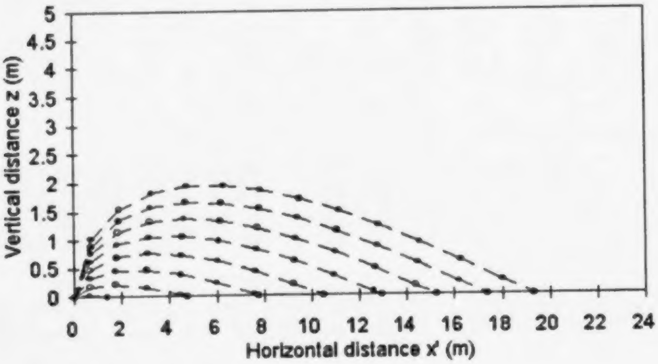

(b)

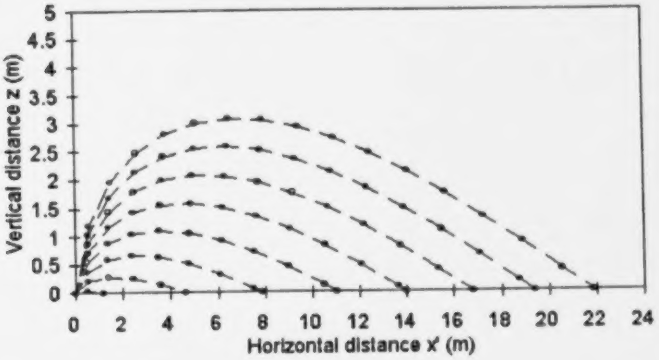

Vertical distance z (m)
Horizontal distance x' (m)
0
0.5
1
1.5
2
2.5
3
3.5
4
4.5
5
0
2
4
6
8
10
12
14
16
18
20
22
24

(c)

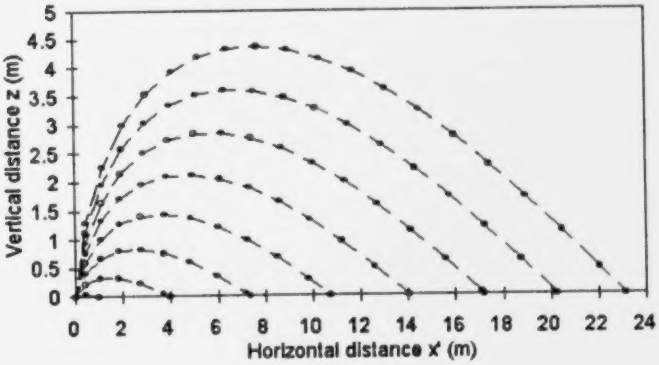

Vertical distance z (m)
Horizontal distance x' (m)
0
0.5
1
1.5
2
2.5
3
3.5
4
4.5
5
0
2
4
6
8
10
12
14
16
18
20
22
24

(d)

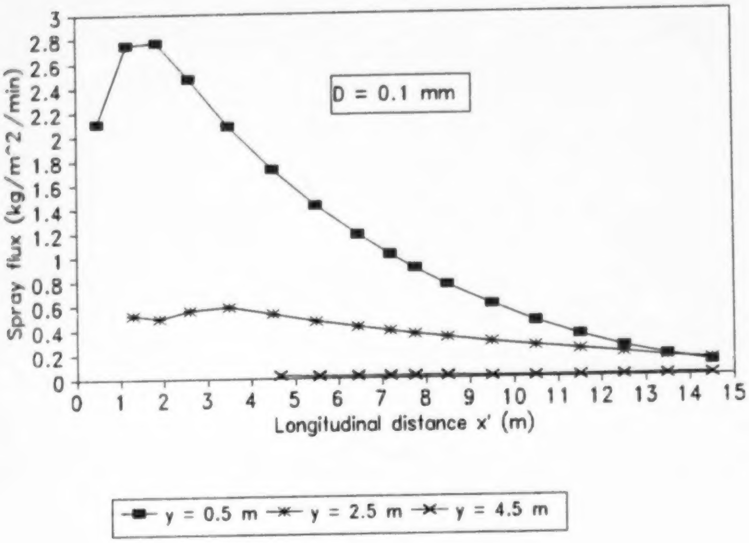

(a)

Figure 3.4.3: Effect of droplet size on the spray flux distribution over the foredeck. a) Droplet diameter D = 0.1 mm, b) Droplet diameter D = 1.0 mm, c) Droplet diameter D = 1.75 mm, d) Droplet diameter D = 3.0 mm. The atmospheric and oceanographic conditions are the standard ones (see text).

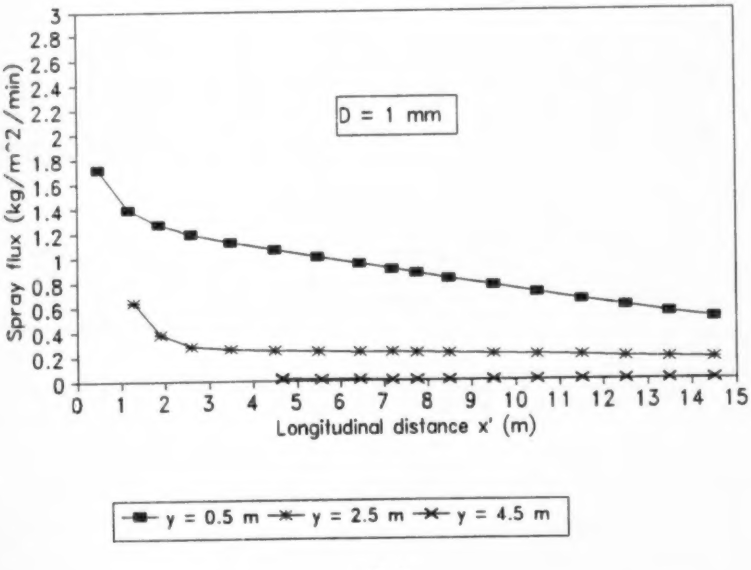

(b)

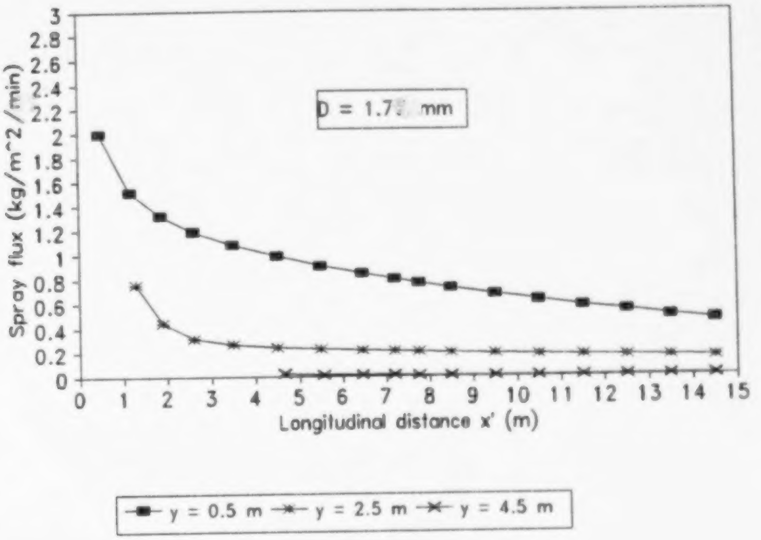
D = 1.75 mm
Spray flux (kg/m^2/min)
0
0.2
0.4
0.6
0.8
1
1.2
1.4
1.6
1.8
2
2.2
2.4
2.6
2.8
3
0
1
2
3
4
5
6
7
8
9
10
11
12
13
14
15
Longitudinal distance x' (m)
y = 0.5 m
y = 2.5 m
y = 4.5 m

(c)

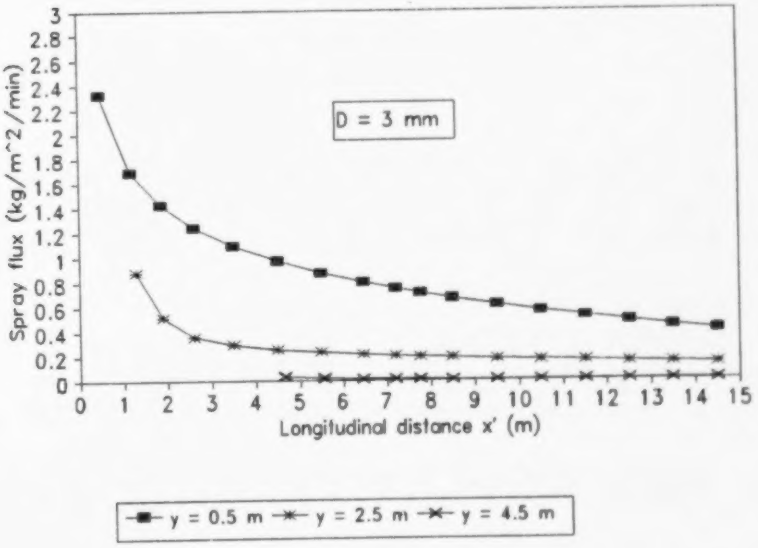
D = 3 mm
Spray flux (kg/m^2/min)
0
0.2
0.4
0.6
0.8
1
1.2
1.4
1.6
1.8
2
2.2
2.4
2.6
2.8
3
0
1
2
3
4
5
6
7
8
9
10
11
12
13
14
15
Longitudinal distance x' (m)
y = 0.5 m
y = 2.5 m
y = 4.5 m

(d)

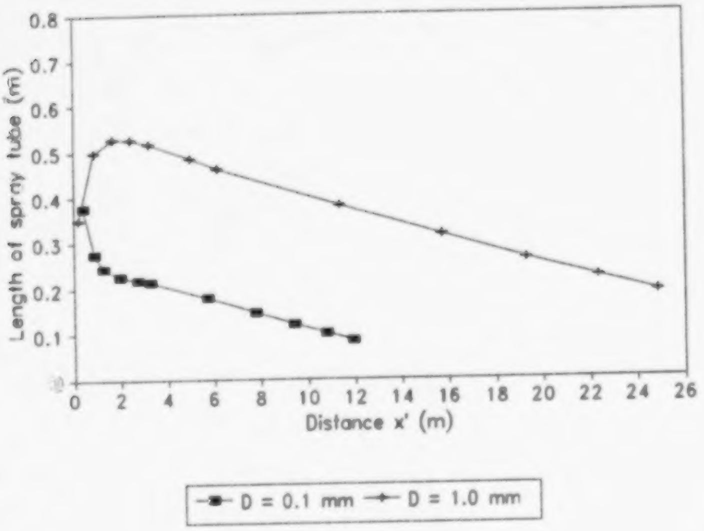

Figure 3.4.4 : Variation of the longitudinal dimension of the spray tube Δx' for two different droplet sizes, 0.1 mm and 1 mm.

with increasing distance (Figure 3.4.4). But, as x' increases, m(x,y,z) decreases. The combined effect of both Δx/Δx' and m(x,y,z) gives rise to a local maximum spray flux in Figure 3.4.3a. This local maximum does not occur in the other three cases (Figures 3.4.3b to 3.4.3d) because the combined effect of the two parameters, Δx/Δx' and m(x,y,z), gives a decreasing spray flux with increasing distance.

For larger droplet diameters of 1 mm, 1.75 mm, and 3 mm, the spray flux distributions on the deck are similar and exhibit a general decline with increasing x'. The gradient near the bulwarks becomes progressively greater for larger droplet diameters. The explanation of this behaviour is once again correlated to the trajectories (Figure 3.4.2b to 3.4.2d). Although smaller droplets reach a lower altitude, they accelerate in the horizontal faster because of their smaller inertia. Thus, smaller droplets are spread over the deck more uniformly. Larger droplets reach a higher altitude, but they are slow to accelerate horizontally due to their larger inertia. Hence, they tend to be concentrated near the bulwarks.

(b) Front of the wheelhouse

No spray is found on the front of the wheelhouse for the case with a droplet diameter of 0.1 mm. The spray flux distributions for the other three droplet sizes are shown in Figures 3.4.5a to 3.4.5c. These figures indicate that a high spray flux and a large vertical flux gradient are found with smaller droplet diameters. The reason for this can readily be seen from Figures 3.4.2b to 3.4.2d. If a vertical line is drawn at x' = 14.5 m to represent the front of the wheelhouse, it is clear that the ratio Δx/Δz' (Equation 2A.1.4 in Appendix 2A) becomes progressive higher for smaller droplet diameters. On the other hand, smaller droplets do not rise very high and therefore less spray reaches the upper portions of the front of the wheelhouse.

(c) Top of the wheelhouse

The grid cells on the top of the wheelhouse are located far from the bow. Hence, it is easier for larger droplets to reach these grid cells than for smaller droplets. As a result, less spray is found on the top of the wheelhouse for smaller droplet diameters than

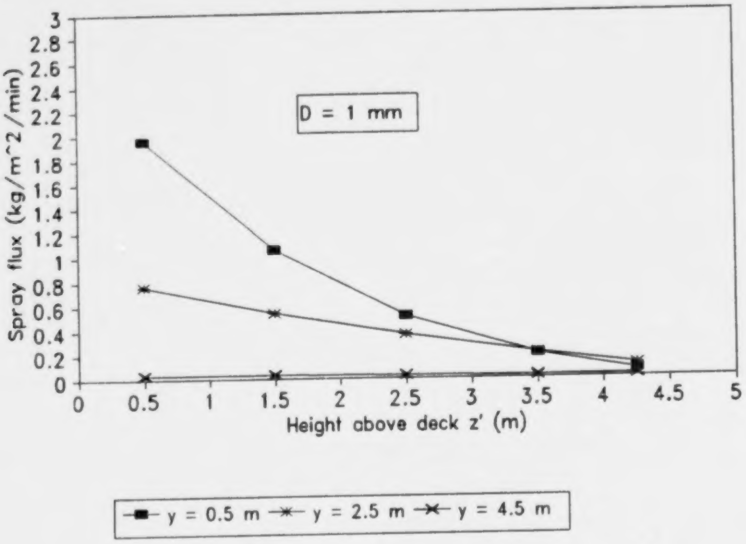

(a)

Figure 3.4.5: Effect of droplet size on the vertical spray flux distribution over the front of the wheelhouse. a) Droplet diameter D = 1.0 mm, b) Droplet diameter D = 1.75 mm, c) Droplet diameter D = 3.0 mm. The atmospheric and oceanographic conditions are the standard ones (see text).

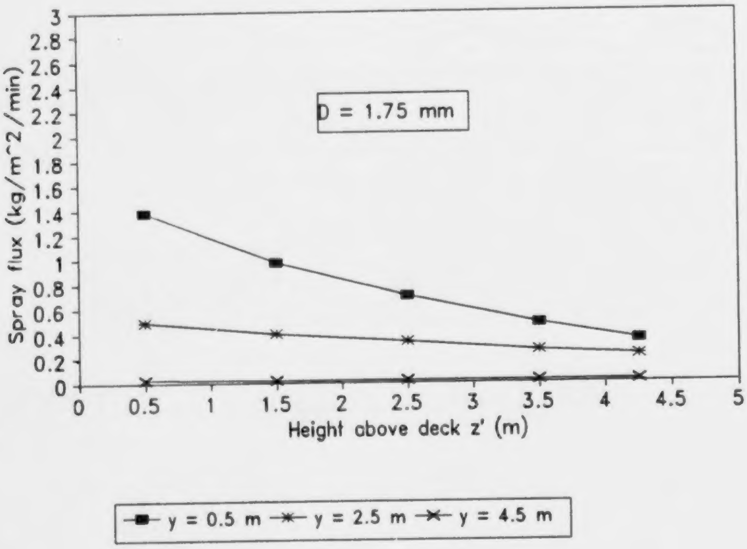

(b)

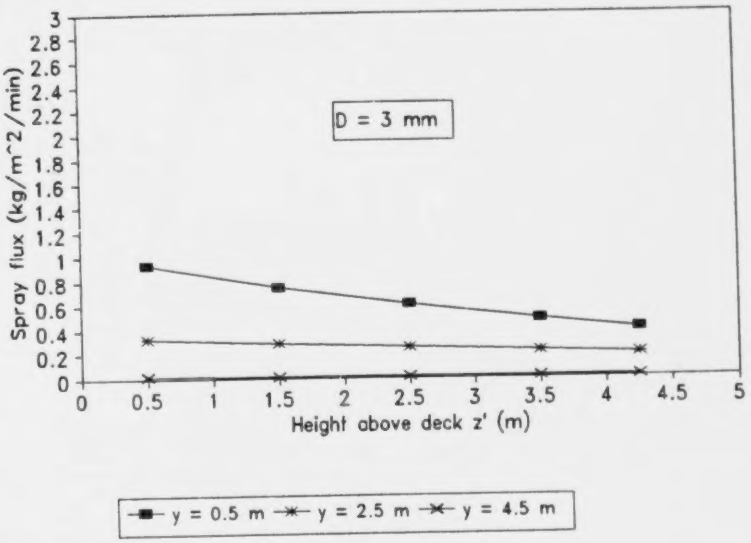
D = 3 mm
Spray flux (kg/m^2/min)
0
0.2
0.4
0.6
0.8
1
1.2
1.4
1.6
1.8
2
2.2
2.4
2.6
2.8
3
Height above deck z' (m)
0
0.5
1
1.5
2
2.5
3
3.5
4
4.5
5
y = 0.5 m
y = 2.5 m
y = 4.5 m

(c)

for larger droplet diameters (Figures 3.4.6a to 3.4.6c).

(d) Mast

The mast is located on top of the wheelhouse and hence is remote from the bow. The vertical spray flux distributions for three different droplet diameters are illustrated in Figures 3.4.7a to 3.4.7c. As for the top of the wheelhouse, more spray is found on the mast for larger droplet diameters than for smaller droplet diameters.

Based on the above sensitivity tests, it can be seen that ship speed and wave height are the major factors which determine the total spray mass impinging onto the entire vessel. This is consistent with the experimental results. The wind speed acts to re-distribute the spray while the wind direction can affect both the total spray mass and the spray flux distribution. The spray droplet size has no significant effect on the total spray mass, but has a profound effect on its distribution. The model's results show that tiny spray droplets (0.1 mm) do not reach the higher elevations in a horizontal wind (although they may do so if the wind has a vertical component due to flow over the superstructure). According to the spray cloud measurements on the 115 m U.S Coast Guard Cutter Midgett in the North Pacific Ocean and the Bering Sea during February and March 1990, Ryerson (1993) found that, at a height of 10 meters above the deck, spray cloud droplet sizes ranged from 0.014 to 7.7 mm with a geometric median of 0.234 mm. Based on the present model results, it can be concluded that the tiny droplets found at high elevations during ship/wave collisions are likely formed by the break up of larger droplets already in the air or are carried upward by a vertical wind component. These two features are not included in the present spray model however.

3.5 Results and Discussion

Three groups of spraying results have been produced to simulate characteristic condition using the spraying model. The first group is a low flux case in which the ship speed and significant wave height are set close to their threshold values (discussed in section 3.4) with a wind speed that is also low. The second group is the standard case,

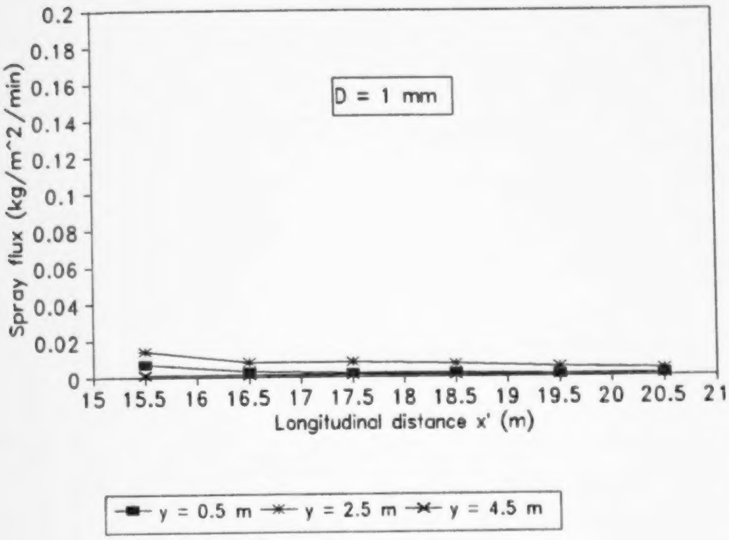

(a)

Figure 3.4.6: Effect of droplet size on the longitudinal spray flux distribution over the top of the wheelhouse. a) Droplet diameter D = 1.0 mm, b) Droplet diameter D = 1.75 mm, c) Droplet diameter D = 3.0 mm. The atmospheric and oceanographic conditions are the standard ones (see text).

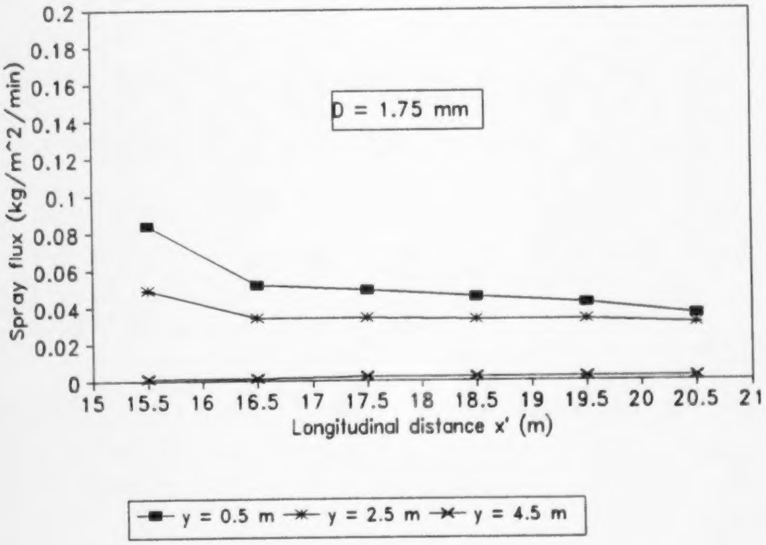

(b)

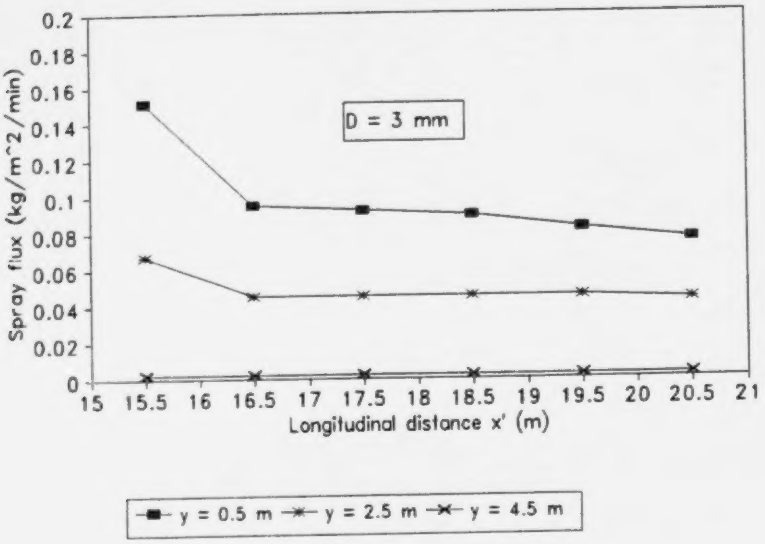
Spray flux (kg/m^2/min)
0.2
0.18
0.16
0.14
0.12
0.1
0.08
0.06
0.04
0.02
0
D = 3 mm
15
15.5
16
16.5
17
17.5
18
18.5
19
19.5
20
20.5
21
Longitudinal distance x' (m)
y = 0.5 m
y = 2.5 m
y = 4.5 m

(c)

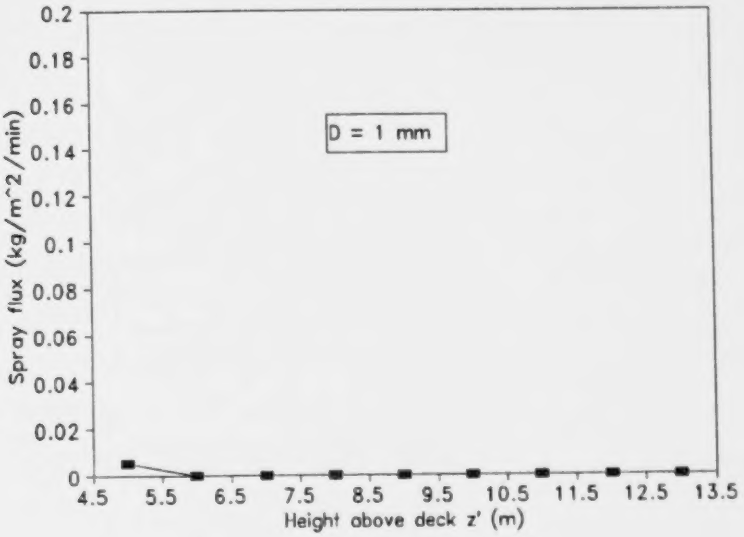

(a)

Figure 3.4.7: Effect of droplet size on the vertical spray flux distribution over the mast. a) Droplet diameter D = 1.0 mm, b) Droplet diameter D = 1.75 mm, c) Droplet diameter D = 3.0 mm. The atmospheric and oceanographic conditions are the standard ones (see text).

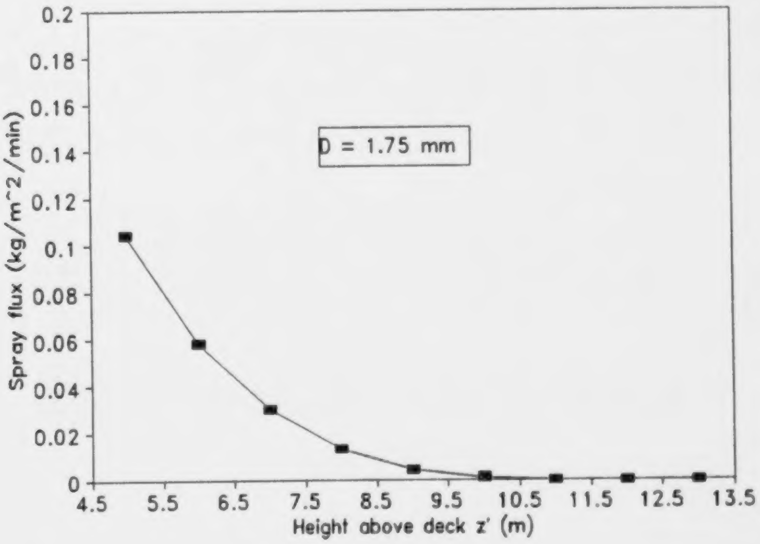

(b)

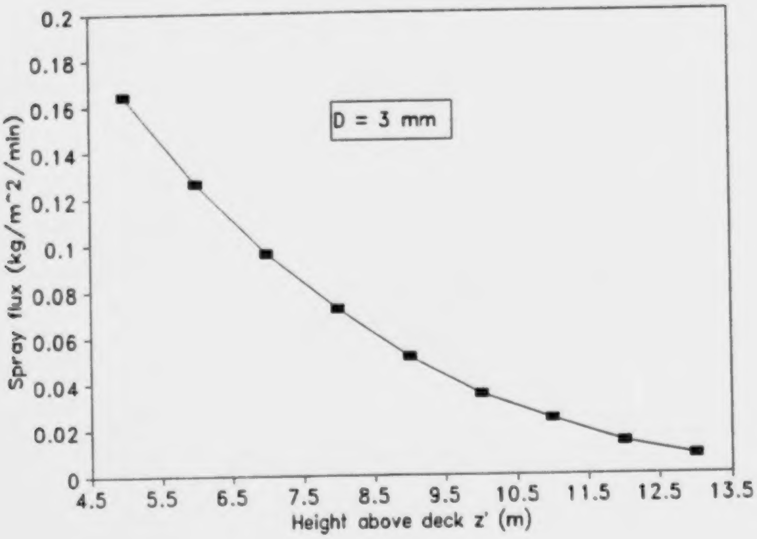
0.2
0.18
0.16
0.14
0.12
0.1
0.08
0.06
0.04
0.02
0
Spray flux (kg/m^2/min)
D = 3 mm
4.5
5.5
6.5
7.5
8.5
9.5
10.5
11.5
12.5
13.5
Height above deck z' (m)

(c)

described in Section 3.4. The third group is an extreme case in which the ship speed, significant wave height, and wind speed are set near their upper limits. These spraying results are meant to collectively reveal the nature of ship/wave collision-generated spray under various atmospheric and oceanographic conditions. Table 3.5.1 gives the total spray mass and the conditions under which the results were obtained. The air temperature, air pressure, and relative humidity are the standard values (see Section 3.4) for all three cases. The extreme case is unrealistic for a medium-sized fishing vessel which would be unable to travel at a speed of 8 ms^{-1} into waves with a significant wave height of 6 m. These two values are chosen simply to illustrate the performance of the spraying model under such extreme conditions.

Case	V_s (ms^{-1})	$H_{1/3}$ (m)	U (ms^{-1})	θ (°)	Total spray mass per minute (kg)
Low	2	2.5	5	0	0.78
	2	2.5	5	10	0.79
	2	2.5	5	45	0.64
	2	2.5	5	90	0.39
Standard	3	4	15	0	68.9
	3	4	15	10	69.5
	3	4	15	45	38.9
	3	4	15	90	18.4
Extreme	8	6	25	0	2.34×10^4
	8	6	25	10	2.27×10^4
	8	6	25	45	1.74×10^4
	8	6	25	90	1.07×10^4

Table 3.5.1 : Total spray mass per minute impinging on the entire vessel for various combinations of ship speed, V_s, significant wave hight, $H_{1/3}$, wind speed U, and wind direction, θ.

I Total Spray Mass on the Entire Vessel

The total spray mass, as indicated in Table 3.5.1, increases dramatically from the low case to the extreme case. This dramatic change is a result of the high power law dependence of the total spray mass on ship speed and significant wave height (Equation 3.1). In general, increasing the wind direction from 0° (head wind) to 90° (beam wind) causes a significant decrease in the total spray mass received. The explanation is that as the wind shifts away from the head wind direction, more grid cells lie beyond the spray zone and more spray droplets fly over the side of the ship and return to the ocean. As mentioned in Section 3.4, the methods used to calculate the spray flux for $\theta = 0°$ and for $0° < \theta \leq 90°$ are different. This gives rise to the situation in which the total spray mass received at $\theta = 10°$ is slightly greater ($< 1\%$) than that at $\theta = 0°$ in the low and standard cases (Table 3.5.1). However, this small error is considered to be insignificant within the overall context of the model.

II Spray Flux Distribution

In this section, the spray flux distribution for the three cases of Table 3.5.1 will be discussed. The spray flux distribution under different atmospheric and oceanic conditions is complex and depends on one or more of the following factors:

1) The location of the grid cell relative to the spray source point : spray flux decreases as the distance of the grid cell from the spray source point increases. The spray flux also decreases with increasing height.

2) The location of the spray source point: a grid cell which has a spray source point nearer to the centreline will receive a higher spray flux than one which has a spray source point farther from the centreline.

3) For a wind direction of 0°, the magnitude of the spray flux to a horizontally oriented grid cell is determined in part by the ratio $\Delta x/\Delta x'$ (Equations 2A.1.1 and 2A.1.5), and that to a vertically oriented grid cell, by the ratio $\Delta x/\Delta z'$ (Equations 2A.1.4 and 2A.1.6). A higher ratio implies a higher spray flux.

4) For a wind direction other than 0°, the spray flux to a grid cell depends on the area ratio (ABCD)/(A'B'C'D') (Equations 2A.2.1, 2A.2.8, 2A.2.12). Again, a higher ratio implies a higher spray flux.

5) Shadowing effect : some of the grid cells may not receive spray because the spray droplet trajectory is blocked by the superstructure. Grid cells located on top of the wheel house, near the bottom of the mast, and behind the wheelhouse are prone to shadowing.

The spray flux distribution under different conditions can be explained in a simple way by taking into account the above five factors. It is found that, for a given wind direction, the spray flux distribution patterns for the low, standard, and extreme cases are very similar. The minor differences among these three cases can be explained by one or a combination of the above five factors. Therefore, for simplicity, only the standard case will be discussed in detail here. The results for the low and extreme cases are given in Appendix 2B. It should be noted that only the spray fluxes along Column 1 ($y = 0.5$ m), Column 3 ($y = 2.5$ m), and Column 5 ($y = 4.5$ m) are considered.

a) Wind direction $\theta = 0°$

Because of symmetry, only the spray flux distribution over the starboard half of the vessel is shown (Figures 3.5.1a to 3.5.1d). For head winds, the centre of a grid cell and its spray source point both lie along the same longitudinal line. As shown in Figures 3.5.1a and 3.5.1b, the spray flux decreases longitudinally and exponentially over the deck, and vertically and exponentially over the front of the wheelhouse. This distribution pattern can be explained by factor (1). Along Column 5, the spray source point is remote from the centreline and thus the spray flux is negligibly small along this column both on the deck and on the front of the wheelhouse. On the top of the wheelhouse, much less spray (<0.1 kgm^{-2}min^{-1}) is received compared to the deck and the front of the wheelhouse. The explanation is related to factor (3). The grid cells on the top of the wheelhouse are oriented horizontally and are higher in elevation. Thus, they intercept the oncoming spray at a small angle to the surface. Hence, the ratio $\Delta x/\Delta x'$ is small and results in a small spray flux. Along Columns 1 and 3, on top of the wheelhouse, the spray flux decreases with distance. However, along Column 5, the spray flux increases

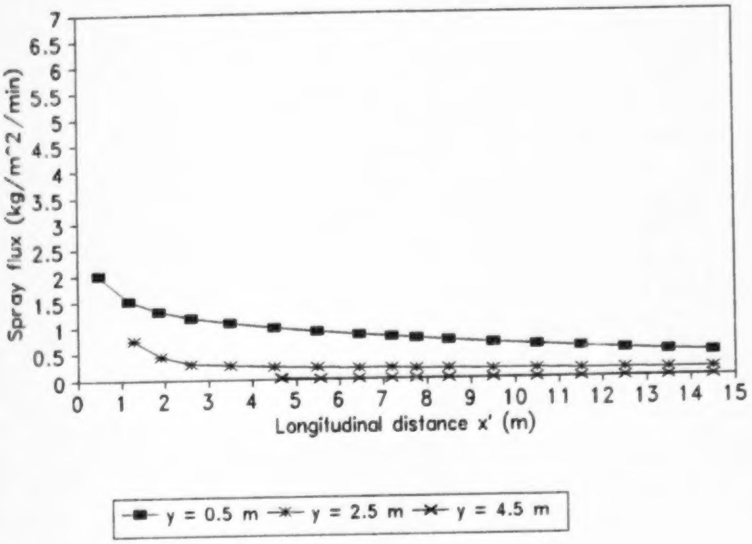

(a)

Figure 3.5.1: Spray flux distribution over various components under standard conditions for a wind direction of 0°. a) The foredeck, b)The front of the wheelhouse. c)The top of the wheelhouse, d)The mast.

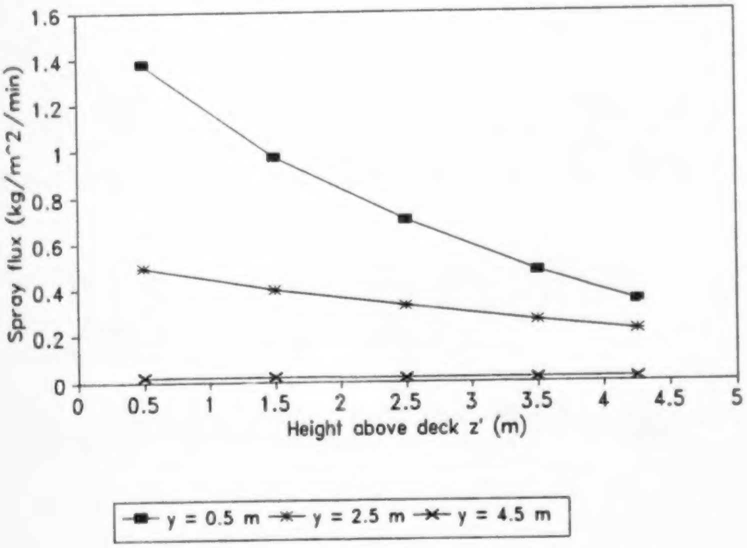

(b)

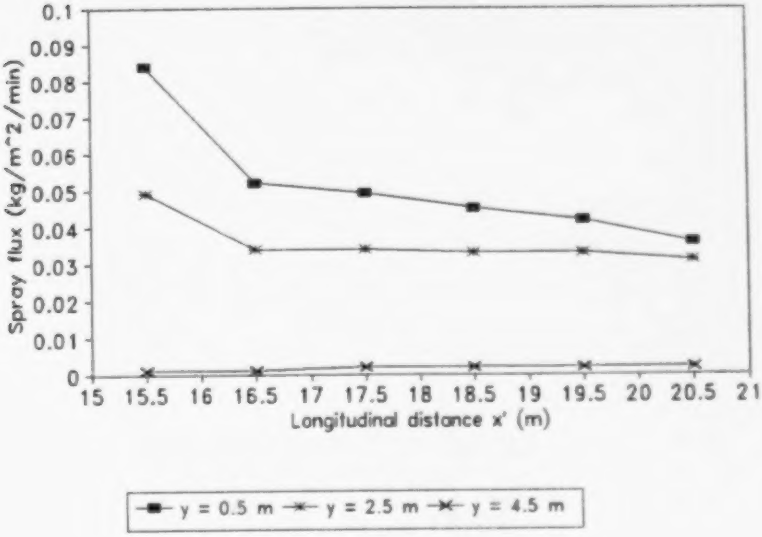
Spray flux (kg/m^2/min)
0.1
0.09
0.08
0.07
0.06
0.05
0.04
0.03
0.02
0.01
0
15
15.5
16
16.5
17
17.5
18
18.5
19
19.5
20
20.5
21
Longitudinal distance x' (m)
y = 0.5 m
y = 2.5 m
y = 4.5 m

(c)

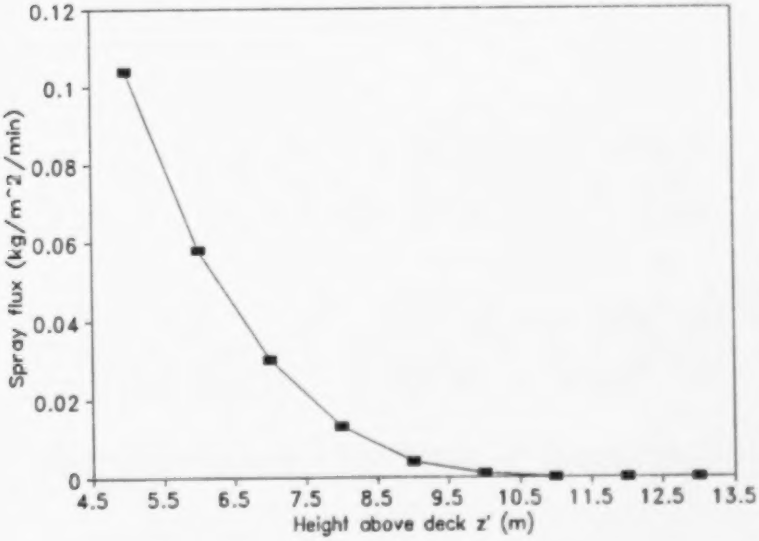
Spray flux (kg/m^2/min)
0.12
0.1
0.08
0.06
0.04
0.02
0
4.5
5.5
6.5
7.5
8.5
9.5
10.5
11.5
12.5
13.5
Height above deck z' (m)

(d)

slightly with distance. This is due to the combined effects of factors (1) and (3). Factor (1) suggests that the spray flux should decrease longitudinally. However, at the same time, the spray interception angle increases longitudinally, and so the ratio $\Delta x/\Delta x'$ increases (Equation 2A.1.5). The net result of these two factors gives rise to the noted spray flux distribution along Column 5 on top of the wheelhouse.

The spray flux distribution on the mast can be explained by factor (1); the spray flux decreases vertically and exponentially.

b) Wind direction $\theta = 10°$

For wind directions other than 0°, the spray flux distributions on the port and starboard sides are different as shown in Figures 3.5.2a to 3.5.2g.

θ is defined to be positive when the y-component of the oncoming wind is directed from port to starboard. Therefore, over the port side of the deck, as the longitudinal distance of a grid cell increases, the spray source point moves away from the centreline. Thus, the spray flux decreases longitudinally and exponentially as indicated in Figure 3.5.2a. On the starboard side of the deck, the situation is different (Figure 3.5.2b). For Columns 3 and 5, the spray flux decreases initially and then increases. The reason is that, for these two columns, as the longitudinal distance of the grid cell increases, the spray source point moves towards the centreline. This combined effect (factors (1) and (2)) results in the distribution pattern shown in Figure 3.5.2b.

The spray flux distribution on the port side of the front of the wheelhouse can be explained in a similar manner as the port side of the deck (Figure 3.5.2c). Over the starboard side, Figure 3.5.2d shows that the spray flux along Column 3 is highest; the Column 1 flux is lower, and the Column 5 flux is the lowest. The explanation is directly related to factors (1) and (2). The spray source points for the grid cells on Column 3 are nearer to the centreline than are those for Column 1, and this gives a higher spray flux along Column 3. Along Column 5, the grid cells are already far from the centreline. For such a small wind direction (10°), the spray source points corresponding to the grid cells along Column 5 are still farther from the centreline than are the source points for Columns 1 and 3. Hence, the spray flux along Column 5 is the lowest.

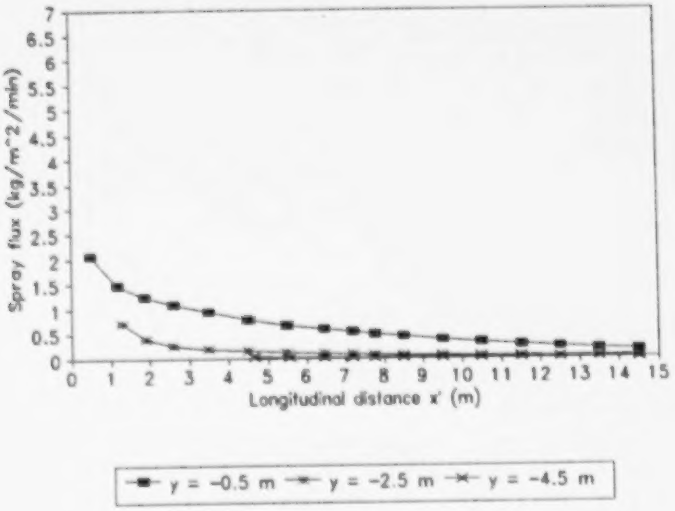

(a)

Figure 3.5.2: Spray flux distribution over various components under standard conditions for a wind direction of 10°. a) The foredeck (port), b) The foredeck (starboard), c) The front of the wheelhouse (port), d) The front of the wheelhouse (starboard), e) The top of the wheelhouse (port), f) The top of the wheelhouse (starboard), g) The mast.

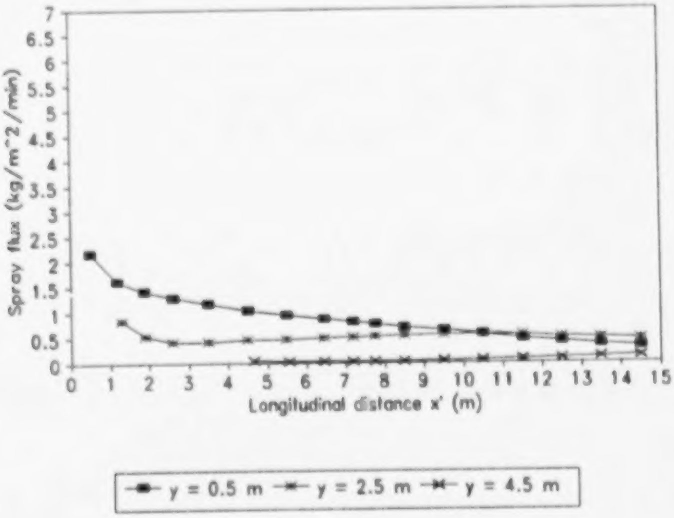

(b)

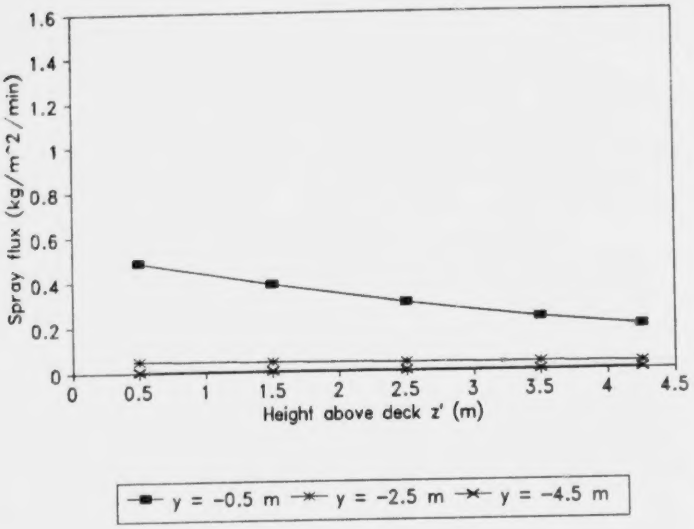
Spray flux (kg/m^2/min)
1.6
1.4
1.2
1
0.8
0.6
0.4
0.2
0
0
0.5
1
1.5
2
2.5
3
3.5
4
4.5
Height above deck z' (m)
y = -0.5 m
y = -2.5 m
y = -4.5 m

(c)

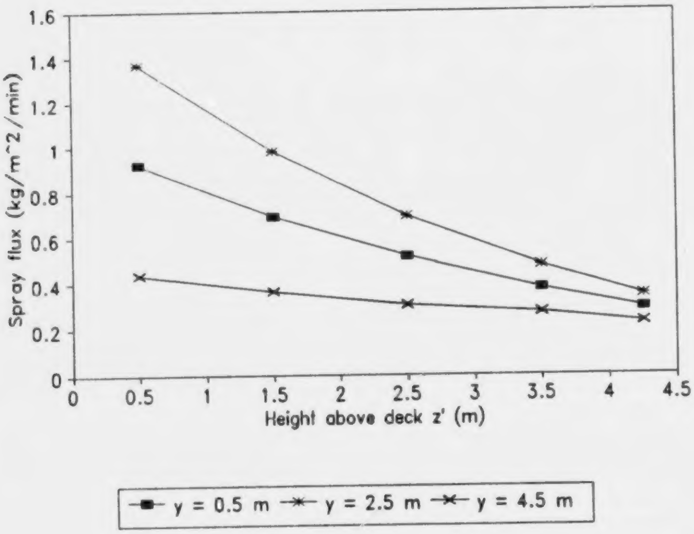
Spray flux (kg/m^2/min)
1.6
1.4
1.2
1
0.8
0.6
0.4
0.2
0
0
0.5
1
1.5
2
2.5
3
3.5
4
4.5
Height above deck z' (m)
y = 0.5 m
y = 2.5 m
y = 4.5 m

(d)

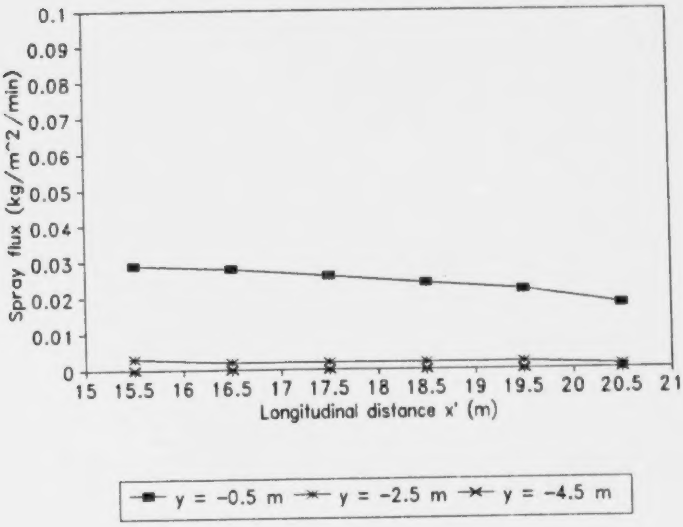
Spray flux (kg/m^2/min)
0
0.01
0.02
0.03
0.04
0.05
0.06
0.07
0.08
0.09
0.1
15
15.5
16
16.5
17
17.5
18
18.5
19
19.5
20
20.5
21
Longitudinal distance x' (m)
y = -0.5 m
y = -2.5 m
y = -4.5 m

(e)

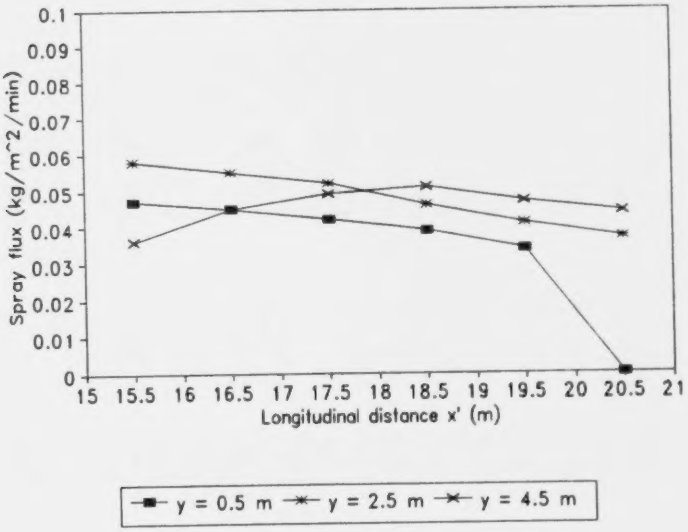
Spray flux (kg/m^2/min)
0
0.01
0.02
0.03
0.04
0.05
0.06
0.07
0.08
0.09
0.1
15
15.5
16
16.5
17
17.5
18
18.5
19
19.5
20
20.5
21
Longitudinal distance x' (m)
y = 0.5 m
y = 2.5 m
y = 4.5 m

(f)

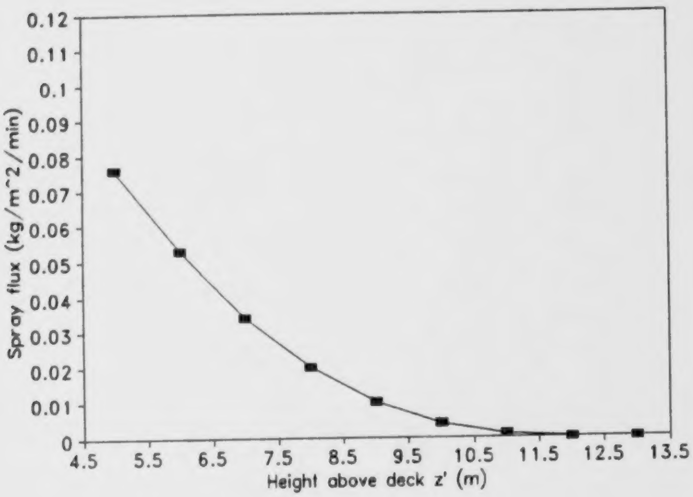
0.12
0.11
0.1
0.09
0.08
0.07
0.06
0.05
0.04
0.03
0.02
0.01
0
Spray flux (kg/m^2/min)
4.5
5.5
6.5
7.5
8.5
9.5
10.5
11.5
12.5
13.5
Height above deck z' (m)

(g)

The flux over the port side of the top of the wheelhouse decreases with longitudinal distance (Figure 3.5.2e). The spray flux distribution over the starboard side is more complicated (Figure 3.5.2f). The spray flux decreases as a function of distance for Columns 1 and 3, and the spray flux on Column 3 is higher than on Column 1. This occurs because the grid cells of Column 3 have spray source points nearer the centreline. The last grid cell of Column 1 receives no spray because the droplet trajectory is blocked by the front of the wheelhouse (shadowing effect). On Column 5, the spray flux increases over the first four grid cells and then decreases. Three factors may be responsible for this pattern: factor (1), the location of the grid cell, factor (2), the location of the spray source point, and factor (4), the ratio of Area(ABCD)/Area(A'B'C'D').

The spray flux distribution on the mast decreases exponentially with height (factor (1)) (Figure 3.5.2g).

c) Wind direction $\theta = 45°$

When the wind shifts to 45°, more grid cells lie beyond the spray receiving zone. Thus, no spray is received on the port side of the top of the wheelhouse, and on the mast. The spray flux distribution on the other components is shown in Figures 3.5.3a to 3.5.3e.

Figure 3.5.3a shows the spray flux distribution on the port side of the deck. This distribution pattern is similar to those of the previous cases for $\theta = 0°$, and $\theta = 10°$, and can be explained in the same way. On the starboard side, the spray flux distribution becomes more complex (Figure 3.5.3b). The spray flux along Column 1 decreases monotonically with distance, since the location of the spray source point also moves farther from the centreline with increasing distance (factors (1) and (2)). Along Column 3, the spray flux decreases over the first two grid cells, then increases in the next cell, and finally decreases again over the rest of the cells. This is due to the combined effects of factors (1) and (2). The distribution over Column 5 can also be explained in the same way. In general, for a longitudinal distance greater than 4 m, the spray flux increases along the transverse direction (y'-axis). Thus, the spray flux along Column 5 is highest. The explanation is that the cells farther from the centreline have spray source points

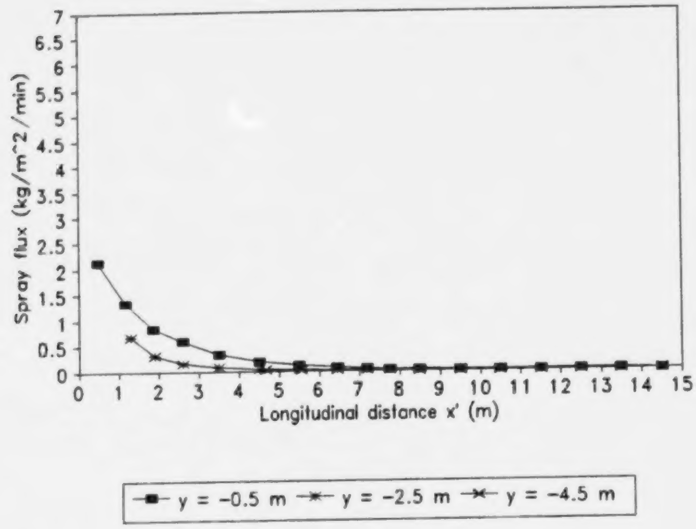

(a)

Figure 3.5.3: Spray flux distribution over various components under standard conditions for a wind direction of 45°. a) The foredeck (port), b) The foredeck (starboard), c) The front of the wheelhouse (port), d) The front of the wheelhouse (starboard), e) The top of the wheelhouse (starboard).

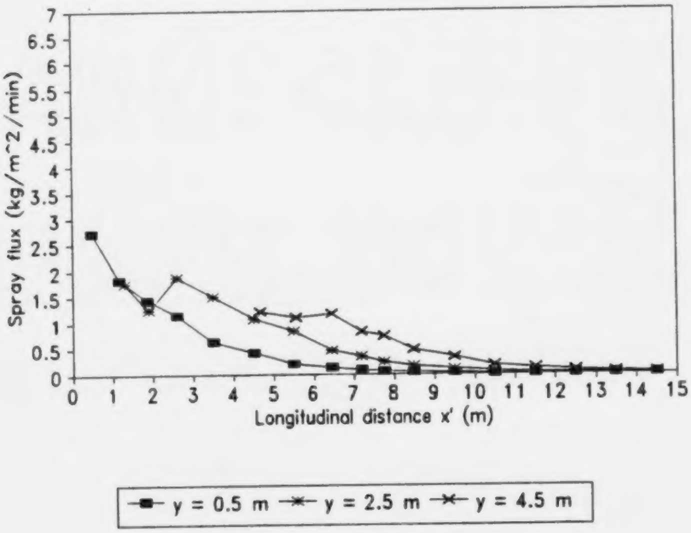

(b)

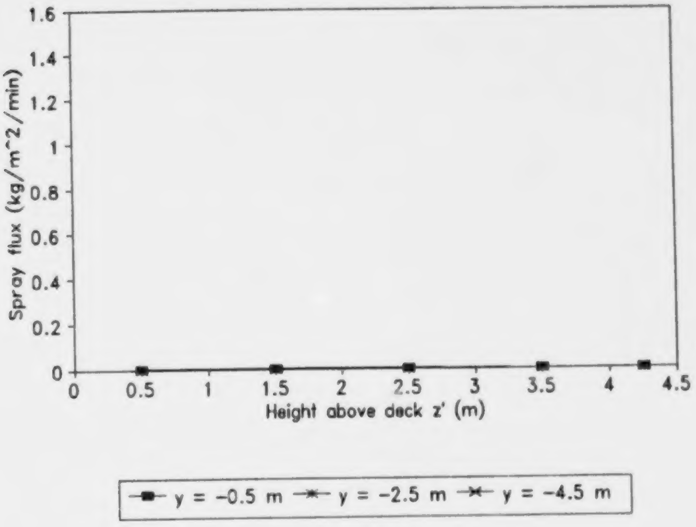

Spray flux (kg/m^2/min)
1.6
1.4
1.2
1
0.8
0.6
0.4
0.2
0
0.5
1
1.5
2
2.5
3
3.5
4
4.5
Height above deck z' (m)
y = -0.5 m
y = -2.5 m
y = -4.5 m

(c)

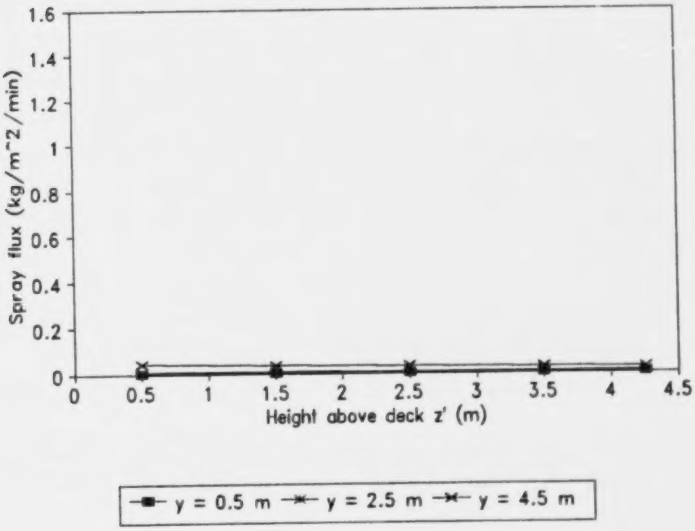

Spray flux (kg/m^2/min)
1.6
1.4
1.2
1
0.8
0.6
0.4
0.2
0
0.5
1
1.5
2
2.5
3
3.5
4
4.5
Height above deck z' (m)
y = 0.5 m
y = 2.5 m
y = 4.5 m

(d)

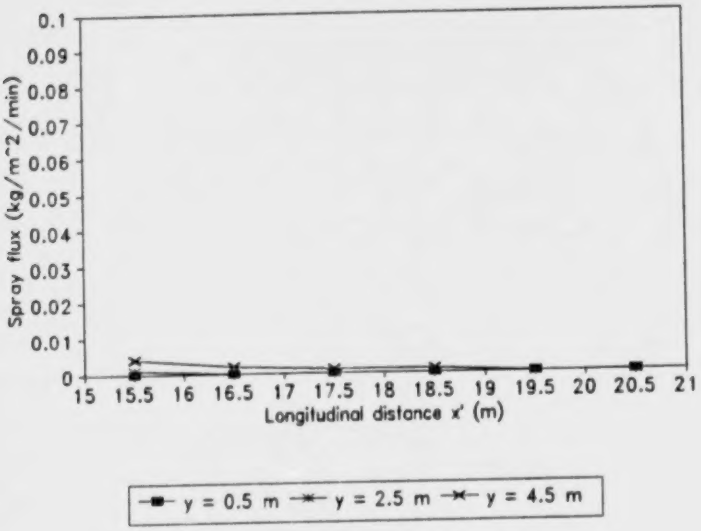

0.1
0.09
0.08
0.07
0.06
0.05
0.04
0.03
0.02
0.01
0
Spray flux (kg/m^2/min)
15
15.5
16
16.5
17
17.5
18
18.5
19
19.5
20
20.5
21
Longitudinal distance x' (m)
y = 0.5 m
y = 2.5 m
y = 4.5 m

(e)

closer to the centreline.

Only a negligible amount of spray is received on the port side of the front of the wheelhouse (Figure 3.5.3c) since cells located here have spray source points far from the centreline.

The spray flux distribution on the front and top of the wheelhouse on the starboard side is similar (Figures 3.5.3d and 3.5.3e), decreasing vertically and longitudinally respectively. In addition, the spray flux also increases transversely. The reasons for this have been discussed above for the starboard side of the deck and will not be repeated here.

d) Wind direction $\theta = 90°$

With beam winds, only the deck receives spray (Figures 3.5.4a and 3.5.4b). On the port and starboard sides, the spray flux decreases more rapidly with distance compared with all the other cases discussed above. This implies a strong effect of factors (1) and (2). Over the starboard side, the spray flux varies exponentially but it is smoother than for $\theta = 45°$ (Figure 3.5.4b). This pattern may be explained by factors (1) and (2). The especially high spray flux on the first grid cell in Columns 1 and 3 is related to factor (4) in which the ratio of Area(ABCD)/Area(A'B'C'D') becomes very large.

3.6 Concluding Remarks on the Spraying Model

A mathematical method for predicting spraying of the MT Zandberg had been developed based on the empirical spray flux Equation 3.1, the droplet trajectory Equation 3.2.1, and on continuity of mass. Two approaches to calculate the spray flux to different ship components for cases with $\theta = 0°$ and with $\theta > 0°$ have also been presented. Two numerical models, one for $\theta = 0°$ and the other for $0° < \theta \leq 90°$, have been designed to generate spray flux distributions over the foredeck, the wheelhouse, and the mast.

Sensitivity tests have shown that the ship speed and significant wave height are the two major parameters which determine the total spray mass. The wind speed and wind direction act to re-distribute the spray. In addition, as the wind direction changes

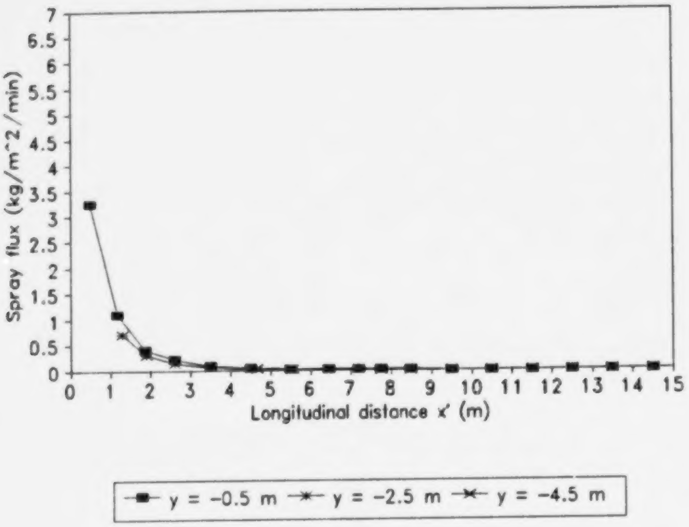

(a)

Figure 3.5.4: Spray flux distribution over various components under standard conditions for a wind direction of 90°. a) The foredeck (port). b) The foredeck (starboard).

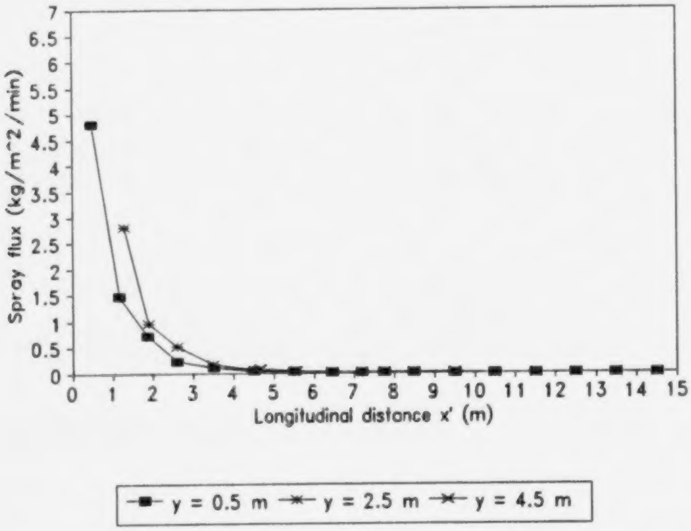

(b)

from head to beam winds, the total spray mass decreases significantly. The droplet size has a profound effect on the spray distribution but only a small effect on the total spray mass.

Spraying predictions for three case studies, low, standard, and extreme, have also been produced. It is found that with head winds, the spray flux distribution depends mainly on the wind speed and the location of the grid cell. For wind directions other than 0°, the spray flux distribution becomes complex and depends on the wind speed and on one or more of the five factors discussed in Section 3.5. Finally, there is a major limitation to the present spraying model. The nature of the experimental spraying data limits the numerical model to cases in which the wave motion is opposite to the ship's course. Other limitations of the spraying model include (a) monodisperse spray droplet size, (b) no droplet break-up along the trajectory, and (c) no vertical wind component.

CHAPTER 4 A NOVEL SHIP ICING MODEL

The derivation of the spray flux equation based on the experimental data obtained at IMD/NRC was discussed in Chapter 3. A sensitivity test and some spraying results were also presented. The spray flux equation is derived for continuous spray generation. However, in the natural environment, the spray generation is intermittent and the frequency of spray generation depends on the frequency of ship/wave collision. Thus, it is necessary to know the seaway condition for a specific wind speed and fetch.

Once the spray droplets are generated along the perimeter of the hull, they are immediately acted on by the wind drag and fly through the air as the ship moves forward. Eventually, they will either impinge on the surface of the ship or return back to the ocean. In addition, if the air temperature is lower than the sea-surface temperature, the temperature of the droplets will fall during their flight. Then, some of the droplets impinging on the surface of the ship will be frozen and accreted on its surface. Because of brine entrapment during freezing, the accretion will be spongy. After a sufficiently long time, many tonnes of spongy ice can accumulate on the ship's surface.

In this chapter, the seaway condition will be discussed first. A review of the thermodynamic properties of brine and saline ice will be presented in Section 4.2. In Section 4.3, the spray droplet temperature evolution will be discussed. The physics of brine flow and ice accretion on the ship's surface will be presented in Sections 4.4 and 4.5. Finally, the model implementation, sensitivity tests, and results and discussion are presented in Sections 4.6, 4.7, and 4.8.

4.1 Seaway Condition

It has been suggested that the amount of spray generated and the frequency of spray generation during ship/wave collisions are related to significant wave height ($H_{1/3}$), wave phase speed (V_p), wave period (P_o), and wavelength (λ) (Zakrzewski, 1987). Thus, it is necessary to know these four quantities for a given wind speed and fetch. For the purpose of modelling, it is assumed that each wave encounter which leads to spray generation is identical. According to Bretschneider (1973), for a fully-developed sea, the significant wave height and wave phase speed may be fitted by:

$$H_{1/3} = A_1\left(\frac{U^2}{g}\right)\tanh\left[B_1\left(\frac{gF}{U^2}\right)^{m_1}\right] \tag{4.1.1}$$

$$V_p = A_2 U tanh\left[B_2\left(\frac{gF}{U^2}\right)^{m_2}\right] \tag{4.1.2}$$

where

U: wind speed at a 10 meter height (ms^{-1}).
F: fetch (m).
A_1: constant = 0.283.
B_1: constant = 0.0125.
m_1: constant = 0.42.
A_2: constant = 1.2.
B_2: constant = 0.077.
m_2: constant = 0.25.

According to Khandekar (1989), the significant wave height is defined as "the mean of the highest one-third of the waves present in the sea at any given time". The wave period and wavelength are given by (Lighthill, 1978):

$$P_o = \frac{2\pi}{g} V_p \tag{4.1.3}$$

$$\lambda = \frac{2\pi}{g} V_p^2 \tag{4.1.4}$$

For a ship heading of 180° (perpendicular to the wave crests), the ship/wave encounter period is given by:

$$P_{en} = \frac{\lambda}{V_{rw}} = \frac{g}{2\pi}\left(\frac{P_o^2}{V_{rw}}\right) \qquad (4.1.5)$$

where P_{en} is the time interval (in seconds) between two successive ship/wave collisions, and V_{rw} is the velocity of the ship (in ms^{-1}) relative to the oncoming waves ($\vec{V}_{rw} = \vec{V}_s + \vec{V}_p$).

It is observed that not every ship/wave encounter generates spray. In fact, spray generation depends on slamming of the hull into the wave. According to Zakrzewski (1986), for a medium-size fishing vessel, the frequency of spray generation per minute can be approximated by the empirical formula of Panov (1971):

$$F_{spg} = 15.78 - 18.04e^{-\frac{4.26}{P_{en}}} \qquad (4.1.6)$$

This empirical formula has been discussed by Zakrzewski (1987) and is found to agree well with observed values. Then, the time interval between successive spray events, P_{spg} (s), can be calculated by:

$$P_{spg} = \frac{60}{F_{spg}} \qquad (4.1.7)$$

Zakrzewski (1986) used dimensional analysis to derive an approximate formula for the duration of spray cloud residence above the vessel. Calculations from this formula show that the period of direct spraying (P_{sp}) ranges from 5-7 seconds over a wide range of conditions. This result seems unrealistic for a medium size fishing vessel (MFV). On the other hand, Zakrzewski (1992) applied the same formula but with a different constant to calculate the period of direct spraying for the U.S. Coast Guard Cutter Midgett which is substantially larger than a MFV. It was found that the period typically ranges from 3-5 seconds for the Midgett (Lozowski and Zakrzewski, 1992). In addition, based on video data, Zakrzewski (1992) found that the spraying duration can even be less than 1 second for the Midgett. This suggests that the duration of spraying can vary over a large range depending on the atmospheric and oceanographic conditions. Because of the uncertainty of the formula derived by Zakrzewski, and the lack of further experimental information regarding the spraying period, it was decided not to use Zakrzewski's formula. As a first approximation, the duration of spraying is assumed to be a constant value which is appropriate and representative for a MFV. In order to determine this value, different durations of spraying, ranging from 1 second to 7 seconds have been tried in the present icing model. The reason for using the present model to test the effect of duration of spraying on icing is that, to our best knowledge, only the models of Zakrzewski et al. (1991) and the present one include spray intermittency effect. The specific atmospheric and oceanographic condition (the total spray mass per spray event is constant even if the period of spraying changes) used as input parameters to the present model are: air temperature -10 °C, air pressure 1000 mb, relative humidity 75 %, sea-surface temperature 2 °C, wind speed 15 ms^{-1}, wind direction 0°, fetch 200 nautical miles, ship speed 3 ms^{-1}, duration of simulation 1 hour. Figure 4.1.1 shows how the total ice load changes with different spraying durations. It is found that under these conditions the total ice load varies only ~ 3 % as the duration of spraying increases from 1 second to 7 seconds. As indicated in Figure 4.1.2, the local ice thickness (vertical depth of ice accretion) along the longitudinal line $y = 0.5$ m changes substantially near the bow for different durations of spraying. However, the difference decreases as the distance from the bow increases and at $x = 10$ m, there is no difference at all. This icing behaviour is complicated and depends on various factors such as the amount of spray impinging on the vessel, the sea-surface temperature, and the heat transfer from the icing surface to the air. In the present case (Figures 4.1.1 and 4.1.2), the reason for higher ice accumulation with a shorter spray duration is that the brine which remains on the surface after splashing has a longer spray-free period to freeze. For longer durations of spraying, the spray-free period is shorter, and thus the brine remaining on the surface has less time to freeze. It should be mentioned here that under low wind speeds ($U < 10$ ms^{-1}) and

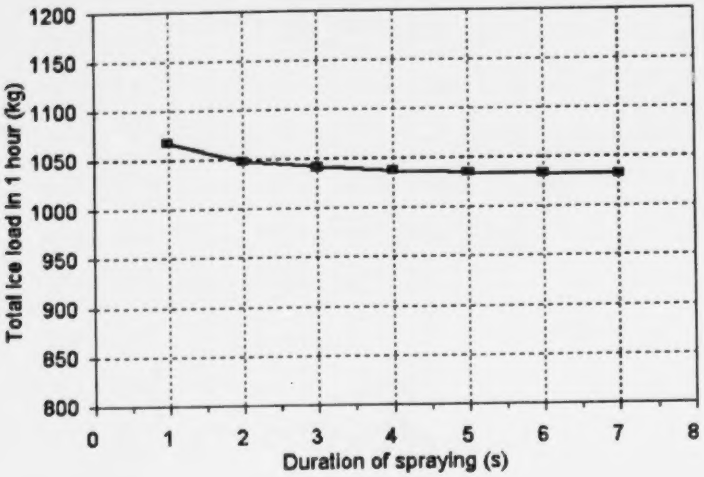

Figure 4.1.1: Variation of total icing load with spraying duration.

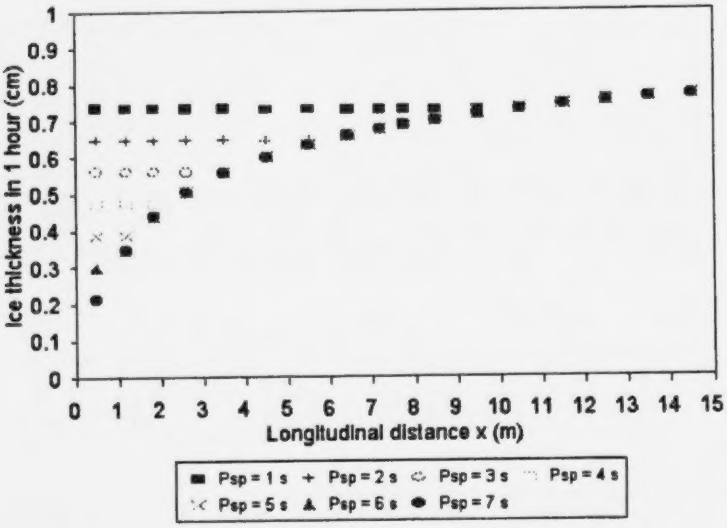

Figure 4.1.2: Ice thickness distribution along the column y = 0.5 m over the deck as a function of spraying duration, P_{sp}.

high ship speeds (V_s > 5 ms^{-1}), the spray generation interval (P_{spg}) can be as short as 4 seconds. Thus, one must be careful in choosing a constant value for the duration of spraying (P_{sp}), since P_{sp} can not exceed P_{spg}. Based on the above discussion, a constant value of 3.5 seconds has been chosen for the duration of spraying.

It is assumed that all grid cells on the ship's surface receive spray simultaneously and that they are exposed to spray for same the period of time (P_{sp}). After spraying, there is a spray-free period which lasts for (P_{spg} - P_{sp}) seconds before the next spray.

In Chapter 3, the spray flux expression for m(x',y',z') is formulated as if it were continuous and is expressed in $kgm^{-2}min^{-1}$. Taking into account the intermittency of the spray, the spray flux m_{sf} in $kgm^{-2}s^{-1}$ for a single spraying event is calculated by:

$$m_{sf} = \frac{m(x',y',z')}{F_{spg}P_{sp}} \qquad (4.1.8)$$

4.2 Thermodynamic Properties of Brine and Saline Ice

Let us first consider an ice surface which is covered with a thin brine film. During the freezing process, essentially only the pure water component can be frozen to form ice crystals at the solid/liquid interface. Much of the salt is rejected to the surrounding fluid, thereby increasing its salinity. In addition, because of constitutional supercooling along the crystallization front, dendritic ice is formed (Knight 1967, Weeks and Ackley 1982). Brine pockets of high salinity are entrapped inside the resulting ice matrix. This brine entrapment process results in a form of saline ice which is often described as spongy. It is assumed here that there is thorough mixing between the brine pockets formed among the dendrites and the brine film flowing alongside them (Chung, 1989). Hence, as the brine pockets form, their salinity will be the same as that of the adjacent brine film. As long as freezing continues, the salinity of the brine film continues to change because salt is continuously rejected. The salinity of the brine film also affects its thermodynamic properties. Consequently, it is worthwhile to review here the effect of salinity on those thermodynamic properties.

Since we are interested in spray icing, let us consider a vertical surface which is superimposed with grid cells as shown in Figure 4.2.1. Suppose this vertical surface is covered with a smooth ice surface and on top of it, a thin brine film which is flowing vertically downward. In addition, spray droplets are impinging upon the brine film. For a given time interval Δt (which is a subdivision of the spraying period), the total available brine on grid cell (j,k) includes: (i) mass of brine remaining on grid cell (j,k) following accretion during the previous time step and run-off in the present time step, $M_{l(j,k)}$ (kg), (ii) mass of brine flowing into grid cell (j,k) from the grid cell (j,k+1) in time Δt, $M_{f(j,k+1)}$ (kg), and (iii) spray droplets impinging onto (j,k). Then, assuming no lateral flow, the net brine flux to grid cell (j,k) in time Δt can be expressed by:

$$m_{bt(j,k)} = m_{sf(j,k)} + \frac{M_{f(j,k+1)} + M_{l(j,k)}}{A_{(j,k)}\Delta t} \qquad (4.2.1)$$

where $m_{sf(j,k)}$ is the direct spray flux to the grid cell (j,k) as given by Equation 4.1.8 and $A_{(j,k)}$ is the grid cell surface area. $M_{f(j,k+1)}$ is given by:

$$M_{f(j,k+1)} = \rho_{b(j,k+1)}\delta_{b(j,k+1)}\langle U_{bz(j,k+1)}\rangle \Delta y \Delta t \qquad (4.2.2)$$

where

$\rho_{b(j,k+1)}$: density of the brine remaining on grid cell (j,k+1) after ice accretion in the previous time step (kgm^{-3}).

$\delta_{b(j,k+1)}$: thickness of the brine remaining on grid cell (j,k+1) after ice accretion in the previous time step (m).

$\langle U_{bz(j,k+1)}\rangle$: mean vertical velocity of the brine film leaving grid cell (j,k+1) (ms^{-1}).

Δy: width of the grid cell (m).

The calculation of $\langle U_{bz(j,k+1)}\rangle$ and $\delta_{b(j,k)}$ will be presented in Section 4.4 and 4.5 respectively. For the present, it is assumed that these two parameters are known. The brine mass $M_{l(j,k)}$ remaining on grid cell (j,k) after run off in time Δt is given by:

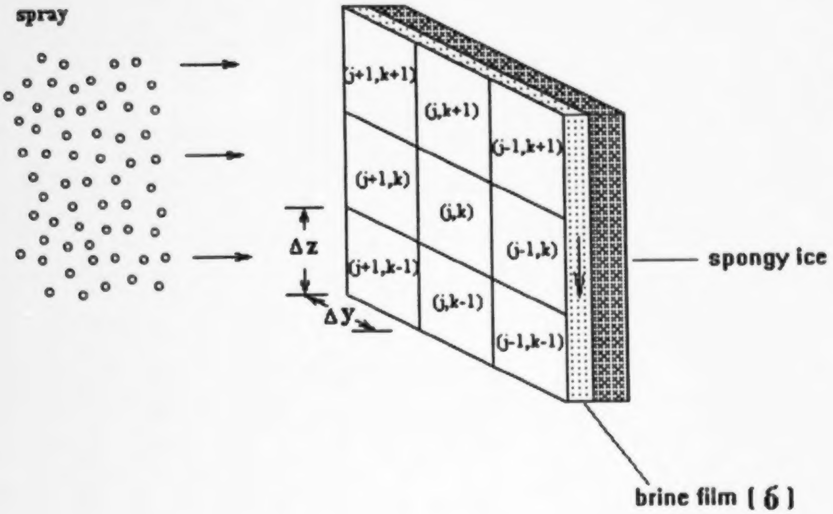
spray
(j+1,k+1)
(j,k+1)
(j-1,k+1)
(j+1,k)
(j,k)
(j-1,k)
(j+1,k-1)
(j,k-1)
(j-1,k-1)
Δz
Δy
spongy ice
brine film [δ]

Figure 4.2.1 : Spray icing on a vertical surface with a brine film thickness δ.

$$M_{l(j,k)} = \rho_{b(j,k)} \delta_{b(j,k)} (\Delta z - \langle U_{bz(j,k)} \rangle \Delta t) \Delta y \tag{4.2.3}$$

where Δz is the height of the grid cell (m).

Assuming thorough mixing of the incoming brine from the above three different sources, the salinity of the total brine flux to grid cell (j,k) can be calculated by:

$$S_{bt(j,k)} = \frac{(m_{sf(j,k)} A_{(j,k)} \Delta t S_{sea} + M_{f(j,k+1)} S_{b(j,k+1)} + M_{l(j,k)} S_{b(j,k)})}{(m_{bt(j,k)} A_{(j,k)} \Delta t)} \tag{4.2.4}$$

where

S_{sea}: the salinity of the impinging spray which is the same as that of sea-surface brine, assuming that the evaporation of spray droplets is negligibly small.

$S_{b(j,k+1)}$: the salinity of the brine flowing from grid cell (j,k+1) after ice accretion.

$S_{b(j,k)}$: the salinity of the brine leaving grid cell (j,k) after ice accretion.

The mean temperature of the total brine flux to grid cell (j,k) is:

$$T_{mean(j,k)} = \frac{X_1}{X_2} \tag{4.2.5}$$

where X_1 and X_2 are given by:

$$X_1 = m_{sf(j,k)} A_{(j,k)} \Delta t C_{sea} T_{im(j,k)} + M_{f(j,k+1)} C_{b(j,k+1)} T_{s(j,k+1)}$$

$$+ M_{l(j,k)} C_{b(j,k)} T_{s(j,k)} \tag{4.2.6}$$

$$X_2 = m_{sf(j,k)} A_{(j,k)} \Delta t C_{sea} + M_{f(j,k+1)} C_{b(j,k+1)} + M_{l(j,k)} C_{b(j,k)} \tag{4.2.7}$$

where

C_{sea}: the specific heat capacity of the impinging spray, which is taken to be the same as that of the sea surface brine ($Jkg^{-1}k^{-1}$).

$C_{b(j,k+1)}$: the specific heat capacity of the brine leaving grid cell (j,k+1) after ice accretion ($Jkg^{-1}k^{-1}$).

$C_{b(j,k)}$: the specific heat capacity of the brine leaving grid cell (j,k) after ice accretion ($Jkg^{-1}k^{-1}$).

$T_{im(j,k)}$: the temperature of the spray droplets impinging on grid cell (j,k) (°C).

Knowing the magnitude, salinity and mean temperature of the total brine flux to grid cell (j,k), the thermodynamic properties of the brine entering this grid cell can be calculated.

a) The equilibrium freezing temperature

According to Makkonen (1987), the equilibrium freezing temperature (°C) of brine may be approximated by:

$$T_{s(j,k)} = -54.0 S_{bt(j,k)} - 600 S^3_{bt(j,k)} \tag{4.2.8}$$

where $S_{bt(j,k)}$ is the salinity expressed as a fraction.

b) The equilibrium vapour pressure

The equilibrium vapour pressure over brine with a temperature $T_{s(j,k)}$ and a salinity $S_{bt(j,k)}$ is given by (Makkonen, 1987):

$$e_{s(j,k)} = (1 - 0.537 S_{bt(j,k)}) e(T_{s(j,k)}) \qquad (4.2.9)$$

where $e(T_{s(j,k)})$ is the equilibrium vapour pressure over a plane pure water surface at $T_{s(j,k)}$ and both $e_{s(j,k)}$ and $e(T_{s(j,k)})$ are expressed in mb. Using the Clausius Clapeyron equation (Iribarne and Godson, 1981), $e(T_{s(j,k)})$ can be calculated by:

$$e(T_{s(j,k)}) = \exp[-\frac{6763.6}{T_{s(j,k)}} - 4.9283 \ln(T_{s(j,k)}) + 54.23] \qquad (4.2.10)$$

where $T_{s(j,k)}$ is expressed here in K.

c) The latent heat of fusion

The latent heat of fusion of a spongy accretion can be calculated using (Makkonen, 1987):

$$L_{fs} = (1 - \lambda) L_f \qquad (4.2.11)$$

where L_f is the specific latent heat of fusion of pure water at $T_{s(j,k)}$, and λ is the liquid fraction of the ice matrix.

The liquid fraction of sea spray ice accretions has not yet been systematically investigated. Lesins et al. (1980) performed fresh water icing experiments on a rotating cylinder to simulate the growth of hailstones. The experimental results gave a liquid fraction up to 0.6, depending on the rotating rate. Gates et al. (1986) also performed wind tunnel experiments to determine the sponginess of spray icing using fresh water. It was found that for a rotating cylinder, the average measured liquid fraction is 0.28. But, for a non-rotating cylinder, this value was reduced to 0.20 (Gates et al., 1986). Based on experimental studies on the growth of spongy ice near the forward stagnation point of a disc situated in a dense, supercooled, fresh water spray, Lock and Foster (1988) found that the liquid fraction of the spongy accretion ranges from 0.35 to 0.65.

According to Weeks and Lofgren (1967), Cox and Weeks (1975), and Tsurikov (1965), when sea ice forms at low growth rates, the liquid fraction is approximately 0.26. Makkonen (1987) used this value as the liquid fraction in his sea spray icing model. This choice seems reasonable. It is also consistent with the fresh water experimental results discussed above. Therefore, as a first approximation, a value 0.26 is used for the liquid fraction λ in the present model.

Since the equilibrium freezing temperature of saline ice is below 0 °C, the effect of temperature on L_f should be taken into account. Chung (1989) performed a fitting of the data on latent heat of fusion provided by Iribarne and Godson (1985). He found that in the temperature range from 0 °C to -15 °C, L_f can be calculated with negligibly small error by:

$$L_f = 2.24x10^3 T_{s(j,k)} + 3.334x10^5 \qquad (4.2.12)$$

where $T_{s(j,k)}$ is in °C.

d) The specific heat capacity

The specific heat capacity of the brine can be approximated by the equation (Chung 1989):

$$C_{bt(j,k)} = (1 - S_{bt(j,k)})\,C_w \qquad (4.2.13)$$

where C_w is the specific heat capacity of pure water. Since it is not strongly dependent on temperature, a value of 4218 $Jkg^{-1}K^{-1}$ at 0 °C has been used.

e) The salinity of the ice accretion

The salinity of the spongy ice accretion is (Makkonen 1987):

$$S_{I(j,k)} = \frac{\lambda}{1 - (1-\lambda) F_r} S_{bt(j,k)} \qquad (4.2.14)$$

where

λ: The liquid fraction of the accretion.

F_r: The accretion fraction which is defined as the fraction of the incoming brine that is incorporated into the ice matrix.

f) The salinity of the brine remaining on the surface

During the freezing of brine, salt is rejected to the surrounding fluid and thus its salinity is increased. Therefore, the salinity of the brine that remains on the surface after ice accretion is (Makkonen, 1987):

$$S_{b(j,k)} = \frac{S_{bt(j,k)}}{1 - (1-\lambda) F_r} \qquad (4.2.15)$$

g) The density of the brine remaining on the surface

The density of the brine that remains on the surface after accretion is (Chung 1989):

$$\rho_{b(j,k)} = \left(1 + \frac{S_{b(j,k)}}{1 - S_{b(j,k)}}\right) \rho_w \qquad (4.2.16)$$

where ρ_w is the density of pure water which is taken to be 1000 kgm^{-3}.

h) The density of the spongy ice accretion

The density of the spongy ice accretion which consists of pure ice and brine pocket inclusions is given by (Chung 1989):

$$\rho_{ac(j,k)} = \frac{\rho_i \rho_{b(j,k)}}{(1-\lambda)\,\rho_{b(j,k)} + \lambda \rho_i} \qquad (4.2.17)$$

where ρ_i is the density of pure ice which is taken to be 917 kgm^{-3}.

i) The dynamic viscosity of the brine

The dynamic viscosity of the brine that remains on the surface after accretion must also be calculated in order to determine the brine flow rate (to be discussed later). The effect of salinity and temperature on dynamic viscosity have been presented by Unterberg (1966) in graphical form. His results have been used to derive two polynomial equations with which the dynamic viscosity of brine as a function of salinity and temperature can be approximated. These two polynomial equations are:

$$\begin{aligned}\mu_{bo} = {} & 1.78653x10^{-3} + 1.23022x10^{-3}S_{b(j,k)} + 1.14271x10^{-2}S^2_{b(j,k)} \\ & + 2.61285x10^{-2}S^3_{b(j,k)}\end{aligned} \qquad (4.2.18)$$

and

$$\begin{aligned}\mu_b = {} & \mu_{bo} - 5.52148x10^{-5}T_{s(j,k)} + 9.69236x10^{-7}T^2_{s(j,k)} \\ & - 8.74769x10^{-9}T^3_{s(j,k)} + 3.07292x10^{-11}T^4_{s(j,k)}\end{aligned} \qquad (4.2.19)$$

where

μ_{bo}: the dynamic viscosity of brine of salinity $S_{b(j,k)}$ (expressed as a fraction) at 0 °C ($kgm^{-1}s^{-1}$).

μ_b: the dynamic viscosity of brine of salinity $S_{b(j,k)}$ at the equilibrium surface temperature $T_{s(j,k)}$ in °C.

j) The kinematic viscosity of brine

The kinematic viscosity of the brine remaining on the surface is simply:

$$\nu_b = \frac{\mu_b}{\rho_{b(j,k)}} \qquad (4.2.20)$$

This completes the calculation of the thermodynamic properties of the brine film and of the saline ice. At the beginning of the next time step, the brine which remains on the grid cell surface is immediately mixed with the impinging spray and with the brine running down from the grid cell above. The calculation of the thermodynamic properties of this new brine mixture is then repeated in the same manner as above.

4.3 Temperature of the Impinging Spray Droplets

In Chapter 3, the calculation of the spray flux to a grid cell located on the surface of the ship was discussed in detail. The droplet temperature evolution during its flight through the air will be discussed in the present section. It is well known that the temperature of the impinging spray is crucial to determining the ice accretion rate (Zakrzewski et al., 1992). At the moment the spray droplet is injected into the airstream at the perimeter of the hull, its temperature is taken to be the sea-surface temperature. Once the spray droplet moves through the air, its temperature falls as heat is transferred away from the droplet's surface to the air. The possible nucleation of a spray droplet (i.e part of a spray droplet freezes) during its flight is neglected here, and thus the temperature of the droplet may supercool to well below its equilibrium freezing temperature. This assumption seems valid since the freezing of spray droplets in the air requires freezing nuclei. The presence of snow or of frazil ice in the sea surface may provide a source of freezing nuclei to allow the spray droplets to freeze. Blackmore and Lozowski (1993) found that if droplet nucleation was taken into account in their icing model, it was in better agreement with observation for extreme icing cases. Hence, nucleation may be an important factor in spray icing. However, the conditions necessary for nucleation to occur remain unclear and require further investigation. Thus we will ignore nucleation here.

For a droplet of 1.75 mm in diameter which has a total flight time of only a few seconds, evaporation can be neglected. Andreas (1989) developed a model to calculate the droplet size evolution. He found that a droplet 1.14 mm in diameter, with a salinity of 21.4 %, and a temperature of 8.1 °C, in an airstream at 20.4 °C with a relative humidity of 8 %, experienced negligibly small evaporation (loss < 1 % in mass) in the first 10 seconds. Thus we will ignore the effect of droplet evaporation on its mass, but not on its heat transfer.

Based on the assumption that the airstream properties are fixed, and do not change as a result of feedback of heat and momentum from the spray cloud, the temperature evolution of a droplet flying through the air can be calculated by the following heat conservation equation:

$$\frac{dT_d}{dt} = \frac{6}{d\rho_b C_b}(Q_C + Q_E + Q_R) \tag{4.3.1}$$

where

T_d: instantaneous temperature of the spray droplet (assumed to be well mixed) (°C).

d: spray droplet diameter (m).

ρ_b: density of the spray droplet which is taken to be the same as that of sea-surface brine (kgm^{-3}).

C_b: specific heat capacity of the spray droplet, which is taken to be the same as that of sea-surface brine ($Jkg^{-1}K^{-1}$).

Q_C: heat flux to the air due to convection (Wm^{-2}).

Q_E: heat flux due to evaporational cooling of the droplet (Wm^{-2}).

Q_R: heat flux to the air due to long wave radiation (Wm^{-2}).

The convective heat flux term is given by (Holman, 1981):

$$Q_c = h_d(T_d - T_a) \tag{4.3.2}$$

where h_d is the heat transfer coefficient for a spherical droplet of diameter d given by:

$$h_d = \frac{k_a Nu}{d} \tag{4.3.3}$$

where

k_a: conductivity of air ($Wm^{-1}K^{-1}$).

Nu: droplet Nusselt number (dimensionless).

The conductivity of air depends on its temperature (Makkonen 1988):

$$k_a = 0.0242 + 0.000073T_a \tag{4.3.4}$$

where T_a is in °C. The Nusselt number for a spherical droplet is given by Ranz and Marshall (1952):

$$Nu = 2 + 0.6Pr^{1/3}Re^{0.5} \tag{4.3.5}$$

Pr is the Prandtl number and Re is the droplet Reynolds number which is given by:

$$Re = \frac{|\vec{V}_d - \vec{U}\ |\ d}{\nu_a} \tag{4.3.6}$$

where $\overline{V}_d$ is the instantaneous velocity vector of the droplet, $\overline{U}$ is the wind vector, and ν_a is the kinematic viscosity of the airstream. The constant in Equation 4.3.5 accounts for heat conduction. It can be neglected at high Reynolds numbers. Zakrzewski et al. (1991) used another formula in their icing model, suggested by Michieev and Michieeva

(1973):

$$\begin{aligned} Nu &= 0.49Re^{0.5} && for && Re < 10^3 \\ Nu &= 0.24Re^{0.6} && for && Re > 10^3 \end{aligned} \qquad (4.3.7)$$

The Reynolds number of a droplet over its entire trajectory typically ranges from 500 to 6000 for ship icing. Within this range of Reynolds number, the Nusselt numbers calculated by Equations 4.3.5 and 4.3.7, on average, differ by about 10 % or less. This typically leads to a similar relative difference in impinging droplet temperature and in ice thickness. In view of this small difference and for consistency with previous marine icing models, we have chosen Equation 4.3.7 in the simulation of droplet cooling.

The evaporative heat flux term Q_E is given by (Zakrzewski and Lozowski, 1991):

$$Q_E = h_d\left(\frac{Pr}{Sc}\right)^{1/3}\left(\frac{\epsilon L_e}{C_p P_a}\right)\left(e_s(T_d) - RHe(T_a)\right) \qquad (4.3.8)$$

where

L_e: the specific latent heat of vaporization of pure water at 0 °C (Jkg^{-1}).

C_p: specific heat capacity of air at constant pressure ($Jkg^{-1}K^{-1}$).

$e_s(T_d)$: equilibrium vapour pressure over the surface of a brine droplet at the droplet temperature T_d (mb).

$e(T_a)$: equilibrium vapour pressure over a plane surface of pure water at the air temperature T_a (mb).

P_a: air pressure (mb).

$\in$: ratio of the molecular weights of water and dry air (0.622).

Pr: prandtl number.

Sc: schmidt number.

RH: relative humidity (expressed as a fraction).

The ratio $(Pr/Sc)^{1/3}$ is close to unity (~ 1.1). The specific heat capacity of air is a function of temperature and is given by (Chung, 1989):

$$C_p = 1004 + 0.046T_a \qquad (4.3.9)$$

with T_a in °C. Both $e_s(T_d)$ and $e(T_a)$ in Equation 4.3.8 can be calculated using Equations 4.2.9 and 4.2.10. Because the droplets are large, curvature effects are negligible.

Assuming that the emissivities of the droplet surface and its environment are both unity, the radiative heat flux term can be expressed by (Zemansky and Dittman, 1981):

$$Q_R = \sigma(T_d^4 - T_a^4) \qquad (4.3.10)$$

where σ is the Stefan Boltzmann constant ($Wm^{-2}K^{-4}$).

The droplet trajectory to a grid cell target has already been calculated in the spraying model. In order to calculate the droplet's temperature evolution, and hence its final temperature on impact, Equation 4.3.1 is integrated numerically along the trajectory using an Euler forward difference method with a time step of 10^{-3} s.

Figure 4.3.1 shows an example of a droplet trajectory and its temperature evolution. The droplet is injected into the airstream at the bow with an initial vertical velocity of 20 ms^{-1} and a temperature of 2.0 °C. Then, dragged by the wind, the droplet follows a skewed-parabolic trajectory and falls back onto the deck after 1.9 seconds at a distance of about 22 m from the source point. The impingement temperature is about -2.4 °C.

4.4 Physics of Brine Flow

(a) Vertically Falling Liquid Film

In marine spray icing, the ice surface is usually covered by a thin brine film and its flow rate directly affects the icing rate and also the total amount of spongy ice which can be accreted. For simplicity we neglect wind stress on the film and assume that on vertical surfaces, such as the front of the wheelhouse and the mast, the brine film moves only vertically downward. On such surfaces, the brine film thickness varies with height

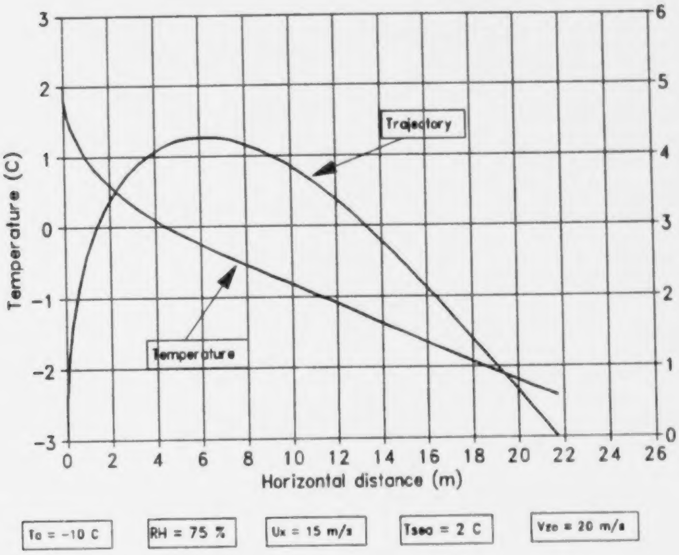

Figure 4.3.1: A droplet trajectory and its temperature evolution. The droplet diameter is 1.75 mm.

depending on the local spray flux and icing rate. Under normal circumstances, the film thickness decreases with increasing height. Thus, the flow rate at different locations also varies, depending on the thickness. In view of the importance of film thickness, we will now discuss how it may be calculated.

Consider a liquid film of uniform thickness δ on a vertical grid cell (Figure 4.4.1a). Experimental observations show that waves appear on the surface of the liquid film even at a very low flow rate (Dukler and Bergelin, 1952). It becomes extremely difficult to determine the flow rate if both wave motion and film turbulence are taken into account. Hence, as a first approximation, the wave motion is neglected and the flow is assumed to be laminar. These assumptions were first made by Nusselt (1916) to derive an equation to calculate the thickness of a vertically falling film. With these assumptions, only the forces of gravity and viscosity remain in the boundary layer equation. Thus, the steady-state vertical velocity profile (Figure 4.4.1b) within the liquid film can be represented by:

$$\nu_b \frac{d^2 U_{bz}}{dx^2} = -g \qquad (4.4.1)$$

where

ν_b: the kinematic viscosity of the brine film (m^2s^{-1}).

U_{bz}: the vertical flow velocity in the brine film (considered positive if downward) (ms^{-1}).

x: horizontal coordinate normal to the plane of the brine film (m).

g: acceleration due to gravity (ms^{-2}).

Using the boundary conditions $U_{bz} = 0$ at $x = 0$ and $dU_{bz}/dx = 0$ at $x = \delta$, Equation 4.4.1 may be solved for U_{bz}:

$$U_{bz} = \frac{g}{2\nu_b}(2\delta - x)x \qquad (4.4.2)$$

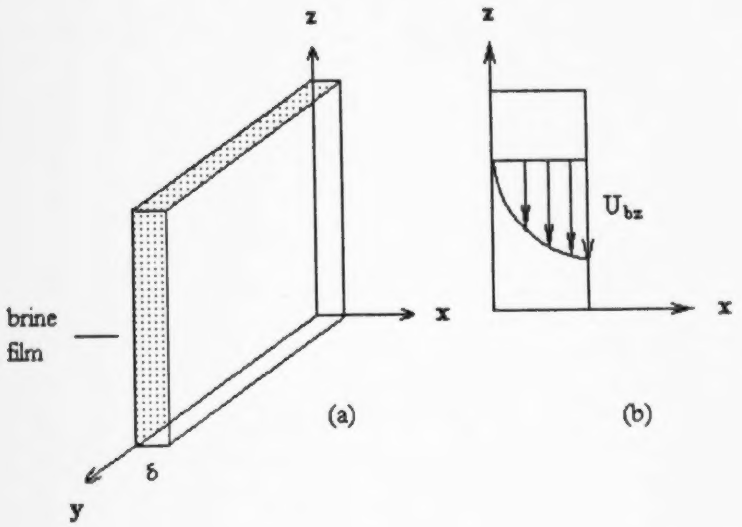
z
z
U_bz
x
x
brine
film
(a)
(b)
δ
y

Figure 4.4.1 : a) Liquid film of uniform thickness on a vertical grid cell. b) Vertical velocity profile within the liquid film.

We are interested in the average velocity for the entire layer of the liquid film, which is given by:

$$\langle U_{bz} \rangle = \frac{1}{\delta}\int_0^{\delta} U_{bz}\,dx \tag{4.4.3}$$

Substituting Equation 4.4.2 into 4.4.3, yields:

$$\langle U_{bz} \rangle = \frac{g\delta^2}{3\nu_b} \tag{4.4.4}$$

For very high spray fluxes which imply a very thick liquid film, Equation (4.4.4) can not be applied directly to the entire layer of the liquid film because a large portion of the outer layer of the liquid film will merely fall under gravity with little frictional retardation leaving only a thin film behind flowing along the surface according to Equation 4.4.2. Since Equation (4.4.4) is valid only for laminar flow, when the film thickness in the model becomes greater than the maximum possible thickness of a laminar layer, the excess liquid is assumed to fall under gravity and to disappear immediately. In other words, in the model simulation, the maximum thickness of the liquid film on a vertical surface is not allowed to exceed that of a laminar layer.

According to Dukler and Bergelin (1952), the laminar and buffer regions as suggested by Nikuradse (1933) can be grouped into an effective laminar layer in which Nusselt's Equation 4.4.4 is satisfied. According to Nikuradse (1933), the maximum thickness of this effective laminar layer δ_L is given by:

$$\eta = \frac{\sqrt{g\delta^3}}{\nu_b} = 30 \tag{4.4.5}$$

Therefore,

$$\delta_L = \left(\frac{30\nu_b}{\sqrt{g}}\right)^{\frac{2}{3}} \tag{4.4.6}$$

Substituting Equation 4.4.6 into 4.4.4, the corresponding maximum mean brine film velocity is:

$$\langle U_{bz}\rangle_{max} = 31.07\,(g\nu_b)^{\frac{1}{3}} \tag{4.4.7}$$

From Equations 4.4.6 and 4.4.7, it can be seen that both δ_L and $<U_{bz}>_{max}$ are functions of the kinematic viscosity of the brine. In the present case, the film consists of brine whose kinematic viscosity depends on salinity and temperature and can be calculated by Equations 4.2.18, 4.2.19, and 4.2.20.

Figure 4.4.2 shows how the maximum film thickness (δ_L) and the corresponding maximum mean vertical velocity ($<U_{bz}>_{max}$) vary with kinematic viscosity. A maximum kinematic viscosity of about 3.0×10^{-6} m^2s^{-1} occurs with a salinity of ~20 % and a liquid temperature of -15 °C. This is an extreme case which seldom occurs in spray icing. Hence, it can be concluded that the maximum laminar brine film thickness on a vertical surface is less than 1 mm and the corresponding mean vertical velocity does not exceed 1 ms^{-1}. These values are very useful in determining the choice of the time step in the icing model. This will be discussed in Section 4.6.

(b) Horizontal Liquid Film

On a horizontal surface, the motion of the brine film is very sensitive to the pitching and rolling of the ship and thus the brine flow may be unsteady and random. Consequently, we make the simple assumption that a brine film lying on a horizontal surface (e.g the deck or the top of the wheelhouse) does not move, on average, in any direction. For very high spray fluxes, a horizontal surface (e.g the deck) may be flooded with a huge amount of water (greenwater) which will quickly run off and leave a thin

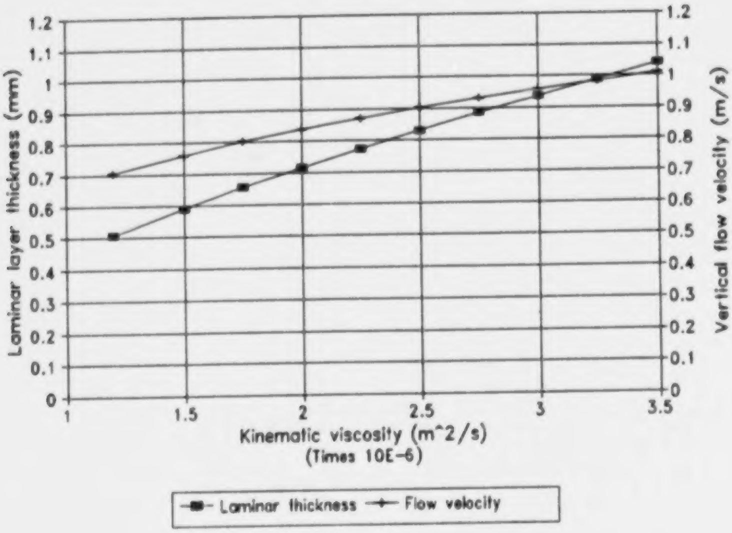

Figure 4.4.2 : Maximum laminar brine film thickness and the corresponding maximum mean vertical velocity vs kinematic viscosity.

film lying on the surface. Thus, it is necessary to estimate the maximum thickness of the residual brine film residing on a horizontal surface. If the maximum thickness of the brine film that remains on a horizontal surface is δ_h, then, when the liquid layer thickness in the model exceeds δ_h, the excess brine is treated as greenwater and simply removed.

Let us consider a wetting liquid which is poured slowly onto a flat horizontal surface to form a circular pool of a certain size. This pool of liquid will spread outward slowly, reaching an equilibrium state with a thickness δ_h as shown in Figure 4.4.3. We assume that the radius R of this pool of liquid is much greater than its thickness δ_h. In Figure 4.4.3, the interfacial forces acting on the liquid boundary are also shown. In view of the force balance, the equilibrium thickness, δ_h, can be calculated in the following way (Marion and Hornyak, 1982).

The change in surface energy of the pool if δ_h is decreased by $d\delta_h$ is given by:

$$dW_{1a} = \gamma_b dS \tag{4.4.8}$$

where γ_b is the surface tension of the liquid (Nm^{-1}), and dS is the change in the surface area of the liquid-air interface corresponding to the change in δ_h. From Figure 4.4.3, the surface area of the liquid-air interface is approximately:

$$S = \pi R^2 + 2\pi R\delta_h \tag{4.4.9}$$

The derivative of S with respect to δ_h is:

$$\frac{dS}{d\delta_h} = 2\pi(R + \delta_h)\frac{dR}{d\delta_h} + 2\pi R \tag{4.4.10}$$

For an incompressible fluid:

$$dV = \pi R^2 d\delta_h + 2\pi R\delta_h dR = 0 \tag{4.4.11}$$

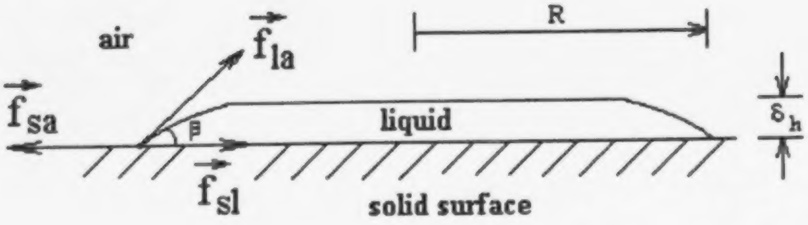

air
$\vec{f}_{la}$
R
$\vec{f}_{sa}$
β
liquid
δ_h
$\vec{f}_{sl}$
solid surface

Figure 4.4.3: Cross-section of a circular pool of liquid at rest on a horizontal surface. β is the wetting angle of the liquid. f_{sa}, f_{sl}, and f_{la} are solid-air, solid-liquid, and liquid-air interface forces respectively.

where V is the volume of the liquid. Equation 4.4.11 can be expressed as:

$$\frac{dR}{d\delta_h} = -\frac{R}{2\delta_h} \tag{4.4.12}$$

Substituting Equation 4.4.12 into 4.4.10, dS becomes:

$$dS = (\pi R - \frac{\pi R^2}{\delta_h})\, d\delta_h \tag{4.4.13}$$

With Equation 4.4.13, Equation 4.4.8 can be rewritten as:

$$dW_{1a} = \gamma_b \pi R (\frac{\delta_h - R}{\delta_h})\, d\delta_h \tag{4.4.14}$$

For R $>>$ δ_h, Equation 4.4.14 becomes:

$$dW_{1a} = -\frac{\gamma_b \pi R^2}{\delta_h} d\delta_h \tag{4.4.15}$$

dW_{la} (positive) is the energy required to spread the liquid when its thickness is reduced by $d\delta_h$ (negative).

The work done by surface tension along the perimeter of the liquid-solid boundary corresponding to a change of $d\delta_h$ is:

$$dW_{1s} = (f_{sl} - f_{sa})\, dS' \tag{4.4.16}$$

where

f_{sl}: the surface force at the solid-liquid interface (Nm^{-1}).

f_{sa}: the surface force at the solid-air interface (Nm^{-1}).

Since, f_{sl}-f_{sa} = $-f_{la}\cos\beta$ = $-\gamma_b\cos\beta$, S' = πR^2, and $dS'/d\delta_h$ = $-(\pi R^2)/\delta_h$ (from Equation

4.4.12), then:

$$dW_{ls} = \gamma_b \cos\beta \frac{\pi R^2}{\delta_h} d\delta_h \qquad (4.4.17)$$

dW_{ls} is negative and is the energy available to spread the liquid such that its thickness changes by $d\delta_h$.

Let us now consider the change in gravitational potential energy during spreading of the liquid. The potential energy of the liquid is given by:

$$PE = \frac{1}{2}\pi R^2 \rho_b g \delta_h^2 \qquad (4.4.18)$$

When the liquid spreads outward, the change in PE is:

$$d(PE) = \frac{1}{2}\pi \rho_b g R^2 \delta_h d\delta_h \qquad (4.4.19)$$

Equation 4.4.12 has been used in deriving Equation 4.4.19. d(PE) is the potential energy given up when the liquid spreads so that its thickness changes by $d\delta_h$.

When the liquid film shown in Figure 4.4.3 is in a state of equilibrium, then the sum of dW_{la}, dW_{ls}, and d(PE) should be zero (Marion and Hornyak, 1982), i.e:

$$dW_{la} + dW_{ls} + d(PE) = 0 \qquad (4.4.20)$$

Using Equation 4.4.20, δ_h may be shown to be:

$$\delta_h = \sqrt{\frac{2\gamma_b(1-\cos\beta)}{\rho_b g}} \qquad (4.4.21)$$

If the liquid is water with slight contamination and lies on a glass surface, the wetting angle β is ~ 20° (Marion and Hornyak, 1982). Since the wetting angle of brine is not known, a value of 20° is assumed here as a first approximation. It is conceivable that, for brine on spongy marine ice, β may be close to zero in which case δ_b could be very small.

Using the graphical results from Unterberg (1966), two polynomial equations have been derived to calculate the surface tension γ_b as a function of salinity and temperature. These are:

$$\gamma_{bo} = 7.5604x10^{-2} + 3.3979x10^{-2}S_b - 7.0x10^{-2}S_b^2 + 0.37S_b^3 \tag{4.4.22}$$

and

$$\gamma_b = \gamma_{bo} - 1.4x10^{-4}T_s \tag{4.4.23}$$

where γ_{bo} is the surface tension (Nm^{-1}) of the brine as a function of fractional salinity S_b at 0 °C, and T_s is the brine temperature (°C). Equation 4.4.22 is valid for a salinity ranging from 0 % to 24 % before saturation takes place (Unterberg, 1966). For Equation 4.4.23, it is applicable for a temperature ranging from 0 °C to boiling (Unterberg, 1966). This equation can be extended to a temperature well below 0 °C (for example -10 °C) without causing a significant error.

From Equations 4.2.16, 4.4.22, and 4.4.23, it can be seen that γ_b increases for increasing S_b and decreasing T_s. But, as S_b increases, ρ_b increases as well. For a given temperature, the ratio of γ_b/ρ_b increases as S_b decreases. Table 4.4.1 gives an example on how the ratio of γ_b/ρ_b and δ_b changes as the salinity increases at a brine temperature of 0 °C.

S_b (fraction)	γ_{bo} (10^{-3}Nm^{-1})	ρ_b (kgm^{-3})	γ_{bo}/ρ_b (10^{-5}m^{3}s^{-2})	δ_h (mm)
0.00	75.604	1000.0	7.5604	0.9641
0.04	76.875	1041.7	7.3800	0.9526
0.08	78.064	1087.0	7.1819	0.9397
0.12	79.313	1136.4	6.9796	0.9264
0.16	80.764	1190.5	6.7842	0.9133
0.20	82.560	1250.0	6.6048	0.9011
0.24	84.842	1315.8	6.4480	0.8904

Table 4.4.1: Variation of γ_b/ρ_b and δ_h with salinity at a brine temperature of 0 °C.

Table 4.4.1 shows that at T_s = 0 °C, δ_h is a maximum for fresh water and a minimum for brine of salinity 0.24. Changes in temperature do not cause any significant change in these two extreme values. Since the variation of δ_h with salinity is small, we simplify the problem further, by using a constant value of δ_h = 1 mm for the maximum brine film thickness residing on a horizontal surface, regardless of the salinity and temperature of the brine film. This approximation gives a conservative prediction of the maximum possible amount of brine on a horizontal surface which is available for ice accretion. The sensitivity of the present icing model to δ_h has been tested using two different brine film thicknesses (δ_h = 1 mm and δ_h = 0.1 mm). Under an extreme icing condition, which will be presented in Section 4.8, the difference in the total ice load on the deck and the top of the wheelhouse using these two brine film thicknesses is 11 %.

4.5 Physics of Ice Accretion

Under favourable conditions, when spray droplets impinge on the surface of the ship and form a brine film, spongy ice will be accreted on the surface because heat is lost from the brine film to the air. In the model, the ship's surface is divided into components (the deck, wheelhouse, and mast) on which is superimposed a network of grid cells. We will describe the workings of the model by first considering a grid cell located on a vertical surface (Figure 4.5.1). The heat transfer equation is applied to this grid cell in order to calculate its icing rate. The icing rate on any other grid cell on any other component can be calculated in a similar manner.

Two assumptions should be mentioned here. The first assumption is that heat conduction between the icing interface and the underlying material is neglected. The second assumption is that freezing takes place at the liquid/solid interface at the liquid's equilibrium freezing temperature determined from Equation 4.2.8. This means that supercooling in the liquid film is not taken into account. Hence, the heat balance for the spongy ice accretion on the surface of the grid cell can be represented by the following equation:

$$q_{c(j,k)} + q_{e(j,k)} + q_{r(j,k)} = q_{s(j,k)} + q_{f(j,k)} \qquad (4.5.1)$$

where

$q_{c(j,k)}$: the heat flux due to forced convection from the surface (Wm^{-2}).

$q_{e(j,k)}$: the heat flux due to evaporation from the surface (Wm^{-2}).

$q_{r(j,k)}$: the heat flux due to net long wave radiative heat transfer away from the surface (short wave radiative heat transfer is ignored) (Wm^{-2}).

$q_{s(j,k)}$: the heat flux associated with cooling of the total incoming brine flux to its equilibrium freezing temperature (Wm^{-2}).

$q_{f(j,k)}$: the heat flux due to the release of latent heat of freezing (Wm^{-2}).

We will now discuss each term of Equation (4.5.1) individually.

a) Convective heat flux $q_{c(j,k)}$

The heat flux due to convection can be calculated by (Holman, 1981):

$$q_{c(j,k)} = h_{(j,k)}(T_{s(j,k)} - T_a) \qquad (4.5.2)$$

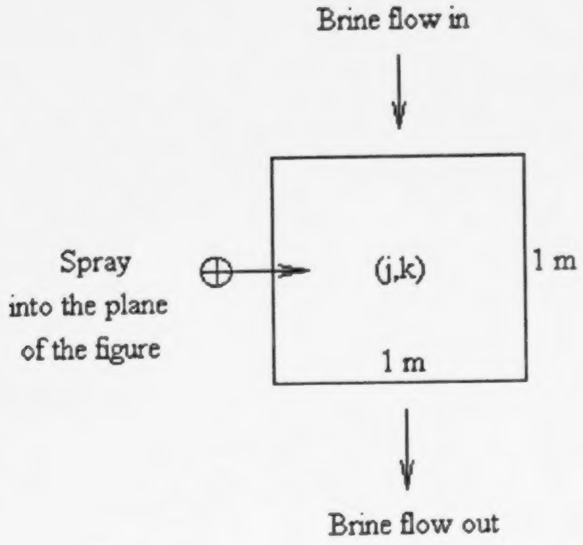
Brine flow in
Spray
into the plane
of the figure
(j,k)
1 m
1 m
Brine flow out

Figure 4.5.1 : A grid cell located on a vertical surface.

where

$h_{(j,k)}$: the heat transfer coefficient for grid cell (j,k) ($Wm^{-2}K^{-1}$).

$T_{s(j,k)}$: the equilibrium freezing temperature of the brine film on the surface of grid cell (j,k) (°C).

T_a: the air temperature (°C).

The heat transfer coefficient is related to the surface Nusselt number, Nu, by:

$$h_{(j,k)} = \frac{k_a Nu}{L} \tag{4.5.3}$$

where L is a characteristic length of the surface in question and k_a is the thermal conductivity of air. The complicated structure of the ship makes the Nusselt number and the characteristic length difficult to determine. No reference to external heat transfer from ships of any kind could be found, and certainly there have been no heat transfer measurements from the Zandberg. Consequently, various approximations are employed in order to solve the problem. To do this, the three components (the deck, the wheelhouse and the mast) are treated separately as in Lozowski et al. (1992).

The mast is represented by a circular cylinder of constant diameter. Under the environment in which ship icing occurs, the flow over the mast is very likely to be highly turbulent. For example, with a relative air speed of 5 ms^{-1} and a diameter of 0.58 m, the Reynolds number of the flow will be about 2.3×10^5, which, according to Zukauskas (1985), is within the turbulent flow regime. Thus, the overall Nusselt number for the ship mast is (Zukauskas, 1985):

$$Nu = 0.023 Pr^{0.4} Re^{0.8} \tag{4.5.4}$$

where Pr is the Prandtl number (0.711 for air) and Re is the Reynolds number which typically will lie in the range from 2×10^5 to 10^7. The characteristic length L in Equation 4.5.3 for the mast is simply its diameter.

The foredeck and the deck behind the wheelhouse are represented by flat plates.

Again, the flow over these two surfaces is turbulent. The overall Nusselt number for parallel flow over a smooth flat plate under a turbulent flow regime is given by (Kreith and Black, 1980):

$$Nu = 0.036 Pr^{0.33} Re^{0.8} \tag{4.5.5}$$

for a Reynolds number in the range $5x10^5$ to 10^7. Because the wind direction is arbitrary, the characteristic length for the deck is taken in the model to be the square root of the total deck surface area. Hence, for the foredeck, L is 11.7 m while for the deck behind the wheelhouse L is 19.2 m.

The wheelhouse is represented by a box mounted on a horizontal surface. Quite a few research papers have been published on the heat transfer from rectangular polyhedra (Motwani et al., 1985, Test et al., 1980, and Test et al., 1981), square prisms (Igarashi, 1984 and 1985), and wall mounted cubes (Chyu et al., 1991). However, they deal only with low Reynolds numbers ($Re < 10^5$) and are thus not quite relevant to the present situation. For a large body such as the wheelhouse, the Reynolds number will typically exceed 10^6. In addition, the flow over a box-like structure is turbulent even for low Reynolds numbers, as suggested by the above authors. For high Reynolds number flows, the only Nusselt number data readily available are for cylinders, spheres, and flat plates. Figure 4.5.2 compares the Nusselt numbers for these three different objects. The Nusselt number for a flat plate lies between that for a sphere and a cylinder. In the model, the Nusselt number for a flat plate is used to approximate that for the wheelhouse. Thus, the icing prone portion of the wheelhouse is subdivided into two flat plates, representing the top and front sides. Since the right and left sides, and the back side of the wheelhouse do not receive spray in the model, they are ignored. Thus, we have one flat plate representing the front of the wheelhouse and another representing the top of the wheelhouse. The Nusselt number for these two surfaces is calculated using Equation 4.5.5. The characteristic lengths for these two surfaces are defined as for the deck. L is 7.2 m for the front and 8.3 m for the top of the wheelhouse. Hence, using Equations 4.5.4 and 4.5.5, together with the appropriate characteristic lengths, the heat

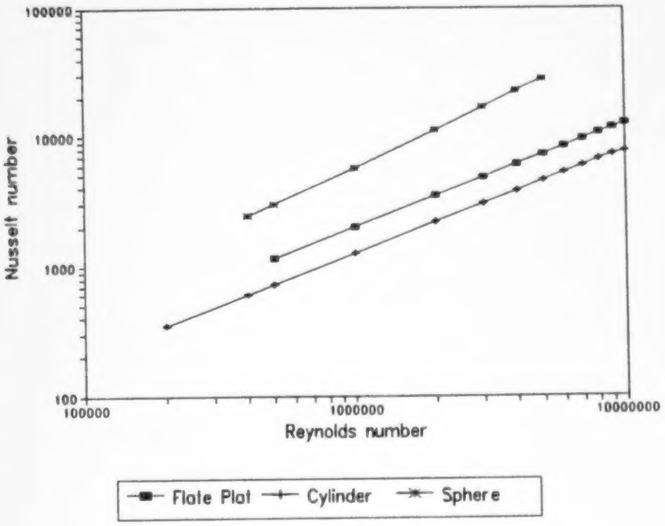

Figure 4.5.2: A comparison of the Nusselt number as a function of Reynolds number under a turbulent flow regime for a cylinder (in cross flow), a flat plate (in parallel flow), and a sphere.

transfer coefficients for various components of the ship can be calculated.

b) Evaporative heat flux $q_{e(i,j)}$

The heat flux due to evaporative cooling can be represented by (Zakrzewski and Lozowski, 1991):

$$q_{e(j,k)} = h_{(j,k)} \left(\frac{Pr}{Sc}\right)^{1/3} \left(\frac{\epsilon L_e}{C_p P_a}\right) \left(e_s(T_{s(j,k)}) - RHe(T_a)\right) \qquad (4.5.6)$$

where

$e_s(T_{s(j,k)})$: the equilibrium vapour pressure over the brine film surface at the equilibrium surface temperature $T_{s(j,k)}$.

$e(T_a)$: the equilibrium vapour pressure over a plane surface of pure water at the air temperature T_a.

Pr: Prandtl number of air.

Sc: Schmidt number of air.

ϵ: ratio of the molecular weights of water and dry air.

Both $e_s(T_{s(j,k)})$ and $e(T_a)$ are calculated using Equations 4.2.9 and 4.2.10.

c) Radiative heat flux $q_{r(j,k)}$

Assuming black body radiation, the net heat flux due to the net transfer of long wave radiation to and from the grid cell surface is (Zemansky and Dittman, 1981)):

$$q_{r(j,k)} = \sigma \left(T^4_{s(j,k)} - T^4_a\right) \qquad (4.5.7)$$

where

σ is the Stefan Boltzmann constant ($Wm^{-2}K^{-4}$).

$T_{s(j,k)}$ and T_a are in degrees K.

d) Sensible heat flux $q_{s(j,k)}$

The total brine flux to the grid cell has a salinity $S_{bt(j,k)}$ (Equation 4.2.4) and a mean temperature $T_{mean(j,k)}$ (Equation 4.2.5). This brine must cool to its equilibrium freezing temperature before freezing takes place. The heat exchange in this process is:

$$q_{s(j,k)} = m_{bt(j,k)} C_{bt(j,k)} (T_{mean(j,k)} - T_{s(j,k)}) \qquad (4.5.8)$$

where

$m_{bt(j,k)}$: the total brine flux to the grid cell ($kgm^{-2}s^{-1}$).

$C_{bt(j,k)}$: the specific heat capacity of this brine ($Jkg^{-1}K^{-1}$).

$m_{bt(j,k)}$ is calculated using Equations 4.2.1 to 4.2.3 and $C_{bt(j,k)}$ using Equation 4.2.13. For horizontal surfaces, no brine flow is considered. In these cases, the total brine flux $m_{bt(j,k)}$ consists of i) the incoming spray and ii) the brine remaining on the grid cell surface after ice accretion in the previous time step. In other words, $M_{f(j,k+1)}$ is zero in Equation 4.2.1.

e) Latent heat flux $q_{f(j,k)}$

Saline ice contains numerous brine pockets and thus is spongy. Because of this brine entrapment, the liquid fraction has to be taken into account in calculating the heat flux due to spongy ice formation. Thus:

$$q_{f(j,k)} = L_{fs} I_{(j,k)} \qquad (4.5.9)$$

where

L_{fs}: the latent heat of fusion for spongy ice (Jkg^{-1}).

$I_{(j,k)}$: the spongy ice growth mass flux ($kgm^{-2}s^{-1}$).

L_{fs}, which depends on the liquid fraction λ, is given by Equation 4.2.11.

Using Equations 4.5.1, 4.5.2, and 4.5.6 to 4.5.9, the accretion rate $I_{(j,k)}$ can be calculated. The accretion fraction is then defined by:

$$F_I = \frac{I_{(j,k)}}{m_{bt(j,k)}} \qquad (4.5.10)$$

The ice load on a given grid cell (j,k) at time $t_n = n\Delta t$ is given by:

$$m_I(t_n) = m_I(t_{n-1}) + I_{(j,k)}A_{(j,k)}\Delta t \qquad (4.5.11)$$

where

$m_I(t_n)$: the ice load on the grid cell at time t_n (kg).

$m_I(t_{n-1})$: the ice load on the grid cell at the previous time step t_{n-1} (kg).

$A_{(j,k)}$: the surface area of the grid cell (m^2).

The shape and the surface area of the grid cells, particularly those on the mast, will change with time as the ice builds up. Taking this effect into consideration would complicate the model, without necessarily changing the results significantly. Thus, this effect is ignored in the model and every grid cell has a constant surface area. Hence, the ice thickness on the grid cell at time t_n is:

$$h^*(t_n) = h^*(t_{n-1}) + \frac{I_{(j,k)}}{\rho_{ac(j,k)}}\Delta t \qquad (4.5.12)$$

where

$h^*(t_n)$: the spongy ice thickness on the grid cell at time t_n (m).

$h^*(t_{n-1})$: the spongy ice thickness on the grid cell at time t_{n-1} (m).

$\rho_{ac(j,k)}$: the density of the spongy ice accretion on the grid cell which is calculated from Equation 4.2.17 (kgm^{-3}).

The thickness of the brine remaining on the grid cell surface, $\delta_{b(j,k)}$, after ice accretion can readily be calculated by:

$$\delta_{b(j,k)} = \left(\frac{m_{bt(j,k)} - I_{(j,k)}}{\rho_{b(j,k)}}\right)\Delta t \qquad (4.5.13)$$

where $\rho_{b(j,k)}$ is the density of the brine that remains on the grid cell surface after ice accretion and can be calculated from Equation 4.2.16.

The time from the beginning of one spray to the beginning of the next is one period of the spray and icing cycle (P_{spg} from Equation 4.1.7). In the model, only one cycle is considered. Within each cycle, there are two distinct intervals. The first interval consists of the time during which airborne spray is impinging onto a grid cell. During the second interval, there is no direct spray impingement, but freezing and surface brine flow may continue. It is assumed that there is no heat transfer to the underlying material during the entire period of the spray and icing cycle.

A certain amount of brine will remain on the ship's surface after one period of the spray and icing cycle. The remaining brine can not accumulate indefinitely from one cycle to another because of brine drainage. To model the long-term drainage of brine is extremely complicated and beyond the scope of this thesis. Therefore, it was decided to ignore the brine which remains on the ship's surface after one cycle of the icing calculation. This is similar to the procedure used by Zakrzewski et al. (1992) in order to reduce the computational time. At the end of the cycle, only a small amount of brine will likely remain on the ship's surface and the salinity of this brine will be higher than that of the new incoming brine. Thus, neglecting this remaining brine at the end of the cycle should not cause underestimation of the icing rate.

The icing load over a longer period may be extrapolated by simply multiplying the single spray ice load by the number of spray events (Zakrzewski et al., 1992). Hence, after N hours, the ice load and thickness on the grid cell (j,k) are given by:

$$M_{I(j,k)} = 60.0 m_{I(j,k)} N f_{spg} \qquad (4.5.14)$$

and

$$H^*_{(j,k)} = 60.0 h^*_{(j,k)} N f_{spg} \qquad (4.5.15)$$

where

$M_{I(j,k)}$: the total ice load on the grid cell after N hours (kg).

$H^*_{(j,k)}$: the total ice thickness on the grid cell after N hours (m).

$m_{I(j,k)}$: the ice load on the grid cell after a single spray event (kg).

$h^*_{(j,k)}$: the ice thickness on the grid cell after a single spray event (m).

f_{spg}: the frequency of spray generation (min^{-1}).

Finally, the total ice load over the entire vessel is simply:

$$M_{Itot} = \sum_{j,k} M_{I(j,k)} \qquad (4.5.16)$$

where the summation covers all the grid cells over the surface of the vessel.

4.6 Model Implementation

The icing model is programmed in Fortran and is listed in Appendix 4. A diskette containing the model source files is included in a packet at the end of the thesis. The input parameters for the model include:

a) Air temperature, relative humidity, air pressure, sea- surface temperature, wind speed and direction, fetch, ship speed, and duration of the simulation.

b) Coordinates of the perimeter of the hull, grid cell centre coordinates, grid cell surface areas, unit normal vectors to the grid cell surface.

c) Spray flux and droplet impingement temperature for every grid cell. This information is derived from the spraying model which is coded as a subroutine of the icing model.

The output of the icing model includes the spongy ice thickness (cm), spongy ice mass (kg), and spongy ice accretion rate ($kgm^{-2}hr^{-1}$) for every grid cell. In addition, the total accretion mass (kg) for the entire vessel and the overall icing rate ($kghr^{-1}$) are also calculated from the model.

As discussed in Section 4.4, the brine film on a vertical surface usually has a mean vertical velocity below 1 ms^{-1}. This information is useful in determining the time step used in the icing model. All the grid cells located on vertical surfaces (i.e the front of the wheelhouse and the mast), except those located along the top row of the front of the wheelhouse, have a height of 1 m. Hence it is appropriate to use a time step $\Delta t \leq$ 1 second. If $\Delta t >$ 1 second, the brine may pass through more than one grid cell within a single time step. If this were to occur, calculation of the total brine flux to a grid cell may be erroneous. The grid cells on the top row of the front of the wheelhouse have a length of 0.5 m. Hence the brine film velocity for these grid cells is not allowed to exceed 0.5 ms^{-1} in the model.

It is not necessary to use a very small time step to simulate the icing process because the icing rate should not normally change rapidly over a time scale of less than a second. Thus, a time step of 1 second has been chosen for use in the icing model.

As discussed in Section 4.4, the brine flow rate on a vertical surface is calculated based on an effective laminar layer approximation. Therefore, in the icing model simulation, if the brine film thickness on a vertical surface exceeds the corresponding effective laminar layer thickness, the excess brine is simply ignored. Thus, at the end of each time step, after the calculation of the spongy ice accretion, if the brine film remaining on the grid cell surface is greater than the corresponding effective laminar layer thickness, the brine film thickness is set equal to the effective laminar layer thickness.

For horizontal surfaces (i.e the deck and the top of the wheelhouse), it was determined in Section 4.4 that the maximum brine film thickness is approximately 1 mm. Thus, whenever the brine film thickness on these surfaces exceeds 1 mm, the excess brine is treated as "greenwater". Since it takes a while for this green water to return back to the sea, at the end of the spray event (i.e $t = P_{sp}$), if the brine film thickness is greater than 1 mm, the excess brine is ignored.

It was mentioned in Section 4.5 that a single spray cycle consists of two time intervals. The first time interval terminates at the end of spraying. This time ($t = P_{sp}$) is usually not an integral multiple of Δt. Thus, the last time step in the first time interval is allowed to be less than one second in the model. The second time interval begins at the end of spraying and ends at the start of the next spray. The final time step in this time interval is also allowed to be less than one second in the model. Figure 4.6.1 illustrates this situation.

In the current icing model, as in Zakrzewski et al. (1992), brine flow from component to component (e.g from the mast to the top of the wheelhouse, or from the front of the wheelhouse to the deck, etc) is not considered. Thus, brine which exits a particular component is neglected. This assumption is made in order to make the model structure less complicated, and simplify the brine accounting problem since the details of the excess brine flow over the vessel would be exceedingly difficult to work out in detail.

4.7 Sensitivity Tests

The severity of spray icing is largely determined by the atmospheric and oceanographic conditions. Under mild conditions, spray icing is unlikely to occur. Under severe weather with sub-freezing temperatures and high winds, spray icing is likely to occur on most small to medium size vessels. Sometimes, under extreme conditions, tonnes of ice can be accumulated within an hour. A sensitivity test will now be performed to show the effect of the environmental and operating parameters on the total ice load. The standard condition is T_a = -10 °C, P_a = 1000 mb, RH = 75 %, T_{sea} = 2 °C, U = 15 ms^{-1}, $\theta = 0°$, F = 200 n.m, and V_s = 3 ms^{-1}, S_{sea} = 3.3 %. Many icing researchers have shown that icing is insensitive to atmospheric pressure (Zakrzewski et al., 1992). Thus, it will not be included in the sensitivity test. In the sensitivity tests, one parameter is changed while the others are maintained at their standard values.

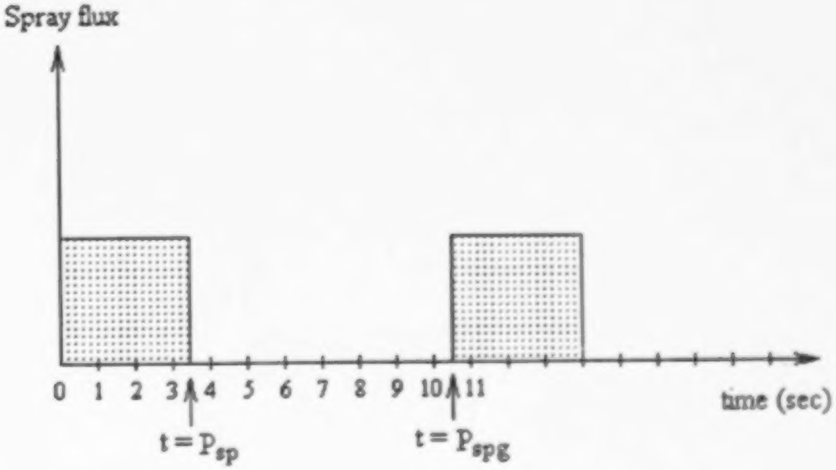

Figure 4.6.1: Periods of spraying during two spray cycles. The shaded region represents the period of spraying (P_{sp}), after which there is a quiescent period without spray. P_{spg} is the period of one complete cycle of spray generation.

Table 4.7.1 summarizes the total ice load accumulated in one hour on the entire vessel under different atmospheric and oceanographic conditions. Figure 4.7.1a shows how the total ice load over the entire vessel varies with air temperature. At an air temperature just below the equilibrium freezing temperature of sea-surface brine, only a very little is accumulated (< 0.2 tonnes/hour). However, as the air temperature drops, the heat transfer from the icing surface to the air increases almost linearly, and so does the total ice load. At an air temperature of -25 °C, more than 2.2 tonnes of ice are accumulated in one hour.

Decreasing the relative humidity increases the evaporative heat loss from the icing surface, thus increasing the icing rate. As indicated in Figure 4.7.1b, the total ice load increases by about 32 % when the relative humidity drops from 100 % to 0 %.

The effect of sea-surface temperature on the ice load is complicated. For a wind speed of 15 ms^{-1}, the ice load increases by only 37 % as the sea-surface temperature decreases from +6 °C to -2 °C (Figure 4.7.1c). But, for a higher wind speed of 25 ms^{-1}, the ice load increases by a factor of eight as the sea-surface temperature drops from +1 °C to -2 °C (Figure 4.7.1d). The explanation is directly related to the sensible heat flux term q_s in Equation 4.5.1. In the model, all of the incoming spray is assumed to contribute its sensible heat to the heat balance. Thus, a higher spray flux implies a more significant effect of the term q_s on the ice accretion rate (Equations 4.5.1 and 4.5.8). The amount of spray generated with a wind speed of 15 ms^{-1} (wave height 4 m) is much less than that generated with a wind speed of 25 ms^{-1} (wave height 8 m). At a low sea-surface temperature (e.g < 0 °C), the spray droplets impinging on most of the grid cells are likely to be supercooled. Therefore, the term q_s in Equation 4.5.1 becomes a heat sink. At low wind speeds, less spray can be produced, and hence the amount of spray available for ice accretion is limited. As a result, the icing rate does not increase significantly as the sea-surface temperature decreases. With high wind speeds, much more spray is produced, and, the effect of the term q_s in Equation 4.5.1 becomes much more significant. As a result, the ice accretion rate increases sharply as the sea-surface temperature drops below a threshold value (i.e when the q_s term changes from a source to a sink term for most of the grid cells).

Table 4.7.1 : Effect of atmospheric and oceanographic conditions on the total ice accumulation over the entire vessel in 1 hour (n.m. means nautical miles).

T_a (°C)	RH (%)	T_{sea} (°C)	U (ms^{-1})	θ (°)	V_s (ms^{-1})	F (n.m.)	S_{sea} (%)	Total ice load (tonnes)
-10.0	75.0	2.0	15.0	0.0	3.0	200.0	3.3	1.06
-2.0	75.0	2.0	15.0	0.0	3.0	200.0	3.3	0.18
-5.0	75.0	2.0	15.0	0.0	3.0	200.0	3.3	0.53
-15.0	75.0	2.0	15.0	0.0	3.0	200.0	3.3	1.52
-20.0	75.0	2.0	15.0	0.0	3.0	200.0	3.3	1.92
-25.0	75.0	2.0	15.0	0.0	3.0	200.0	3.3	2.28
-10.0	0.0	2.0	15.0	0.0	3.0	200.0	3.3	1.29
-10.0	25.0	2.0	15.0	0.0	3.0	200.0	3.3	1.21
-10.0	50.0	2.0	15.0	0.0	3.0	200.0	3.3	1.14
-10.0	100.0	2.0	15.0	0.0	3.0	200.0	3.3	0.98
-10.0	75.0	-2.0	15.0	0.0	3.0	200.0	3.3	1.27
-10.0	75.0	-1.0	15.0	0.0	3.0	200.0	3.3	1.21
-10.0	75.0	0.0	15.0	0.0	3.0	200.0	3.3	1.16

T_a (°C)	RH (%)	T_{sea} (°C)	U (ms^{-1})	θ (°)	V_s (ms^{-1})	F (n.m.)	S_{sea} (%)	Total ice load (tonnes)
-10.0	75.0	1.0	15.0	0.0	3.0	200.0	3.3	1.10
-10.0	75.0	3.0	15.0	0.0	3.0	200.0	3.3	1.02
-10.0	75.0	4.0	15.0	0.0	3.0	200.0	3.3	0.98
-10.0	75.0	5.0	15.0	0.0	3.0	200.0	3.3	0.95
-10.0	75.0	6.0	15.0	0.0	3.0	200.0	3.3	0.93
-10.0	75.0	8.0	15.0	0.0	3.0	200.0	3.3	0.90
-10.0	75.0	10.0	15.0	0.0	3.0	200.0	3.3	0.88
-10.0	75.0	12.0	15.0	0.0	3.0	200.0	3.3	0.86
-10.0	75.0	14.0	15.0	0.0	3.0	200.0	3.3	0.86
-10.0	75.0	2.0	5.0	0.0	3.0	200.0	3.3	0.0
-10.0	75.0	2.0	8.0	0.0	3.0	200.0	3.3	0.01
-10.0	75.0	2.0	10.0	0.0	3.0	200.0	3.3	0.07
-10.0	75.0	2.0	12.0	0.0	3.0	200.0	3.3	0.41
-10.0	75.0	2.0	18.0	0.0	3.0	200.0	3.3	1.47
-10.0	75.0	2.0	20.0	0.0	3.0	200.0	3.3	1.67
-10.0	75.0	2.0	22.0	0.0	3.0	200.0	3.3	1.86
-10.0	75.0	2.0	24.0	0.0	3.0	200.0	3.3	1.98

T_a (°C)	RH (%)	T_{sea} (°C)	U (ms^{-1})	θ (°)	V_s (ms^{-1})	F (n.m.)	S_{sea} (%)	Total ice load (tonnes)
-10.0	75.0	2.0	25.0	0.0	3.0	200.0	3.3	2.05
-10.0	75.0	2.0	15.0	10.0	3.0	200.0	3.3	1.07
-10.0	75.0	2.0	15.0	30.0	3.0	200.0	3.3	0.71
-10.0	75.0	2.0	15.0	45.0	3.0	200.0	3.3	0.42
-10.0	75.0	2.0	15.0	60.0	3.0	200.0	3.3	0.27
-10.0	75.0	2.0	15.0	75.0	3.0	200.0	3.3	0.20
-10.0	75.0	2.0	15.0	90.0	3.0	200.0	3.3	0.14
-10.0	75.0	2.0	15.0	0.0	1.0	200.0	3.3	0.14
-10.0	75.0	2.0	15.0	0.0	2.0	200.0	3.3	0.78
-10.0	75.0	2.0	15.0	0.0	5.0	200.0	3.3	1.17
-10.0	75.0	2.0	15.0	0.0	8.0	200.0	3.3	1.15
-10.0	75.0	2.0	15.0	0.0	3.0	50.0	3.3	0.16
-10.0	75.0	2.0	15.0	0.0	3.0	100.0	3.3	0.66
-10.0	75.0	2.0	15.0	0.0	3.0	300.0	3.3	1.24

T_a (°C)	RH (%)	T_{sea} (°C)	U (ms^{-1})	θ (°)	V_s (ms^{-1})	F (n.m.)	S_{sea} (%)	Total ice load (tonnes)
-10.0	75.0	2.0	15.0	0.0	3.0	400.0	3.3	1.33
-10.0	75.0	2.0	15.0	0.0	3.0	500.0	3.3	1.39
-10.0	75.0	2.0	15.0	0.0	3.0	600.0	3.3	1.43
-10.0	75.0	2.0	15.0	0.0	3.0	200.0	0.0	1.43
-10.0	75.0	2.0	15.0	0.0	3.0	200.0	1.0	1.32
-10.0	75.0	2.0	15.0	0.0	3.0	200.0	2.0	1.20
-10.0	75.0	2.0	15.0	0.0	3.0	200.0	4.0	0.98

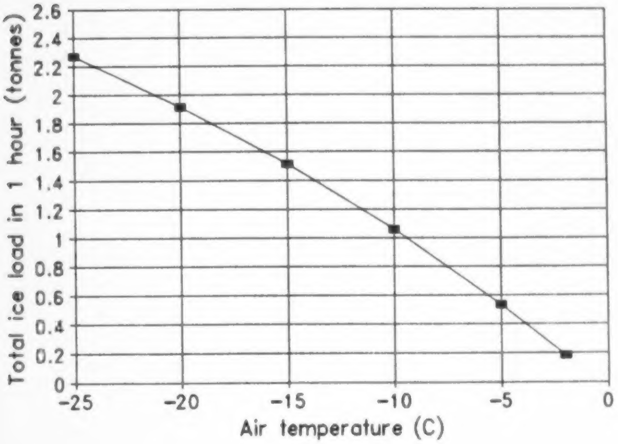

(a)

Figure 4.7.1 : A sensitivity test of the icing model.
(a) Total one hour ice load vs air temperature.
(b) Total one hour ice load vs relative humidity.
(c) Total one hour ice load vs sea-surface temperature ($U = 15\ ms^{-1}$).
(d) Total one hour ice load vs sea-surface temperature ($U = 25\ ms^{-1}$).
(e) Total one hour ice load vs wind speed.
(f) Total one hour ice load vs fetch.
(g) Total one hour ice load vs wind direction.
(h) Total one hour ice load vs ship speed.
(i) Total one hour ice load vs sea-surface salinity.
Other conditions are the standard values given in the text.

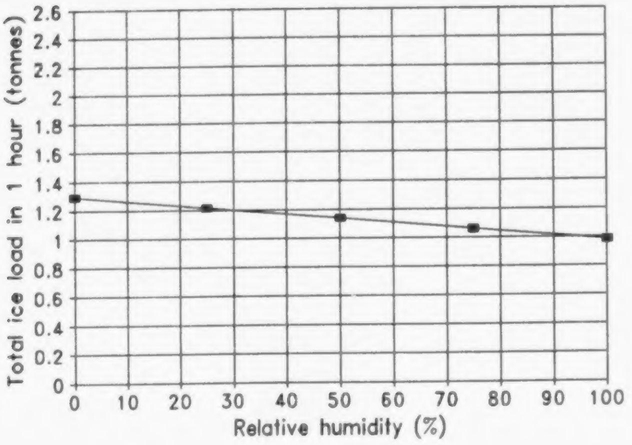
Total ice load in 1 hour (tonnes)
0
0.2
0.4
0.6
0.8
1
1.2
1.4
1.6
1.8
2
2.2
2.4
2.6
0
10
20
30
40
50
60
70
80
90
100
Relative humidity (%)

(b)

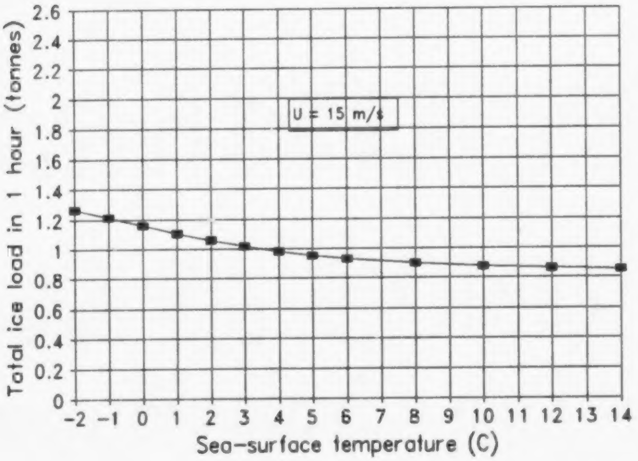
Total ice load in 1 hour (tonnes)
U = 15 m/s
0
0.2
0.4
0.6
0.8
1
1.2
1.4
1.6
1.8
2
2.2
2.4
2.6
−2
−1
0
1
2
3
4
5
6
7
8
9
10
11
12
13
14
Sea-surface temperature (C)

(c)

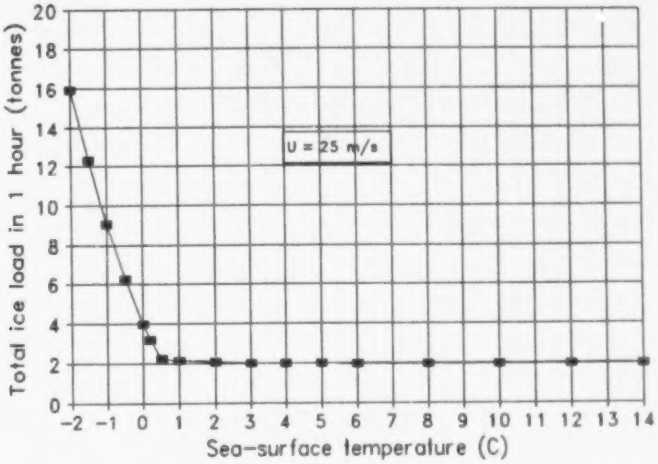
Total ice load in 1 hour (tonnes)
0
2
4
6
8
10
12
14
16
18
20
U = 25 m/s
-2
-1
0
1
2
3
4
5
6
7
8
9
10
11
12
13
14
Sea-surface temperature (C)

(d)

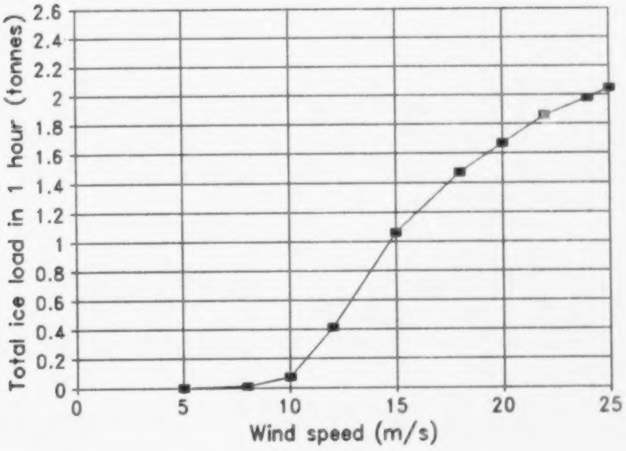
Total ice load in 1 hour (tonnes)
0
0.2
0.4
0.6
0.8
1
1.2
1.4
1.6
1.8
2
2.2
2.4
2.6
0
5
10
15
20
25
Wind speed (m/s)

(e)

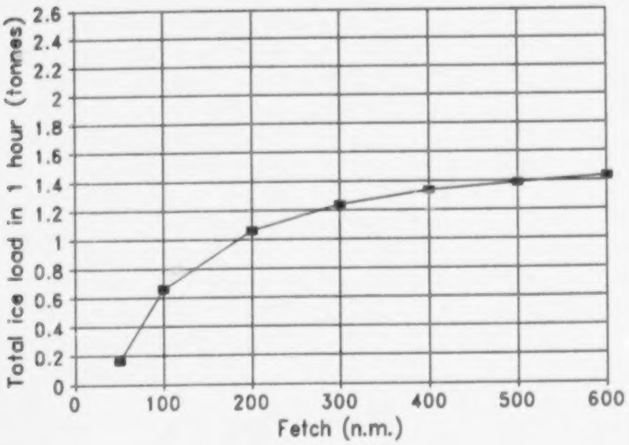
Total ice load in 1 hour (tonnes)
2.6
2.4
2.2
2
1.8
1.6
1.4
1.2
1
0.8
0.6
0.4
0.2
0
0
100
200
300
400
500
600
Fetch (n.m.)

(f)

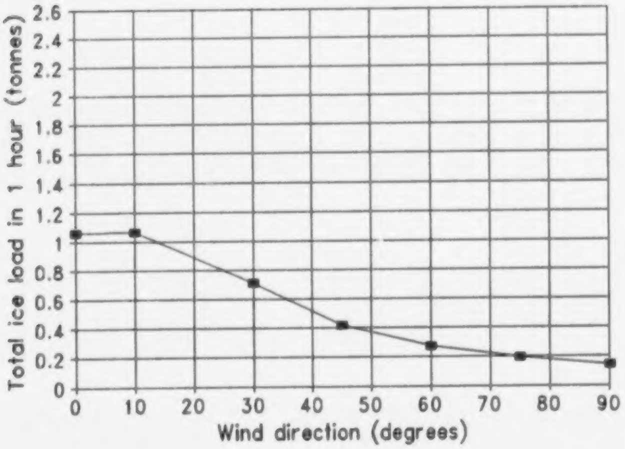
Total ice load in 1 hour (tonnes)
2.6
2.4
2.2
2
1.8
1.6
1.4
1.2
1
0.8
0.6
0.4
0.2
0
0
10
20
30
40
50
60
70
80
90
Wind direction (degrees)

(g)

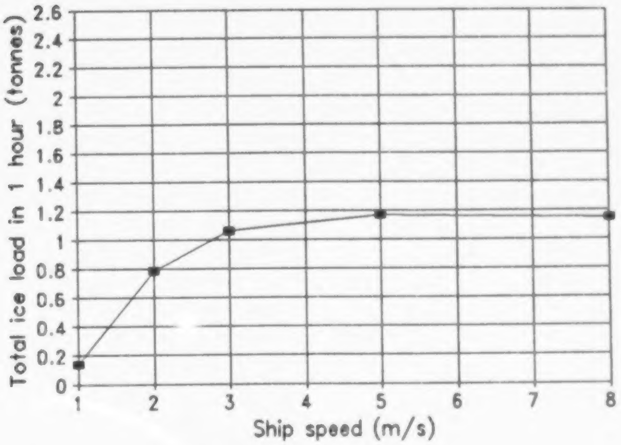
Total ice load in 1 hour (tonnes)
0
0.2
0.4
0.6
0.8
1
1.2
1.4
1.6
1.8
2
2.2
2.4
2.6
1
2
3
4
5
6
7
8
Ship speed (m/s)

(h)

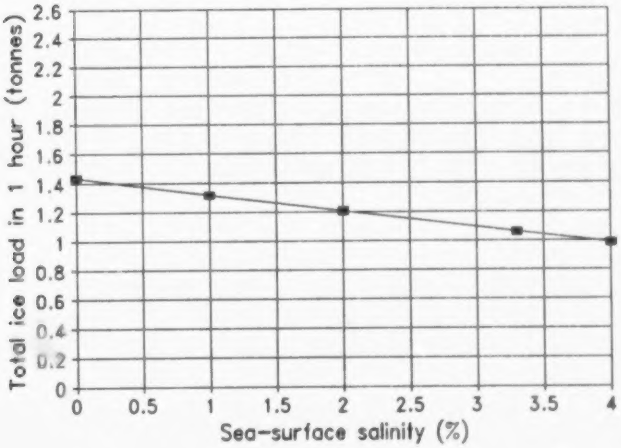
Total ice load in 1 hour (tonnes)
0
0.2
0.4
0.6
0.8
1
1.2
1.4
1.6
1.8
2
2.2
2.4
2.6
0
0.5
1
1.5
2
2.5
3
3.5
4
Sea-surface salinity (%)

(i)

Of course, it is very likely that when the spray flux is high, only a fraction of it near the solid/liquid interface will contribute to the sensible heat transport. As a result, the model may overestimate the icing rate for cases with low sea-surface temperature and high wind speed. How to determine this fraction and its relation to the spray flux is still largely unknown and requires further research. Kachurin et al. (1974) suggested that only 20 - 30% of the impinging spray is involved in sensible heat exchange. This fraction is surely not universal and should depend on various factors such as the quantity of impinging spray and the atmospheric conditions. Hence for the present, all incoming spray is assumed to contribute sensible heat transport.

It is also apparent in Figures 4.7.1c and 4.7.1d that, as the sea-surface temperature continues to increase, the ice accumulation never reaches zero, but approaches an asymptotic limit. For $U = 15$ ms^{-1} with $T_{sea} > 10$ °C, and for $U = 25$ ms^{-1} with $T_{sea} > 1$ °C, the total ice loads accumulated in 1 hour are around 0.8 tonnes and 2 tonnes respectively, and they do not vary much thereafter. The explanation here is related to one of the model assumptions. As in most other icing models, it is assumed here that the incoming spray reaches its equilibrium freezing temperature once the spray droplets impinge on the surface and form a brine film. Therefore, at the end of each time step, the temperature of the brine film is at its equilibrium freezing temperature. But this is only true if the latent heat flux term q_f in Equation 4.5.1 is greater than or equal to zero. For the case with $q_f > 0$, icing takes place and the temperature of the brine film will always be at its equilibrium freezing temperature. If $q_f = 0$, no icing can take place, but the temperature of the brine will still remain at its equilibrium freezing temperature. Then, after spraying, the brine remaining on the surface will start to freeze as heat is carried away from the brine film surface. As a result, ice builds up on the surface during the interval between sprays.

Up to this point, the assumption that the brine film reaches its equilibrium freezing temperature is still valid. However, if q_f becomes negative during the spraying period, then at the end of each time step, the temperature of the brine film should be higher than its equilibrium freezing temperature. Therefore, at the end of spraying, the brine film temperature should also be higher than its equilibrium freezing temperature.

Thus, during the spray-free period, it must take some time for the brine film, which remains on the surface, to cool down to its equilibrium freezing temperature before freezing occurs. If the air temperature is not low enough or if the sea-surface temperature is too high, it may happen that no ice can be formed. In this case, the icing rate will be zero. The present model, however, does not take this particular situation into consideration. In the model, we simply assume that, during the spraying period, even if $q_f < 0$, the brine film is still at its equilibrium freezing temperature at the end of each time step. Therefore, during the spray-free period, ice forms under all circumstances as long as the air temperature is below the equilibrium freezing temperature of the sea-surface brine. This explains why the ice load becomes invariant to the sea-surface temperature beyond a certain threshold. Thus, the model tends to overestimate the icing rate for high sea-surface temperatures.

In addition, the model also neglects the possibility of melting. For example, when $q_f < 0$, part of the ice accumulated in the previous spraying cycle should melt. But, since the model simulates only one spray cycle, this is not a feasible calculation. Future model development will rectify this situation.

The above discussion reveals one of the limitations of the present icing model. However, we may ask if such a situation with low air temperature and high sea-surface temperature is possible. Zakrzewski and Lozowski (1989) have assembled data from more than 100 ship icing events. In these records, the air temperature and sea-surface temperature are listed. They are plotted in Figure 4.7.2. It can be seen that over all of the recorded icing events, the air temperature ranges from 0 °C to -22 °C. In 97 % of the cases, the sea- surface temperature was below 3 °C and there were only 3 cases in which the sea-surface temperature was as high as 5 °C. Therefore, it can be concluded that with sub-freezing air temperatures in winter, it is very unlikely that the sea- surface temperature will exceed 5 °C. At a sea-surface temperature of 5 °C, it may be possible that $q_f < 0$ for some grid cells on the deck near the bow. However, even for this case, the error should not be significant compared to the total ice load for the entire vessel.

In most current spray icing models (for instance Makkonen (1987), Blackmore and Lozowski (1993)), a continuous spraying process is assumed. Hence, there is no

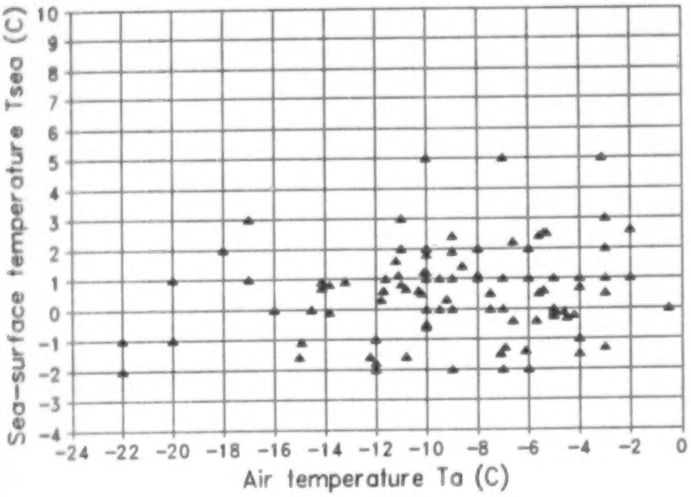

Figure 4.7.2: Scattergram of observed air temperature and sea-surface temperature from Soviet icing data (Zakrzewski and Lozowski, 1989).

spray-free period in these models. As a result, with high droplet impingement temperatures, these models will predict a zero icing rate. However, in ship spray icing, there exists a quiescent period between spraying events. Thus, with cool sea-surface temperatures, icing may not occur on the ship surface during the spraying period, but may occur during the quiescent period. Moreover the incoming spray during the next spraying event may not be able to melt this ice entirely. In such a case, continuous icing models may underestimate the icing rate.

The effect of wind speed on the total ice load is dramatic. Increasing the wind speed will increase the wave height and thus increase the amount of spray impinging onto the entire vessel. In addition, higher winds also imply higher convective and evaporative heat transfer from the icing surface. As shown in Figure 4.7.1e, there is very little ice accumulation when the wind speed is less than about 10 ms^{-1}. This occurs because at low wind speeds, the spray flux to the ship is small and the convective heat transfer is low as well. But, as the wind speed increases to 25 ms^{1}, the total ice load increases abruptly to more than 2 tonnes per hour. This implies that wind speed is a crucial factor in severe icing, especially when the air and sea-surface temperatures are very low.

The wave height is related to fetch according to Equation 4.1.1. Hence, as the fetch increases, the wave height also increases. This also means that more spray is generated. Thus, the total ice load increases as the fetch increases because more spray is available for ice accretion (Figure 4.7.1f). However, the total ice load tends to approach an asymptotic limit when the fetch becomes very long (Figure 4.7.1f). For a very long fetch, the wave height is high and there is a lot of spray produced. In the present case, the droplet impingement temperature is generally above the equilibrium freezing temperature, and hence q_s becomes a large heat source which can restrain ice growth. However, with a low sea-surface temperature (< 0 °C for example), the situation is quite different. A very long fetch may mean a lot of supercooled spray droplets and in such cases q_s becomes a large heat sink which allows the ice growth to continue.

Since the ship heading is constrained by the experimental spraying data to be 0° directly into the waves, changing the wind direction simply changes the spray flux and its distribution as discussed in Chapter 3. Figure 4.7.1g shows that when the wind direction shifts from head wind to beam wind, less spray is received on the ship and thus the total ice load is also less. It is found that the total ice load at $\theta = 10°$ is a little greater than that at $\theta = 0°$. This feature is artificial since, as mentioned in Chapter 3, it occurs because of the different spray calculation methods applied when $\theta = 0°$ and when $\theta > 0°$.

Figure 4.7.1h shows that increasing the ship speed will initially increase the ice load abruptly. However, once the ship speed reaches about 5 ms^{-1}, the total ice load starts to decrease slightly. To understand the reasons for this, we must first understand the different ways in which ship speed may affect spray icing: a) Increasing the ship speed will increase the amount of spray impinging on the vessel. b) Increasing the ship speed will decrease the flight time of the spray droplets to reach their individual targets, thus increasing the spray impingement temperature. c) Increasing the ship speed implies an increase in the relative speed of the ship and the air, and hence, the convective heat transfer from the icing surface will also increase. Factor c) always has a positive effect and factor b) a negative effect on the icing rate. The effect of factor a) on icing can be either positive or negative depending on the sea-surface temperature. For low sea-surface temperatures, the effect is positive while for high sea- surface temperatures it is negative. Increasing the ship speed provides more spray on board to allow icing to take place. Thus, the ice load increases as ship speed increases. But, when the ship speed becomes high ($V_s > 5$ ms^{-1} in the present case), there is much more spray splashed on the ship, and if the droplet impingement temperature is above the equilibrium freezing temperature, then the sensible heat flux term q_s may become large enough to stabilize or even decrease the ice growth rate, as shown in Figure 4.7.1h.

Figure 4.7.1i illustrates how the total ice load is affected by the sea-surface salinity. Assuming a constant liquid fraction λ independent of salinity, a decreasing salinity means a higher equilibrium freezing temperature. Thus, as the salinity decreases from 4 to 0 %, the total ice load increases linearly by 45 %.

These sensitivity tests show that the present icing model is very sensitive to air temperature, wind speed, fetch, ship speed, and salinity. Shifting the wind direction from head wind to beam wind reduces the ice accumulation. The relative humidity has a less significant effect on the total ice accumulation on ship. The sea-surface temperature has a complicated effect on the total ice accumulation. For low wind speeds, the effect is less significant while for high wind speeds, the effect becomes dramatic. The model fails to predict a zero ice load with high sea-surface temperatures. However, according to the Soviet data, a situation with low air temperature and high sea-surface temperatures is unrealistic.

4.8 Results and Discussion

I. A Case Study - "Blue Mist II"

To illustrate the performance of the icing model, the sinking of the "BLUE MIST II", which occurred on the night of February 18, 1966, is used as a case study. On that night, the side trawler "BLUE MIST II" (length 37 m, displacement 330 tonnes) and all of its crew disappeared about 37 miles to the west of Cape Anguille, Newfoundland. The cause of this tragedy is still unknown. However, on the same night, three other trawlers in the area all reported severe icing. It is also known that the weather on that night was extremely rough with an air temperature below -17 °C, winds gusting in excess of 70 knots from the North East, and waves at least 7 metres high. In this case study, the Zandberg is placed in the same environment and the icing model is used to simulate the total ice accumulation and its distribution over the vessel. In addition, while the ship heading is fixed at 180° (head sea), the wind direction is allowed to change from 0° to 90° so that the effect of wind direction on the total ice load and its distribution can be illustrated. To reproduce as closely as possible the conditions on that night, the following atmospheric and oceanographic parameters are used: T_a = -18 °C, P_a = 1000 mb, RH = 75 %, T_{sea} = 0 °C, U = 30 ms^{-1}, θ = 0°, 15°, 45°, 90°, F = 100 n.m, V_s = 3 ms^{-1}. It should be mentioned here that a wind speed of 30 ms^{-1} and a fetch of 100 n.m give rise to a significant wave height of 7.7 metres. This significant wave height is beyond the range of validity of the model spraying experiment in which the maximum significant wave height, when converted to full scale, is 5 meters. However, in order to examine

3

PM-1 3½"x4" PHOTOGRAPHIC MICROCOPY TARGET
NBS 1010a ANSI/ISO #2 EQUIVALENT

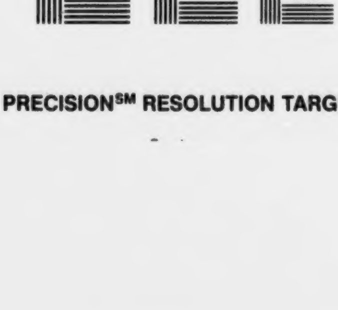
1.0
4.5
5.0
5.6
6.3
7.1
8.0
2.8
3.2
3.6
4.0
2.5
2.2
2.0
1.1
1.8
1.25
1.4
1.6

PRECISION℠ RESOLUTION TARGETS

this particular icing event, the significant wave height is allowed to go beyond its range of strict validity.

The total ice load accumulated on the entire vessel in one hour for different wind directions is shown Figure 4.8.1. The maximum ice load occurs under head winds (θ = 0°) with 10.8 tonnes of ice accumulated and thickness ranging up to 60 cm. Shifting the wind direction from 0° to 15° does not cause a significant decrease in the total ice accumulation. However, for wind directions of 30° and greater, the total ice load decreases significantly. For beam winds (θ = 90°), less than 1 tonne/hour of ice is accreted. The reasons for the dependence of the total ice load on wind direction have been explained in Section 4.7.

In the following discussion, the effect of wind direction on the ice thickness distributions over different ship components will be shown. For head winds (θ = 0°), because of symmetry, only the ice distribution on the starboard side is shown. For wind directions greater than 0°, the distributions on both port and starboard sides are shown. In addition, for simplicity, only the ice thickness along the grid columns corresponding to y = ±0.5 m, y = ±2.5 m, and y = ±4.5 m are shown.

(a) Wind direction $\theta = 0°$

The ice thickness distribution on the deck is shown in Figure 4.8.2a. It can be seen that along the two columns corresponding to y = 0.5 m and 2.5 m, the ice thickness is less than 2 cm and it is uniform up to a distance of x = 3.5 m. Beyond this point, the ice thickness increases longitudinally with a maximum ice thickness of 9.3 cm at x = 14.5 m and y = 0.5 m. These results may be explained as follows. For a given environmental condition, the ice thickness on a grid cell depends on (i) the droplet impingement temperature, (ii) the spray flux, and (iii) the salinity of the brine remaining on the surface after ice accretion. Factor (iii) is not so significant in general. But, under low spray flux conditions, it plays a more important role. For those grid cells near the bow along y = 0.5 m and 2.5 m, the spray flux is high and the droplet impingement temperature is above the equilibrium freezing temperature. Hence, the sensible heat flux term q_s in Equation 4.5.1 becomes a heat source. Because of the high spray flux, q_s

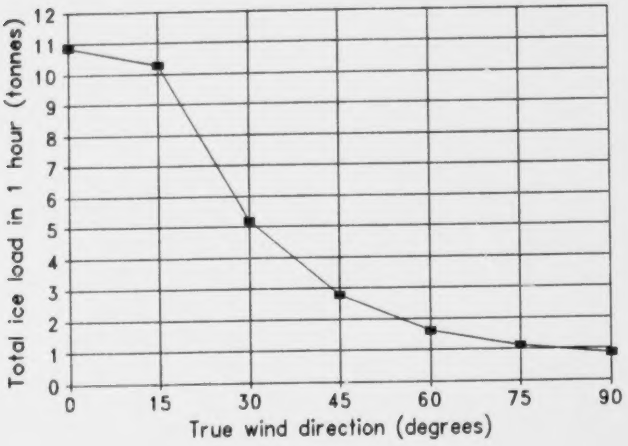

Figure 4.8.1: One hour total ice load accumulated on the Zandberg for different wind directions, under conditions similar to those experienced by the Blue Mist II (see text for details).

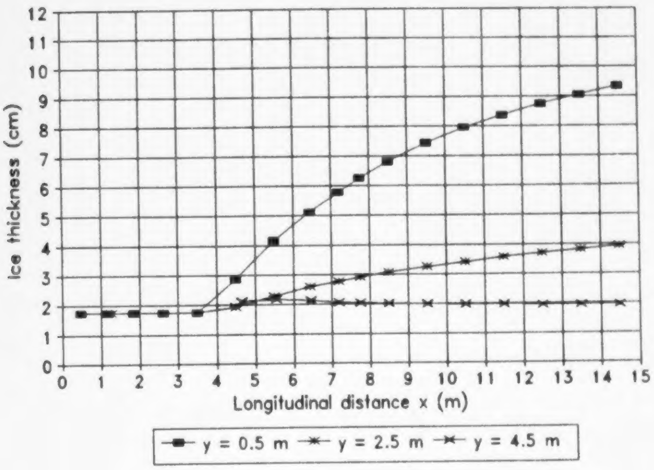

(a)

Figure 4.8.2: One hour ice thickness distribution over various components for a wind direction of 0°. a) The foredeck. b) The front of the wheelhouse. c) The top of the wheelhouse. d) The mast.

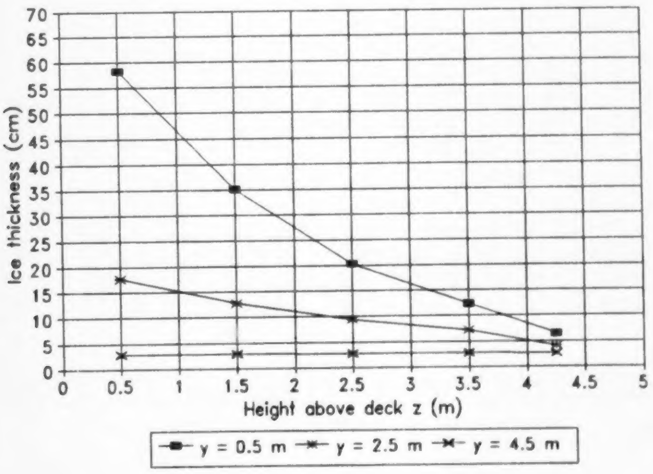

(b)

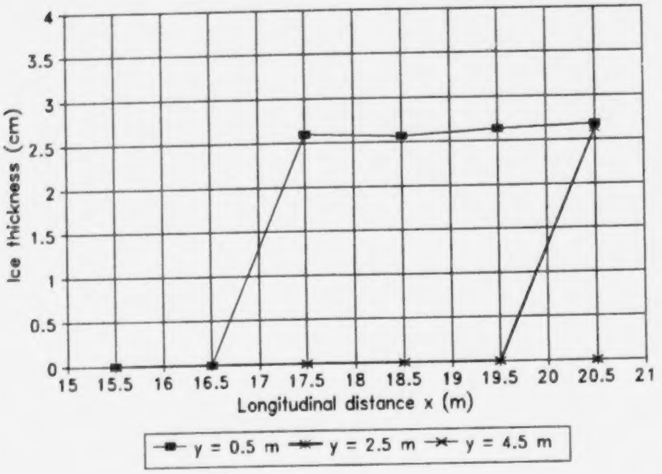
Ice thickness (cm)
4
3.5
3
2.5
2
1.5
1
0.5
0
15
15.5
16
16.5
17
17.5
18
18.5
19
19.5
20
20.5
21
Longitudinal distance x (m)
y = 0.5 m
y = 2.5 m
y = 4.5 m

(c)

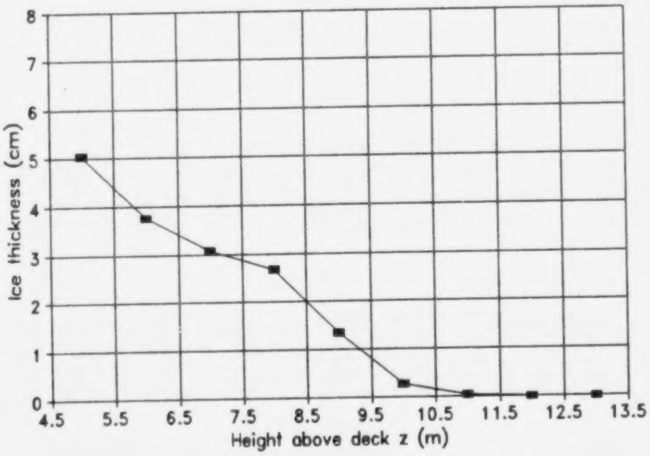
Ice thickness (cm)
8
7
6
5
4
3
2
1
0
4.5
5.5
6.5
7.5
8.5
9.5
10.5
11.5
12.5
13.5
Height above deck z (m)

(d)

becomes large enough to make q_f negative during the spraying interval. Consequently, ice does not form here during the spraying period. However, during the spray-free interval, after run off, the brine remaining on those grid cells has a uniform thickness and is at the equilibrium freezing temperature. Since the heat transfer is the same everywhere on the deck, the accretion rate on these grid cells is also the same. This explains why the ice thickness is uniform on the grid cells near the bow ($x < 3.5$ m). Farther from the bow, along the lines $y = 0.5$ m and 2.5 m, the droplet impingement temperature is lower and may even be supercooled. In addition, the spray flux decreases longitudinally. The result is that q_s in Equation 4.5.1 becomes a smaller heat source or a heat sink. This gives rise to a positive value of q_f during the spraying interval. In addition, q_f increases longitudinally. As a result, the ice thickness increases longitudinally for $x > 3.5$ m.

The ice thickness along the line $y = 4.5$ m behaves quite differently. The ice thickness initially increases slightly and then decreases gradually thereafter. The reason is quite simple. Along the line $y = 4.5$ m, which is far from the centreline, the spray flux is small and also decreases longitudinally. Thus, the effect of the sensible heat flux term q_s in Equation 4.5.1 is small. The slight increase in ice thickness in the first two grid cells is due to the slight decrease in the heat source term q_s which gives rise to a slight increase in q_f. After the first two grid cells, though, the droplet impingement temperature is lower, but due to the lack of spray, the amount of ice that can be accreted is limited. In addition, since the spray flux is small, the salinity effect may also contribute to suppress the growth rate. Therefore, the ice thickness decreases longitudinally after the first two grid cells.

Another characteristic revealed in Figure 4.8.2a is that the highest thickness generally occurs along the centreline and it decreases transversely. This is directly related to the transverse spray flux distribution. As discussed in Chapter 3, the spray flux decreases transversely. At the same time, for the same longitudinal distance x, the droplet impingement temperature on the grid cells nearer the centreline is lower due to a longer trajectory path. A lower spray flux with a higher droplet impingement temperature may give rise to a higher icing rate than a higher spray flux with a lower droplet impingement temperature. The outcome will depend on the magnitude and sign of the term q_s, and the amount of spray that is available for ice accretion. In the present case, however, it turns out that the icing rate is higher near the centreline.

The icing rate is much higher on the front of the wheelhouse as indicated in Figure 4.8.2b. In chapter 3, it was mentioned that, due to its orientation, the front face may receive a lot of spray. In addition, the front face is farther from the spray source than most grid cells on the deck. Therefore, with the given sea-surface temperature of 0 °C, the droplet impingement temperature is supercooled. Combined with a high spray flux, the heat sink q_s in Equation 4.5.1 becomes very significant. For instance, in the first time step calculation, along the column $y = 0.5$ m, the term q_s for the grid cell located at the foot of the wheelhouse ($z = 0.5$ m) is 1.4×10^5 Wm^{-2} which is 7.8 times greater than that for the grid cell located at the end of the deck ($x = 14.5$ m). In addition, as indicated in Section 5, the front of the wheelhouse has a characteristic length 1.6 times shorter than the foredeck. Hence, the heat transfer coefficient h for the front of the wheelhouse is 1.1 times that for the foredeck. It turns out that the term q_f for the former is 7.3 times greater than that for the latter. Thus, a much higher ice thickness occurs on the front of the wheelhouse than on the deck under the present conditions. Since the front of the wheelhouse and the deck are treated independently in the model and no brine flow is allowed from the former to the latter, therefore, there exists a discontinuity at the boundary between the deck and the front of the wheelhouse (Figure 4.8.2a and 4.8.2b).

Along the two columns corresponding to $y = 0.5$ m and 2.5 m, the ice thickness decreases upward. The chief reason for this is that less spray is received as z increases along the front face. Brine rundown from grids above to grids below is also a factor causing more ice accretion on the lower part of the wheelhouse. Along the column corresponding to $y = 4.5$ m, the ice thickness does not vary much with height because the vertical spray flux gradient is very small at locations far from the centreline. Since the spray flux usually decreases laterally, the ice thickness also decreases laterally. The maximum ice thickness is located at $x = 15$ m, $y = 0.5$ m, and $z = 0.5$ m.

Because of the shadowing effect on the top of the wheelhouse, some grid cells along the columns y = 0.5 m and y = 2.5 m, and all grid cells along the column y = 4.5 m experience no ice accretion as shown in Figure 4.8.2c. The ice thickness on this component is also much less than that on the deck and on the front of the wheelhouse. This is because much less spray impinges on this component due to its orientation and elevation.

The ice thickness distribution on the mast is shown in Figure 4.8.2d. The distribution is not quite smooth. But, in general, the ice thickness decreases upward due to the fact that less spray impinges at higher elevations. This ice thickness distribution is consistent with photographs of ice accretion on ship masts.

(b) Wind direction $\theta = 15°$

As the wind direction shifts to 15°, the ice thickness distribution also changes and becomes asymmetrical, although the total ice load is reduced only slightly. Over the port side of the deck (Figure 4.8.3a), the ice thickness distribution near the bow (x < 3.5 m) along the columns y = -0.5 m and -2.5 m is uniform. This is similar to the case for $\theta = 0°$ (Figure 4.8.2a) and can be explained in the same way. For x > 3.5 m, the ice thickness distribution along the columns y = -0.5 m and -2.5 m increases initially for several metres and then gradually decreases. Along the line y = -4.5 m, the ice thickness initially increases for a short distance and then decreases to zero at x = 13.5 m. The above distribution pattern is directly related to the amount of spray received on different grid cells, and to the droplet impingement temperature on these grid cells. Over the port side of the ship, the spray flux always decreases both longitudinally and away from the centreline. Along the columns y = -0.5 m and -2.5 m, the ice thickness increases to a maximum when the combined effect of the spray flux and the droplet impingement temperature gives rise to a minimum heat source or a maximum heat sink, q_f. After that, q_f decreases and so does the ice thickness. Along the column y = -4.5 m, a similar argument applies except that the lower spray flux and steeper spray flux gradient along this line cause a still more rapid decrease in ice thickness.

The ice thickness distribution over the starboard side of the vessel (Figure 4.8.3b) exhibits a more complex pattern. Again, the distribution pattern is directly related to the

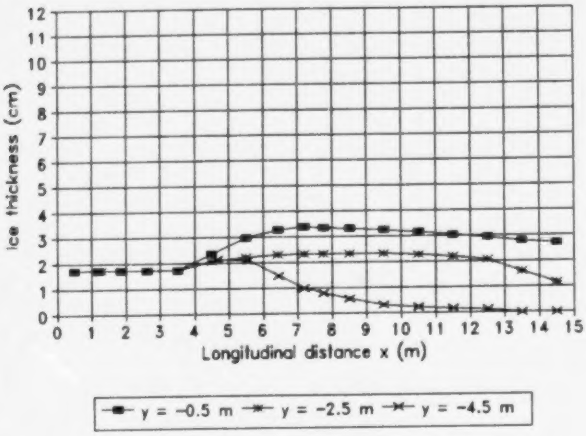

(a)

Figure 4.8.3: One hour ice thickness distribution over various components for a wind direction of 15°. a) The foredeck (port). b) The foredeck (starboard). c) The front of the wheelhouse (port). d) The front of the wheelhouse (starboard). e) The top of the wheelhouse (starboard). f) The mast.

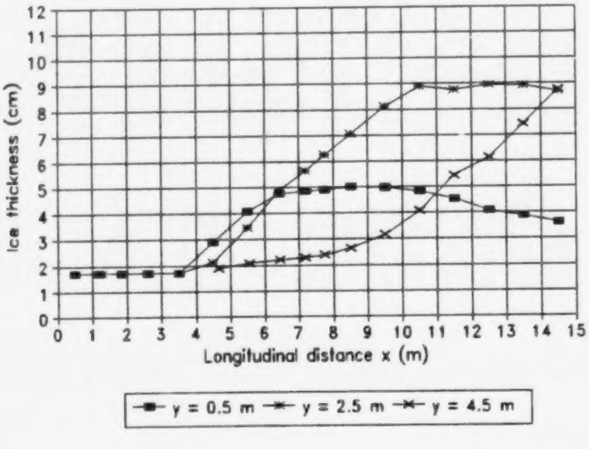

(b)

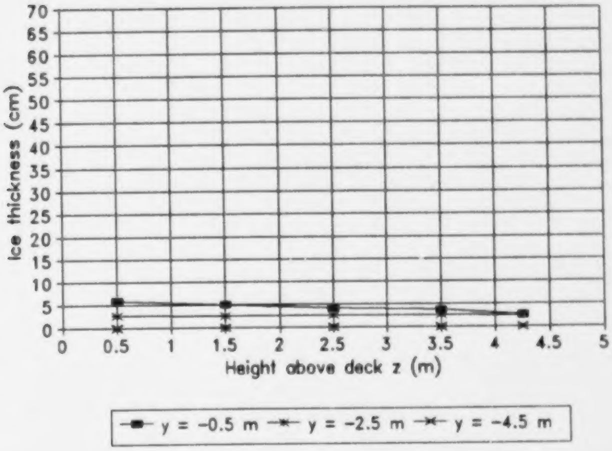
Ice thickness (cm)
70
65
60
55
50
45
40
35
30
25
20
15
10
5
0
0
0.5
1
1.5
2
2.5
3
3.5
4
4.5
5
Height above deck z (m)
y = -0.5 m
y = -2.5 m
y = -4.5 m

(c)

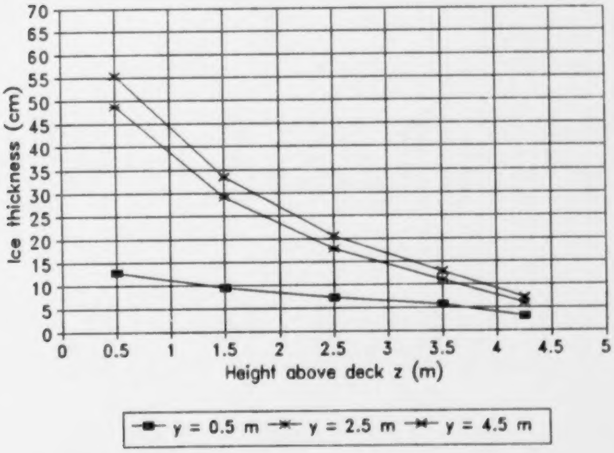
Ice thickness (cm)
70
65
60
55
50
45
40
35
30
25
20
15
10
5
0
0
0.5
1
1.5
2
2.5
3
3.5
4
4.5
5
Height above deck z (m)
y = 0.5 m
y = 2.5 m
y = 4.5 m

(d)

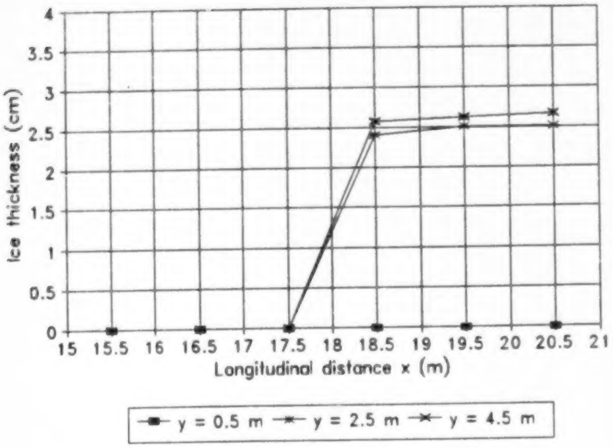
Ice thickness (cm)
0
0.5
1
1.5
2
2.5
3
3.5
4
15
15.5
16
16.5
17
17.5
18
18.5
19
19.5
20
20.5
21
Longitudinal distance x (m)
y = 0.5 m
y = 2.5 m
y = 4.5 m

(e)

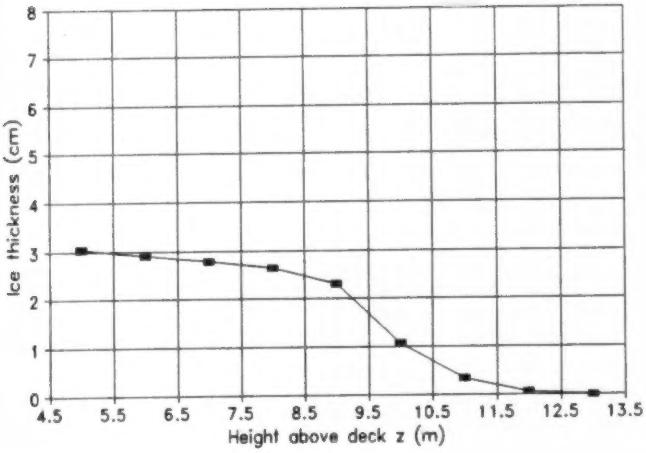
Ice thickness (cm)
0
1
2
3
4
5
6
7
8
4.5
5.5
6.5
7.5
8.5
9.5
10.5
11.5
12.5
13.5
Height above deck z (m)

(f)

amount of spray received on each grid cell and the droplet impingement temperature. For $x < 3.5$ m, the ice thickness along the columns $y = 0.5$ m and 2.5 m is uniform. The explanation of this uniformity has been given earlier for the case $\theta = 0°$. Along the line $y = 0.5$ m, at $x > 3.5$ m, the ice thickness increases initially for several metres and then decreases thereafter. The explanation is similar to that given for the port side. Along the column $y = 2.5$ m, the ice thickness increases rapidly to near 9 cm at $x = 10.5$ m and then shows little variation beyond that point. This occurs because along this column, the spray flux increases longitudinally over a certain distance and then decreases. Also, the trajectory path is longer for those grid cells located farther from the bow, and this gives rise to a lower droplet impingement temperature. The combined effect results in the distribution shown in Figure 4.8.3b. Along the column $y = 4.5$ m, the ice thickness increases continuously. This is the result of an increasing spray flux and a decreasing droplet impingement temperature along the entire length of this column. An overview of the ice thickness distribution over the deck indicates that the maximum ice thickness does not occur along the centreline, but at a position away from the centreline towards the wheelhouse end of the deck ($x = 14.5$ m, $y = 3.5$ m, not shown in Figure 4.8.3a). This shift of the local maximum is a result of the wind direction shift, which causes the maximum value of q_f to shift to this location. Therefore, shifting the wind direction to 15° causes the local maximum ice thickness to move away from the centreline.

The ice thickness distribution over the front of the wheelhouse decreases upward (Figures 4.8.3c and 4.8.3d) and is asymmetrical with respect to the centreline. Over the port half (Figure 4.8.3c), the amount of ice accreted is much less than that over the starboard half (Figure 4.8.3d). The explanation is that much less spray is received over the port side when the wind direction changes from 0° to 15°. Along the column $y = -4.5$ m, no ice accretion occurs because there is no spray received along that column on the front face of the wheelhouse. The maximum ice thickness is located at $x = 15$ m, $y = 3.5$ m, and $z = 0.5$ m (not shown in the figure). This shifting in the location of the maximum ice thickness is again a result of the shift in wind direction.

On top of the wheelhouse, no spray reaches the grid cells on the port side, and hence there is no ice accretion there. Figure 4.8.3e shows the ice thickness distribution over the starboard side. Only those grid cells located farther back and away from the centreline receive spray and thus experience ice accretion. The maximum ice thickness is located along the line y = 3.5 m.

The ice thickness distribution on the mast, as shown in Figure 4.8.3f, decreases gradually near the base and more sharply to zero at a higher elevation. This distribution is directly related to the amount of spray received on the different grid cells.

(c) Wind direction $\theta = 45°$

For a wind direction of 45°, the total ice accumulation is significantly less and the ice load distribution becomes highly asymmetrical. Basically, the ice thickness distribution can be explained in a similar way as for the case with $\theta = 15°$. The uniform ice thickness region over the deck (Figure 4.8.4a and 4.8.4b) retreats further toward the bow. Also, much less ice accretion is found on those grid cells near the wheelhouse end of the deck due to the shifting wind direction. The maximum ice thickness occurs at x = 7.293 m and y = 5.053 m.

Figures 4.8.4c and 4.8.4d show the ice thickness distribution on the front of the wheel house. Again, the ice thickness is much less compared with the case for $\theta = 15°$. Also, the gradient is very small and the ice thickness does not vary much in the vertical. The location of the maximum ice thickness is located at x = 15 m, y = 5.375 m, and z = 0.5 m.

The entire surface of the top of the wheelhouse, and the entire mast do not receive any spray. Thus, no ice accretion is found on these two components.

(d) Wind direction $\theta = 90°$

No ice is accreted on the entire wheelhouse and mast due to the lack of spray. The ice thickness distribution on the deck shows a high degree of symmetry (Figures 4.8.5a and 4.8.5b). The reason is that for a wind direction of 90° blowing from the port to the starboard, the spray received by grid cells over the port side is not significantly different from that received by grid cells over the starboard side. The uniform ice thickness region is now reduced to a very small area. Many grid cells toward the

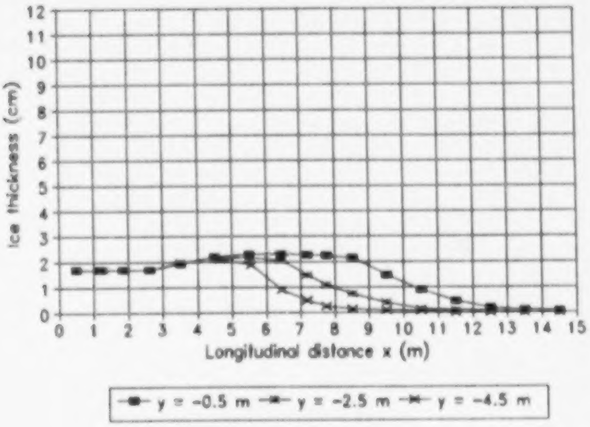

(a)

Figure 4.8.4: One hour ice thickness distribution over various components for a wind direction of 45°. a) The foredeck (port). b) The foredeck (starboard). c) The front of the wheelhouse (port). d) The front of the wheelhouse (starboard).

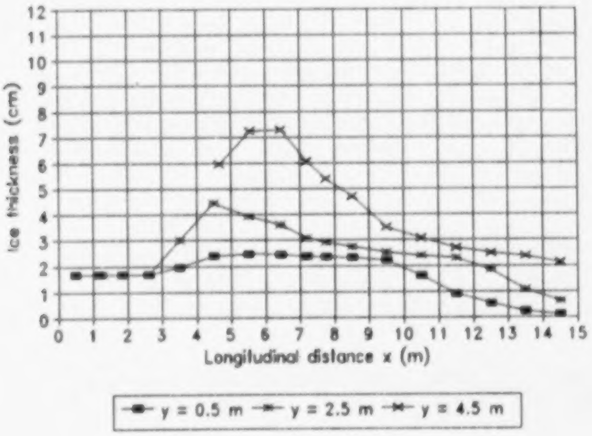

(b)

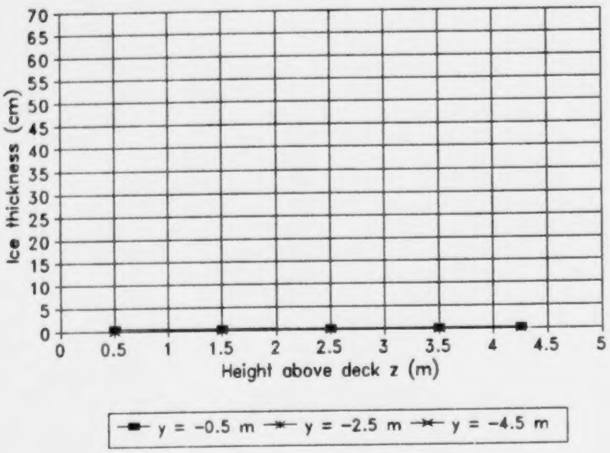
Ice thickness (cm)
0
5
10
15
20
25
30
35
40
45
50
55
60
65
70
Height above deck z (m)
0
0.5
1
1.5
2
2.5
3
3.5
4
4.5
5
y = -0.5 m
y = -2.5 m
y = -4.5 m

(c)

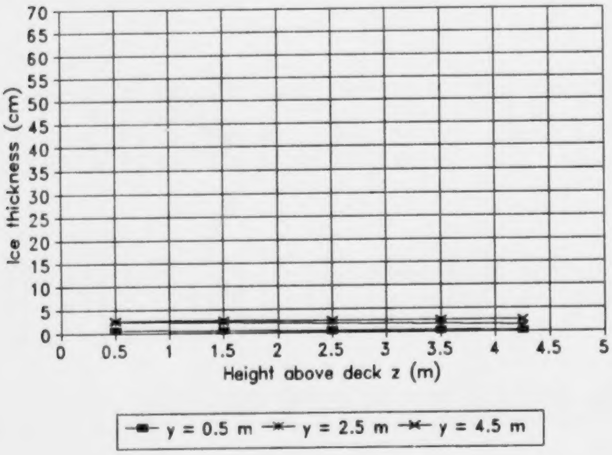
Ice thickness (cm)
0
5
10
15
20
25
30
35
40
45
50
55
60
65
70
Height above deck z (m)
0
0.5
1
1.5
2
2.5
3
3.5
4
4.5
5
y = 0.5 m
y = 2.5 m
y = 4.5 m

(d)

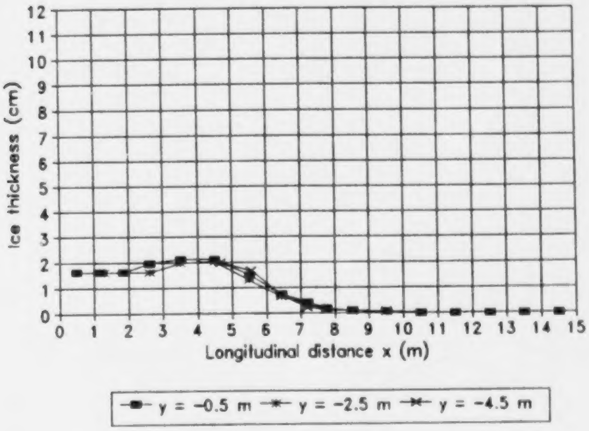

(a)

Figure 4.8.5: One hour ice thickness distribution over various components for a wind direction of 90°. a) The foredeck (port). b) The foredeck (starboard).

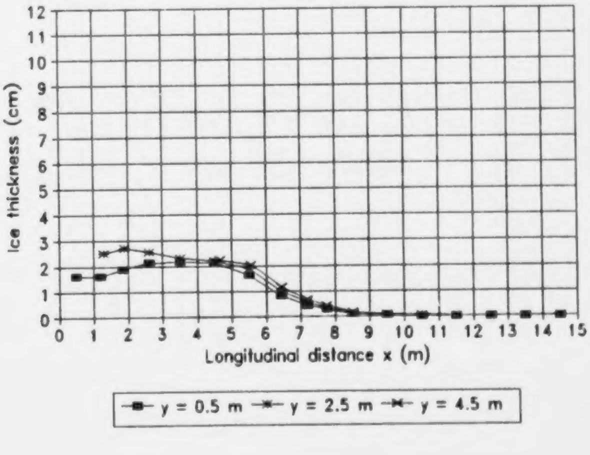

(b)

wheelhouse end of the deck have no ice accretion. The ice accretion zone retreats towards the bow. The maximum ice thickness is located at x = 1.888 m and y = 2.393 m, which is closer to the centreline than for the case of $\theta = 45°$.

An overview of the ice thickness distribution indicates that, for non-head winds, ice is accreted more rapidly on the downwind side of the ship. However, according to the official report on the sinking of the fishing vessel "CAPE ASPY" (Transportation Safety Board of Canada, 1994), it was pointed out that in beam and quartering winds, ice accumulates more rapidly on the windward side of the ship. This contradictory result is due to a basic limitation of the spraying model. Because of the experimental configuration, the ship heading is fixed at 180°. The wind direction in the numerical model can be changed from 0° (head wind) to 90° (beam wind). However, in the natural environment, the wind and waves usually arrive from the same direction.

In the model simulation, the spray source point that generates maximum spray flux is always located at the bow. Thus, under non-head winds, in the numerical model, the area of high spray flux shifts away from the centreline towards the downwind side of the ship. This gives rise to a higher icing rate over the downwind side.

In the natural environment, under non-head winds, the waves will tend to make a side impact with the hull. Hence, the spray source point that produces the maximum spray flux will be located along the windward side of the hull. In addition, the ship/wave collision in this case is less violent than with head seas. Therefore, the vertical extent of the spray cloud may also be less. As a result, comparatively more spray will impinge on the windward side of the ship. Hence, more ice will be accreted on the windward side than on the downwind side. In order to overcome this limitation of the spraying model, more experimental work on non-head sea ship/wave collisions will be required.

II Model Evaluation

There are several ways in which the present icing model can be evaluated. In the following discussion, a comparison will be made between the results of the present icing model and the prediction of the icing nomogram developed by Comiskey et al. (1984). Subsequently, a more in-depth discussion will be presented comparing the predictions of the present icing model with icing data from the NOAA Icing Data Report (Pease and Comiskey, 1985) and the Soviet Marine Icing Data report (Zakrzewski and Lozowski, 1989).

(i) Icing Nomogram

Wise and Comiskey (1980) developed a nomogram to predict a categorical icing rate for specific environmental conditions. It was subsequently discovered, however, that the icing rate in each category was too low and did not agree with observations. Consequently, Comiskey et al. (1984) modified the nomogram by doubling the icing rate in each category so that it now agrees better with their observations. The predictions from this nomogram have been compared with those from the present icing model. A discussion of this comparison is presented in Appendix 3A. In general, the model agrees with the nomogram for light, moderate, and heavy icing categories. However, for very heavy and extreme icing categories, the model tends to underestimate the icing rate.

(ii) NOAA Icing Data

Pease and Comiskey (1985) collected 85 icing observations in Alaskan waters on vessels ranging from 20 - 115 metres in length from 1979 to 1983. In this data set, the average icing rate for the entire vessel (cm/hr) and the air sea parameters are tabulated based on ship icing reports.

In the present icing model, the ship heading is limited to 180° (directly into the waves) while the wind direction is allowed to change from 0° (head wind) to 90° (beam wind). Because of this limitation, only cases with ship headings of 180 ± 45° are chosen for comparison with the model predictions. Among these cases, those with ships located in the lee of an island or in an otherwise undeveloped sea are excluded. As a result, only fourteen cases are considered in the comparison. These fourteen cases are listed in Appendix 3B.

The average icing rate expressed in cm/hr in the NOAA Report is converted to tonnes/hr for the Zandberg by multiplying it by the area of the icing zone on the Zandberg and the average spongy ice density. The area of the icing zone for the

Zandberg is taken to be the foredeck, and the front and top of the wheelhouse. These three components have a total area of 258.4 m^2. The mast and the deck behind the wheelhouse are neglected because the amount of ice accumulated on these two components is generally small compared with that accreted on the other three components. The spongy ice density (for a liquid fraction of 0.26) ranges from 937 to 985 kgm^{-3} at salinities ranging from 0 to 20 ‰. As an estimate, a density of 961 kgm^{-3} at a salinity of 10 ‰ is used as the average spongy ice density. This approximation should not cause a significant error since it is within ±3 % of the two extreme values.

A comparison between the model predicted and the observed icing rates is shown in Figure 4.8.6a. The solid triangles represent the icing rate while the crosses show the model predicted spray mass in tonnes/hr. Corresponding spray and ice masses are connected by vertical lines. It is obvious that the present icing model underestimates the icing rate for all cases. Of the fourteen cases, there are seven in which the model predicted spraying rates are less than the observed icing rates. Thus, insufficient spray production in the model is one of the reasons for underestimating the icing rates. This suggests two possible explanations. The first is that, under the same condition, Zandberg may actually produce less spray during ship/wave collisions than the types of vessels included in the NOAA report. This could be a matter of difference in ship design. The second possibility is that the amount of spray generated in the scale-model experiment, when scaled up to full-scale, is less than that actually produced in full-scale ship/wave collisions for the same type of ship. This may be especially true for low wave heights and ship speeds because, under these conditions, only a very little spray was collected on the deck of the model ship in the experiments. The observed wave heights and ship speeds for the above seven cases are generally low. It is therefore recommended that further research on full-scale ship/wave collision generated spray needs to be carried out.

By dropping those cases in which the model predicted spraying rate is less than the observed icing rate, the model predictions agree a little better with the observed values. But, the model still underestimates the observed icing rate (Figure 4.8.6b). Thus, it implies that there may be other reasons responsible for the model's underestimation. We will postpone the search for these reasons to Section 4.8II (iii) after we have

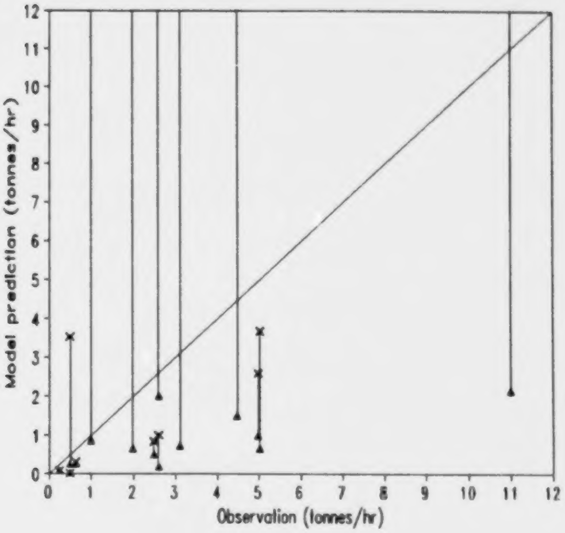

(a)

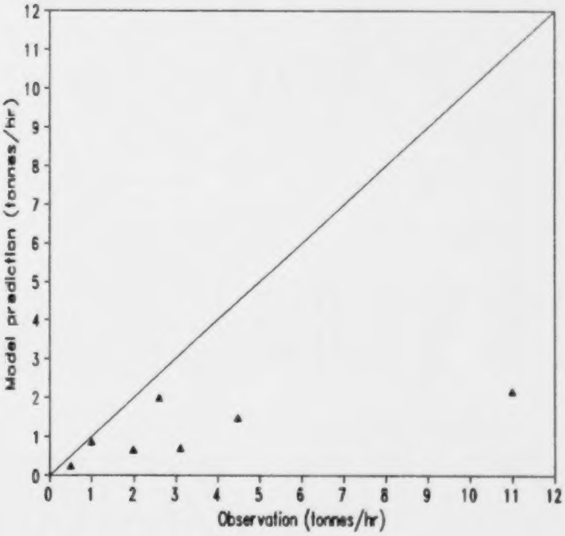

(b)

Figure 4.8.6: A comparison between model predictions and NOAA icing data (the latter in cm/hr converted to equivalent mass loads on the Zandberg as described in the text). (a) Icing rates (solid triangles) and model predicted spraying rates (crosses). (b) Only those cases with model predicted spraying rate greater than the observed icing rate.

discussed the Soviet icing data.

(iii) Soviet Icing Data

During the 1960's and 70's, comprehensive field investigations of freezing spray were carried out by Soviet scientists. More than 100 papers and reports pertaining to these investigations were carefully reviewed and documented by Zakrzewski and Lozowski (1989). In this report, observed icing rates (in tonnes/hour) for different sizes of fishing vessel are tabulated as a function of atmospheric and oceanographic conditions. Since the present icing model is ship specific, only those cases with a ship of comparable size to the "Zandberg" (length > 35 m) are used for comparison. Also in the present model, the ship heading is fixed at 180°. Therefore, of all the above cases, only those with a ship heading of 180° ± 30° are used in the comparison. There are twenty-one icing cases which satisfy the above criteria (see Appendix 3C). These twenty-one icing observations are used for comparison with the present model's icing predictions. The results are shown in Figure 4.8.7a. In this figure, the solid squares represent the model icing rates and the crosses indicate the model spraying rates. It is apparent that the model generally underestimates the icing rates, especially for those cases in which the spraying rates are less than the observed icing rates. This situation is similar to that discussed in Section 4.8II (ii) for the NOAA icing data. Eliminating the ten cases in which the model-predicted spraying rates are less than the observed icing rates, the model results are in better agreement with the observed data (Figure 4.8.7b). However, the model still underestimates cases with high observed icing rates.

The above comparisons of the model predictions with the icing nomogram, NOAA and Soviet icing data indicate that the present icing model generally underestimates icing rates. This discrepancy persists, though to a lesser extent, even when those cases in which the model predicted spraying rates are less than the observed icing rates are omitted. The magnitude of underestimation is greater for cases with higher observed icing rates (by as much as 100 %). Apart from the fact that the present model does not generate sufficient spray to account for the observed icing in some cases, there are several other possible explanations for this discrepancy.

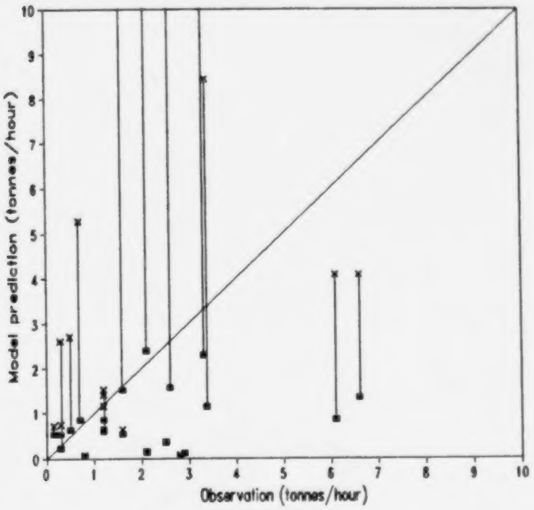

(a)

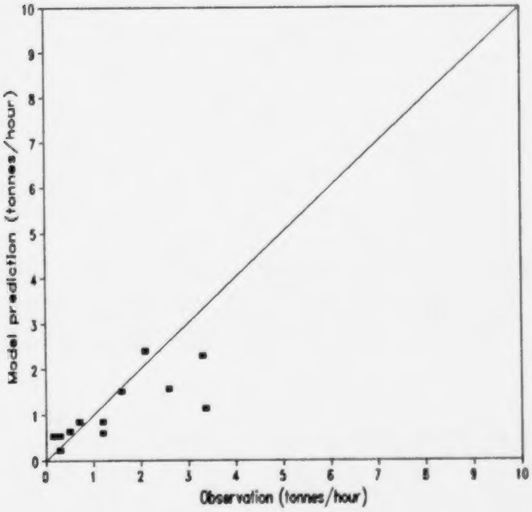

(b)

Figure 4.8.7: A comparison between model predictions and Soviet observations. (a) Icing rates (solid squares) and model predicted spraying rates (crosses). (b) Only those cases with model predicted spraying rate greater than the observed icing rate.

(a) The model ship, Zandberg, as used in the present simulation does not include such items as rigging machinery, handrails etc. These components increase the surface area for icing. In addition, the location of the wheelhouse and mast also have an effect on the ice accretion rate.

(b) In the icing model, it is assumed that all the impinging spray contributes to sensible heat exchange (q_s in Equation 4.5.1). As a result of this assumption, the model predicts no ice accretion during spraying for high sea-surface temperatures and high spray fluxes. In fact, this may not be true because only a fraction of the impinging spray participates in the sensible heat exchange (Kachurin et al., 1974). Thus the model tends to underestimate icing rates for conditions with high sea-surface temperatures and high spray fluxes. In order to examine this argument, the icing rate for the "Blue Mist II" case has been recalculated using two "reduced" sensible heat fluxes: $0.2q_s$ and $0.01q_s$ (i.e 20 and 1 % of the original value). Table 4.8.1 shows the icing rates corresponding to q_s, $0.2q_s$, and $0.01q_s$ for different sea- surface temperatures. It is found that for low sea-surface temperature (e.g 0 °C), the icing rates are decreased by 48 and 58 % respectively when q_s is reduced by 80 % and 99 %. However, for high sea-surface temperature (> 3 °C), the icing rates are increased by 5 and 20 % respectively for these two reduced values of q_s.

Icing rates (tonnes/hour)

T_{sea} (°C)	q_s	$0.20q_s$	$0.01q_s$
0	10.8	5.664	4.497
0.5	8.688	5.189	4.468
1.0	6.740	4.750	4.440
3.0	3.536	3.726	4.329
5.0	3.460	3.630	4.224

Table 4.8.1: Icing rates corresponding to different fractions of q_s and various sea-surface temperatures.

For conditions with higher air temperatures (-5 °C and -10 °C) and sea-surface temperature (5 °C), reducing q_s by 80 or 99 % increases the icing rate by no more than 20 % (see Table 4.8.2). Thus, it can be concluded that the possibility that all the impinging spray participates in the sensible heat exchange can only be partly responsible for the discrepancy between model and observations. Hence, we consider yet a third possibility.

Icing rate (tonnes/hour)

T_a (°C)	q_s	$0.20q_s$	$0.01q_s$
-5.0	0.948	0.992	1.100
-10.0	1.938	2.04	2.323

Table 4.8.2: Icing rates corresponding to different fractions of q_s for different air temperatures with a constant sea- surface temperature of 5 °C.

(c) In the present icing model, as discussed in Section 4.5, the foredeck, the front and the top of the wheelhouse are represented by three smooth flat plates, and, their Nusselt numbers are for smooth flat plates of different characteristic lengths. However, in actuality, an icing surface is almost always rough. This roughness can increase the Nusselt number (and hence the heat transfer) because a rough surface has a larger effective area, and the flow over a rough surface is more turbulent (Narten, 1985). The influence of surface roughness on the heat transfer distribution around an isothermal cylinder was studied by Narten (1985). He found that medium-scale roughness increases the average heat transfer from the cylinder by 44 % for Reynolds numbers ranging from 4×10^4 to 1.2×10^5. From his studies, it was also concluded that the influence of roughness on heat transfer increases with increasing Reynolds number. As mentioned in Section 4.5, the Reynolds number for flows over the deck, and the front and top of the wheelhouse is typically larger than 10^6. Consequently, the Nusselt numbers for these three components should be increased by at least 50 % if the effect of surface roughness were taken into account. Increasing the Nusselt numbers for these three components by

100 % results in much better agreement with both the NOAA and Soviet icing data as indicated in Figure 4.8.8. This figure shows that the model slightly overestimates the Soviet icing data, but still underestimates the NOAA icing data. However, in general, the agreement is good.

Based on the above analysis, the use of Nusselt numbers for smooth surfaces in the heat conservation Equation 4.5.1 is most likely the major cause for the discrepancy between the model and observations. By taking into account the influence of surface roughness on the heat transfer, the performance of the model can be substantially improved. Another factor which may, to a lesser extent, be responsible for the model's underestimation is the uncertainty in the fraction of the impinging spray which participates in the sensible heat exchange with the icing surface. Other factors such as ship architecture and various types of gear on the deck which are not considered in the present model, may also affect the model performance to a certain extent.

4.9 Concluding Remarks on the Ship Icing Model

A three-dimensional computer model has been developed to simulate ship spraying and icing. This model makes use of spraying data obtained during model experiments performed at the Institute for Marine Dynamics, National Research Council. Spray droplet trajectories, droplet temperature evolution, and brine flow are also included in the model simulation. In calculating the ice accretion rate on the deck and on the wheelhouse, the heat transfer coefficient for a smooth flat plate under a turbulent flow regime is used as a first approximation. Therefore, in spite of the necessary assumptions, the model is highly physically based.

The model sensitivity tests show that except for air pressure and relative humidity, all parameters have a significant effect on the model. Coupling effects, for example between the sea-surface temperature, wind speed, and air temperature further complicate the model's response.

The "BLUE MIST II" case study reveals the following results regarding the icing model:

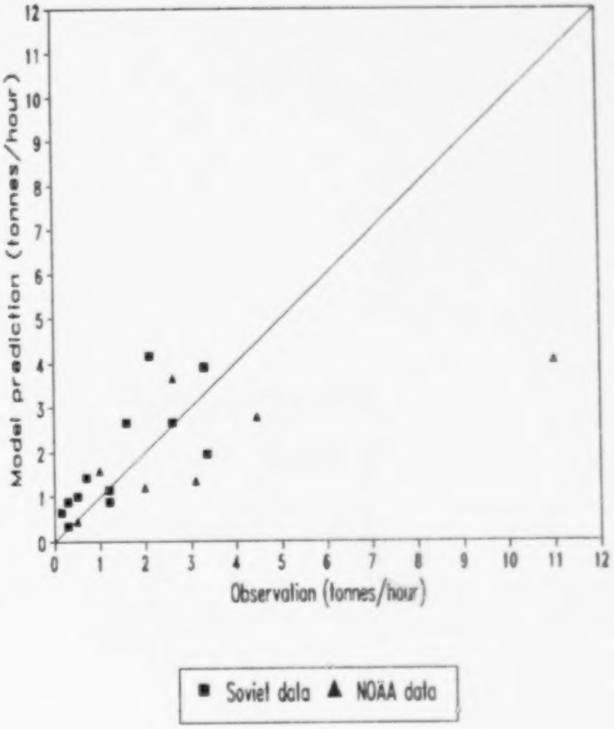

Figure 4.8.8: A comparison between model predicted icing rates (with a doubled Nusselt number) and NOAA and Soviet icing data. Cases with model predicted spraying rates smaller than the observed icing rates have been omitted.

(1) Maximum ice load occurs under head winds.

(2) Changing the wind direction from 0° to 15° reduces the total icing load only slightly, but results in a highly asymmetrical ice load distribution over the deck and the wheelhouse.

(3) The minimum ice load occurs with beam winds. The ice load distribution is relatively symmetrical in this case.

(4) Changing the wind direction from head winds causes the location of the maximum ice thickness to shift away from the centreline. However, for a wind direction > 45°, the location of the maximum ice thickness moves back slightly towards the centreline.

(5) For a wind direction greater than 45°, there is no ice accretion on the top of the wheelhouse and the mast. For a wind direction of 90°, no ice accretion is found on the entire wheelhouse and the mast.

The model underestimates the icing rate when compared with the Comiskey et al. icing nomogram, and NOAA and Soviet icing data. Several possible reasons for the model's discrepancy have been proposed and discussed. It is found that ignoring the influence of the roughness of the icing surface on heat transfer could be the major cause for the model's underestimation of icing rates. Increasing the Nusselt number by a factor of two gives much better agreement between the model's predictions and the observed icing rates.

CHAPTER 5 EFFECT OF ICING ON SHIP STABILITY

Ice accretion on a ship can affect its navigation in various ways. It can change the ship's centre of mass, moments of inertia, hydrostatic particulars (Derrett, 1990) such as displacement, draught, tonnes per centimetre immersion (T.P.C), centre of buoyancy, transverse metacentric height, centre of flotation, and the moment to change trim by one centimetre (M.C.T.C). Definitions of these hydrostatic particulars are given in Section 5.2. Since ice accretion typically forms unevenly over the surface of the ship, the ship may trim and list simultaneously. When the centre of mass of the ship is raised above the metacentre as a result of ice accretion, the ship possesses a negative metacentric height ($GM < 0$) and is considered to be unstable. The simplest way to determine the static stability of a ship is to use the transverse stability curves (i.e the righting lever or the GZ curves). In the following discussion, the effect of icing on the ship's centre of mass, moments of inertia, hydrostatic particulars, transverse stability, trim, and list will be examined.

Another way to analyze the effect of icing on the ship's stability is through ship dynamics analysis. Icing on a ship changes its hydrostatic conditions and these in turn affect the dynamic performance of the ship. Even a ship under a statically stable condition may be in danger of capsize in the presence of waves. In the present study, the ship dynamics model of Pawlowski and Bass (1991) will be used to evaluate the dynamic performance of the stern trawler Zandberg under the severe icing conditions discussed in Chapter 4. The results of this dynamic analysis will be presented in Chapter 6.

We define a frame of reference with x positive towards the bow, y positive towards the starboard, z positive upward, and the origin (O) at the baseline vertically below the original (uniced) centre of mass of the ship. The changes in the ship's hydrostatic conditions as a result of ice accretion will be calculated with respect to this frame of reference. Figure 5.1 shows this frame of reference and the dimensions of the ship.

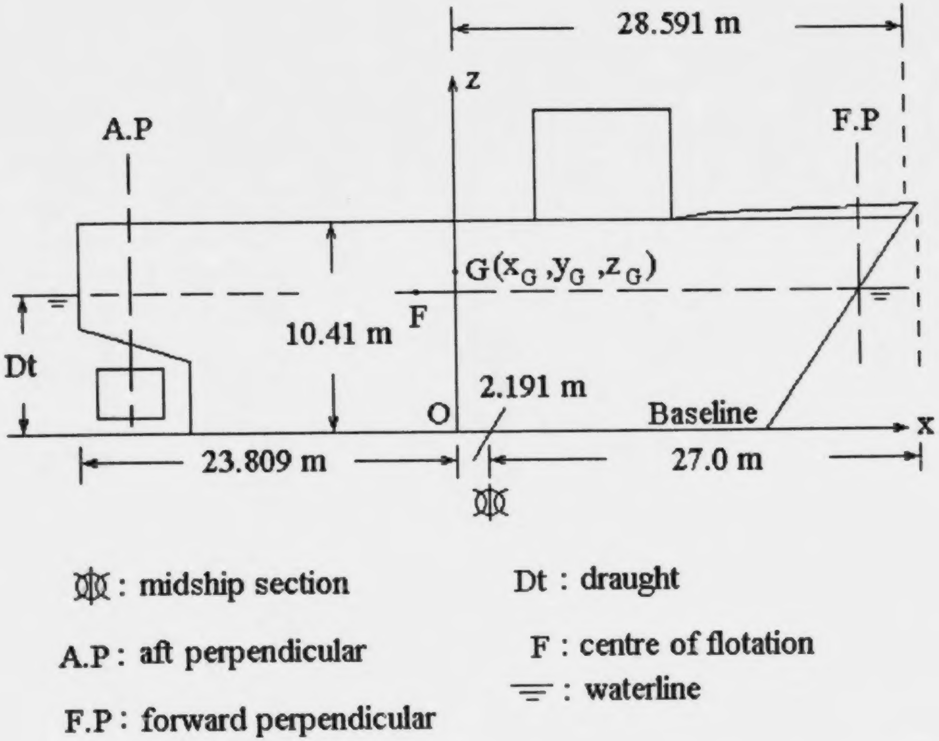
28.591 m
z
A.P
F.P
G(x_G, y_G, z_G)
10.41 m
F
Dt
2.191 m
O
Baseline
x
23.809 m
27.0 m
⌘ : midship section
Dt : draught
A.P : aft perpendicular
F : centre of flotation
≡ : waterline
F.P : forward perpendicular

Figure 5.1: A schematic diagram showing the frame of reference used in this chapter and the dimensions of the stern trawler MT Zandberg.

5.1 Centre of Mass and Moments of Inertia

(a) Centre of mass

In the icing model, the geometrical centres of the grid cells are specified in a frame of reference whose origin is located at the bow (see Figure 5.1.1). Consequently, it is convenient to adopt this frame of reference temporarily in the calculation of the coordinates of the new centre of mass of the ship with ice accretion. Subsequently, they will be transformed to the frame of reference shown in Figure 5.1.

The original ice-free centre of mass of the ship is located at the point G(x_G, y_G, z_G), and the coordinates of the geometrical centre of grid cell i are (x_i, y_i, z_i). Each grid cell is assumed to be covered with a homogeneous layer of ice with thickness h^*_i and mass m_i. Then the centre of mass of the ice accretion on each grid cell on the deck or the top of the wheelhouse is located at (x_i, y_i, $z_i+h^*_i/2$). For grid cell on the front of the wheelhouse, the centre of mass is located at ($x_i-h^*_i/2$, y_i, z_i). Since ice accreted on the mast has a semi-circular shape, its centre of mass is located approximately at ($x_i-D/2-h^*_i/2$, y_i, z_i) (the error of this latter approximation is negligible since the amount of ice accreted on the mast is small compared with the total ice accretion on the entire ship). Then, the new centre of mass of the ship with its ice accretion with respect to O' can be calculated from (Fowles, 1977):

$$\vec{r}'_G = \frac{\sum m_i \vec{r}_i + M_{ship}\vec{r}_G}{M_{Itot} + M_{ship}} \qquad (5.1.1)$$

where

m_i: the ice load on grid cell i (kg).

$\vec{r}'_G$: the position vector of the centre of mass of the ship with ice accretion (m).

$\vec{r}_i$: the position vector of the centre of mass of the ice accretion on each grid cell i (m).

$\vec{r}_G$: the position vector of the ice-free centre of mass of the ship (m).

M_{Itot}: the total ice accretion load for the entire ship (kg).

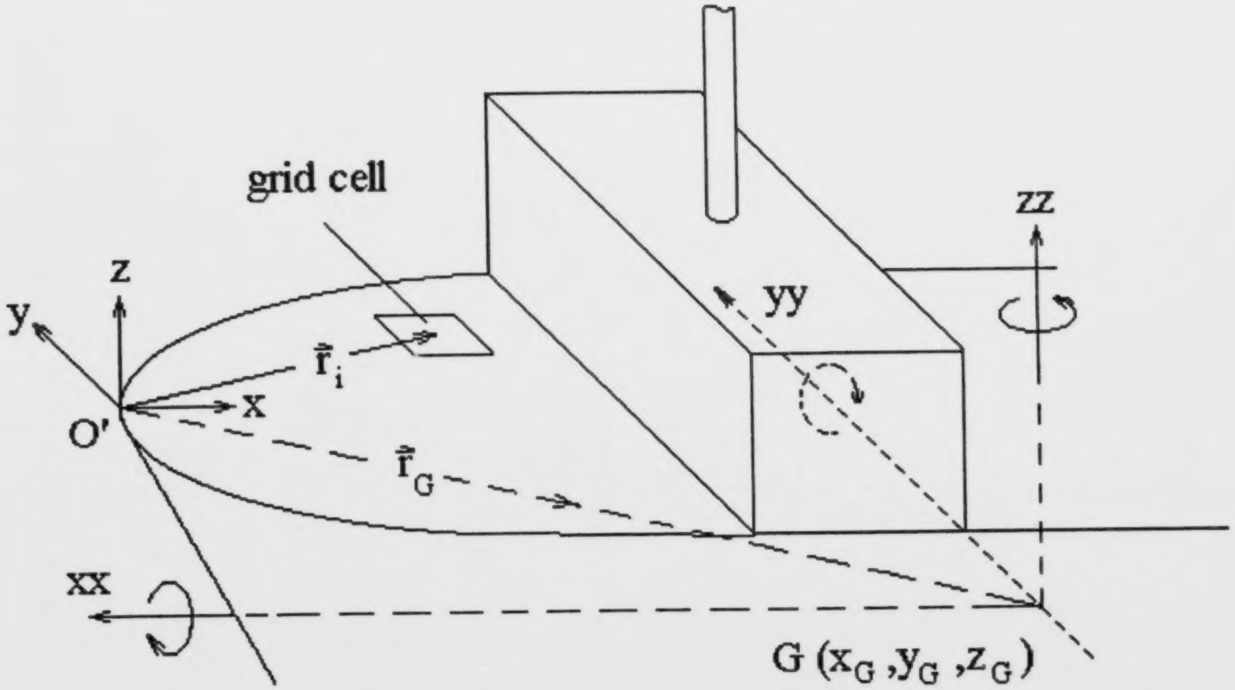
grid cell
z
y
O'
x
$\vec{r}_i$
$\vec{r}_G$
xx
yy
zz
G (x_G, y_G, z_G)

Figure 5.1.1: The frame of reference used in the calculation of the coordinates of the new centre of mass of the ship with ice accretion. The axes of rotation through the original centre of mass are also shown.

M_{ship}: the mass of the ice-free ship (kg).

All the position vectors are relative to O' as shown in Figure 5.1.1. The summation in Equation 5.1.1 is over all the grid cells. Finally the coordinates (x'_G, y'_G, z'_G) can easily be transformed to the frame of reference centred on O as shown in Figure 5.1.

(b) The moments of inertia

Let us first consider the case without ice accretion. The centre of mass of the ship is located at G(x_G, y_G, z_G) with respect to the O' system of reference (see Figure 5.1.1). The ship can rotate along the longitudinal axis xx, the transverse axis yy, and the vertical axis zz with moments of inertia I_{xx}, I_{yy}, and I_{zz} respectively. When the topside of the ship is loaded with ice, both the axes of rotation and the moments of inertia will change.

These new moments of inertia can be expressed as (Fowles, 1977):

$$I'_{xx} = I_{xx} + \sum m_i (y'^2_i + z'^2_i) \tag{5.1.2}$$

$$I'_{yy} = I_{yy} + \sum m_i (x'^2_i + z'^2_i) \tag{5.1.3}$$

$$I'_{zz} = I_{zz} + \sum m_i (x'^2_i + y'^2_i) \tag{5.1.4}$$

where I'_{xx}, I'_{yy}, and I'_{zz}, are the new moments of inertia of the ship (with ice accretion) about the longitudinal (xx), transverse (yy), and vertical (zz) axes, and x'_i, y'_i, and z'_i are the coordinates of the centre of mass of the ice accretion on grid cell i relative to the ice-free centre of mass of the ship G(x_G, y_G, z_G). The summations in Equations 5.1.2 to 5.1.4 are over the grid cells.

The coordinates (x'_i, y'_i, z'_i) can be readily expressed in terms of (x_i, y_i, z_i) and (x_G, y_G, z_G). For grid cells on the deck or the top of the wheelhouse:

$$(x_i', y_i', z_i') = (x_i - x_G, y_i - y_G, z_i + \frac{h_i^*}{2} - z_G) \qquad (5.1.5)$$

For grid cells on the front of the wheelhouse:

$$(x_i', y_i', z_i') = (x_i - \frac{h_i^*}{2} - x_G, y_i - y_G, z_i - z_G) \qquad (5.1.6)$$

and for grid cells on the mast:

$$(x_i', y_i', z_i') = (x_i - \frac{D}{2} - \frac{h_i^*}{2} - x_G, y_i - y_G, z_i - z_G) \qquad (5.1.7)$$

The summations of Equation 5.1.2 to 5.1.4 can be decomposed into individual summations over the deck, the front and the top of the wheelhouse, and the mast. Using Equations 5.1.2 and 5.1.5 to 5.1.7, the moment of inertia of the iced ship about the longitudinal axis xx becomes:

$$\begin{aligned} I_{xx}' = I_{xx} &+ \sum_{deck/top} m_i[(y_i - y_G)^2 + (z_i + \frac{h_i^*}{2} - z_G)^2] \\ &+ \sum_{front} m_i[(y_i - y_G)^2 + (z_i - z_G)^2] \\ &+ \sum_{mast} m_i[(y_i - y_G)^2 + (z_i - z_G)^2] \end{aligned} \qquad (5.1.8)$$

Likewise, using Equations 5.1.3 and 5.1.5 to 5.1.7, 5.1.4 and 5.1.5 to 5.1.7, the moments of inertia of the iced ship about the transverse (yy), and vertical (zz) axes are given by:

$$
\begin{aligned}
I'_{yy} = I_{yy} &+ \sum_{deck/top} m_i[(x_i-x_G)^2 + (z_i+\frac{h_i^*}{2}-z_G)^2] \\
&+ \sum_{front} m_i[(x_i-\frac{h_i^*}{2}-x_G)^2 + (z_i-z_G)^2] \\
&+ \sum_{mast} m_i[(x_i-\frac{D}{2}-\frac{h_i^*}{2}-x_G)^2 + (z_i-z_G)^2]
\end{aligned}
\tag{5.1.9}
$$

and

$$
\begin{aligned}
I'_{zz} = I_{zz} &+ \sum_{deck/top} m_i[(x_i-x_G)^2 + (y_i-y_G)^2] \\
&+ \sum_{front} m_i[(x_i-\frac{h_i^*}{2}-x_G)^2 + (y_i-y_G)^2] \\
&+ \sum_{mast} m_i[(x_i-\frac{D}{2}-\frac{h_i^*}{2}-x_G)^2 + (y_i-y_G)^2]
\end{aligned}
\tag{5.1.10}
$$

So far we have obtained the moments of inertia of the iced ship about the axes xx, yy, and zz which pass through the centre of mass of the uniced vessel, G. However, because of the ice accretion, the centre of mass of the ship may have shifted to a new position G'(x'$_G$, y'$_G$, z'$_G$) (see Figure 5.1.2). Then, the new axes of rotation which pass through G' will be xx', yy', and zz'. The new centre of mass G'(x'$_G$, y'$_G$, z'$_G$) relative to the point O can be readily obtained (Section 5.1, Part a). Using the parallel axis theorem (Fowles, 1977), the moments of inertia of the iced ship (I'$_{xx'}$, I'$_{yy'}$, I'$_{zz'}$) about the axes xx', yy', zz' are (Fowles, 1977):

$$
I'_{xx'} = I'_{xx} - (M_{Itot} + M_{ship})\, l_{xx}^2 \tag{5.1.11}
$$

$$
I'_{yy'} = I'_{yy} - (M_{Itot} + M_{ship})\, l_{yy}^2 \tag{5.1.12}
$$

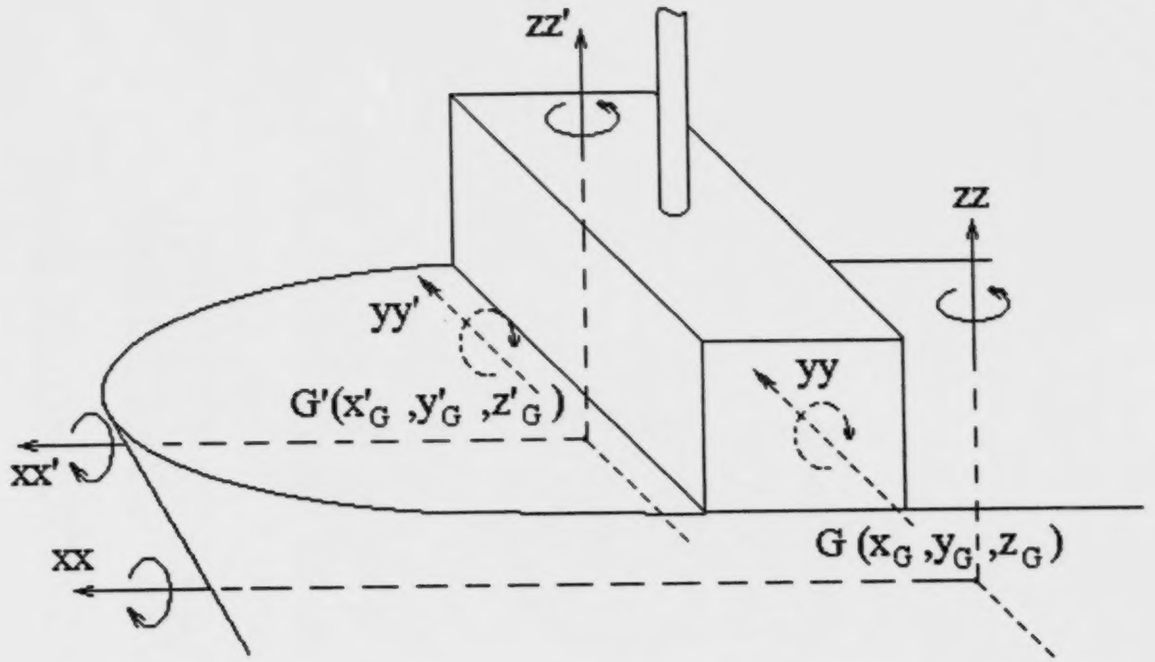

Figure 5.1.2: The rotational axes and centres of mass of a ship under conditions with and without ice accretion. G' and G are respectively the centres of mass of the ship with and without ice accretion. xx, yy and zz are the rotational axes for the case without ice accretion while xx', yy' and zz' for the case with ice accretion.

$$I'_{zz'} = I'_{zz} - (M_{Itot} + M_{ship})\, l^2_{zz} \qquad (5.1.13)$$

where l_{xx}, l_{yy}, and l_{zz} are respectively the perpendicular distances between the axes xx' and xx, yy' and yy, and zz' and zz. Since the coordinates of $G'(x'_G, y'_G, z'_G)$ and $G(x_G, y_G, z_G)$ with respect to O are known, l_{xx}, l_{yy}, and l_{zz} can be calculated from the following equations (Fowles, 1977):

$$l^2_{xx} = (y'_G - y_G)^2 + (z'_G - z_G)^2 \qquad (5.1.14)$$

$$l^2_{yy} = (x'_G - x_G)^2 + (z'_G - z_G)^2 \qquad (5.1.15)$$

$$l^2_{zz} = (x'_G - x_G)^2 + (y'_G - y_G)^2 \qquad (5.1.16)$$

The above computations for the changes of the centre of mass and the moments of inertia as a result of ice accretion on the Zandberg have been programmed using Fortran 77 code (see Appendix 7). The inputs to this program include:

(i) Ice load on each grid cell calculated from the icing model and the duration of the icing event.

(ii) Mass (or displacement) of the ship.

(iii) Centre of mass of the ship without ice accretion which is taken from the Stability Information Booklet for the M.F.V. Zandberg (Marystown Shipyard Ltd., 1982).

(iv) Original moments of inertia of the ship without ice accretion. They are not specified in the stability information booklet. As a first approximation, the radius of gyration about the longitudinal axis is taken to be 35 % of the beam, and the radii of gyration about the transverse and vertical axes are taken to be the same and equal to 25 % of the length between the forward and aft perpendiculars (Pawlowski, personal communication). Knowing the radii of gyration about the three axes, the respective moments of inertia can be determined.

The outputs from this program are:

(i) The new centre of mass of the ship with ice accretion.

(ii) The new moments of inertia of the ship with ice accretion.

The code for this program (shgeom.for) is listed in Appendix 4.

5.2 Hydrostatic Particulars

The hydrostatic particulars of a ship are usually expressed in tabular or graphical form from which various hydrostatic information corresponding to different draughts can be obtained. This information includes: draught, displacement, trim, tonnes per centimetre immersion (T.P.C), moment to change trim one centimetre (M.C.T.C), centre of buoyancy, centre of flotation, and transverse metacentre. All of this hydrostatic information is usually based on an even keel condition (i.e the lowest boundary (assumed straight) of the moulded surface of the ship is oriented horizontally). The definitions and meanings of these hydrostatic terms are summarized as follows.

a) Draught: the vertical distance between the waterline and the baseline which is parallel to the waterline and represents the lowest boundary of the moulded surface of the ship (see Figure 5.1). The draught is usually given for an even keel condition. For an uneven keel condition (i.e the ship has a longitudinal inclination), the draught varies longitudinally (see Figure 5.1). In this case, the draught of the ship may be specified in various way such as the draught at the forward and aft perpendiculars, the draught at midship, or the draught at the centre of flotation (see Figure 5.1).

b) Displacement: it is the mass of the volume of brine displaced by the ship. According to Archimedes Principle, the weight of the displaced water is equivalent to the weight of the ship. Displacement is closely related to draught. Increasing the displacement of a ship means increasing its draught as well.

c) Tonnes per centimetre immersion (T.P.C.): the mass which must be added to or removed from a ship in order to change its mean draught by 1 cm (Derrett, 1990). Usually, T.P.C. changes with draught because the waterplane area varies with increasing immersion of the hull (Δdisplacement = Δdraught x waterplane area x brine density).

d) Moment to change trim one centimetre (M.C.T.C.): the moment required to change the trim by 1 cm. Trim is defined as the longitudinal inclination of a ship. When a ship is inclined longitudinally, both the draught at the forward and aft perpendiculars will change. The change trim one centimetre means that the change of draught at the forward perpendicular added to that at the aft perpendicular is equal to one centimetre.

e) Centre of buoyancy (B): the point through which the force of buoyancy acts upwards with a magnitude equal to the weight of water displaced by the ship (Derrett, 1990). The centre of buoyancy is also the centre of mass of the underwater volume. For a ship at rest in still water, the centre of buoyancy and the centre of mass of the ship lie along the same vertical line.

f) Transverse metacentre (M): when a ship is heeled at an angle ϕ, its centre of buoyancy will move off the ship's centreplane (from B to B_1) as a result of the inclination (see Figure 5.2.1a and 5.2.1b). The vertical line through the centre of buoyancy intersects the original vertical through the original centre of buoyancy, at the point M (see Figure 5.2.1b). This point M is called the transverse metacentre (Moore, 1967). For a given draught or displacement, the metacentre M will remain practically at the same location (i.e independent of the angle of heel) as long as the angle of heel is small ($< 15°$). The metacentre at small angles of heel is also called the initial transverse metacentre. This point is usually specified with respect to the keel. The distance between the centre of mass of the ship and the metacentre is called the transverse metacentric height (GM). It is a measure of the initial static stability of the ship. When M lies above G (i.e $GM > 0$), the ship is initially statically stable. When M lies below G (i.e $GM < 0$), the ship is initially statically unstable. A more detailed discussion of the transverse stability of the ship will be presented in Section 5.3, Part b. The longitudinal metacentre and the longitudinal metacentric height, which are related to longitudinal inclination, are defined in similar ways to the transverse ones. Usually, the longitudinal metacentre is very much higher than the centre of mass. This means that a ship seldom capsizes longitudinally.

g) Centre of flotation (F): the point on the ship's waterplane through which the axes of rotation (xx and yy) pass when the ship is inclined, either transversely or longitudinally,

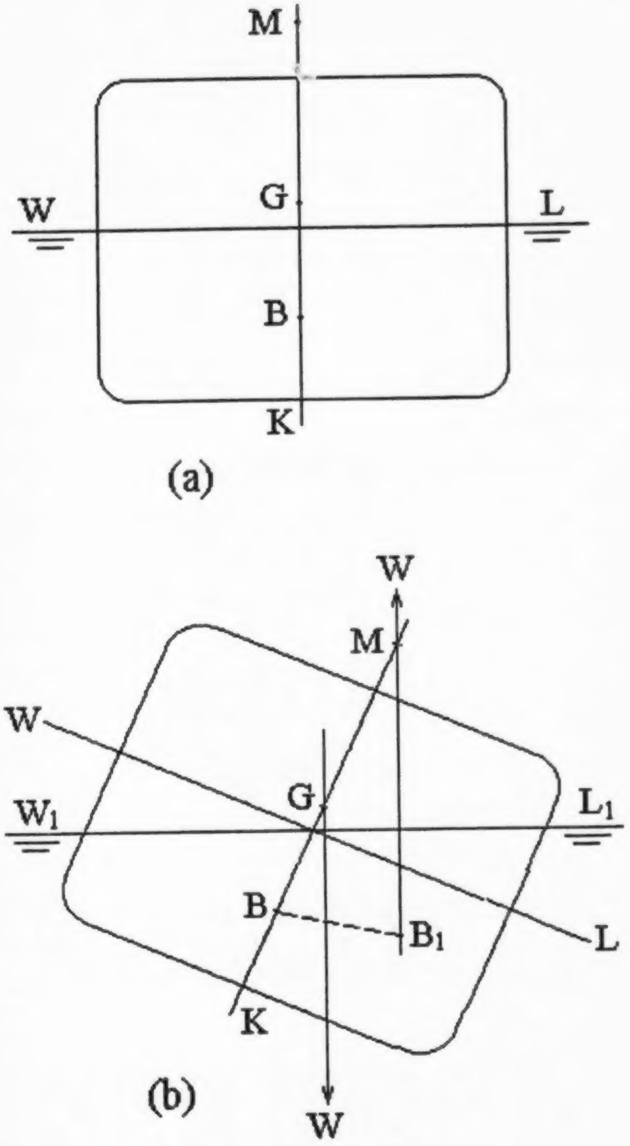

Figure 5.2.1: A schematic front view diagram of a ship showing how the transverse metacentre is defined. (a) the ship is in an upright position. (b) the ship is heeled to a small angle. WL and W_1L_1 represent the waterlines, B and B_1 the centres of buoyancy, G the centre of mass, M the metacentre, K the keel, and W the displacement of the ship.

or both (Moore, 1967). Figure 5.2.2 shows that when a ship trims, while its displacement remains constant, the volume of the immersed wedge (with centre of mass at g_1) must equal that of the emerged wedge (with centre of mass at g_2). It can be shown that the centre of flotation F is in fact the centroid of the waterplane area (Moore, 1967). The location of the centre of flotation changes with draught.

The detailed methods for determining the above hydrostatic particulars can be found in any book on naval architecture (e.g Derrett, 1990) and they will not be discussed here. The hydrostatic particulars at various draughts for the stern trawler MT Zandberg can be found on pages 7 and 8 of the Stability Information Booklet for the M.F.V. Zandberg. The table is reproduced here in Table 5.2.1. The measurements given are based on an even keel condition. All vertical measurements are relative to the baseline and longitudinal measurements are relative to the midship section.

In the subsequent analysis of the effect of icing on stability, the Zandberg is assumed initially to have a "Half Load" condition described on p.22-23 of the Stability Information Booklet for the M.F.V. Zandberg (loading condition no.4). The displacement and draught of the ship are 1224.7 tonnes and 5.39 metres respectively. It is assumed that the ship is of even keel. A summary of the hydrostatic conditions corresponding to a draught of 5.39 m is given in Table 5.2.2.

Draught (m)	Displacement (tonnes, t)	T.P.C (t/cm)	M.C.T.C (t.m)	L.C.B (m)
5.39	1224.7	4.43	13.82	-1.175

L.C.F (m)	KB (m)	KM (m)	KG (m)	GM (m)
-3.442	3.658	6.748	6.131	0.617

Table 5.2.2: Hydrostatic particulars for the stern trawler Zandberg under Loading Condition no.4 (from Stability Information Booklet) with a draught of 5.39 m.

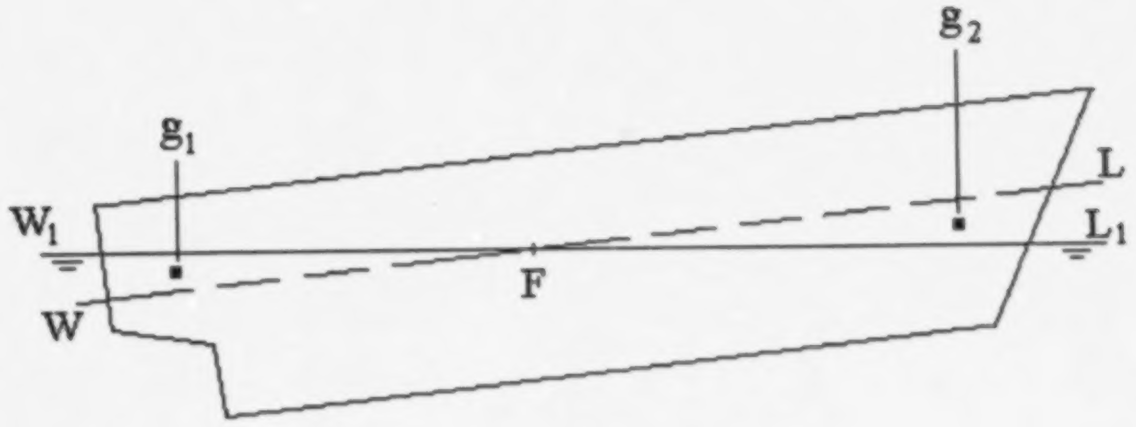

Figure 5.2.2: A schematic diagram showing the centre of flotation F of a ship. g_1 and g_2 are respectively the centres of mass of the immersed and emerged wedges.

Draught (m)	Displacement (tonnes, t)	T.P.C (t/cm)	M.C.T.C (t-m)	L.C.B (m)	L.C.F (m)	KB (m)	KM (m)
4.50	854.1	3.76	9.03	-0.428	-1.823	3.086	6.632
4.75	951.7	4.01	10.90	-0.611	-2.616	3.244	6.660
5.00	1055.0	4.21	12.36	-0.834	-3.118	3.405	6.693
5.25	1162.6	4.36	13.38	-1.059	-3.376	3.564	6.728
5.50	1273.7	4.48	14.16	-1.267	-3.493	3.723	6.763
5.75	1387.4	4.58	14.76	-1.454	-3.468	3.880	6.798
6.00	1503.5	4.68	15.50	-1.611	-3.505	4.036	6.839
6.25	1621.6	4.74	15.89	-1.746	-3.377	4.191	6.880
6.50	1741.4	4.82	16.52	-1.858	-3.347	4.345	6.926

Table 5.2.1: Hydrostatic particulars for the stern trawler MT Zandberg (taken from the Stability Information Booklet for the M.F.V. Zandberg, 1982).

Note:

(1) L.C.B: Longitudinal distance of the centre of buoyancy from midship.

(2) L.C.F: Longitudinal distance of the centre of flotation from midship.

(3) For L.C.B and L.C.F, positive value means forward of midship whereas negative means aft of midship.

(4) KB: The height of the centre of buoyancy above the keel.

(5) KM: The height of the metacentre above the keel.

The quantities shown in Table 5.2.2 were obtained by interpolating in Table 5.2.1 with a displacement of 1224.7 tonnes and a zero trim (even keel). The corresponding quantities shown on p.22-23 of the Stability Information Booklet are slightly different because the booklet assumes the ship trims at the stern by 0.888 m.

When the ship is iced, all the quantities in Table 5.2.2 will change according to the amount and distribution of the ice load. The new hydrostatic conditions with ice can be calculated using linear interpolation based on the information given in Table 5.2.1.

5.3 List, Stability Curves, Energetics of Static Stability and Trim

(a) List

List can be defined as the transverse inclination of a ship. It is usually caused by an uneven loading condition over the port and starboard sides of a ship. Under these conditions, the centre of mass of the ship shifts towards the side with heavier loading and thereby creates a listing moment. Thus, the ship lists to a certain angle of heel until the transverse centre of buoyancy lies vertically under the shifted centre of mass. The listing of a ship is particularly important for its stability because it is much easier for a ship to capsize transversely than longitudinally, because the transverse metacentric height GM is much shorter than the longitudinal metacentric height. Consequently, an asymmetrical ice load distribution (w.r.t. centreline) is the most dangerous to the ship's stability.

In Section 5.3b, the construction of the stability curves for a ship with its centre of mass off the centreplane will be discussed. Once the stability curves for a ship under asymmetrical icing conditions have been constructed, the angle of loll (listing angle at which the ship will stay at rest in still water) can readily be determined. In this case, the ship will lie at rest at the angle of loll, as long as stability can be regained when the ship heels beyond the angle of loll.

(b) Stability curves

The stability curves are a set of curves which give the righting arms about an "assumed" centre of mass (located on the centreplane) for any angle of heel (up to 90°) at any particular displacement. Using this information, the righting arms for the actual centre of mass can be calculated. In the present case, the stability curves for the Zandberg are based on an assumed centre of mass located at the point K' (see Figure 5.3.1) which lies 1.0 metre above the baseline on the centreplane. The stability curves may be found in the Stability Information Booklet (p.48-54). Figure 5.3.1 illustrates the situation when the ship is heeled. In this Figure, K'N is the righting arm about the point K' (assumed centre of mass). The values of K'N for the Zandberg at different draughts are shown in Table 5.3.1. For the actual centre of mass (point G in Figure 5.3.1), the righting arm (GZ) about the point G is:

$$GZ = K'N - K'G\sin\phi \qquad (5.3.1)$$

where ϕ is the angle of heel.

Let us now assume that ice has been accreted on the topside of the ship and thus the centre of mass of the ship has been raised to the point G_1 (Figure 5.3.1). Then, knowing K'N corresponding to the new draught, the new righting arm (G_1Z_1) about the new centre of mass G_1 is:

$$G_1Z_1 = K'N - K'G_1\sin\phi \qquad (5.3.2)$$

With an asymmetrical ice load distribution, the centre of mass of the ship is raised, and also shifted away from the centreplane to the point G_2 (see Figure 5.3.2). Then, the righting arm G_2Z_2 about the centre of mass G_2 can be calculated by (Moore, 1967):

$$G_2Z_2 = K'N - K'G_1\sin\phi - G_1G_2\cos\phi \qquad (5.3.3)$$

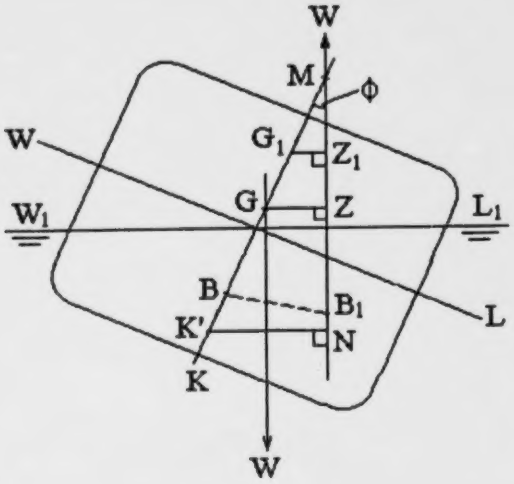
W
M
Φ
W
G1
Z1
G
Z
W1
L1
B
B1
L
K'
N
K
W

Figure 5.3.1: The righting arm (G_1Z_1) of an iced ship with its centre of mass G_1 located on the centreplane.

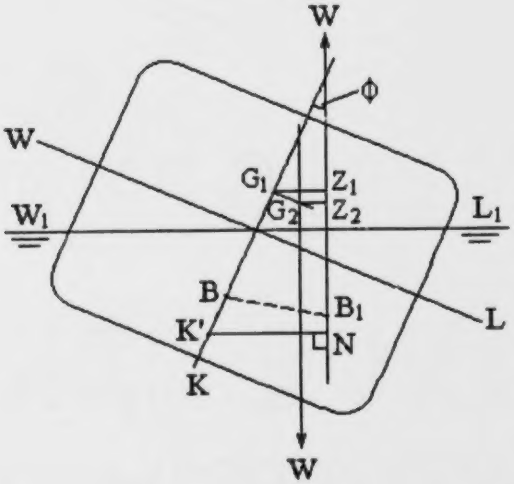
W
Φ
W
G1
Z1
G2
Z2
W1
L1
B
B1
L
K'
N
K
W

Figure 5.3.2: The righting arm (G_2Z_2) of an iced ship with its centre of mass G_2 located off the centreplane.

Draught (m) and displacement (t)	2.5 m 519 t	3.0 m 677 t	3.5 m 854 t	4.0 m 1055 t	4.5 m 1274 t	5.0 m 1504 t
ϕ (°)	K'N (m)	K'N (m)	K'N (m)	K'N (m)	K'N (m)	K'N (m)
5°	0.500	0.490	0.491	0.496	0.503	0.509
10°	0.995	0.977	0.979	0.991	1.004	1.017
20°	1.947	1.928	1.936	1.964	1.996	2.026
30°	2.816	2.821	2.851	2.904	2.937	2.925
40°	3.610	3.646	3.684	3.703	3.698	3.664
50°	4.370	4.342	4.322	4.329	4.328	4.285
60°	4.979	4.939	4.919	4.877	4.811	4.730
70°	5.453	5.449	5.366	5.230	5.125	5.049
80°	5.648	5.645	5.601	5.517	5.355	5.227

Table 5.3.1: K'N data for the stern trawler Zandberg under different loading conditions (taken from the *Stability Information Booklet for the M.V.F. Zandberg*, 1982). The draught is measured from the horizontal datum line (1 metre above the keel) passing through the point K' (see Figure 5.3.1).

Let us assume that the centre of mass is located at $G_2(x, y, z)$ relative to the point K' vertically below the original centre of mass of the ship (without ice accretion) along the centreplane. Then, $K'G_1 = z$ and $G_1G_2 = y$. This means that, under icing conditions, knowing the new centre of gravity G_2 of the ship with respect to the point K', the righting curves (G_2Z_2) can be constructed as a function of angle of heel and draught.

The K'N values given in the Stability Information Booklet are based on zero inclination (i.e the ship has zero trim). Under icing conditions, as a result of an uneven ice load distribution, the ship may trim. Therefore, the K'N values given in the booklet may not be accurate for the iced Zandberg. However, unless there is an abrupt change in the underwater shape of the hull, the K'N values provided in the stability booklet are still reliable. This is true as long as the ship does not trim to such an extent that the bow immerses in water.

Information about a ship's stability can be deduced from an inspection of the stability curves. A positive righting arm (GZ) means that the ship experiences a moment to return it to its initial position when it is heeled (that is, it is statically stable). A negative righting arm implies that when a ship is inclined to a small angle, it tends to heel still further (that is, it is statically unstable). A zero righting arm means that when a ship is heeled to a small angle, it will tend to remain at that angle (that is, it is statically neutral).

A typical stability curve for a ship with the centre of mass located along the centreplane and below the metacentre (i.e GM is positive, see Figure 5.3.3a) is illustrated in Figure 5.3.4a. If now the centre of mass is raised to G_1 as a result of ice accretion, the righting arm will be reduced to G_1Z_1 as shown in Figure 5.3.3a. The GZ curve shown in Figure 5.3.4a will now move closer to the ϕ axis ($GZ = 0$).

If G is raised above the metacentre M (e.g to G_1' as shown in Figure 5.3.3a), the value of GM is negative. This means that the ship has a negative righting arm and is initially unstable. Two possible situations for a ship with negative GM are shown in Figures 5.3.4b and 5.3.4c. In Figure 5.3.4b, the ship possesses a negative righting arm up to a heeling angle ϕ_1, and thereafter the righting arm becomes positive. This means that when the ship is inclined to a small angle, it continues to heel until the centre of

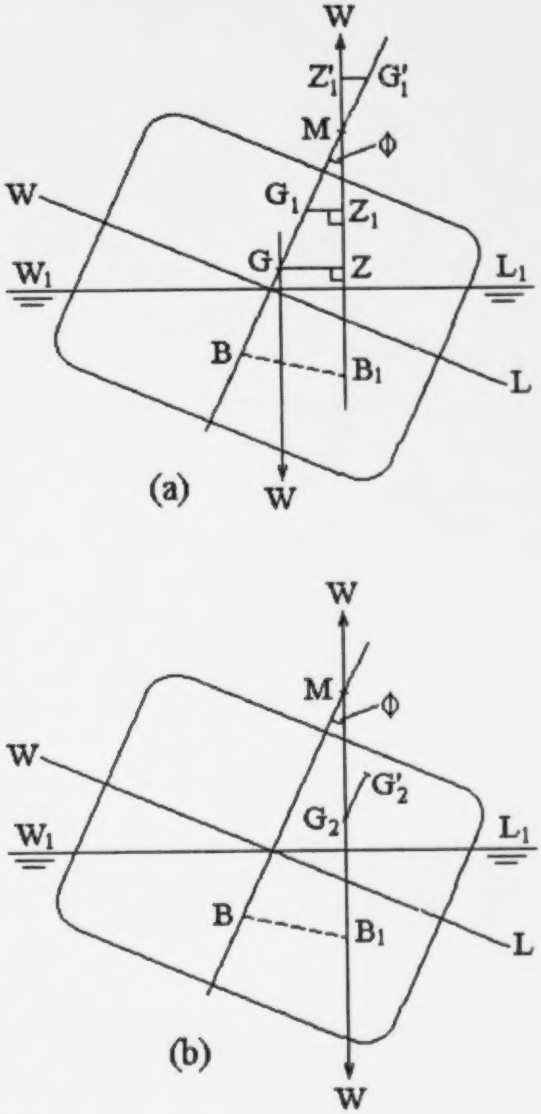
W
Z'1
G'1
M
Φ
W
G1
Z1
G
Z
W1
L1
B
B1
L
(a)
W
W
M
Φ
W
G'2
G2
W1
L1
B
B1
L
(b)
W

Figure 5.3.3: Changes in the metacentric height (GM) for various locations of a ship's centre of mass, G, G_1, G'_1, G_2, G'_2. (a) centre of mass located along the centreplane. (b) centre of mass located off the centreplane.

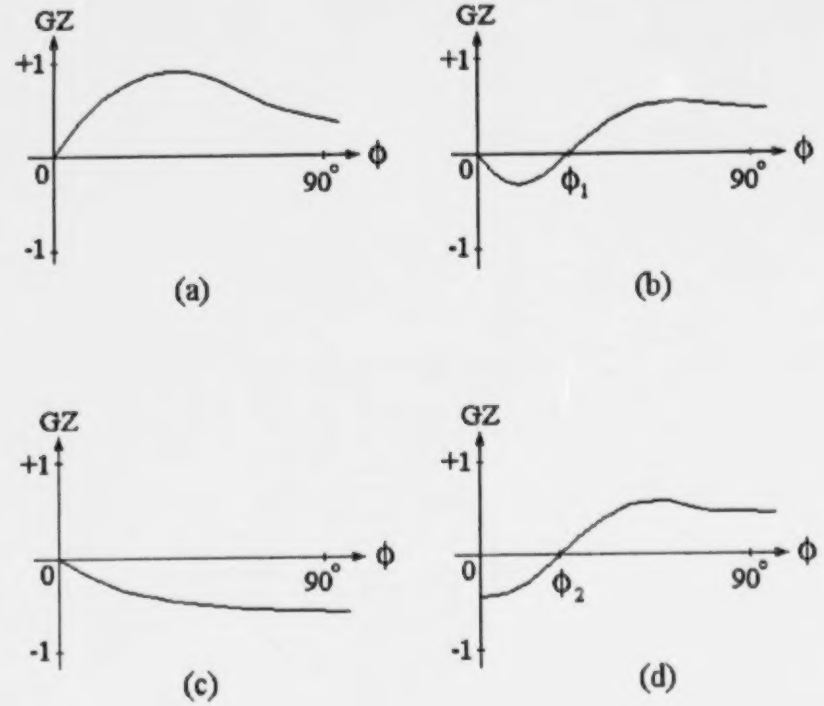

Figure 5.3.4: Stability curves for various locations of a ship's centre of mass. (a) centre of mass located below metacentre. (b) and (c) centre of mass located above metacentre. (d) centre of mass located off the centreplane.

buoyancy moves outward to lie vertically under G_1' (see Figure 5.3.3a). At this moment, the righting arm becomes zero. The angle of heel at which $G_1'Z_1' = 0$ corresponds to the angle ϕ_1 in Figure 5.3.4b. If the ship is heeled beyond ϕ_1, the righting arm becomes positive and provides a moment to return the ship to the position $G_1'Z_1' = 0$ (i.e at a heel angle of ϕ_1). The angle ϕ_1 is called the angle of loll, that is the angle at which a ship will lie at rest in still water (Derrett, 1990). Figure 5.3.4c shows a second possibility: the righting arm is negative for the entire range of ϕ. This means that the ship heels in the direction of the perturbation and will continue to heel until it capsizes.

Let us consider a third case in which the centre of mass is located at a position off the centreplane (see Figure 5.3.3b). In this case, the ship cannot rest in an upright position. Instead the ship heels towards the side where the centre of mass is located until the centre of buoyancy lies vertically under the centre of mass G_2 (see Figure 5.3.3b). The ship is stable at this particular angle of heel ϕ_2, since the metacentre M at this angle of heel lies above the centre of mass G_2 (see Figure 5.3.3b). A stability curve for such a case is shown in Figure 5.3.4d. Raising the centre of mass to the point G'_2 (see Figure 5.3.3b) above the metacentre will have the same effects as for the case when the ship's centre of mass is located along the centreplane. Thus the ship will either heel further towards the low side to another equilibrium position at a larger angle of heel, or heel continuously until it capsizes.

(c) Energetics of static stability

The work required to heel a ship to a certain angle can also be obtained from the stability curve. Consider the stability curve Figure 5.3.5a. The work, W_a, required to heel the ship from its upright position to a position with angle of heel ϕ_a can be calculated by (Moore, 1967):

$$W_a = \int_0^{\phi_a} (GZ)\, Wg\, d\phi \qquad (5.3.4)$$

where W is the displacement of the ship and g is the acceleration due to gravity. In order

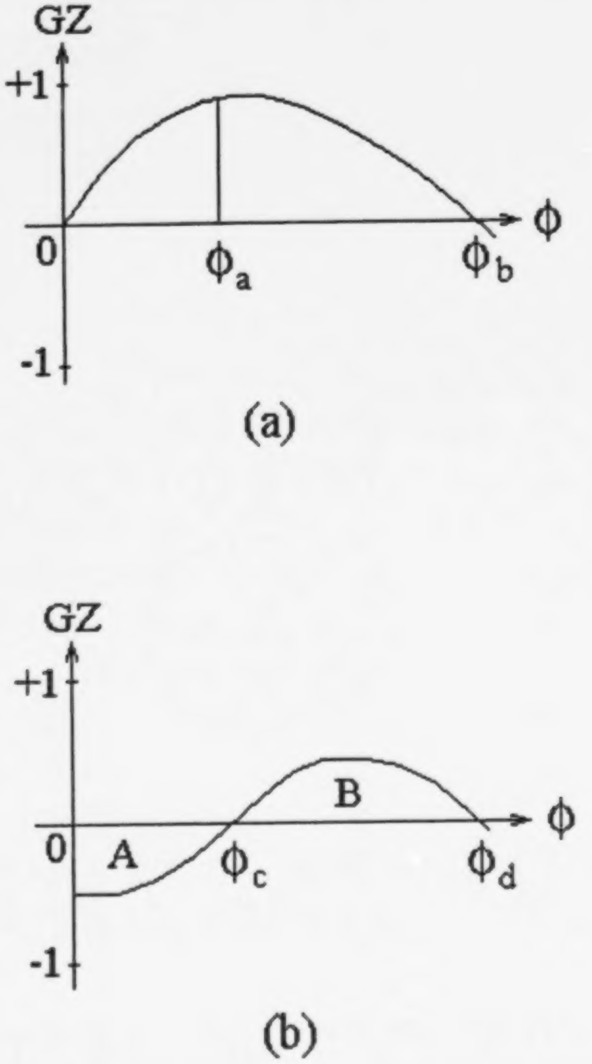

Figure 5.3.5: Relationship between stability curves and work required to heel a ship. The work is defined here as the area under the curve times the displacement of the ship (Wg).

to capsize the ship, it has to be heeled beyond the angle ϕ_b. Thus, the work required to capsize the ship is:

$$W_b = \int_0^{\phi_b} (GZ)\, Wg d\phi \tag{5.3.5}$$

Consider another case in which the stability curve is given in Figure 5.3.5b. According to Equation 5.3.5, the work, W_A, in Region A is negative which means that kinetic energy is created in heeling the ship from 0° to ϕ_c. The work, W_B, in Region B is positive which means that work is required to heel the ship from ϕ_c to ϕ_d. Neglecting water resistance, if $|W_A|$ is greater than $|W_B|$, then the kinetic energy which is derived from potential energy in Region A is large enough to overcome the restoring "buoyant energy" in Region B and cause the ship to capsize. If $|W_A|$ is less than $|W_B|$, the ship will not capsize but will eventually return to a heel angle of ϕ_c. For a small perturbation (e.g small waves), the ship simply rolls about the angle ϕ_c. If water resistance is included, $|W_A| - |W_R|$ must exceed $|W_B|$ in order to capsize the ship, where $|W_R|$ is the work done against water resistance.

On a normal ship, the angle ϕ_b in Figure 5.3.5a which signifies the range of positive stability is somewhat imprecisely defined because the stability curves are usually based on the assumption that the superstructure is not "effective" in terms of the stability (Moore, 1967). However, for very large angles of heel, water may be shipped through topside openings and consequently reduce the ship's stability. Thus, a ship may capsize before it reaches ϕ_b. For instance, the freeboard of the Zandberg in the present study is 5.02 m. The half beam is 5.75 m. Thus, when the angle of heel is greater than $\tan^{-1}(5.02/5.75) = 41°$, the deck will immerse in water and the ship may be in danger of capsizing.

(d) Trim

Trim may be defined as the longitudinal inclination of a ship caused by the addition, removal, and shifting of weights (Derrett, 1990). Consider a ship of length L floating at rest in still water on an even keel (see Figure 5.3.6a). The locations of the centre of mass G, centre of buoyancy B, and centre of flotation F are also indicated. Suppose a load with mass w on board is shifted forward over a distance x_d to a new position as shown in Figure 5.3.6b. Then, the centre of mass will shift forward as well to a new position G_1. The distance, GG_1, is equal to $(wx_d)/W$ (Derrett, 1990), where W is the displacement of the ship. A trimming moment $W(GG_1) = w(x_d)$ is thereby produced and the ship trims at the bow about the point F until the centre of buoyancy B_1 lies vertically under the point G_1 (see Figure 5.3.6b). Let the new draught measured at the forward and aft perpendiculars be t_{Ff} and t_{Af} respectively (see Figure 5.3.6b). Since the ship is initially on an even keel, the total change of trim, t, is $t_{Ff} - t_{Af}$, which may be calculated (in cm) from (Derrett, 1990):

$$t = \frac{trimming\ moment}{M.C.T.C} = \frac{wx_d}{M.C.T.C} \qquad (5.3.6)$$

The change of draught at the aft perpendicular is (Derrett, 1990):

$$\Delta t_{Af} = \frac{lt}{L} \qquad (5.3.7)$$

where l is the longitudinal distance between the aft perpendicular and the centre of flotation. Then, the change of draught at the forward perpendicular is simply $\Delta t_{Ff} = t - \Delta t_{Af}$. In Figure 5.3.6b, considering triangle W_1CL_1, the trim angle γ can readily be approximated by:

$$\gamma = \tan^{-1}\left(\frac{t}{L}\right) \qquad (5.3.8)$$

The centre of flotation F is the point through which the axis of rotation (yy) passes when a ship trims. Thus, a weight loaded at the point F does not produce trim. However, the ship's draught will increase uniformly. Now, if this load is shifted forward

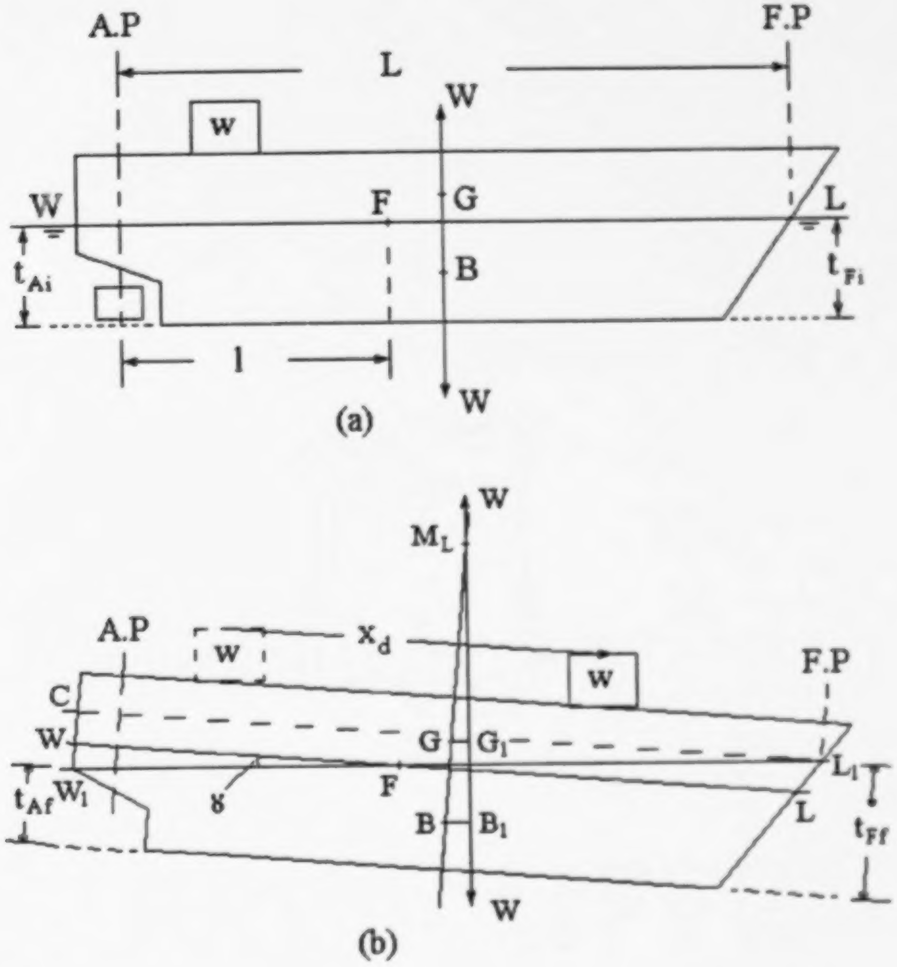
A.P
F.P
L
W
w
W
F
G
L
t_{Ai}
B
t_{Fi}
l
W
(a)
W
M_L
A.P
w
x_d
w
F.P
C
W
G
G_1
L_1
t_{Af}
W_1
γ
F
L
B
B_1
t_{Ff}
W
(b)

Figure 5.3.6: Schematic diagrams showing the trimming of a ship. (a) even keel (no trim). (b) trim. L is the length between F.P and A.P, l the distance between A.P and F, w the mass load, x_d the distance over which the mass load is shifted. t_{Fi} and t_{Ai} are respectively the draught at F.P and A.P when the ship is on even keel. t_{Ff} and t_{Af} are respectively the draught at F.P and A.P when the ship trims. γ is the angle of trim.

or aft, the ship will trim accordingly. This procedure, together with Equation 5.3.6, is applied to calculate the trimming of a ship when it is accreted with ice. Since under icing, the ice mass is distributed over the topside of the ship, it is convenient to treat the entire ice accretion as a single mass with its centre of mass located at (x', y', z') relative to O (see Figure 5.1).

For a given icing condition, the new centre of mass of the iced ship (x'_G, y'_G, z'_G) has been calculated from Equation 5.1.1. Thus, the centre of mass of the ice (x', y', z') relative to the point O can be calculated by:

$$x' = \frac{(M_{ship} + M_{Itot})\, x'_G}{M_{Itot}} \qquad (5.3.9)$$

$$y' = \frac{(M_{ship} + M_{Itot})\, y'_G}{M_{Itot}} \qquad (5.3.10)$$

$$z' = \frac{(M_{ship} + M_{Itot})\, z'_G - M_{ship} z_G}{M_{Itot}} \qquad (5.3.11)$$

Knowing (x', y', z'), we calculate the trim as follows. First we assume that the entire ice load acts at the centre of flotation, F. The ship's draught then increases uniformly. The new draught and M.C.T.C. can readily be obtained from Table 5.2.1. Then, the point at which the ice load acts is shifted from the point F to the point (x', y', z'). For those cases in which the ice load distribution is asymmetrical about the centreline, the ship will trim and list simultaneously. Usually, trim and list are treated separately and independently (Derrett, 1990). Therefore, the x_4 in Equation 5.3.6 is simply the longitudinal distance between the centre of flotation, F, and the centre of mass of the ice load. Since the longitudinal distance of F and the original centre of mass of the ship from the mid-ship section are known, x_4 can readily be calculated.

It should be mentioned here that the M.C.T.C. in Table 5.2.1 is based on the assumption that the ship is upright. Hence, when a ship lists, the values of M.C.T.C. in Table 5.2.1 is not entirely correct. However, unless there is an abrupt change in the under water shape of the hull, these values can still be considered as good approximations.

As mentioned in Section 5.3.3, Part b, the K'N values given in the Stability Information Booklet for the Zandberg are erroneous if the ship trims to an extent that its bow is immersed. For the present case, at a draught of 5.39 m, Zandberg has a freeboard of 5.02 m and a length (between F.P and A.P) of 45 m, the trim angle at which the bow becomes immersed is $\gamma_{im} \approx \tan^{-1}(10.04/45) = 12.6°$. For a deeper draught, the length at waterline of the ship increases and the freeboard decreases and so γ_{im} will be less than 12.6°.

A theoretical discussion of the potential effects of ice accretion on the ship's centre of mass, moments of inertia, hydrostatic particulars, static stability, trim, and list have been presented in this chapter. In Chapter 6, quantitative hydrostatic stability results for the stern trawler Zandberg under the icing conditions described in Chapter 4 will be presented and discussed. Using the ship dynamics model of Pawlowski and Bass (1991), some preliminary results on the dynamic performance of the Zandberg under icing conditions will also be presented and discussed.

CHAPTER 6 RESULTS AND DISCUSSION

6.1 Summary of the Icing Results

The icing model predicts severe icing on the Zandberg under the atmospheric and oceanographic conditions which the side trawler "Blue Mist II" encountered during the night of the tragedy (see Section 4.8, Part I for details). However, comparisons of the model results with the nomogram of Comisky et al. (1984), and with NOAA and Soviet icing data indicate that the present model still tends to underestimate the icing rate (see Section 4.8, Part II). Various factors which may cause this underestimation have been discussed, and it was concluded that the influence of the surface roughness on the Nusselt number could be the major cause. Increasing the Nusselt number for the deck, and the wheelhouse by 100 % to account for roughness effects brings the model's predictions into much better agreement with the observed data. Consequently, in the following analysis of the effect of icing on ship stability, the icing model is run for the conditions encountered by "Blue Mist II", but with a new Nusselt number which is twice the original one for the deck, and the wheelhouse.

Three sets of icing data have been generated for three different wind directions, $\theta = 0°$, $15°$, and $45°$. The details of the ice load distribution corresponding to each wind direction are similar to those discussed in Section 4.8, and thus will not be presented here. Table 6.1.1 gives the total ice load at different times for the three wind directions. The ratios of the total ice load to the displacement of the ship are also calculated. Figure 6.1.1 gives a summary for the one hour ice load distribution over the ship.

Using the above icing data, the changes in the centre of mass, moments of inertia, hydrostatic particulars, stability curves, trim, and list will be calculated using the

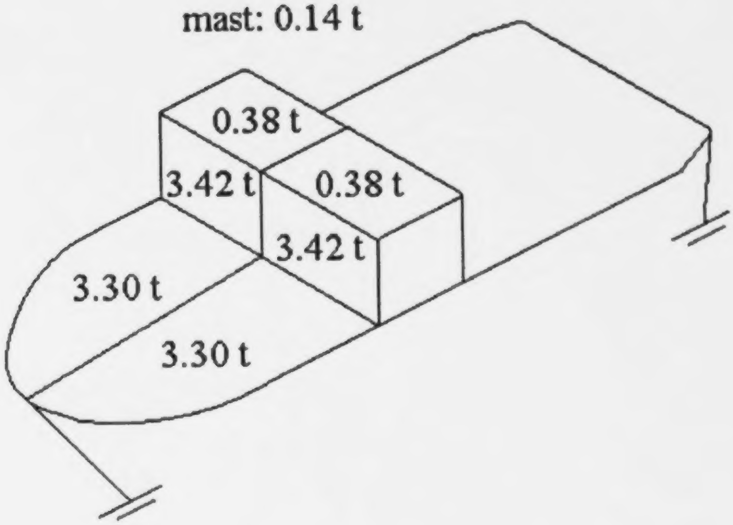
mast: 0.14 t
0.38 t
3.42 t
0.38 t
3.42 t
3.30 t
3.30 t

(a)

Figure 6.1.1: Final one hour ice load distribution for the stern trawler Zandberg under the conditions encountered by "Blue Mist II" for three different wind directions: (a) 0°, (b) 15°, and (c) 45°.

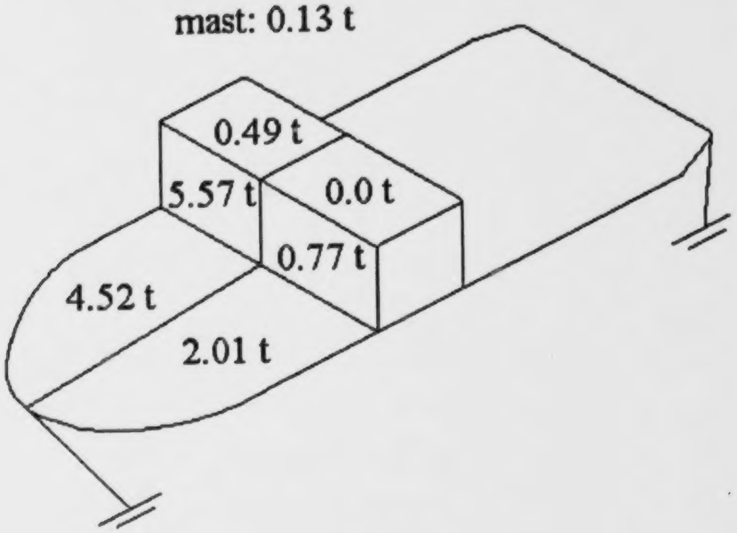
mast: 0.13 t
0.49 t
5.57 t
0.0 t
0.77 t
4.52 t
2.01 t

(b)

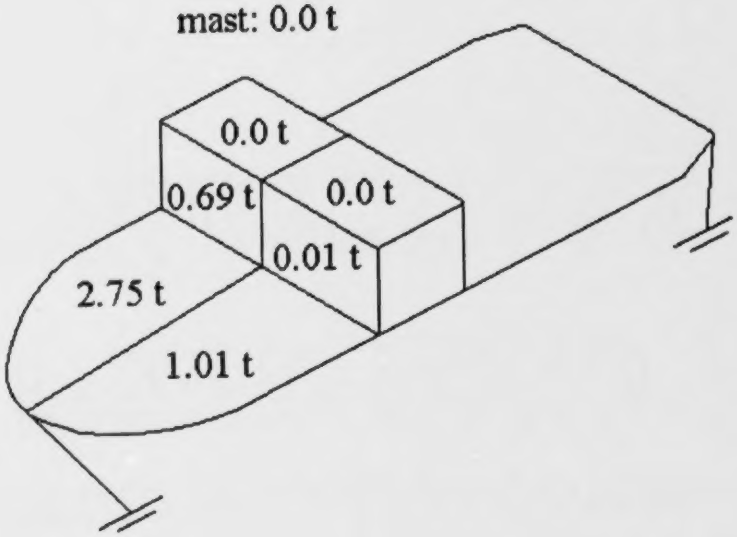
mast: 0.0 t
0.0 t
0.69 t
0.0 t
0.01 t
2.75 t
1.01 t

(c)

Wind Directions

	0°		15°		45°	
Time (hr)	ice load (t)	% of ship displ.	ice load (t)	% of ship displ.	ice load (t)	% of ship displ.
0	0.0	0.0	0.0	0.0	0.0	0.0
5	71.8	5.9	67.5	5.5	22.4	1.8
10	143.6	11.7	135.0	11.0	44.8	3.7
15	215.3	17.6	202.5	16.5	67.1	5.5
20	287.1	23.4	270.0	22.0	89.5	7.3

Table 6.1.1: Absolute and relative icing load as a function of time for the stern trawler Zandberg under the conditions encountered by "Blue Mist II" (refer to Section 4.8 where details of the conditions are given).

theories and equations discussed in Chapter 5. It should be noted that although the details of the ice load distribution are not presented here, they are used in the calculations.

6.2 Centre of Mass and Moments of Inertia

(a) Centre of mass

The initial coordinates of the centre of mass of the ship, relative to the system of reference (with origin O) shown in Figure 5.1, under loading condition no.4 (with a total displacement of 1224.7 tonnes) is (0, 0, 6.131 m). Using Equation 5.1.1, the new centre of mass of the ship under the loading conditions given in Table 6.1.1 have been calculated, and the results are presented in Table 6.2.1. In this table, the centre of mass at the end of each 5 hour interval is indicated. It can be seen that the shifting in the centre of mass is very closely associated with the ice load distribution (compare Figure 6.1.1 and Table 6.2.1).

For a wind direction of 0°, the ice load is symmetrical about the centreline (see

	Wind Directions		
	0°	15°	45°
Time (hrs)	Centre of mass (x, y, z) m	Centre of mass (x, y, z) m	Centre of mass (x, y, z) m
0	(0, 0, 6.131)	(0, 0, 6.131)	(0, 0, 6.131)
5	(0.905, 0.0, 6.433)	(0.867, 0.104, 6.412)	(0.365, 0.035, 6.215)
10	(1.751, 0.0, 6.712)	(1.682, 0.197, 6.674)	(0.718, 0.070, 6.301)
15	(2.545, 0.0, 6.972)	(2.453, 0.281, 6.919)	(1.059, 0.103, 6.386)
20	(3.297, 0.0, 7.214)	(3.186, 0.358, 7.149)	(1.389, 0.135, 6.472)

Table 6.2.1: The centre of mass of the Zandberg at various times under the three ice loading conditions given in Table 6.1.1 and illustrated in Figure 6.1.1.

Figure 6.1.1a). 46 % of the total ice load is accreted on the deck and 48 % on the front of the wheelhouse. Since the initial (uniced) centre of mass of the ship is located 28.591 m from the bow (i.e behind the wheelhouse) and 4.279 m below the deck, the above ice loading distribution causes the centre of mass to shift forward and upward. Over the 20 hour icing period, the centre of mass is shifted forward by 3.297 m (an average 0.165 m/hr) and upward by 1.083 m (an average 0.054 m/hr).

Non-head winds lead to asymmetrical ice loads. Figure 6.1.1b shows that, for a wind direction of 15° from port, much more ice is accreted on the starboard than on the port side of the ship. On the deck, 33 % of the total ice load is accreted on the starboard side and about 15 % on the port side. 41 % of the total ice accretion is found on the starboard side and only 6 % is found on the port side of the front of the wheelhouse. As a result of this uneven ice loading condition, after an icing period of 20 hours, the centre of mass has shifted to starboard by 0.358 m (an average 0.0179 m/hr), forward by 3.186 m (an average 0.159 m/hr), and upward by 1.018 m (an average 0.051 m/hr).

For a wind direction of 45°, much less ice is accreted compared with 0° and 15°. Consequently, the shift in the centre of mass is smaller. Over the 20 hour icing period, the centre of mass shifts toward starboard side by 0.135 m (an average 0.0068 m/hr), forward by 1.389 m (an average 0.069 m/hr), and upward by 0.341 m (an average 0.017 m/hr).

Although the total ice load with a wind direction of 15° is a little less than that for 0°, the beam wind case has a stronger effect on the ship's transverse stability. With a wind direction of 15°, the large ice loading and asymmetrical distribution cause the ship's centre of mass to move away from the centreplane. This can drastically reduce the ship's transverse stability and cause the ship to list. For a wind direction of 45°, the total ice load is much less, and hence its effect on the ship's stability is also much less compared with the previous two cases. A more detailed discussion of the effect of icing on ship's stability will be presented in Section 6.4.

(b) Moments of inertia

The initial (ice-free) moments of inertia of the Zandberg are not specified in the stability information booklet. Hence, as a first approximation, the radius of gyration about the longitudinal axis, xx, is taken to be 35 % of the beam (Pawlowski, personal communication). The radii of gyration about the transverse and vertical axes are taken to be the same and equal to 25 % of the length between the forward and aft perpendiculars (Pawlowski, personal communication). Using the formula $I = Mk^2$, where k is the radius of gyration and M the mass of the ship, the initial moments of inertia of the Zandberg are found to be 19840.9, 155001.1, and 155001.1 tonne-m about the axes xx, yy, and zz respectively.

Using the equations derived in Section 5.1b, the changes in the moments of inertia resulting from ice accretion can be calculated. For the ice loading conditions given in Table 6.1.1, the new moments of inertia about the axes xx', yy', and zz' are given in Table 6.2.2. It is apparent from Table 6.2.2 that ice accretion increases the ship's moments of inertia. For wind directions of 0° and 15°, the moments of inertia increase by about 50 % over the 20 hour icing period. For a wind direction of 45°, since the load is much less than that of the previous two cases, the moments of inertia increase by only about 20 % over the same interval.

6.3 Hydrostatic Particulars

When a ship accretes ice, it may trim and list simultaneously. To determine the hydrostatic particulars at various angles of trim and heel is beyond the scope of this thesis. However, in the present study, the objective is to calculate the stability curves, trim and list under icing conditions. Therefore in order to do this, we first assume that all the ice mass acts at the centre of flotation so that there is a uniform change in draught, and the ship remains in its upright and even keel position. Then, the hydrostatic particulars corresponding to each new draught can be determined. Once this has been done, the centre of mass of the entire ice accretion is shifted back to its original position. Finally, using the equations discussed in Section 5.3, the stability curves, trim, and list

	Wind Directions		
	0°	15°	45°
Time (hrs)	$(I'_{xx'}, I'_{yy'}, I'_{zz'})$ tonne-m	$(I'_{xx'}, I'_{yy'}, I'_{zz'})$ tonne-m	$(I'_{xx'}, I'_{yy'}, I'_{zz'})$ tonne-m
0	(19840.9, 155001.1, 155001.1)	(19840.9, 155001.1, 155001.1)	(19840.9, 155001.1, 155001.1)
5	(22351.2, 176441.1, 174594.9)	(22451.4, 175661.3, 174295.5)	(20566.0, 165007.4, 164724.1)
10	(24749.5, 197161.8, 193581.4)	(24951.8, 195756.0, 193084.4)	(21309.5, 174732.8, 174141.6)
15	(27056.4, 217394.9, 212171.7)	(27362.1, 215487.2, 211557.1)	(22072.3, 184193.1, 183269.1)
20	(29289.4, 237347.3, 230555.2)	(29699.2, 235039.1, 229886.7)	(22855.0, 193403.4, 192121.2)

Table 6.2.2: The moments of inertia of the ship after different icing periods under the three ice loading conditions described in Table 6.1.1 and Figure 6.1.1.

under the various ice loading conditions given in Table 6.1.1 and Figure 6.1.1 can be calculated. In all these calculations, the effect of wind forces on the ship hull and superstructure is not accounted for.

Table 6.3.1 gives the hydrostatic particulars for the three different icing cases corresponding to wind directions 0°, 15°, and 45° after five different icing periods. The tonnes per centimetre immersion (T.P.C) and the centre of buoyancy (B) are not included in the table because they will not be directly involved in the analysis of the ship's stability. Table 6.3.1 indicates that GM becomes negative (instability) for wind directions of 0° and 15° after 15 hours of icing. Because of the asymmetrical ice load distribution with a wind direction of 15°, the ship becomes unstable and capsize in less than 10 hours since the entire stability curve is negative at 10 hours (see Figure 6.4.1b). A more detailed discussion of the stability curves will be presented in Section 6.4a. The effect of icing on the other hydrostatic particulars are obvious (Table 6.3.1) and they will not be discussed here.

6.4 Stability Curves, Trim, and List

(a) Stability curves

Knowing the centre of mass and hydrostatic information under the three icing conditions for wind directions 0°, 15°, and 45°, the corresponding transverse stability curves can be calculated using the formulae presented in Section 5.3b. The results are shown in Figures 6.4.1a to 6.4.1c. Five stability curves are plotted for each case at time intervals of 5 hours.

For a wind direction of 0°, Figure 6.4.1a shows that the righting arm of the ship and the range of positive stability decreases rapidly with time as the mass of the ice accretion increases. This reduction in stability is closely related to the reduction in the metacentric height (see Table 6.3.1, Figure 5.3.1, and Equation 5.3.2). At 10 hours, the range of positive stability reduces to about 40°. This means that if the ship is heeled beyond that angle, it will capsize. Using Equation 5.3.5, the work energy under the GZ curves is +0.36 MJ. Under severe icing conditions, waves are unusually high and may

(a) $\theta = 0°$

Time (hrs)	ice load (t)	displ. (t)	draught (m)	KM (m)	KG (m)	GM (m)	L.C.F (m)	M.C.T.C (t-m)
0	0.0	1224.7	5.390	6.748	6.131	0.617	-3.442	13.817
5	71.8	1296.5	5.550	6.770	6.433	0.337	-3.488	14.280
10	143.6	1368.3	5.708	6.792	6.712	0.080	-3.472	14.659
15	215.3	1440.0	5.863	6.817	6.972	-0.155	-3.485	15.095
20	287.1	1511.8	6.018	6.842	7.214	-0.372	-3.496	15.527

Table 6.3.1: The hydrostatic particulars of the Zandberg after different icing periods under the three ice loading conditions given in Table 6.1.1. (a) a wind direction of 0°, (b) a wind direction of 15°, (c) a wind direction of 45°.

KM is the vertical distance between the keel (baseline) and the transverse metacentre.

KG is the vertical distance between the keel and the centre of mass.

GM is the metacentric height.

L.C.F is the longitudinal centre of flotation measured from mid-ship section.

M.C.T.C is the moment to change trim one centimetre.

(b) $\theta = 15°$

Time (hrs)	ice load (t)	displ. (t)	draught (m)	KM (m)	KG (m)	GM (m)	L.C.F (m)	M.C.T.C (t-m)
0	0.0	1224.7	5.390	6.748	6.131	0.617	-3.442	13.817
5	67.5	1292.2	5.541	6.769	6.412	0.357	-3.489	14.258
10	135.0	1359.7	5.689	6.789	6.674	0.115	-3.474	14.614
15	202.5	1427.2	5.836	6.812	6.919	-0.107	-3.481	15.014
20	270.0	1494.7	5.981	6.836	7.149	-0.313	-3.502	15.444

(c) $\theta = 45°$

Time (hrs)	ice load (t)	displ. (t)	draught (m)	KM (m)	KG (m)	GM (m)	L.C.F (m)	M.C.T.C (t-m)
0	0.0	1224.7	5.390	6.748	6.131	0.617	-3.442	13.817
5	22.4	1247.1	5.440	6.755	6.215	0.540	-3.465	13.973
10	44.8	1269.5	5.490	6.762	6.301	0.461	-3.489	14.130
15	67.1	1291.8	5.540	6.769	6.386	0.383	-3.489	14.256
20	89.5	1314.2	5.589	6.775	6.472	0.303	-3.484	14.374

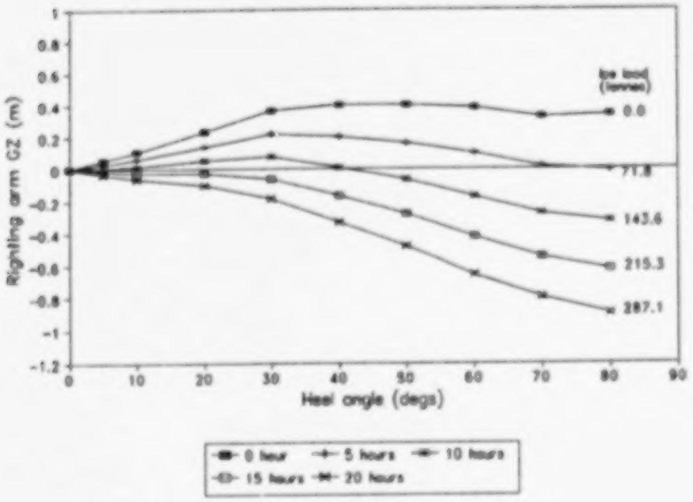

(a)

Figure 6.4.1: Stability curves for the Zandberg under the different ice loading conditions given in Table 6.1.1 for three different wind directions: a) 0°, b) 15°, and c) 45°.

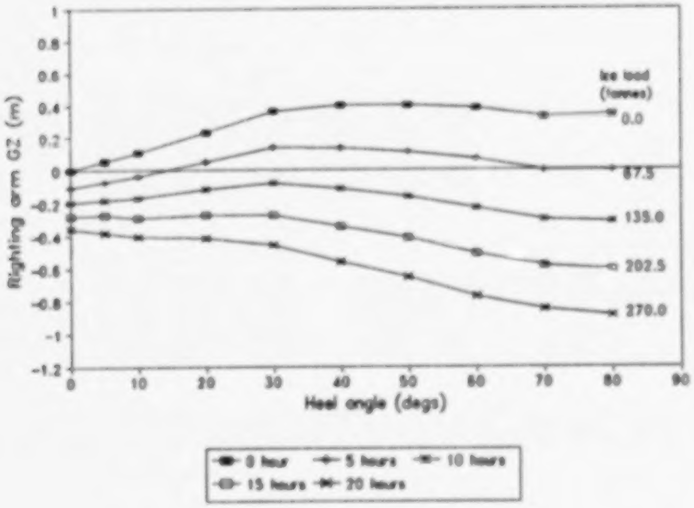

(b)

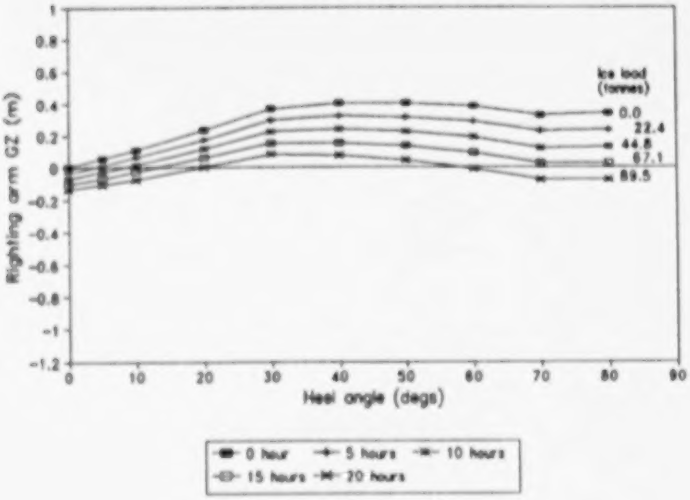
Righting arm GZ (m)
1
0.8
0.6
0.4
0.2
0
-0.2
-0.4
-0.6
-0.8
-1
-1.2
0
10
20
30
40
50
60
70
80
90
Heel angle (degs)
Ice load (tonnes)
0.0
22.4
44.8
67.1
89.5
0 hour
5 hours
10 hours
15 hours
20 hours

(c)

have enough energy to roll the ship beyond the angle at which positive stability vanishes, thereby causing the ship to capsize. At 15 hours, the entire stability curve is negative, corresponding to a negative initial metacentric height GM (see Table 6.3.1). Under this condition, the ship is considered as statically unstable and subject to capsize. As a result of the reduction in the righting arm due to ice accretion, the ship may experience a prolonged roll period before it actually reaches the moment of capsize. This prolonged roll period is a sign that the ship is losing stability.

With a wind direction of 15°, the asymmetrical ice load distribution has a drastic effect on the ship's transverse stability as shown in Figure 6.4.1b. The shifting of the centre of mass away from the centreplane due to heavier ice loading on one side causes the ship to list to 14.3° (at which point the righting arm is zero) at 5 hours. The ship possesses instability from 0° to 14.3°, stability from 14.3° to 69.4°, and instability after that. Using Equation 5.3.5, it is found that the work required is -0.18 MJ to heel from 0° to 14.3°, and +1.08 MJ to heel from 14.3° to 69.4°. As discussed in Section 5.3, the ship may be considered to capsize when its deck becomes immersed in water. For the draught of the ship at 5 hours (see Table 6.3.1), the deck immerses in water at a 40° angle of heel. The work required to heel from 14.3° to 40° is +0.54 MJ. Neglecting water resistance, if the waves impart an additional rolling energy of 0.36 MJ to the ship, it may capsize. Although Table 6.3.1 indicates that GM is still positive at 10 hours, the stability curves in Figure 6.4.1b show that the righting arm is negative for the entire range of angles of heel. This is the result of the asymmetrical ice load distribution which causes the centre of mass of the ship to shift away from the centreplane (see Equation 5.3.3 and Figure 5.3.2). Hence, the ship is in a statically unstable condition and will tend to capsize in less than 10 hours. As shown in Figure 6.4.1b, before the ship reaches the capsize moment, the listing angle increases continuously and the ship may also experience a prolonged roll period.

For a wind direction of 45°, the amount of ice accreted is much less than at 0° and 15° (see Table 6.1.1). Therefore, even though the ship experiences an asymmetrical ice loading condition, its stability does not vanish as rapidly as in the previous two cases. Figure 6.4.1c and Table 6.4.2 show how the righting arm decreases with time and the listing angle increases with time. It can be seen by inspection that, up to 15 hours, the rolling work (energy under the GZ curves) is positive. Therefore, the ship may be considered stable regardless of the effect of waves. However, at 20 hours, the ship is subject to capsize. As indicated in Figure 6.4.1c, the righting arm is negative from 0° to 19.9°, positive from 19.9° to 57°, and negative beyond that. Using Equation 5.3.5, the work to heel from 0° to 19.9° is -0.33 MJ, and from 19.9° to 57°, it is +0.43 MJ. The ship is considered to capsize at a heel angle of 40° when the deck becomes immersed in water. The heeling work from 19.9° to 40° is 0.27 MJ. Thus, the energy available to capsize the ship (0.33 MJ) exceeds the righting energy (0.27 MJ). Neglecting water resistance, the ship will roll from its upright position and accelerate toward the angle of heel at which the righting arm is zero. Beyond that angle, the rolling motion will encounter a righting buoyant force and thus decelerate. However, the ship will still roll to capsize before its roll energy diminishes to zero. Taking into account the effect of waves, the ship may capsize before 20 hours. Again, the signs before the ship capsizes are a prolonged roll period and increased listing angle.

(b) Trim

Using the method described in Section 5.3d, the trimming of the ship with ice accretion can be calculated. The results for the three icing cases are shown in Tables 6.4.1a to 6.4.1c. Icing with a wind direction of 0° causes the greatest trim. The reason is that this icing case produces the greatest accretion load and also the longest longitudinal shift of the centre of mass. The wind direction of 15° produces a slightly lesser ice load and so the trim is slightly less. With a wind direction of 45° the ice load is much less. As shown in Table 6.4.1c, the trim produced is much less than the previous two cases.

The effect of trim on ship manoeuvring can readily be seen by examining the draught of the ship at the forward and aft perpendiculars, t_F and t_A (see Table 6.4.1a). At 20 hours, with a wind direction of 0°, the draught at the forward and aft perpendiculars is 8.032 m and 4.581 m respectively. With this draught, the waterline is just 2.378 m below the deck at the forward perpendicular. At the stern, the bottom of

(a) $\theta = 0°$

Time (hrs)	Change in trim t (m)	Draught at F.P t_F (m)	Draught at A.P t_A (m)	Angle of Trim γ (°)
0	0.0	5.390	5.390	0.0
5	0.887	6.065	5.178	1.128
10	1.760	6.731	4.971	2.231
15	2.612	7.384	4.772	3.300
20	3.451	8.032	4.581	4.346

(b) $\theta = 15°$

Time (hrs)	Change in trim t (m)	Draught at F.P t_F (m)	Draught at A.P t_A (m)	Angle of Trim γ (°)
0	0.0	5.390	5.390	0.0
5	0.847	6.033	5.186	1.077
10	1.683	6.667	4.984	2.134
15	2.506	7.295	4.789	3.168
20	3.312	7.914	4.602	4.173

(c) $\theta = 45°$

Time (hrs)	Change in trim t (m)	Draught at F.P t_F (m)	Draught at A.P t_A (m)	Angle of Trim γ (°)
0	0.0	5.390	5.390	0.0
5	0.346	5.64	5.294	0.441
10	0.686	5.888	5.202	0.873
15	1.021	6.132	5.111	1.298
20	1.350	6.373	5.023	1.715

Table 6.4.1: The trimming conditions of the ship at different icing periods under the three ice loading conditions given in Table 6.1.1.

the hull appears above the waterline. The draught at the forward and aft perpendiculars with a wind direction of 15° is only slightly different from the case with a wind direction of 0°. The trim with a wind direction of 45° is much smaller compared with the previous two cases.

The trimming of the ship due to ice accretion can jeopardize navigation in various ways. The foredeck may more readily be flooded with greenwater from oncoming waves. Shipping of water over the foredeck can reduce the ship's stability. At the stern, the rudder and propeller may rise above the waterline. Under such a condition, the ship could at best move forward at very low speed in order to avoid the flooding of greenwater.

(c) List

The listing angle of the ship γ resulting from ice accretion can readily be obtained from the stability curves shown in Figure 6.4.1a to 6.4.1c. Table 6.4.2 gives the results for the three icing cases given in Table 6.1.1.

For a wind direction of 0°, the ice load distribution is symmetrical about the centreline. The ship does not appear to list in the first 10 hours. After this time, when the righting arm becomes negative for the entire range of angles of heel, the ship immediately lists to capsize.

The asymmetrical ice load distribution with a wind direction of 15° causes the ship to list after the first 5 hours. At 5 hours, the angle of list about which the ship rolls is 14.3°. After 5 hours, the righting arm continues to decrease, and it becomes negative for the entire range of angles of heel after 10 hours.

For a wind direction of 45°, the icing rate is much lower, and as a result, the listing angle increases with time at a much slower pace. Over the entire 20 hour icing period, the listing angle increases to 19.9°.

Listing of the ship can adversely affect its navigational safety. It can cause flooding of the deck and thereby reduce the ship's stability. If the ship turns in a direction opposite to the direction of list, the centrifugal force will further increase the angle of list.

	Wind direction		
	$\theta = 0°$	$\theta = 15°$	$\theta = 45°$
Time (hrs)	γ (°)	γ (°)	γ (°)
0	0.0	0.0	0.0
5	0.0	14.3	4.2
10	0.0	unstable	8.6
15	unstable	unstable	13.5
20	unstable	unstable	19.9

Table 6.4.2: The listing angle of the ship after different icing periods under the three ice loading conditions given in Table 6.1.1.

The analysis of the stability curves, trim, and list has provided an overview of the effect of ice accretion on the ship's static stability. Slightly off-head winds under severe icing conditions produce near maximum ice accretion rates, with a highly asymmetrical load distribution. This icing situation has the most severe effect on the ship's stability. A reduction in the magnitude of the righting arm, along with trimming and listing of the ship, can severely jeopardize the ship's manoeuvring and cause the ship to capsize. In the next section, the ship dynamics model of Pawlowski and Bass (1991) will be used to analyze the dynamic performance of the Zandberg under the icing conditions given in Table 6.1.1.

6.5 Implementation of the Ship Dynamics Analysis

The ship dynamics model of Pawlowski and Bass (1991) has been used to simulate ship motions for a given wave spectrum. Once the hull geometry is specified, the ship's motion depends principally on its centre of mass, moments of inertia, hydrostatic particulars, static stability, speed, and the wave spectrum, all of which are model inputs. One of the outputs of the model is a time series of heave, surge, sway, pitch, roll, and yaw. A complete discussion of the ship dynamics model can be found in Pawlowski and Bass (1991).

The ship dynamics model also requires input data which are fixed and do not change as a result of icing. Consequently, they will not be presented in detail here. A more complete description of the input data required for the ship dynamics model can be found in Dunphy (1993).

However, it is worthwhile mentioning the input data file "geom2.dat". This file requires the hull of the Zandberg to be digitized into geometric panel data. In order to do this, the original line drawings provided by the ship builders, Marystown Shipyard Ltd., Marystown, Newfoundland (see Figure 6.5.1) were used. The initial digitization was prepared at the University of Alberta. Checking and smoothing of the panel data was done at NRC/IMD by Dr. Jacek Pawlowski. Finally, a complete set of the panel data for the hull of the Zandberg was produced (see Figure 6.5.2). In the ship dynamics model, the hydrodynamic force on each panel is calculated so that the motions of the ship can be simulated.

A complete synchronization of the icing and dynamic simulations is not possible at present due to some fundamental problems regarding the limits of some of the input data for the ship dynamics model. For instance, when using a wave height greater than 4.5 m with a ship speed of 3 ms^{-1}, the motion of the Zandberg simulated by the dynamics model becomes unrealistically large. The explanation of this unrealistic behaviour may be due to resonance between the natural frequency of the ship and the frequency of the oncoming wave. By trial and error, it was found that the ship dynamics model behaves much more realistically when the wave height and ship speed are reduced to 4.5 m and 1 ms^{-1} respectively. Unfortunately, the trimming of the ship must be zero in the dynamics model (i.e even keel). This means that the trimming which results from the icing cannot be incorporated into the ship dynamics model. However, as will be discussed later, the effect of icing on pitch is reflected in the ship dynamics simulation. To relax the above limitations would require much further development of the ship dynamics model, a subject beyond the scope of this thesis.

Because of licensing and compiling difficulties, the ship dynamics model was run

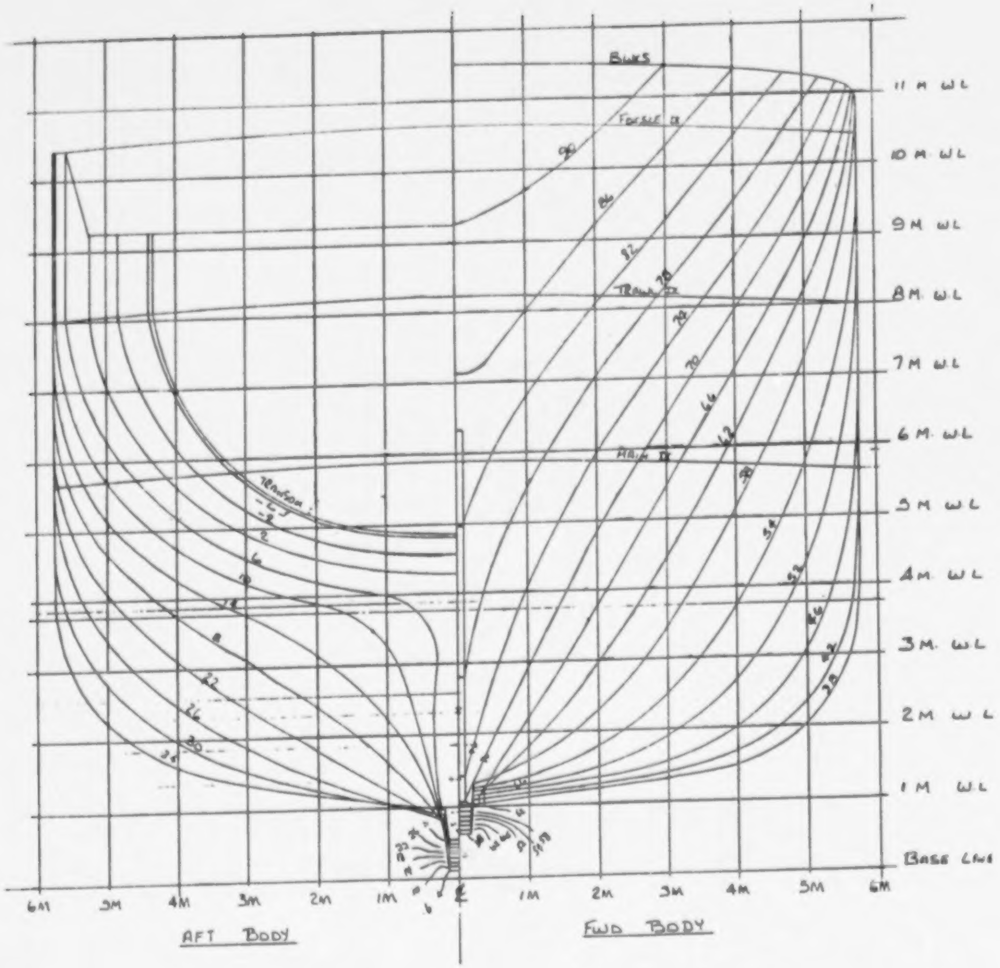
BWKS
FO'C'SLE
TRAWL
MAIN
TRANSOM
11 M WL
10 M WL
9 M WL
8 M WL
7 M WL
6 M WL
5 M WL
4 M WL
3 M WL
2 M WL
1 M WL
BASE LINE
6M
5M
4M
3M
2M
1M
℄
1M
2M
3M
4M
5M
6M
AFT BODY
FWD BODY

Figure 6.5.1: The original line drawings (reduced) for the stern trawler Zandberg (front view).

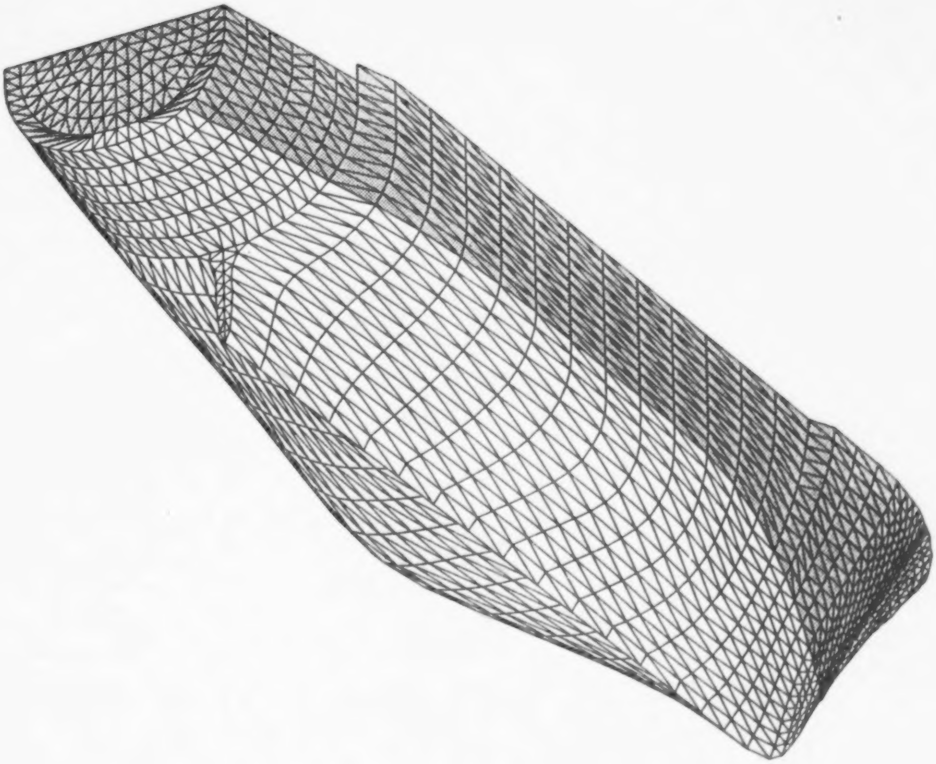

Figure 6.5.2: Digitization of the Zandberg's hull into panels.

by Dr. Jacek Pawlowski and Dr. Xu Qi at the Institute for Marine Dynamics. The results were then returned for analysis at the University of Alberta. Because of the above limitations, we decided to choose only one case to illustrate the effect of icing on ship dynamics. In Sections 6.2 to 6.4, it was shown that icing under the conditions encountered by the Blue Mist II, with a wind direction of 15°, has a strong effect on the static stability of the Zandberg (see Table 6.4.2). Consequently, we decided to use this icing condition as a case study to illustrate the effect of icing on the Zandberg's dynamic performance. An icing period of three hours was used. The total ice accumulation, centre of mass, moments of inertia, and various hydrostatic conditions after 3 hours of icing are shown in Table 6.5.1.

Time (hrs)	3.0
Ice Load (tonnes)	40.5
Displacement (tonnes)	1265.2
Centre of Mass (x, y, z) m	(0.527, 0.063, 6.302)
Moments of Inertia $(I'_{xx'}, I'_{yy'}, I'_{zz'})$ (tonne-m^2)	(21421.6, 167477.2, 166649.7)
Draught (m)	5.481
KM (m)	6.76
KG (m)	6.302
GM (m)	0.458
L.C.F (m)	-3.484
M.C.T.C (tonne-m)	14.1

Table 6.5.1: Icing load, centre of mass, moments of inertia, and various hydrostatic particulars of the Zandberg after 3 hours of ice accretion (definitions of symbols are referred to Table 6.3.1).

The static stability curves (GZ) corresponding to 0 hours (no ice) and 3 hours (with ice) are shown in Figure 6.5.3. It is apparent that after three hours of icing, the Zandberg still possesses a degree of static stability even though it has a list angle of 7.7°. In view of this, a three hour icing period is a good choice because it may permit the identification of dynamic instability even when the vessel is statically stable.

Two ship dynamics simulations were produced. The first was with no ice load (0 hours) and the second with the 3 hour ice loading condition. In order to be consistent with the icing model, the ship heading in the dynamics model is fixed at 180° (head seas). As mentioned earlier the ship dynamics model performs more realistically with a wave height of 4.5 m and a ship speed of 1 ms^{-1}. Consequently, we have used these values instead of the estimated values of 7.7 m wave height and 3 ms^{-1} ship speed. These two values were used in the icing model to produce the ice load. It is a reasonable and likely practice to reduce ship speed once a ship is heavily loaded with ice. However, reducing the wave height from 7.7 m to 4.5 m may result in an underestimation of the effect of icing on the Zandberg's dynamic stability. Thus the present results on the effect of icing on ship dynamics must be viewed as preliminary, requiring further verification.

6.6 The Effect of Icing on Ship Dynamics

Figure 6.6.1 shows a time series of the computed motions of the Zandberg, with an irregular wave spectrum of significant wave height 4.5 m (measured from peak to peak) and a ship speed 1 ms^{-1} at 0 hours (no ice). The time step of the simulation is 0.5164 seconds. Since the ship heading is 180°, and the waves are unidirectional, the ship performs only pitch, heave, and surge motions. The surge motion is simply the forward progression of the ship and is not shown in the figure. As shown in Figure 6.6.1, the heave amplitudes are generally less than ± 2.5 m. The pitch amplitude is basically within $\pm 10°$. According to the stability curve (Figure 6.5.3) and the ship motions (Figure 6.6.1) at 0 hour, Zandberg is statically and dynamically stable.

After 3 hours of ice accretion, under extreme conditions, the situation changes dramatically. Figure 6.5.3 shows that the ship, although still in a statically stable

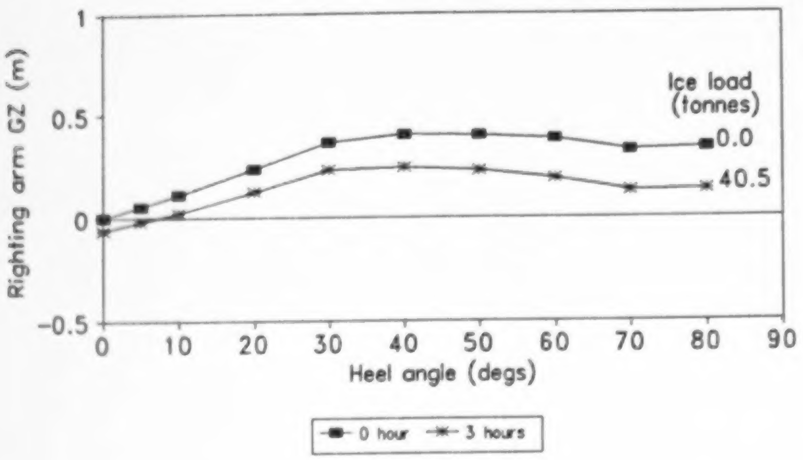

Figure 6.5.3: Stability curves (GZ) for the Zandberg at 0 hours (no ice) and 3 hours (with ice).

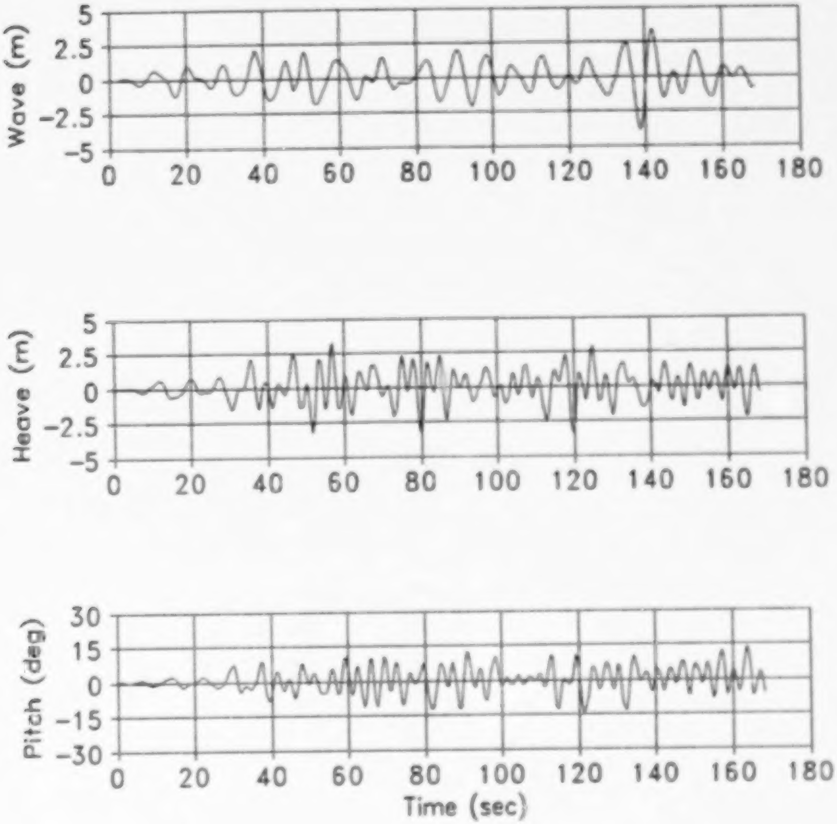

Figure 6.6.1: Time series of the computed motion of the Zandberg with a wave spectrum of significant wave height 4.5 m and a ship speed 1 ms^{-1} at 0 hours (no ice). The wave amplitude is measured relative to a calm water surface.

condition, has a reduced static stability. Figure 6.6.2 shows the ship motion at 3 hours with ice under the same wave spectrum (with exactly the same wave train) and ship speed. The listing of the ship (see Figure 6.6.2) as a result of asymmetrical ice loading (Table 6.5.1), combined with the action of the oncoming waves, induces asymmetrical ship motions. These motions are coupled with each other and they interact with the oncoming waves. The ship starts to roll with an amplitude ~ ±10° at ~ 30 seconds about its mean position (7.7° from vertical). At 140 seconds, the roll amplitude rapidly increases to about 30°. At about 168 seconds, the ship rolls to starboard, where heaviest ice load has accreted, and capsizes.

The time series of the sway motion shown in Figure 6.6.2 indicates that the ship drifts to port at an average speed of about 1.5 ms^{-1}. The cause of this lateral motion of the ship is not obvious. Only very small yaw motions are computed, as shown in Figure 6.6.2. This small yaw motion may be crucial in terms of the dynamic stability of the ship. Yaw motion, combined with the oncoming waves, can cause the ship to roll. The heave and pitch motions shown in Figure 6.6.2 are similar to those without ice (Figure 6.6.1). However, the statistical analysis of ship motions presented in the next section indicates that the pitch motion of the ship with ice loading is in fact different from that without ice loading.

6.7 Statistical Analysis of the Computed Ship Motion

(a) Distributions of the extrema.

The time series of the heave, pitch, and roll motions shown in Figures 6.6.1 and 6.6.2 will now be analyzed using statistical techniques. These time series indicate that ship/wave interaction is fully developed after ~ 30 seconds. Therefore, only those data from 30.4692 seconds to 168.3552 seconds are considered. Analysis of the sway and yaw motions will not be undertaken because the former is not harmonic while the latter is rather small (Figure 6.6.2).

In this part of the study we will examine the occasions in which the motion reverses. We shall refer to all the local peaks as the negative second derivative events

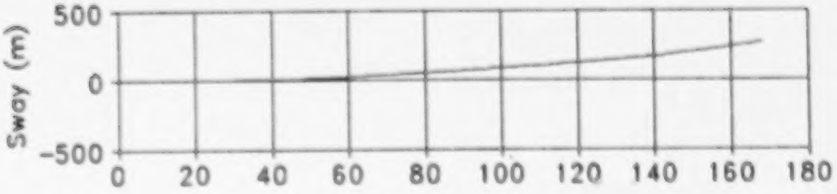

Figure 6.6.2: Time series of the computed motion of the Zandberg with a wave spectrum of significant wave height 4.5 m and a ship speed 1 ms^{-1} at 3 hours (40.5 tonnes ice). The wave train is exactly the same as that in the previous figure. The actual angle of list of the Zandberg is 7.7°. The roll is taken to be positive to the port and negative to the starboard.

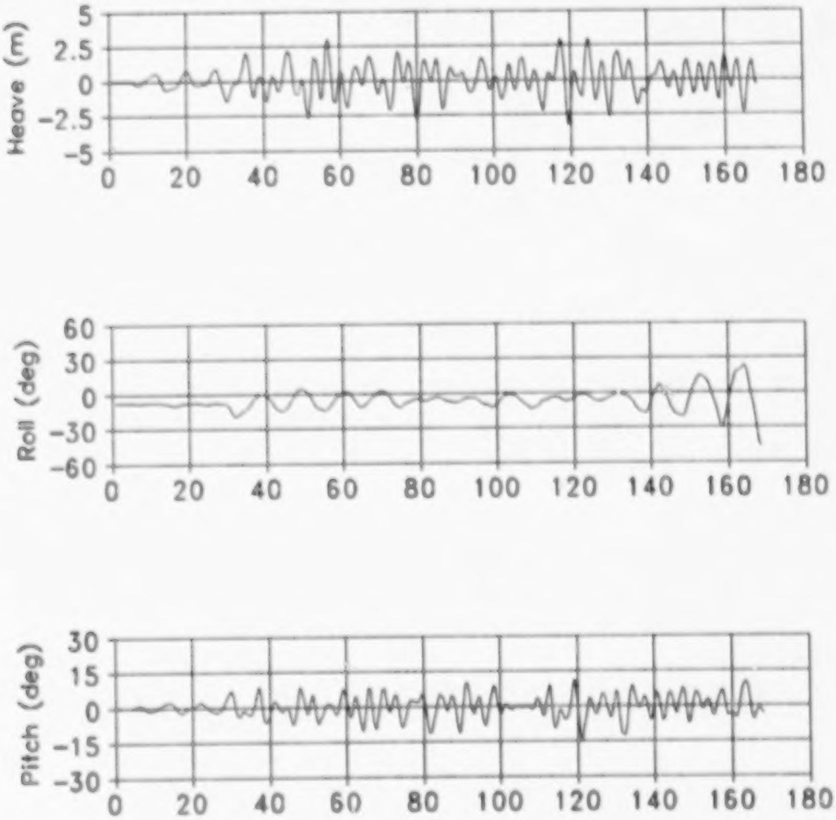

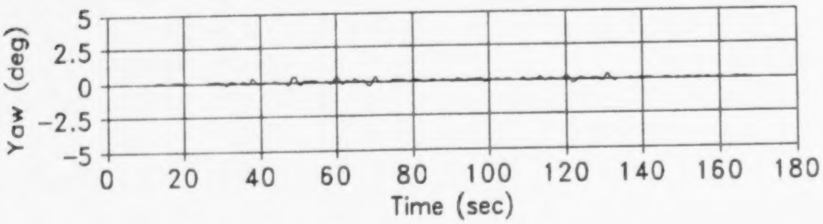
Yaw (deg)
5
2.5
0
-2.5
-5
0
20
40
60
80
100
120
140
160
180
Time (sec)

(-D" peaks) and the positive second derivative events (+D" peaks) (see Figure 6.7.1). It is obvious, from a casual examination of Figures 6.6.1 and 6.6.2, that most of the -D" peaks lie above the axis (i.e the reference line dividing the positive and negative direction of the harmonic motion) and the +D" peaks tend to lie below it.

For heave motions, these extrema are grouped in 0.5 m bins from 0 to ±3.5 m. Figures 6.7.2a and 6.7.2b show the resulting histograms without ice on the ship, while Figures 6.7.2c and 6.7.2d show the histograms with ice. Without ice (Figure 6.7.2a), the -D" peaks are distributed from 0 to 2.5 m with frequencies of occurrence ranging from 7.6 % to 11.4 % (this is of the total number of peaks, i.e -D" peaks plus +D" peaks). Only 2.5 % of the heave peaks have an amplitude exceeding 2.5 m. The -D" peaks which lie below the horizontal axis account for only 1.3 % of the total number of peaks. The distribution of the +D" peaks has a maximum at -1.25 m. The +D" peaks which lie above the horizontal axis account for only 2.5 % of the total number of peaks. Approximately 51 % of the peaks lie above the horizontal axis and 49 % below it.

With ice on the ship, the -D" heave peak has a distribution peak at 1.25 m. 1.2 % of the -D" peaks lie below the horizontal axis. For the +D" peak, the distribution has two maxima with same magnitude. These two maxima occur at -0.75 m and -1.25 m respectively. 3.7 % of the +D" peaks lie above the horizontal axis. The more pronounced (well defined) distribution found in Figures 6.7.2c and 6.7.2d is probably due to the effect of icing in increasing the inertia of the ship, and thereby reducing the heave amplitude. Approximately 52 % of the peaks lie above the horizontal axis and 48 % below it.

Figures 6.7.3a to 6.7.3d show histograms of the pitch angle distribution for cases with and without ice. The pitch extrema are grouped in increments of 2° from 0° to ±16°. Without ice (Figure 6.7.3a), the -D" pitch peaks range from 0° to 14°, with a maximum in the distribution at 7°. The majority of the -D" pitch peaks lie below 8°. Only 1.2 % of the -D" peaks lie below the horizontal axis. The +D" pitch peaks have a distribution with a maximum at -5° (Figure 6.7.3b). Most of the +D" pitch peaks are less than 6°. No +D" pitch peaks lie above the horizontal axis. About 48 % of the peaks lie above the horizontal axis and 52 % below it.

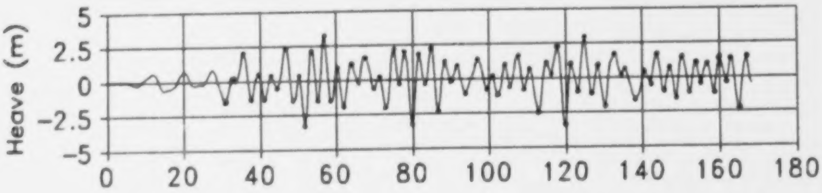

Figure 6.7.1: Local peaks of a time series of ship motion (heave for example). peaks are denoted by black dots. Peaks of local maxima are refered to negative second derivative events (-D" peaks) and peaks of local minima are refered to positive second derivative events (+D" peaks).

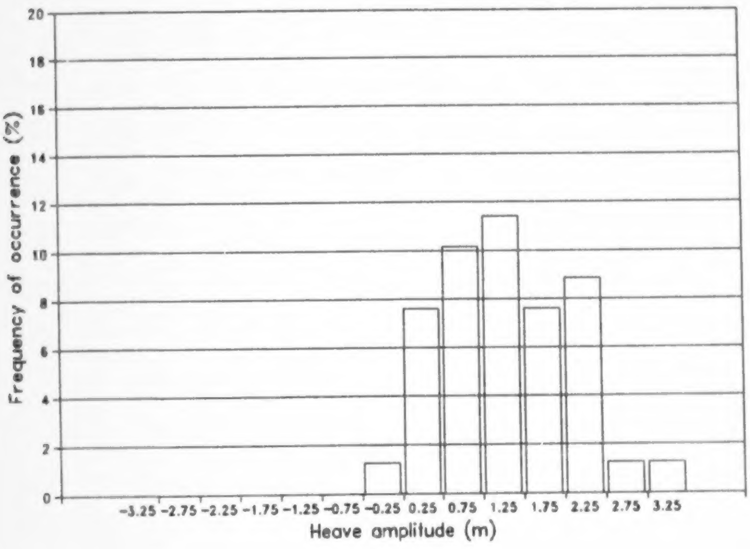

(a)

Figure 6.7.2: Histograms of heave extrema (measured with respect to mean position) without ice: a) -D" peaks, b) +D" peaks; and with ice: c) -D" peaks, d) +D" peaks. On the x-axis, the heave amplitude is referred to the middle of the bin. The number of -D" peaks plus the number of +D" peaks constitutes the total number of peaks.

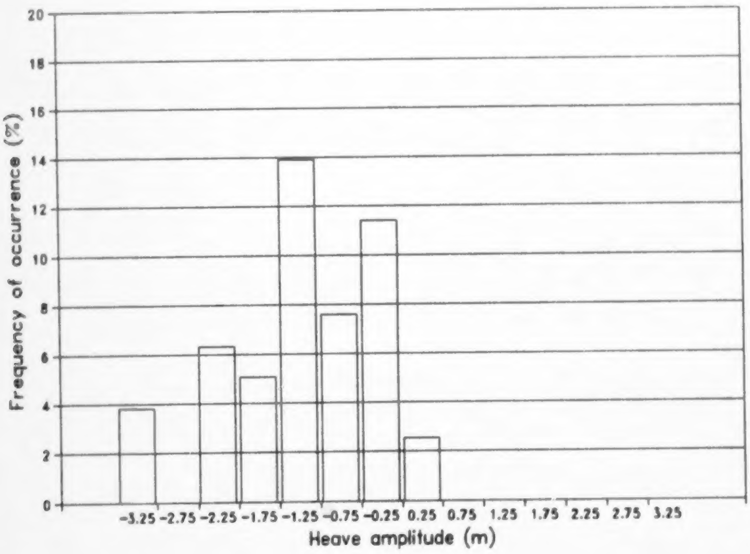

(b)

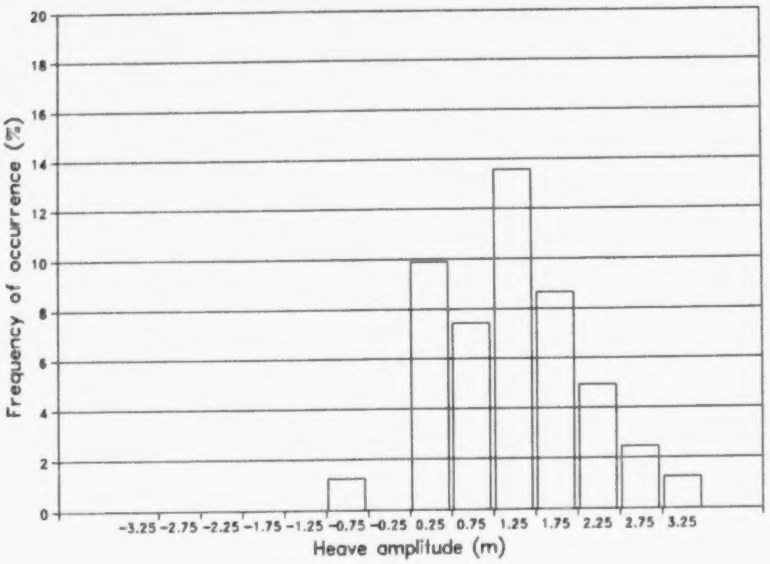
Frequency of occurrence (%)
0
2
4
6
8
10
12
14
16
18
20
-3.25
-2.75
-2.25
-1.75
-1.25
-0.75
-0.25
0.25
0.75
1.25
1.75
2.25
2.75
3.25
Heave amplitude (m)

(c)

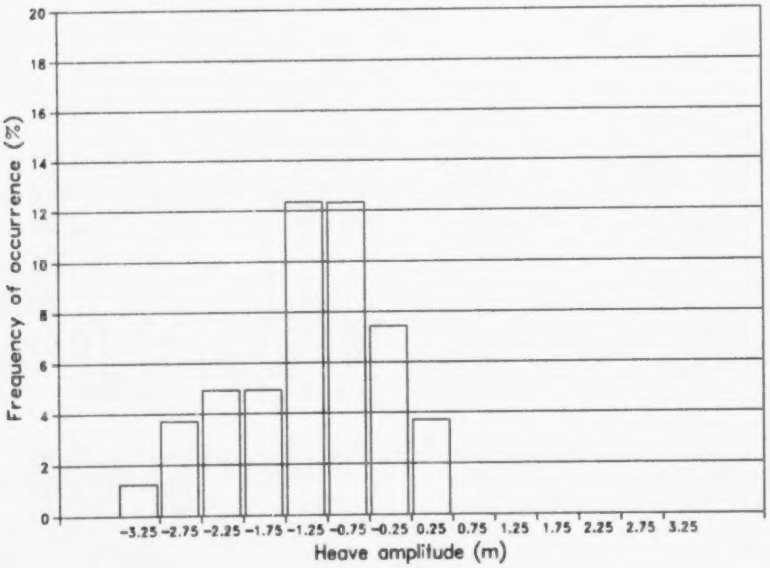
Frequency of occurrence (%)
0
2
4
6
8
10
12
14
16
18
20
-3.25
-2.75
-2.25
-1.75
-1.25
-0.75
-0.25
0.25
0.75
1.25
1.75
2.25
2.75
3.25
Heave amplitude (m)

(d)

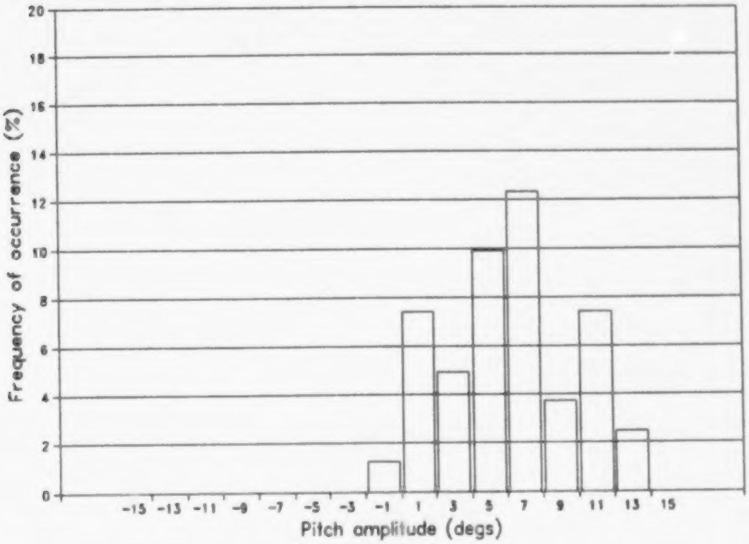

(a)

Figure 6.7.3: Histograms of pitch extrema (measured with respect to mean position) without ice: a) -D" peaks, b) +D" peaks; and with ice: c) -D" peaks, d) +D" peaks. On the x-axis, the pitch amplitude is referred to the middle of the bin. The number of -D" peaks plus the number of +D" peaks constitutes the total number of peaks.

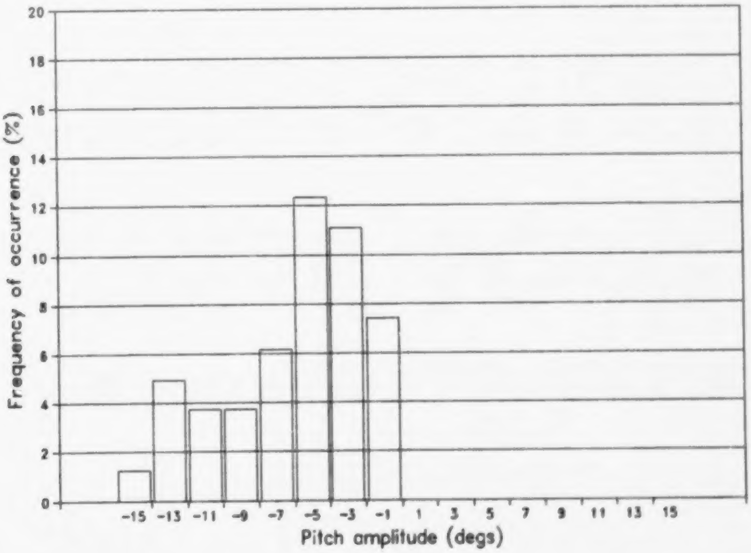

(b)

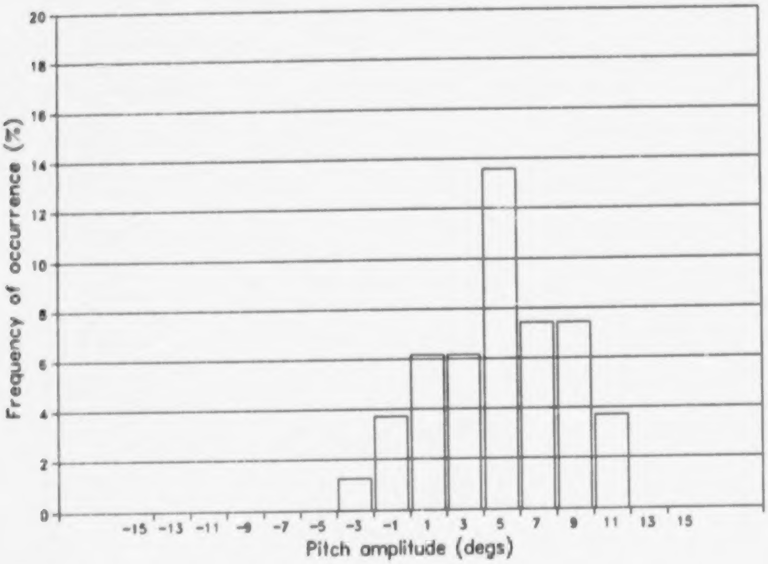
Frequency of occurrence (%)
20
18
16
14
12
10
8
6
4
2
0
-15
-13
-11
-9
-7
-5
-3
-1
1
3
5
7
9
11
13
15
Pitch amplitude (degs)

(c)

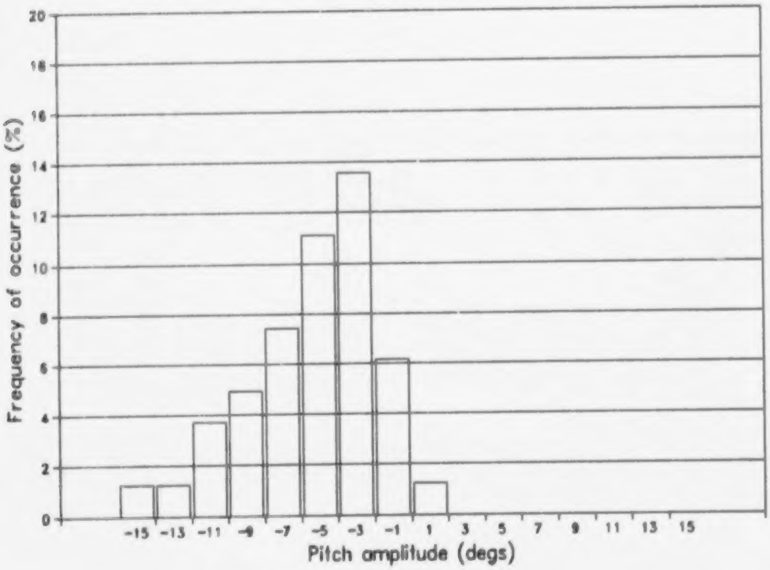
Frequency of occurrence (%)
20
18
16
14
12
10
8
6
4
2
0
-15
-13
-11
-9
-7
-5
-3
-1
1
3
5
7
9
11
13
15
Pitch amplitude (degs)

(d)

With ice, the -D" pitch peaks have a more pronounced (well defined) distribution (Figure 6.7.3c). The maximum occurs at 5°. This is less than the case without ice (~ 7°). The pitch peak range is also reduced from 14° to 12°. This decrease in the pitch range is likely a result of the ice load increasing the moments of inertia of the ship. About 5 % of the -D" pitch peaks lie below the horizontal axis. The +D" pitch peaks have a distribution with the maximum occurs at near -3° (Figure 6.7.3d). This range is less than that for the case without ice which is 5° (see Figures 6.7.3b and 6.7.3d). Again, this is likely because of higher ship moments of inertia as a result of icing. The greater inertia of the ship as a result of icing may also explain why the -D" pitch peaks and +D" pitch peaks have more pronounced (well defined) distributions for the case with ice on ship (Figures 6.7.3c and 6.7.3d). Only about 1.2 % of the +D" pitch peaks lie above the horizontal axis. 46 % of the pitch peaks lie above the horizontal axis and 54 % below it.

For roll, the peaks have been grouped in 5° bins from 0° to 40°. The roll is measured relative to the listing angle of the ship (0° without ice and 7.7° with ice). As discussed in Section 6.6, there is no roll in the simulation without ice. Figures 6.7.4a and 6.7.4b show the distribution of the roll peaks with ice. Most of the roll peaks (both +D" and -D" peaks) lie within the range ±15°. A small fraction (~ 13.8 %) lie outside this range. Nevertheless, it is this small fraction of large roll amplitudes which lead to the ship's capsize (see Figure 6.6.2). As shown in Figure 6.7.4b, the fraction of +D" roll peaks lie above the horizontal line, which denotes the angle of list (7.7°), accounts for 10.3 % of the total number of peaks. About 59 % of the roll peaks are to port while 41 % are to starboard.

(b) Ship motion statistics

Another way to evaluate the effect of ice accretion on ship motion is to calculate statistics. To do this, the entire time series of heave, pitch, and roll sampled every 0.5164 seconds has been used to determine distribution functions. Their statistics have then been calculated and compared. For each parameter, there are 268 data points which fall within the time range (30.4692, 168.3552) seconds. Tables 6.7.1 to 6.7.3 give the

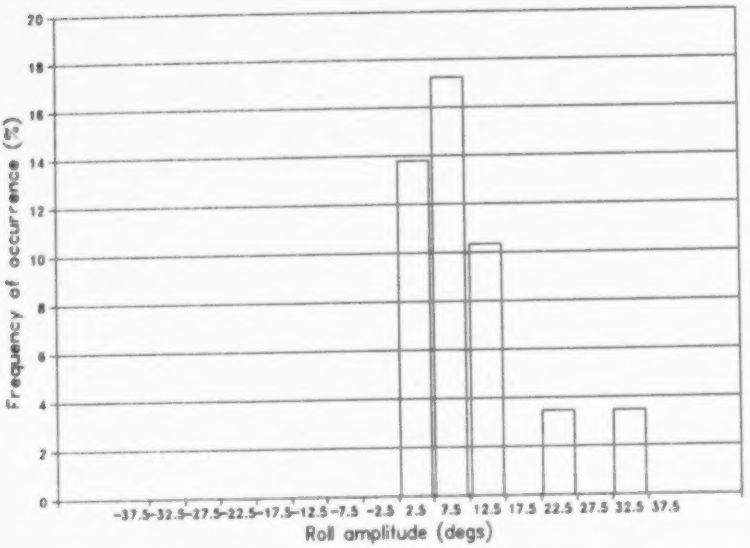

(a)

Figure 6.7.4: Histograms of roll extrema (measured with respect to mean position) with ice: a) -D" peaks, b) +D" peaks. On the x-axis, the roll amplitude is referred to the middle of the bin. The number of -D" peaks plus the number +D" peaks constitutes the total number of peaks.

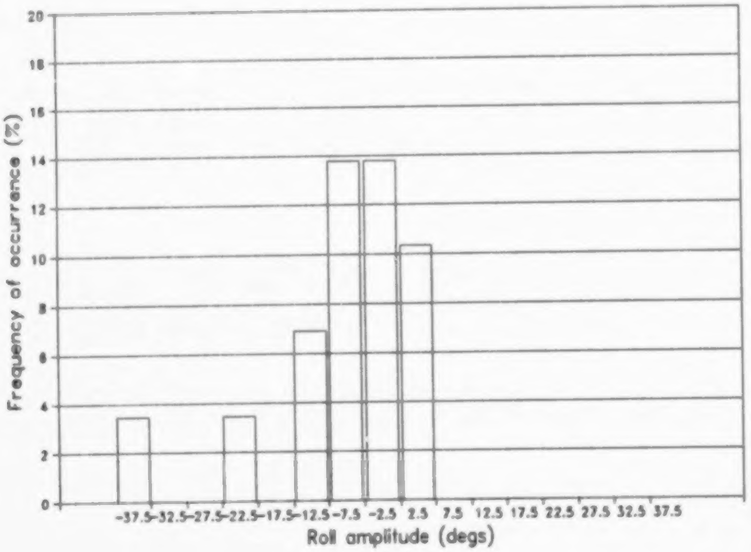

(b)

various statistics for heave, pitch, and roll both with and without ice.

	Heave (m) (no ice)	Heave (m) (with ice)
No. of data points	268	268
Minimum amplitude	-3.378	-3.356
Maximum amplitude	3.303	3.033
Range	6.682	6.389
Mean	0.048	0.032
Standard deviation	1.199	1.176
Skewness	-0.205	-0.070

Table 6.7.1: Heave statistics with and without ice based on the model-simulated data shown in Figures 6.6.1 and 6.6.2.

	Pitch (°) (no ice)	Pitch (°) (with ice)
No. of data points	268	268
Minimum amplitude	-14.356	-14.066
Maximum amplitude	13.682	10.991
Range	28.038	25.057
Mean	0.088	-0.288
Standard deviation	5.576	4.844
Skewness	-0.143	-0.138

Table 6.7.2: Pitch statistics with and without ice based on the model-simulated data shown in Figure 6.6.1 and 6.6.2.

	Roll (°) (no ice)	Roll (°) (with ice)
No. of data points	268	268
Minimum amplitude	0.0	-38.835
Maximum amplitude	0.0	30.35
Range	0.0	69.185
Mean	0.0	1.636
Standard deviation	0.0	8.866
Skewness	0.0	-0.187

Table 6.7.3: Roll statistics with ice based on the model-simulated data shown in Figure 6.6.2.

It is apparent from Table 6.7.1 that the amplitude of the heave motion with ice is slightly less than without ice. The maximum heave amplitudes with ice is 8.2 % less than that without ice. This reduction in the maximum heave amplitude is a result of the effect of the ice load in reducing the ship's upward motion. There is not much change in the minimum heave amplitude however. The reason may be that it is easier for a ship to move downward than upward regardless of the ice load whenever the ship encounters a wave trough, due to the effect of gravity. The heave range is 4.4 % less with ice than without ice. The mean vertical position of the ship over the entire time series is 0.032 m above the calm water level for the case with ice. This is 0.016 m lower than without ice. The standard deviation of the heave motion with ice on ship is 1.9 % less than that without ice on ship. Also indicated in Table 6.7.1 is that the skewness of the heave with ice is 65.9 % less than that without ice. This implies that the heave motion is more symmetrical with ice. Negative skewness means that the distribution skews to the right (i.e to the positive side).

Table 6.7.2 shows the pitch statistics. The maximum pitch angle with ice is 19.7 % less than that without ice. This reduction in the maximum pitch angle may be a direct result of the ice load. The range of the pitch with ice is 10.6 % less than that without ice. As mentioned in Section 6.4b, the ice load on the Zandberg shifts its centre of mass forward and causes the ship to trim by the head. This explains why the ship has a negative mean pitch angle for the case with ice (see Table 6.7.2). There is a large difference in the standard deviation of the pitch between the cases with and without ice on ship. With ice on the ship, the standard deviation of the pitch is 13 % less than without ice. The skewness of the pitch with ice is 3.5 % less than that without ice. This means that the pitch is more symmetrical for the case with ice.

Because of the symmetry of the wave field, there is no roll motion for the case without ice. Consequently, we cannot make an ice/no ice comparison for roll. Table 6.7.3 gives the roll statistics under the condition with the ice load. The mean is specified relative to the equilibrium position of the ship on calm water (see Table 6.7.3). With ice, the ship lists to starboard by 7.7°. Thus the mean angle of roll is $-7.7° + 1.636° = -6.1°$ from vertical (see Figures 6.6.1 and 6.6.2).

In summary, the differences found between the cases with and without ice for pitch are greater than for heave. This suggests that ice on the ship has a greater effect on the pitch motion than on the heave motion. Because of the nature of the numerical simulations, we have no basis for comparing roll motion with and without ice.

(c) Wilcoxon Signed-Rank Test

To show whether ice on ship has a noticeable effect on the heave and pitch motions, the Wilcoxon Signed-Rank Test (Freund and Walpole, 1980) is applied to the heave and pitch data. The purpose of this test is to determine whether two samples of data of equal size, regardless of their distribution, are drawn from the same population. The methodology of the Wilcoxon Signed-Rank Test is referred to Freund and Walpole, 1980.

The Wilcoxon signed-rank test has been applied to the heave data samples with and without ice. It was found that $Z = -0.736$. Using a one-tail test with the level of significance $\alpha = 0.05$ (5 %), the value of Z_α is -1.645. Since $|Z| < |Z_\alpha|$, one cannot reject the null hypothesis (i.e the heave data with and without ice are drawn from the same distribution) at the 5 % confidence level. This test result is consistent with the previous statistical results obtained in Section 6.7b.

For pitch motion, the Wilcoxon signed-rank test gives $Z = -2.396$, while Z_α is again -1.645. Thus, $|Z|$ is greater than $|Z_\alpha|$, implying that the pitch motion in this case with and without ice come from different distributions. This is in keeping with the statistics for pitch motion described in Section 6.7b which indicate a large difference between the two samples.

Based on the Wilcoxon signed-ranks test, it can be concluded that the effect of severe icing on the ship's heave motion is not obvious, but it is apparent in the pitch motion.

6.8 Spectral Analysis of the Ship Motion

The ship's heave, pitch, and roll are oscillatory motions, determined by the interaction of the oncoming wave spectrum and the natural frequencies of the ship. The wave spectrum is a superposition of many wave components with different frequencies. Thus, a given type of ship motion (e.g pitch) should consist of components of different frequencies. In this section, a spectral analysis of the ship motions with and without ice will be performed. In doing so, the relations between the cyclic ship motions, the oncoming wave spectrum and the natural frequencies of the ship will be revealed.

A discrete Fourier transform has been applied to the time series of wave amplitude, heave, pitch, and roll in order to obtain their respective power spectra. For a discrete time series of cyclic data h_k, a discrete Fourier transform can be used to express the series in the frequency domain $H(f_n)$ (Press et al., 1992). If the time series has a total of N data points, then:

$$H(f_n) = \sum_{k=0}^{N-1} h_k e^{2\pi i f_n t_k} \Delta t \qquad (6.8.1)$$

where

Δt: data sampling interval (s).

t_k: $k\Delta t$ (s).

f_n: the fourier frequency (Hz) which is defined by $n/(N\Delta t)$, and n is an integer ranging from 0 to N/2 - 1.

Substituting $t_k = k\Delta t$, Equation 6.8.1 can be rewritten as:

$$H(f_n) = \Delta t \sum_{k=0}^{N-1} h_k e^{\frac{2\pi i k n}{N}} \qquad (6.8.2)$$

Expanding the complex exponential function in terms of sines and cosines:

$$H(f_n) = \Delta t \left[\sum_{k=0}^{N-1} h_k \cos\left(\frac{2\pi k n}{N}\right) + i \sum_{k=0}^{N-1} h_k \sin\left(\frac{2\pi k n}{N}\right)\right] \qquad (6.8.3)$$

The power of the series is defined as (Press et al., 1992):

$$P(f_n) = H(f_n) H^*(f_n) \qquad (6.8.4)$$

where $H^*(f_n)$ is the complex conjugate of $H(f_n)$. Finally, using Equations 6.8.3 and 6.8.4, the one-sided normalized power spectrum, P_N, of the time series may be computed as:

$$P_N(f_n) = \frac{2\Delta t}{N} \left[\left(\sum_{k=0}^{N-1} h_k \cos\left(\frac{2\pi k n}{N}\right)\right)^2 + \left(\sum_{k=0}^{N-1} h_k \sin\left(\frac{2\pi k n}{N}\right)\right)^2\right] \qquad (6.8.5)$$

The factor two in the above equation is necessary for a one-sided power spectrum in order to obtain the correct total power (Press et al., 1992). The power spectrum deduced using Equation 6.8.5 has been tested using a subroutine provided by Press et al. (1992). This subroutine makes use of the Fast Fourier Transform which requires the number of data points to be an integer power of 2. In order to use this subroutine, the time series of wave and ship motions are reduced in size from the original range (30.4692, 168.3552) seconds to (36.6663, 168.3552) seconds, giving a total of 256 data points in each time series. It is expected that this truncation should not result in noticeable errors because the ship/wave interaction needs at least 30 seconds to fully develop (see Figures 6.6.1 and 6.6.2). It was found that the power spectra calculated from Equation 6.8.5 and those calculated using Press et al. (1992) are essentially the same, allowing for the fact that the latter applies a windowing function to the data and hence smoothing to the power spectra. Consequently, we will present here only the results obtained from Equation 6.8.5. This equation has been coded in Fortran 77 and the program is listed in Appendix 4.

(a) Normalized power spectrum of the modelled wave train

The power spectrum of the wave train is shown in Figure 6.8.1. It can be seen that the wave spectrum contains continuous wave components of frequencies ranging from around 0.05 Hz (period 20 s) to 0.25 Hz (period 4 s).

(b) Normalized power spectrum of heave

The power spectra of the heave motions for the cases with and without ice are shown in Figures 6.8.2a and 6.8.2b. These two power spectra are very similar, except for minor differences. The strong peak at $f_n = 0.1135$ Hz and the subsequent smaller peaks with frequency up to 0.2 Hz are clearly a reflection of the wave spectrum (see Figure 6.8.1). A very strong peak appears at $f_n = 0.2799$ Hz. This is the natural frequency of the heave motion under calm water conditions. Assuming that heave in calm water is a simple harmonic motion, and neglecting the effect of added mass and damping, the natural frequency of heave can be approximated by the formula $(1/2\pi)(\rho gA/m)^{1/2}$ (Newmann, 1977), where ρ is the density of sea water, A the waterplane area at a given draught, and m the mass of the ship. Using this formula, the natural frequencies of

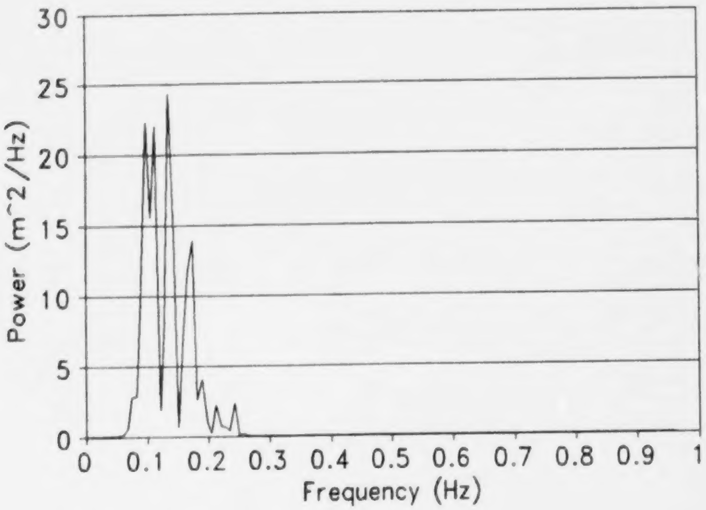

Figure 6.8.1: Normalized power spectrum of the modelled wave train.

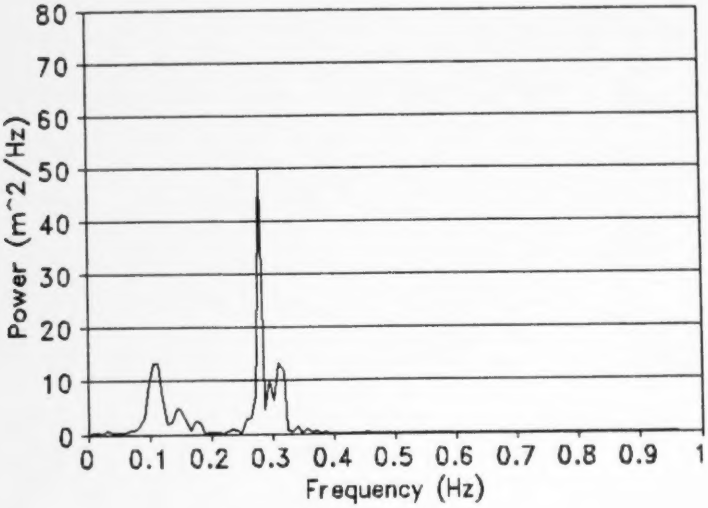

(a)

Figure 6.8.2: Power spectra of heave motion. a) no ice, b) with ice.

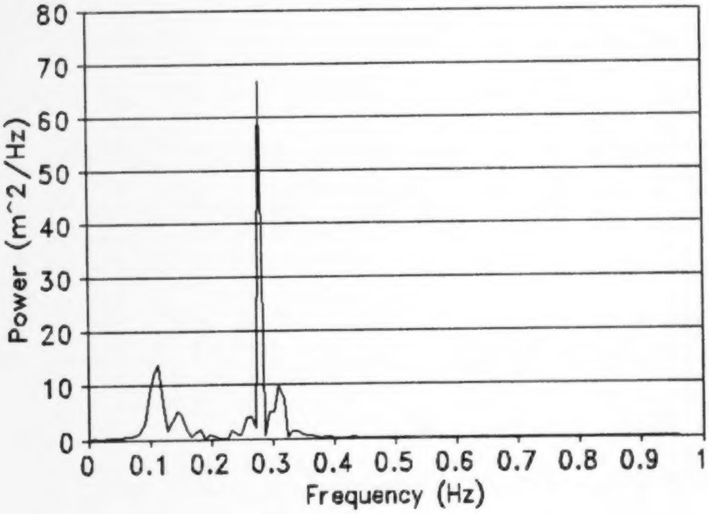

(b)

Zandberg are found to be 0.300 Hz and 0.297 Hz for the cases with and without ice respectively. If both added mass and damping are taken into account, the natural frequency should be smaller. Hence, the peak at $f_n = 0.2799$ Hz is probably the natural heave frequency. The lesser peaks beside the natural frequency peak may be due to a leakage effect or coupled ship motions. In general, the heave spectra are very similar with and without ice.

It is worthwhile mentioning here that the forward motion of the ship (1 ms^{-1}) may have an effect on the resonance of the ship's heave motion. A ship travelling into the wave field will increase the encountering wave frequency by a quantity Δf_n which can readily be shown to have the form $(2\pi V_s f^2)/g$, where V_s is the ship speed and f the frequency of a particular wave component. For the present case, the wave frequencies range from about 0.05 Hz to 0.25 Hz. Thus, Δf_n will range from 0.002 Hz to 0.04 Hz. This means that the range of the encountering frequencies for the ship in motion is 0.052 Hz to 0.29 Hz. This range encompasses the natural frequency of the heave motion. Therefore, resonance may occur with some of the high frequency wave components.

(c) Normalized power spectrum of pitch

Figure 6.8.3 shows the power spectrum of the pitch motion. Once again, the power spectra for the cases with and without ice are similar. The natural frequency of pitch in a calm sea neglecting the effects of added mass and damping, can be approximated by the formula $(1/2\pi)(gGM_L)^{1/2}/k_{yy}$ (Derrett, 1990). Where GM_L is the longitudinal metacentric height of the ship and k_{yy} the transverse radius of gyration. Thus, the natural frequency of pitch for the Zandberg is 0.328 Hz without ice and 0.319 Hz with ice. Again, the observed natural frequency should be lower because of the added mass and damping. The series of peaks located from $f_n \approx 0.1$ Hz to 0.25 Hz reflect the oncoming wave spectrum.

(d) Normalized power spectrum of roll

Only the power spectrum of roll with ice is shown in Figure 6.8.4, since roll motion does not occur in the computations without ice. Three peaks appear in this power

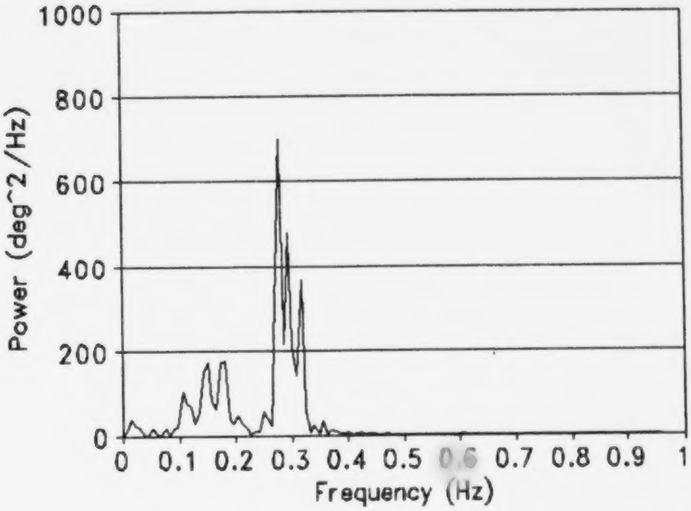

(a)

Figure 6.8.3: Power spectra of pitch motion. a) no ice, b) with ice.

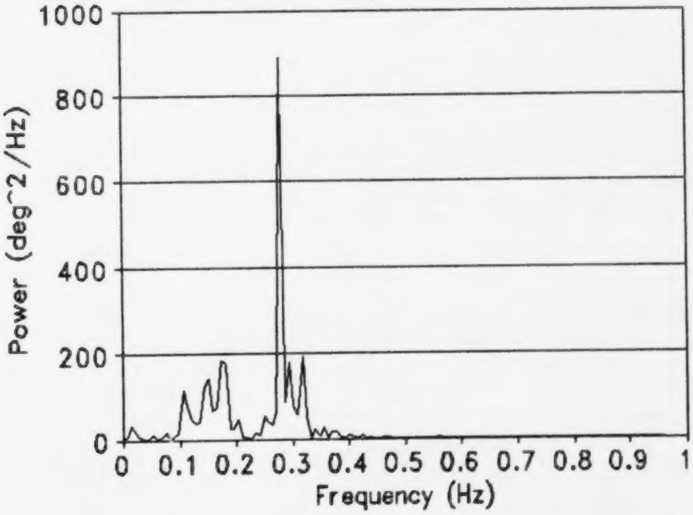

(b)

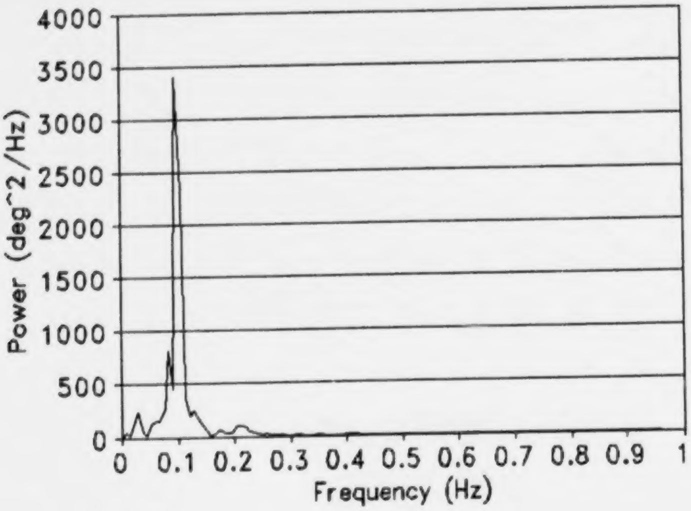

Figure 6.8.4: Power spectrum of roll with ice.

spectrum. They are located at $f_n = 0.0303$, 0.0832, and 0.0983 Hz, the third peak being the strongest of the three. A Comparison with the wave spectrum (Figure 6.8.1) suggests that the second and third peaks correspond with peaks in the wave spectrum. This is also true even when the effect of ship speed on frequency is accounted for (see discussion in Section 6.8b). Neglecting the effects of added mass and damping, the natural frequency of roll is given by $(1/2\pi)(gGM)^{1/2}/k_{xx}$ (Derrett, 1990), where GM is the transverse metacentric height and k_{xx} the longitudinal radius of gyration. The natural frequency of Zandberg approximated from this formula is 0.082 Hz. Because of the added mass and damping effect, the actual natural frequency should be lower. Comparing this possible natural frequency and the peaks in Figures 6.8.4 and 6.8.1, there are two possibilities. The first is that resonance of roll motion may have occurred. The second is that the peak at $f_n = 0.0303$ Hz shown in Figure 6.8.4 may represent the actual natural frequency of roll.

In summary then the spectral analysis indicates that the power spectra of heave as well as pitch are very similar with and without ice. The analysis also shows that heave, pitch, and roll are composed of components related to the oncoming wave spectrum and components related to the natural frequencies of the ship in heave, pitch, and roll.

6.9 Comments on Navigation Safety under Icing Conditions

The results presented in this chapter indicate that ice on a ship can increase its moments of inertia and change its centre of mass. With a symmetrical ice load distribution, the ship's centre of mass is shifted forward and upward. This causes the ship to trim by the head (Derrett, 1990). With an asymmetrical ice load distribution, the ship's centre of mass is shifted forward, upward, and away from the centreplane. Hence, in addition to trimming, the ship will list to the side with the greater ice load. Both the symmetrical and asymmetrical ice load distributions cause a reduction in the static stability of the ship. The effect of icing on the Zandberg's static stability was found to be the most severe with a wind direction of 15°.

The ship dynamics simulations suggest that with a wind direction of 15°, the Zandberg will become dynamically unstable after 3 hours of icing even in a wave field of substantially reduced amplitude. This is a result of the asymmetrical ice load distribution. The listing of the ship combined with the effects of the oncoming waves causes the ship to roll with a large amplitude and eventually to capsize. From the statistical analysis of the ship motions, it was found that the ice load causes an increase in the mass inertia of the ship and thus reduces both the heave and pitch amplitudes. On the other hand, the three hour ice load has a stronger effect on changing the mode of the pitch motion than on the mode of the heave motion. The power spectra of heave (and also pitch) with and without ice are very similar. A spectral analysis shows that the heave, pitch, and roll feature harmonic components of their respective natural frequencies and of the oncoming wave frequencies. This should also be true for the other components of the ship motion.

In view of these icing results and the effect of icing on ship stability, the following navigational strategies may reduce the severe ship icing hazard, by avoiding severe icing encounters. Recommendations (1), (2), (5), and (6) arise principally out of the work in this thesis:

(1) Listening to the forecast and locating potential severe icing areas. The Captain may have to change course where the circumstances allow. The present icing model is user friendly and with an appropriate modification to account for different superstructural configurations, it can be applied to other types of ship. Consequently, it may be possible to install the present icing model on a computer on board the ship for in situ icing forecast purposes. This could help the Captain to make judicious decisions on manoeuvring and de-icing tactics to avoid icing disaster.

(2) Under extreme weather with high winds and rough seas, the captain should try to avoid sailing into an area where both the air and sea-surface temperatures are very low (e.g air temperature < -10 °C and sea-surface temperature < 0 °C). The sensitivity tests of the present icing model suggests that, under such conditions, ice may build up very rapidly on the topside of the ship.

When icing has already been occurring, the following navigational tactics may be helpful:

(3) The captain should reduce the ship speed in order to reduce the amount of spray generated. Reducing ship speed, travelling to the lee of an island, moving to a sheltered area such as a harbour, or changing ship course (when it is safe to do so), can reduce both the rate of ice growth and the risk of dynamic instability.

(4) Whenever it is safe to do so, change the ship course from head seas to quartering, beam, or following seas. This can reduce the amount of spray generated (Transport Canada, 1994).

(5) Beware of asymmetrical (about the centreline) ice load distributions, which may cause the ship to list and lose its stability rapidly. To reduce the hazard of capsize, loads should be moved to maintain the ship close to its upright position. A similar tactic should be applied in the case of trim.

(6) The ice accumulated on the ship should be removed in such a manner that the degree of asymmetry of the ice load distribution (about the centreline) is reduced.

(7) The ice load can decrease the natural frequencies (such as heave, pitch, and roll, etc) of the ship. This could increase the possibility of synchronization and resonance between the ship motions and the forcing provided by the oncoming waves. Reducing ship speed also reduces this possibility.

CHAPTER 7 SUMMARY, CONCLUSIONS AND RECOMMENDATIONS

7.1 Summary and Concluding Remarks on Spray Generation

Based on the 22 spraying experiments performed in the 200 metre wave tank at the Institute for Marine Dynamics, a model- scale spray flux equation has been derived. Using Froude scaling, this model-scale equation has been transformed into a full-scale spray flux equation. This full-scale equation is valid under the condition of no wind drag. This means that the spray is transported onto the deck merely by the relative forward motion of the ship. The total mass of spray generated is determined by the ship speed and significant wave height according to $V_s^3H^7_{1/3}$, and the spray flux distribution is exponential, $e^{\alpha+\beta x}$ with α and β functions of y.

The model-scale experiments indicate an ambiguous effect of wind speed on the spray flux distribution at least within the range of wind speed applied during the experiment. This is unlikely to be the case in the natural environment. In the experiment, the wind speed was scaled down using Froude scaling, but the spray droplet size could not be scaled down. If anything, they were bigger than natural spray droplets. Therefore, wind drag is expected to have an effect on the spray flux distribution at full-scale. However, the mass of spray is determined by ship speed and wave height only, and this should also be true in the natural environment. Thus, the effect of wind drag is merely to transport the spray droplets and re-distribute them over the vessel's surface.

The above concepts have allowed us to develop a three- dimensional spraying model which includes the effect of wind drag. The formulation of this model is based on the full-scale spray flux equation, the droplet trajectory equation, and conservation of spray mass. In order to derive the local spray flux, a three-dimensional grid cell mesh has been superimposed on a simplified representation of the foredeck, wheelhouse and mast of the Zandberg.

Sensitivity tests of the spraying model confirm that the ship speed and significant wave height are the two primary parameters which determine the total spray mass, being found to be proportional to the third power of ship speed and the seventh power of significant wave height. The wind acts to re-distribute the spray mass. As the wind direction changes from head to beam, fewer grid cells lie within the spraying zone and the total spray mass decreases significantly. The droplet size has a complex effect on the spray flux distribution, but only a small effect on the total spray mass.

Spraying predictions have been produced for three case studies. It was found that the spray flux to a grid cell for a particular wind direction depends on the following factors:

(1) Wind speed.

(2) Location of the grid cell.

(3) Location of the spray source point.

(4) For horizontal grid cells, the ratio $\Delta x/\Delta x'$, and for vertical grid cells, the ratio $\Delta x/\Delta z'$ for a wind direction of 0° (see Section 3.5).

(5) For a wind direction other than 0°, the area ratio (ABCD)/(A'B'C'D').

(6) Shadowing effect.

There are two important limitations in the present spraying model. The first is that the nature of the experimental configuration limits the numerical model to situations with head seas. The second is that the experiments were performed with ranges of significant wave height and ship speed of 2.5 to 5 m and 1 to 8 ms^{-1} respectively. Consequently, the full-scale spray flux equation and hence the spraying model is still valid only within these ranges. Beyond these ranges, the results will need further verification.

7.2 Summary and Concluding Remarks on the Ship Icing Model

A three-dimensional icing model has been developed to calculate the local icing rate on the Zandberg. The spraying model which is designed to calculate the local spray flux has been incorporated into the icing model. Spray droplet trajectory and temperature determination, and a brine flow mechanism are all included in the formulation of the icing model.

Sensitivity tests have shown how the icing rate varies with air temperature, wind speed, fetch, ship speed, sea-surface temperature, and sea-surface salinity. It was found that the icing rate is sensitive to all of the above parameters except for the relative humidity which has a less significant effect.

The sinking of the Blue Mist II has been employed as a case study. The conditions encountered by the Blue Mist II have been used as input parameters to the icing model. The model icing results reveal the following:

(1) The maximum ice load occurs with a wind direction of 0° (head wind).

(2) A wind direction of 15° reduces the ice load slightly, but gives rise to a highly asymmetrical ice load distribution over the deck and the wheelhouse.

(3) The minimum ice load occurs with beam winds. The ice load distribution is symmetrical in this case because the spray fluxes to the port and starboard sides of the ship are not so much different from one and other.

The Zandberg icing model underestimates the total ice accretion rate when compared with the Wise and Comiskey's icing nomogram, and with NOAA and Soviet icing observations. Several possible reasons for this discrepancy have been suggested. However, the use of a Nusselt number for smooth surfaces in determining the heat transfer is most likely the major cause. Doubling the Nusselt number to account for the possible influence of surface roughness on heat transfer results in much better agreement with the observed icing data. Another factor which may also be responsible for the model's underprediction, though to a lesser extent, is the assumption that all of the impinging spray takes part in the sensible heat exchange. Yet another explanation may be insufficient spray generated by the spraying model for those conditions with low ship speed and significant wave height. Other factors such as the architecture of the hull and superstructure may also affect the model-observation comparisons.

7.3 Summary and Concluding Remarks on the Effect of Icing on the Ship's Static and Dynamic Stability

In the analysis of the effect of icing on ship stability, under the scenario of Blue Mist II and in order to take into account the surface roughness, a Nusselt number twice of the one for smooth flat plate is used to determine the heat transfer from the deck, the front, and the top of the wheelhouse. With this modification, the model simulations show that in one hour the total ice accretion is 14.36 tonnes for a wind direction of 0°, 13.5 tonnes for a wind direction of 15°, and 4.48 tonnes for a wind direction of 45°.

Knowing the ice loading conditions as a function of time, the effect of icing on the ship's centre of mass, moments of inertia, hydrostatic particulars, stability curves, trim, and list are calculated using the methods and equations discussed in Chapter 5. For a wind direction of 0°, the ice distribution is symmetrical about the centreline, so that the centre of mass is shifted forward and upward. After 20 hours of icing under the Blue Mist II conditions, the centre of mass shifts from (0, 0, 6.131 m) to (3.297 m, 0.0, 7.214 m). For non-head winds, the ice distribution is asymmetrical about the centreline and hence the ship's centre of mass is shifted forward, upward, and away from the centreplane towards the side with the heavier ice load. After 20 hours of icing, the centre of mass shifts to (3.186 m, 0.358 m, 7.149 m) and (1.389 m, 0.135 m, 6.472 m) respectively for cases with wind directions of 15° and 45°. The moments of inertia about all three axes are increased by about 50 % for the cases with wind directions of 0° and 15°, and by 21 % for the case with a wind direction of 45°.

The various hydrostatic particulars (see Table 6.3.1) under icing load conditions have been calculated based on upright, even keel conditions. This has been done by allowing all the ice mass to act at the centre of flotation so that there is a uniform change in draught, and the ship remains in an upright and even keel orientation. The hydrostatic particulars corresponding to each new draught were than determined. In calculating the stability curves, trim, and list of the ship, the centre of mass of the ice was shifted back to its actual position.

It was found that the metacentric height becomes negative with wind directions

0° and 15° at about 15 hours of icing. According to the stability curves, the Zandberg becomes statically unstable at 15 hours with a wind direction of 0°, at 10 hours with a wind direction of 15°, and at 20 hours with a wind direction of 45°. With a wind direction of 0°, the Zandberg trims 2.1° by the head at 10 hours prior to the onset of static instability by 15 hours. With a wind direction of 15°, the Zandberg trims 0.997° by the head and lists 14.3° to starboard at 5 hours prior to the onset of static instability by 10 hours. With a wind direction of 45°, the Zandberg trims 1.202° by the head and lists 13.5° to starboard at 15 hours prior to the onset of static instability by 20 hours. In summary, slightly off-head winds under severe icing conditions produce near maximum ice accretion and an asymmetrical ice distribution. This ice loading condition appears to have the most severe effect on the ship's static stability.

The "Blue Mist II" event has also been used as a case study to demonstrate the effect of icing on the dynamic performance of the Zandberg. A wind direction of 15° and an icing period of three hours were used. Over the three hour icing period, 40.5 tonnes of ice was accreted on the surface of the Zandberg. The stability curves and ship dynamics simulations showed that, at 0 hours (no ice), the Zandberg was statically and dynamically stable. After 3 hours of icing, although the ship remained statically stable, the asymmetrical ice load distribution caused the ship to list to starboard by 7.7°. This listing of the ship, combined with the oncoming wave forces, induced asymmetrical ship motions. The ship rolled with an amplitude of $\sim\pm 10°$ initially, which subsequently increased to about 30° after 140 seconds. At about 168 seconds, the ship rolled to starboard and capsized. A statistical analysis of the ship motions indicated that the ice load increased both the mass and moments of inertia of the ship and thereby reduced both the heave and pitch amplitudes. The effect of icing on pitch was more significant than on heave. The power spectra of heave and pitch for cases with and without ice were similar. A spectral analysis showed that heave, pitch, and roll contained harmonic components of their respective natural frequencies and of the oncoming wave frequencies. Based on these icing predictions and the effects of icing on ship dynamics, some navigation tactics were suggested to minimize the severe icing hazard.

Although the present icing model is technically constrained to the situation with head seas, the wind direction is allowed to change in order to generate an asymmetrical ice distribution (about the centreline). According to the ship dynamics analysis presented in this thesis, an asymmetrical ice distribution can cause a serious problem to the dynamic stability of the Zandberg. As long as more spraying data for non-head seas situations are available, the present icing model can readily be adapted to different ship headings. In addition, this extended model could be used in conjunction with the ship dynamics model in order to evaluate the effect of icing on ship dynamics for various ship headings.

7.4 Recommendations

The present Zandberg icing model takes into account essentially all of the known physical processes related to spray icing. These physical processes include spray generation, droplet dynamics and cooling, brine flow dynamics, and freezing of the brine film. Thus, it can be said that the present icing model is physically based. However, in the modelling of these physical processes, certain experimental limitations, various assumptions and inevitable approximations introduce errors and uncertainties into the model predictions. The present icing model can therefore be improved by improving the modelling of the physical processes. In order to do this, the following suggestions are made. They are not necessarily ranked in order of importance.

1) The present spraying data obtained from towing tank experiments are strictly for the "MT Zandberg". For other types of ships, because of different hull geometries, the spraying data will likely be different. Therefore, in order to generalize the spraying model, more model tests for other types of ships will be necessary.

2) In the scale-model spraying experiment, the ship heading was fixed at 180°. This constraint was introduced by the nature of the towing tank. Thus, the spraying model, which was derived from the experimental data, is strictly valid only for head seas. To

relax this limitation, model spraying experiments using ship headings between 90° (beam seas) and 180° (head seas) will be necessary. Such experiments could perhaps be performed using a remotely controlled model in the seakeeping tank at IMD.

3) The ranges of ship speed and significant wave height within which the full-scale spray flux equation is valid are (1, 8 ms^{-1}) and (2.5, 5 m) respectively. This range of ship speed is probably appropriate for this vessel. In order to account for extreme icing conditions, however, the range of significant wave height should be expanded.

4) The methodology used in the model-scale spraying experiments could be applied to a full-scale spray collection program on a real ship. Not only would such full-scale experiments give more reliable full-scale spraying data, but they could also be used to check the validity of Froude number scaling. The model experiments indicate that, with low ship speed and significant wave height, very little spray is generated. This may not be true in the full-scale environment. The reason is that the force of ship/wave collision in a full-scale environment is stronger than in a model-scale environment. Since the surface tension of sea water is the same for both the full-scale and model-scale environments, the former case will give a higher inertia to surface tension force ratio than the latter case and thereby should produce more spray. According to the model evaluation presented in Section 4.8.II, one of the factors which may contribute to the model's underestimation of icing rate is that not enough spray is generated by the spraying model, especially for those cases with low ship speed and significant wave height.

5) Basic theoretical and experimental investigations of collision-generated spray may help to generalize the present spraying model to other types of ships. It seems that spray generation is dependent on the momentum transfer between the hull and the water surface during ship/wave collision. As a first step, this phenomenon has been simulated with a spherical object falling onto a calm water surface (Sampson et al., 1994).

6) The modelling of the brine film dynamics should be improved if possible by allowing flow from component to component (e.g from the wheelhouse to the deck), and flows on horizontal surfaces. In the Zandberg model, brine is allowed to flow only vertically downward on vertical surfaces. This limitation should be relaxed by allowing horizontal flow driven by three-dimensional wind stress. At present, laminar flow is assumed in the brine film dynamics module. This assumption should be replaced by turbulent flow where appropriate. For horizontal surfaces, the equilibrium brine film thickness is estimated using simple surface tension considerations. This can be verified experimentally.

7) In the Zandberg model we assume that all impinging spray takes part in the sensible heat exchange. As a result, with low air temperature, the model tends to underestimate icing rates for conditions with high sea-surface temperatures and high spray fluxes. Conversely, it overestimates icing rates for conditions with low sea-surface temperatures and high spray fluxes. Wind tunnel investigations are necessary to investigate the fraction of the impinging spray which actually participates in the sensible heat exchange.

8) The roughness of the icing surface increases both the effective surface area and the turbulence intensity. It would seem that both of these factors could cause a significant increase in heat transfer especially at high Reynolds numbers. An accurate determination of the degree of roughness of the icing surface and its effect on heat transfer would certainly help to improve many of the current icing models. Wind tunnel experiments could assist in this determination, but full-scale heat transfer measurements will likely be necessary to resolve the issue.

9) Due to the size and complexity of the superstructure of a ship, the flow over the ship is extremely complex and highly turbulent, especially at high wind speeds. At present, the actual magnitude of the heat transfer coefficient on ship surfaces is largely unknown. Measurements of the local heat transfer coefficient on a full-scale ship is a high priority. Such results could greatly improve the accuracy of predicting icing rates.

10) The present icing model is designed for a specific configuration of the superstructure. However, the model can be modified to investigate different designs for the superstructure. Consequently even the present icing model could be used to evaluate the effect of different superstructural configurations on the total ice load and its distribution.

As for the effect of icing on ship stability, the following recommendations are proposed:

11) The ship dynamics model apparently behaves unrealistically for ship speed and significant wave height beyond 3 ms^{-1} and 4.5 m respectively. Under severe icing conditions, the significant wave height often exceeds 4.5 m. Consequently, in order to produce a more realistic prediction of the effect of icing on ship dynamics, the dynamic model should be modified if feasible to cover a wider range of significant wave height.

12) The ship dynamics model cannot take into account the initial trimming of the ship which is caused by ice loading. Modification of the ship dynamics model to include the trimming of the ship should certainly improve the model prediction of ship motions under icing conditions.

13) The prediction of the effect of icing on ship dynamics in the present study is purely numerical. These results require further verification. This could be done by performing wave tank experiments using an appropriate ship model with a load distribution specifically designed to represent the situation under icing conditions.

14) Icing and ship dynamics are coupled in both directions. We have demonstrated that icing affects ship dynamics. However, the ship dynamics in turn affects the spray generation process and hence the icing rate. Thus, further research on icing and ship dynamics should be directed towards the integration of the icing and ship dynamics models so that they can run simultaneously. Particular attention needs to be paid to the effect of ship dynamics in producing spray.

BIBLIOGRAPHY

Andreas, E.L., 1989: Thermal and size evolution of sea spray droplets. U.S. Army CRREL Report 89-11, Hanover, New Hampshire, 37 pp.

Beck, F. and Liapis, S., 1987: Transient motions of floating bodies at zero forward speed. Journal of Ship Research, Vol. 31, No. 3, pp 164-176.

Blackmore, R.Z. and Lozowski, E.P., 1994: An heuristic freezing spray model for vessel icing. International Journal of Offshore and Polar Engineering, Vol. 4, No. 2, pp 119-126.

Borisenkov, Ye.P., 1969: Physical investigation of hydrometeorlogical complexes favourable for icing on ships. In: Hydrometeorlogical Conditions of Icing on Ships, Arkticheskii i Antarkticheskii Nauchno-Issledovatiel'skii Institut, Leningard, pp 7-20 (in Russian).

Borisenkov, Ye.P., Moltchanov, V.N., Nagurnyi, A.N. and Panov, V.V., 1917: On the possible method of the numerical prediction of hydrometeorlogical conditions of icing on ships. In: Theoretical and Experimental Investigations of Conditions of Icing on Ships. Gidrometeoizdat, Leningrad (in Russian).

Borisenkov, Ye.P. and Panov, V.V., 1972: Primary results and prospects for investigating the hydrometeorlogical conditions of ship icing, Arkticheskii i Antarkticheskii Nauchno-Issledovatiel'skii Institut, Trudy, No. 298, Leningard, pp 5-33 (in Russian).

Borisenkov, Ye.P., Panov, V.V. and Moltchanov, V.N., 1971: Some results of the theoretical calculations of the icing rate on ships. In: Theoretical and experimental investigations of conditions of icing on ships. Gidrometeoizdat, Leningrad, pp 6-15 (in Russian).

Borisenkov, Ye.P., Zablockiy, G.A., Makshtas, A.P., Migulin, A.I. and Panov, V.V., 1975: On the approximation of the spray cloud dimensions. In: Arkticheskii i Antarkticheskii Nauchno-Issledovatiel'skii Institut, Trudy No. 317, Gidrometeoizdat, Leningrad, pp 121-126 (in Russian).

Borisenkov, Ye.P. and Ptchelko, I.G., 1975: Indicators for forecasting ship icing, USA CREEL Draft Translation, No. 481.

Bretschneider, C.L., 1973: Prediction of waves and currents. Look Lab/Hawaii, Vol. 3, No. 1, pp 1-17.

Chang, M.S., 1977: Computations of three-dimensional ship motions with forward speed. Proceeding of the Second International Conference on Numerical Ship Hydrodynamics, pp 124-135.

Chung, K.K., 1989: An experimental and numerical investigation of the growth of saline icicles. M.Sc. Thesis, University of Alberta, 171 pp.

Chung, K.K., Lozowski, E.P. and Zakrzewski, W.P., 1993: Numerical and laboratory investigation of spray generation. Milestone Stone Report No. 6 (Task No. 8). Data Analysis. Prepared for The Institute for Marine Dynamics, National Research Council, St. John's Newfoundland, 51 pp.

Chyu, M.K. and Natarajan, V., 1991: Local heat/mass transfer distributions on the surface of a wall mounted cube. Journal of Heat Transfer, Vol. 113, pp 851 -857.

Comiskey, A.L., Leslie, L.D. and Wise, J.L., 1984: Superstructure icing and forecasting in Alaskan waters. Unpublished draft report submitted by the Arctic Environmental Information and Data Center to Pacific Marine Environmental Laboratory (NOAA), Seattle, 39 pp.

Comiskey, A.L., Leslie, L.D. and Wise, J.L., 1984: Superstructure icing and forecasting in Alaskan waters. Arctic Environmental Information and Data Center, University of Alaska, 30 pp.

Crane, C.L., Eda, H. and Landsburg, A., 1989: Controllability. In: Principles of Naval Architecture, Vol. III, E.V. Lewis, ed., SNAME.

Derrett, D.R., 1990: Ship Stability for Masters and Mates. Heinemann Professional Publishing Ltd, Halley Court, Jordan Hill, Oxford OX2 8EJ, 386 pp.

Dukler, A.E. and Bergelin, O.P., 1952: Characteristics of flow in falling liquid films. Chemical Engineering Progress, Vol. 48, No. 11, pp 557-563.

Dunphy, P., 1993: User manual for ship dynamics simulation program (SDSP). National Research Council of Canada, Institute for Marine Dynamics, St. John's, Newfoundland, 13 pp.

Etter, D.M., 1987: Structured Fortran 77 for Engineers and Scientists. The Benjamin/Cummings Publishing Company, Inc, California, 519 pp.

Faltinsen, O. and Michelsen, F.C., 1974: Motions of large structures in waves at zero Froude number. International Symposium on Dynamics of Marine Vehicles and Structures in Waves, pp 91-106.

Fowles, G.R., 1977: Analytical Mechanics. Holt, Rinehart and Winston, U.S.A, 334 pp.

Freund, J.E. and Walpole, R.E., 1980: Mathematical Statistics. Prentice-Hall, Inc, Englewood Cliffs, N.J. 07632, pp 478-480.

Guo, D., 1985: Handbook of University Mathematics. Sandong Science and Technology Publisher, Jinan, pp 29-30.

Himeno, Y., 1981: Prediction of ship roll damping - state of the art. Rep. No. 239, Department of Naval Architecture and Marine Engineering, University of Michigan.

Hogben, N. and Standing, R.G., 1974: Wave loads on large bodies. International Symposium on Dynamics of Marine Vehicles and Structures in Waves, pp 258-277.

Holman, J.P., 1981: Heat Transfer. McGraw Hill, New York, 570 pp.

Horjen, I. and Vefsnmo, S., 1985: A numerical sea spray icing model including the effect of a moving water film. Proceeding of the International Workshop on Offshore Winds and Icing, Halifax, N.S, pp 152-164.

Hutchison, B.L., 1990: Sea keeping studies: a status report, SNAME, Annual Meeting.

Igarashi, T., 1985: Heat transfer from a square prism to an air stream. Int. J. Heat Mass Transfer, Vol. 28, No. 1, pp 175-181.

Igarashi, T., 1986: Local heat transfer from a square prism to an air stream. Int. J. Heat Mass Transfer, Vol. 29, No. 5, pp 777-784.

Inglis, R.B. and Price, W.G., 1982: A three-dimensional ship motion theory-comparison between theoretical predictions and experimental data of hydrodynamic coefficients with forward speed. Trans. RINA, Vol. 124, pp 141-157.

Iribarne, J.V. and Godson, W.L., 1985: Atmospheric Thermodynamics. D.Reidel Publishing Company, Netherlands, 259 pp.

Kachurin, L.G., Gashin, L.I. and Smirnov, I.A., 1974: Icing rate of small displacement fishing vessels under various hydrometeorlogical conditions. Meteorologiya i Gidrologiya, No. 3, pp 50-60.

Khazanie, R., 1986: Elementary Statistics. Scott, Foresman and Company, U.S.A, 562 pp.

King, B., 1987: Time - domain analysis of wave exciting forces on ships and bodies. Thesis, University of Michigan.

Kirby, J.A., 1985: Spray considerations for vertically sided structures. M.Eng. Thesis, University of Calgary, 86pp.

Knight, C.A., 1967: The Freezing of Supercooled Liquids. New Jersey, D. Van Nostrand Company, INC, 139 pp.

Kreith, F. and Black, W.Z., 1980: Basic Heat Transfer. Harper & Row, New York.

Krylov, A., 1898: A general theory of the oscillation of a ship on waves. Trans. INA, Vol. 40, pp 135-196.

Langmuir, I. and Blodgett, K., 1946: A mathematical investigation of water droplet trajectories. In: Collected Works of Irving Langmuir, Pergamon Press, N.Y., Vol. 10, pp 348-393.

Lee, C.H., Newman, J.N., Kim, M.H. and Yue, D.K.P., 1991: The computation of second order wave loads, OMAE 1991 Conference.

Lewis, E.V., 1967: The motion of ships in waves. In Principles of Naval Architecture, The Society of Naval Architects and Marine Engineers, N.Y., pp 607-717.

Liapis, S.J., 1986: Time - domain analysis of ship motions. Thesis, University of Michigan.

Lighthill, J., 1979: Waves in Fluids. Cambridge University Press, cambridge, 504 pp.

Lin, W.M. and Yue, D.K.P., Numerical solutions for large amplitude ship motions in the time domain. Eighteenth Symposium on Naval Hydrodynamics.

Lock, G.S.H. and Foster, I.B., 1988: Observations on the formation of spongy Ice from fresh water. Unpublished manuscript, University of Alberta, 25 pp.

Lozowski, E.P. and Zakrzewski, W.P., 1990: Advanced modelling of vessel icing. Milestone Report No.2. Submitted to the United States Army Cold Regions Research and Engineering Laboratory Hanover, New Hampshire, U.S.A.

Lozowski, E.P. and Zakrzewski, W.P., 1991: Numerical and laboratory investigations of spray generation. Milestone Report No.2 (Task No.4). Design of a system for the measurement and recording of spray-related parameters on a ship model, 10 pp.

Lozowski, E.P. and Zakrzewski, W.P., 1991: Numerical and laboratory investigations of spray generation. Milestone Report No.3 (Task No.5). Testing the individual components of the spray measurement system at the University of Alberta, 10 pp.

Lozowski, E.P. and Zakrzewski, W.P., 1992: Numerical and laboratory investigations of spray generation. Milestone Report No.4 (Task No.6). Production and assembly of the data collection system and installation at NRC/IMD, 14 pp.

Lozowski, E.P. and Zakrzewski, W.P., 1992: Numerical and laboratory investigations of spray generation. Milestone Report No.5 (Task No.7). Wave tank experiment for the 1:14 scale model of the MT "Zandberg" in the NRC/IMD clear water wave tank, 27 pp.

Lozowski, E.P. and Zakrzewski, W.P., 1992: How it works: The physical and empirical basis for the topside ship icing system. Prepared for U.S. Army CRREL, Hanover, New Hampshire, 03755-1290.

Maeno, N. and Takahashi, T., 1984 (a): Studies on icicles. I. General aspects of the structure and growth of an icicle. Low Temperature Science, Ser.A, 43, pp 125-138. (In Japanese).

Magee, A.R., 1991: Large amplitude ship motions in the time Domain. Thesis, University of Michigan.

Makkonen, L., 1984: Atmospheric icing on sea structures. Monograph 84-2, CREEL, 92 pp.

Makkonen, L., 1987: Salinity and growth rate of ice formed by sea spray. Cold Regions Science and Technology, Vol. 14, pp 163-171.

Makkonen, L., 1988: A model of icicle growth. Journal of Glaciology, Vol 34(116).

Makkonen, L., 1989: Formation of spray ice on offshore structures. CRREL Special Report 89-5, U.S. Army Cold Regions Research Engineering Lab, Hanover, NH, pp 227-309.

Marion, J.B. and Hornyak, W.F., 1982: Physics for Science and Engineering, Part I. Saunders College Publishing, New York, 743 pp.

Mertins, H.O., 1968: Icing on fishing vessels due to spray. Marine Observer, Vol 38(221), pp 128-130.

Marystown Shipyard Ltd., 1982: Stability information booklet for M.F.V. Zandberg 53 metre stern trawler, 99 pp.

Michieev, M.A. and Michieeva, I.M., 1973: Principles of Heat Transfer. Moscow, Energy Publishing House, 319 pp (in Russian).

Moore, C.S., 1967: Intact stability. In Principles of Naval Architecture, The Society of Naval Architects and Marine Engineers, N.Y., pp 54-120.

Motwani, D.G., Gaitonde, U.N. and Sukhatme, S.P., 1985: Heat transfer from rectangular plates inclined at different angles of attack and yaw to an air stream. Journal of Heat Transfer, Vol.107, pp 307-312.

Narten, R., 1985: The influence of several factors on the heat transfer from an isothermal cylinder, PhD. Thesis, Universtity of Alberta, 167 pp.

Newman, J.N., 1970: The second-order time average vertical force on a submerged body flowing beneath a regular wave system, unpublished.

Newman, J.N., 1977: Marine Hydrodynamics. MIT Press, Cambridge, Massachusettes, 402 pp.

Newman, J.N., 1983: Three-dimensional wave interactions with ships and platforms. International Workshop on Ship and Platform Motions, pp 418-442.

Newman, J.N. and Sclavounos, P.D., 1988: The computation of wave loads on large offshore structures. Proceeding of the International Conference on Behaviour of Offshore Structures BOSS'88, pp 605-622.

Nikuradse, J., 1933: Forschungsheft, 361, 1.

Ogilvie, T.F., 1983: Second-order hydrodynamic effects on ocean structures. International Workshop on Ship and Platform Motions, pp 205-265.

Olsen, J., Webb, B.W. and Queiroz, M., 1989: Local three-dimensional convective heat transfer from a heated cube. Presented at the ASME Winter Annual Meeting, San Francisco, pp 7-13.

Overland, J.E., Pease, C.H., Preisendorfer, R.W. and Comiskey, A.L., 1986: Prediction of vessel icing. Journal of Climate and Applied Meteorology, Vol. 25, No. 12, 1793-1806.

Panov, V.V., 1971: On the frequency of splashing the medium fishing vessel with sea spray. In: Theoretical and Experimental Investigation of the Conditions of Icing on Ships. Gidrometeoizdat, Leningrad, pp 87-90 (in Russian).

Panov, V.V., 1971: Calculation of the ice growth rate associated with the spray icing of ships. In: Theoretical and Experimental Investigations of Conditions of Icing on Ships. Arkticheskii i Antarkticheskii Nauchno-Issledovatiel'skii Institut, Leningrad, pp 26-48 (in Russian).

Panov, V.V., 1976: Icing of Ships. Arkticheskii i Antarkticheskii Nauchno-Issledovatiel'skii Institut, Trudy No. 334, Gidro-meteoizdat, Leningrad, 263 pp (in Russian).

Pawlowski, J.S., 1982: The estimation of diffraction force components from the equivalent motion concept. International Shipbuilding Progress, Vol. 29, pp 62-73.

Pawlowski, J.S., 1991: An explicit form of the impermeability condition and its application in hydrodynamics and hydro-elasticity. 6th Int'l Workshop on Water and Floating Bodies, Woods Hole, pp 207-210.

Pawlowski, J.S. and Bass, D.W., 1990: An investigation of vessel stability in waves by means of numerical motion simulations. 4th Int'l Conf. on Stability of Ships and Ocean Vehicles, Naples, pp 217-255.

Pawlowski, J.S. and Bass, D.W., 1991: A theoretical and numerical model of ship motion in heavy seas. Trans. SNAME, 31 pp.

Pawlowski, J.S., Bass, D.W. and Grochowalski, S., 1988: A time domain simulation of ship motions in waves. Proceeding of the Seventeenth Symposium on Naval Hydrodynamics, pp 597-610.

Pease, C.H. and Comiskey, A.L., 1986: Vessel icing in Alaskan waters 1979-1984 data set. NOAA Data Report, ERL PMEL-14, 16 pp.

Peterka, J.A., Meroney, R.N. and Kothari, K.M., 1985: Wind flow patterns about buildings. J. Wind Engrg. and Int. Aero., Vol. 21, pp 21-38.

Press, W.H., Teukoisky, S.A., Vetterling, W.T. and Flannery, B.P., 1992: Numerical Recipes in Fortran. Cambridge, University Press, pp 490-602.

Ranz, W.A. and Marshall, W.R., 1952: Evaporation from drops. Chemical Engineering Progress, Vol. 48, pp 141-180.

Rawson, K.J. and Tupper, E.C., 1983: Basic Ship Theory. Vol. 1. Longman Inc, N.Y., 374 pp.

Ryerson, C.C.,: 1993: Superstructure spray and ice accretion on a large U.S. Coast Guard Cutter. Proceedings of the 6th International Workshop on the Atmospheric Icing of Structures, No. 22-23, pp 280-285.

Salvesen, N., 1974: Second-order steady-state forces and moments on surface ships in oblique regular waves. International Symposium on the Dynamics of Marine Vehicles and Structures in Waves, pp 225-239.

Salvesen, N., Tuck, E.O. and Faltinsen, O., 1970: Ship motions and sea loads. Trans. SNAME, Vol. 78, pp 250-279.

Sampson, R.D., Chung, K.K. and Lozowski, E.P., 1994: Splash mass of a free-falling buoyant sphere. (in preparation)

Sawada, T., 1966: A method of forecasting ice accretion in the waters off the Kurile Islands. Journal of Meteorological Research, Vol. 18, pp 15-23.

Schmitke, R.T., 1979: Improved slamming predictions for the PHHS computer program. Defense Research Establishment Atlantic, Dartmouth, N.S., DREA Technical Memorandum 79/A, 68 pp.

Shekhtman, A.N., 1967: Hydrometeorlogical conditions of icing on ships, Nauchno-Issledovatiel'skii Institut, Aeroklimatologii, Trudy No. 45, Gidrometeoizdat, Moscow, pp 51-63 (in Russian).

Shekhtman, A.N., 1968: The probability and intensity of icing on ships. Nauchno-Issledovatiel'skii Institut, Aeroklimatologii, Trudy No. 50, pp 55-56 (in Russian).

Stallabrass, J.R., 1980: Trawler icing: a compilation of work done at NRC. National Research Council of Canada, Mechanical Engineering Report MD-56, NRC, No. 19372, Ottawa, 103 pp.

Test, F.L., Lessmann, R.C. and Johary, A., 1981: Heat transfer during wind flow over rectangular bodies in the natural environment. Journal of Heat Transfer, Vol. 103, pp 262-267.

Test, F.L. and Lessmann, R.C. 1980: An experimental study of heat transfer during forced convection over a rectangular body. Journal of Heat Transfer, Vol. 102, pp 146-151.

Todd, F.H., 1967: Resistance and propulsion. In Principles of Naval Architecture, The Society of Naval Architects and Marine Engineers, pp 288-462.

Transport Canada: Report of Investigation into Loss of Trawler "BLUE MIST II" with Thirteen on Board, 4 pp.

Transportation Safety Board of Canada, 1994: Downflooding and sinking of the fishing vessel "Cape Aspy" off the South-West Coast of Nova Scotia, 30 January, 1993. Marine Occurrence Report, No. M93M4004, 38 pp.

Unterberg, W., 1966: Thermal properties of salt solutions. British Chemical Engineering, Vol. 11, No. 6, pp 494-495.

Vasil'yeva, G.V., 1966: Hydrometeorlogical conditions promoting the icing of sea-going ships. Rybnoye Khozyaystvo, No. 12, pp 43-45 (in Russian).

Weeks, W.F. and Ackley, S.F., 1982: The growth structure and properties of sea ice. CRREL Monograph, 82-1, 117 pp.

Wise, J.A. and Comiskey, A.L., 1980: Superstructure icing in Alaskan waters. Pacific Marine Environmental Laboratory, Seattle, Washington, NOAA Special Report, 30 pp.

Zakrzewski, W.P., 1987: Splashing a ship with collision-generated spray. Cold Regions Science and Technology, Vol. 14, pp 65-83.

Zakrzewski, W.P., Lozowski, E.P., Blackmore, R.Z. and Gagnon, R., 1988: Recent approaches in the modelling of ship icing. Proceedings of the 9th International Symposium on Ice, Vol. 2, pp 458-476.

Zakrzewski, W.P. and Lozowski, E.P., 1989: Soviet marine icing data. Canadian Climate Centre Report 89-2, Atmospheric Environment Service, 125 pp.

Zakrzewski, W.P. and Lozowski, E.P., 1991: Modelling and forecasting vessel icing. In, "Freezing and Melting Heat Transfer in Engineering," K.C. Cheng and N. Seki, eds., Hemisphere, New York, pp 661-706.

Zarling, J.P., 1980: Heat and mass transfer from freely falling drops at low temperatures. CRREL Report 80-18, Hanover, New Hampshire, 14 pp.

Zukauskas, A.A. and Ziugzda, J., 1985: Heat Transfer of a Cylinder in Crossflow. Hemisphere Publishers, Washington, 208 pp.

APPENDIX 1A

Total spray mass (g) collected on the deck of the model-scale Zandberg in each of the 23 gauges during the course of an entire experimental run. The positions of the numbers depict the relative gauge positions with the gauge nearest the bow at the top (see Figure 2.1). Dashes indicate a negligible mass. The experimental conditions for each run are given Table 2.1.1.

Run #1

439.9

210.2 234.9

137.0 163.5 126.4

56.0 97.8 68.3

28.3 47.1 57.0 51.5

27.3 17.5 18.6 20.0 26.3

12.8 15.7 8.7 9.9 11.4

Run #2

93.8

42.6 66.9

26.4 35.5 31.1

22.2 26.3 19.9

14.5 12.5 18.9 10.3

5.0 8.2 4.9 9.6 8.0

1.5 2.7 1.8 3.5 3.2

Run #3

				117.8				
			20.1		29.4			
		16.3		16.7		12.6		
		7.4		18.6		8.0		
	6.4		5.3		7.4		8.7	
3.1		3.0		4.2		3.6		3.1
1.3		0.2		0.0		0.7		0.8

Run #4

				368.0				
			92.0		199.5			
		53.1		141.3		95.5		
		58.0		128.2		46.2		
	25.6		36.5		68.2		27.8	
6.0		11.8		22.7		16.1		22.8
2.4		3.2		3.5		5.2		8.2

Run #5

				54.7				
			35.9		36.2			
		26.1		29.1		12.9		
		1.4		7.6		2.2		
	---		---		---		---	
---		---		---		---		---
---		---		---		---		---

Run #6

***** Test Failed *****

Run #7

```
                   470.8
              310.3     308.6
         193.0     333.0     186.2
         132.7     237.2      68.7
    49.8      101.5     143.6      78.6
49.8      69.8      81.5      95.5      55.3
37.8      24.5      40.0      22.6      20.5
```

Run #8

```
                    38.7
               16.3      13.6
           6.5       6.7       5.1
           ---       ---       ---
      ---       ---       ---        ---
 ---       ---       ---        ---       ---
 ---       ---       ---        ---       ---
```

Run #9

1101.6

541.5 573.3

199.5 287.1 168.2

112.0 224.5 111.0

76.0 140.0 121.0 71.1

49.8 69.3 103.0 60.4 69.2

27.7 36.6 29.4 25.1 25.5

Run #10

334.2

160.3 112.5

88.0 120.1 86.1

26.7 58.7 36.3

16.9 18.0 25.1 21.9

11.3 12.3 4.9 18.6 16.5

2.8 2.5 1.7 2.8 4.3

Run #11

566.2

260.9 281.8

143.6 285.2 120.6

95.6 209.8 73.8

64.5 85.4 108.0 44.3

25.8 14.0 22.2 23.2 35.4

11.5 8.4 3.2 3.5 9.8

Run #12

810.5
156.0 172.6
46.8 147.9 68.5
49.3 186.9 68.0
19.0 98.7 139.4 41.8
33.4 23.2 38.1 39.7 48.7
6.4 7.4 4.4 3.4 10.0

Run #13

36.1
9.4 26.8
8.9 2.5 5.5
1.7 1.5 2.4
--- --- --- ---
--- --- --- --- ---
--- --- --- --- ---

Run #14

16.9
7.3 4.7
5.4 4.1 2.6
--- --- ---
--- --- --- ---
--- --- --- --- ---
--- --- --- --- ---

Run #15

862.5

221.4 251.6

136.0 248.7 169.9

112.0 217.6 89.1

62.7 102.7 100.5 59.0

50.5 44.1 25.9 44.5 46.8

11.8 10.1 17.4 22.3 12.6

Run #16

927.0

316.3 312.5

232.2 421.1 185.1

154.0 361.3 120.9

119.7 184.8 160.7 68.7

99.8 71.7 58.0 73.2 82.6

24.2 15.4 18.6 24.5 29.0

Run #17

94.1

43.3 37.8

22.5 24.9 25.3

15.2 28.0 13.6

8.2 13.0 9.2 4.2

5.7 5.9 4.8 5.1 6.6

--- --- --- --- ---

Run #18

1100.8

655.8 551.1

357.8 373.3 286.7

215.4 370.9 129.5

105.8 172.4 152.9 103.8

101.7 89.6 90.8 67.5 80.7

28.6 36.6 31.4 36.4 50.3

Run #19

141.7

112.2 125.4

41.7 132.4 58.8

17.9 37.3 24.4

11.3 9.6 14.9 10.5

0.0 1.6 0.6 1.5 2.9

--- --- --- --- ---

Run #20

762.6

239.9 201.6

123.6 223.0 139.5

54.7 136.3 51.0

41.7 74.3 49.2 47.3

30.1 24.3 22.2 26.2 39.2

7.8 7.1 4.2 10.3 6.5

Run #21

1183.4
443.8 402.8
268.3 474.5 257.3
204.0 414.4 157.0
149.2 266.5 184.6 145.0
112.2 118.3 110.3 112.9 116.5
33.1 42.8 23.6 50.5 45.2

Run #22

524.2
172.1 319.6
105.9 193.4 100.0
84.5 124.2 66.8
37.6 61.3 67.0 58.0
37.9 40.9 21.7 39.6 47.4
7.5 10.3 6.6 19.4 14.4

Run #24

856.5
274.2 252.2
117.8 301.8 127.2
95.8 242.5 90.1
50.2 153.2 129.6 74.3
61.1 60.3 49.9 52.1 59.8
22.0 18.6 32.1 29.9 21.4

APPENDIX 1B

Derivation of a Relation Describing the Spray Mass Distribution over the Deck

We begin by making the following assumptions:

(i) The transverse mass distribution along rows B, C, D, and E (see Figure 2.1) is parabolic with a maximum at y=0 (centreline):

$$M(y) = P_2 y^2 + P_o \qquad (1B.1)$$

This equation can be expressed in non-dimensional form as:

$$S(y) = Py^2 + 1 \qquad (1B.2)$$

where, $P = P_2/P_o$, $S(y) = M(y)/P_o$.

(ii) We also assume that the mass distribution for row B has a similar non-dimensional form to that in row C:

$$S_B(Y) = Py^2 + 1 \qquad (1B.3)$$

We make this assumption because row C is close to row B, and we use the information in row C to estimate the 'missing data' (to be discussed later) in row B.

(iii) In view of the above, the transverse mass distribution is clearly assumed to be symmetrical about the x-axis.

For convenience of analysis, we divide the data set as shown in Figure (2.1) into 5 longitudinal columns. These columns are illustrated in Figures (1B.1a) and (1B.1b). Although the mass distribution data collected in the ship splashing experiment is not perfectly symmetrical about the x-axis, we make it symmetrical by averaging the values to the left and right of the line of symmetry (x-axis). Thus, we obtain a modified data set which is symmetrical about the x-axis. The 'missing data' are then calculated by following the procedures described below:

(i) Data in row C, row D, and row E

We have assumed that the transverse mass distribution in these three rows is parabolic (Equation 1B.1). Using the measured data in each row, together with Equation 1B.1, we formulate the coefficients (P_o, P_2, and P) for the transverse mass distribution for each experiment. Subsequently, the "missing data" are then calculated by substituting the appropriate ordinate (y) into the parabolic equation for that row. There are two exceptional cases. In experiment #13, in rows C and D, the mass on the centreline is less than the mass on either side. In these particular cases, the two "missing data" in rows C and D are estimated using linear interpolation. A similar situation also occurs in row E for experiment #3 in which $m_{E1} < m_{E3}$ and $m_{E-1} < m_{E-3}$. Since we do not know the value at $y=0$ (m_{E0}), in this case we simply approximate the three unknown data values by using the average of the four known data values.

(ii) Data in row B

We have assumed that the transverse mass distribution in row B, when expressed in non-dimensional parabolic form, is identical to the non-dimensional parabolic equation in row C (Equation 1B.3). Thus, the "missing data" value m_{B0} can be estimated as: $m_{B0} = m_{B1}/S_B$(at $y=7.8$ cm). Since the transverse mass distribution in experiment #13 (row C) is not taken to be parabolic, we do not use the data in row C to approximate the "missing data" in row B. Owing to the lack of appropriate spray information, we simply assume mass homogeneity in row B in experiment #13.

(iii) Data in row F and row H

There are five gauges in each of these two rows. Since they are located relatively far from the bow, much less water is collected in these ten gauges than is collected in

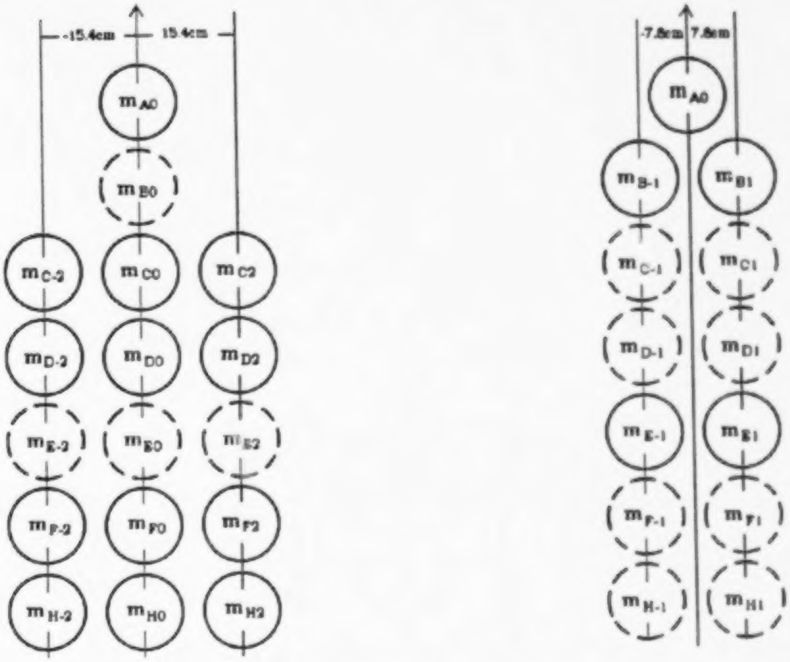
-15.4cm
15.4cm
m_A0
m_B0
m_C-2
m_C0
m_C2
m_D-2
m_D0
m_D2
m_E-2
m_E0
m_E2
m_F-2
m_F0
m_F2
m_H-2
m_H0
m_H2
-7.8cm
7.8cm
m_A0
m_B-1
m_B1
m_C-1
m_C1
m_D-1
m_D1
m_E-1
m_E1
m_F-1
m_F1
m_H-1
m_H1

(a)

(b)

Figure 1B.1: Data set along the longitudinal lines (a) y = 0, ± 15 cm, and (b) y = ± 7.8 cm. The symbols (e.g m_{B0}) enclosed by the dashed circles are mass density data (gcm^{-2}) that must be interpolated from the actual measurements, which are represented by the solid circles.

the other rows. The raw data (Appendix 1A) show that the transverse mass distribution is quite irregular. Hence, the use of a parabolic distribution is discarded and the "missing data" are instead estimated using linear interpolation. For example, the "missing data" in row F can be calculated by:

$$m_{F1} = m_{F-1} = m_{F0} + \frac{7.8}{15.4}\left(m_{F2} - m_{F0}\right) \tag{1B.4}$$

APPENDIX 1C

Normalized collected spray mass (M_{ij}/M_{Gk}) along the lines $y = 0$ and $y = \pm 15.4$ cm, with $x = 27, 43.3, 57.5, 72.7, 89.7, 118.6$, and 149.6 cm (see Figures 2.1 and 1B.1a). The procedures used to obtain the data are described in Appendix 1B. Dashes indicate a negligible mass.

* Data points obtained through interpolation.

Run #1

	0.233	
	0.124*	
0.070	0.087	0.070
0.033	0.052	0.033
0.025*	0.028*	0.025*
0.00995	0.00986	0.00995
0.00680	0.00461	0.00680

Run #2

	0.200	
	0.123*	
0.061	0.076	0.061
0.045	0.056	0.045
0.031*	0.035*	0.031*
0.019	0.010	0.019
0.00658	0.00381	0.00658

Run #3

	0.400	
	0.087*	
0.049	0.057	0.049
0.026	0.063	0.026
0.024*	0.024*	0.024*
0.011	0.014	0.011
0.00153	0.000	0.00153

Run #4

	0.255	
	0.115*	
0.052	0.098	0.052
0.036	0.089	0.036
0.029*	0.038*	0.029*
0.00969	0.016	0.00969
0.00293	0.00242	0.00293

Run #5

	0.265	
	0.190*	
0.095	0.141	0.095
0.00867	0.037	0.00867
---	---	---
---	---	---
---	---	---

Run #6

***** Test Failed *****

Run #7

	0.151	
	0.112*	
0.061	0.107	0.061
0.032	0.076	0.032
0.032*	0.042*	0.032*
0.027	0.026	0.027
0.00757	0.013	0.0757

Run #8

	0.445	
	0.178*	
0.066	0.077	0.066
---	---	---
---	---	---
---	---	---
---	---	---

Run #9

	0.261	
	0.145*	
0.044	0.068	0.044
0.026	0.053	0.026
0.026*	0.033*	0.026*
0.015	0.024	0.015
0.00731	0.00696	0.00731

Run #10

	0.283	
	0.124*	
0.074	0.102	0.074
0.027	0.050	0.027
0.018*	0.019*	0.018*
0.013	0.00412	0.013
0.00227	0.00144	0.00227

Run #11

	0.227	
	0.126*	
0.053	0.114	0.053
0.034	0.084	0.034
0.033*	0.041*	0.033*
0.00745	0.00888	0.00745
0.00238	0.00127	0.00238

Run #12

	0.365	
	0.088*	
0.026	0.067	0.026
0.026	0.084	0.026
0.039*	0.059*	0.039*
0.014	0.017	0.014
0.00241	0.00198	0.00241

Run #13

	0.380	
	0.191*	
0.076	0.027	0.076
0.021	0.015	0.021
---	---	---
---	---	---
---	---	---

Run #14

	0.412	
	0.149*	
0.097	0.099	0.097
---	---	---
---	---	---
---	---	---
---	---	---

Run #15

	0.295	
	0.090*	
0.052	0.085	0.052
0.034	0.075	0.034
0.030*	0.037*	0.030*
0.015	0.00888	0.015
0.00554	0.00595	0.00554

Run #16

	0.228	
	0.089*	
0.051	0.104	0.051
0.034	0.089	0.034
0.035*	0.045*	0.035*
0.018	0.014	0.018
0.00492	0.00458	0.00492

Run #17

	0.256	
	0.111*	
0.065	0.068	0.065
0.039	0.076	0.039
0.027*	0.033*	0.027*
0.015	0.013	0.015
---	---	---

Run #18

	0.212	
	0.121*	
0.062	0.072	0.062
0.033	0.071	0.033
0.027*	0.033*	0.027*
0.015	0.017	0.015
0.00703	0.00606	0.00703

Run #19

	0.190	
	0.190*	
0.068	0.178	0.068
0.028	0.050	0.028
0.015*	0.016*	0.015*
0.00207	0.00081	0.00207
---	---	---

Run #20

	0.328	
	0.107*	
0.057	0.096	0.057
0.023	0.059	0.023
0.024*	0.028*	0.024*
0.011	0.00955	0.011
0.00374	0.00182	0.00374

Run #21

	0.223	
	0.090*	
0.049	0.089	0.049
0.034	0.078	0.034
0.037*	0.044*	0.037*
0.022	0.021	0.022
0.00877	0.00443	0.00877

Run #22

	0.243	
	0.129*	
0.048	0.090	0.048
0.035	0.057	0.035
0.027*	0.031*	0.027*
0.019	0.010	0.019
0.00688	0.00305	0.00688

Run #24

	0.270	
	0.098*	
0.039	0.095	0.039
0.029	0.076	0.029
0.035*	0.048*	0.035*
0.018	0.016	0.018
0.00766	0.010	0.00766

APPENDIX 1D

Normalized collected spray mass (M_{ij}/M_{Gk}) along the lines y = ±7.8 cm, with x = 43.3, 57.5, 72.7, 87.9, 118.6, and 149.6 cm (see Figures 2.1 and 1B.1b). The procedures used to obtain the data are described in Appendix 1B. Dashes indicated a negligible mass.

* Data points obtained through interpolation.

Run #1

0.118	0.118
0.082*	0.082*
0.047*	0.047*
0.028	0.028
0.00991*	0.00991*
0.00573*	0.0573*

Run #2

0.117	0.117
0.072*	0.072*
0.053*	0.053*
0.033	0.033
0.015*	0.015*
0.00519*	0.00519*

Run #3

0.084	0.084
0.055*	0.055*
0.053*	0.053*
0.021	0.021
0.013*	0.013*
0.00078*	0.00078*

Run #4

0.101	0.101
0.086*	0.086*
0.075*	0.075*
0.036	0.036
0.013*	0.013*
0.0027*	0.0027*

Run #5

0.175	0.175
0.129*	0.129*
0.030*	0.030*
---	---
---	---
---	---

Run #6

******* Test Failed *******

Run #7

0.099	0.099
0.095*	0.095*
0.065*	0.065*
0.039	0.039
0.026*	0.026*
0.010*	0.010*

Run #8

0.172	0.172
0.075*	0.075*
---	---
---	---
---	---
---	---

Run #9

0.132	0.132
0.062*	0.062*
0.046*	0.046*
0.031	0.031
0.020*	0.020*
0.00714*	0.00714*

Run #10

0.115	0.115
0.094*	0.094*
0.044*	0.044*
0.018	0.018
0.00866*	0.00866*
0.00185*	0.00185*

Run #11

0.109	0.109
0.098*	0.098*
0.071*	0.071*
0.039	0.039
0.00817*	0.00817*
0.00182*	0.00182*

Run #12

0.074	0.074
0.056*	0.056*
0.069*	0.069*
0.054	0.054
0.016*	0.016*
0.0022*	0.0022*

Run #13

0.191	0.191
0.051*	0.051*
0.019*	0.019*
---	---
---	---
---	---

Run #14

0.147	0.147
0.099*	0.099*
---	---
---	---
---	---
---	---

Run #15

0.081	0.081
0.077*	0.077*
0.064*	0.064*
0.035	0.035
0.012*	0.012*
0.00573*	0.00573*

Run #16

0.077	0.077
0.090*	0.090*
0.075*	0.075*
0.043	0.043
0.016*	0.016*
0.00476*	0.00476*

Run #17

0.110	0.110
0.067*	0.067*
0.067*	0.067*
0.030	0.030
0.014*	0.014*
---	---

Run #18

0.116	0.116
0.069*	0.069*
0.062*	0.062*
0.031	0.031
0.016*	0.016*
0.00654*	0.00654*

Run #19

0.160	0.160
0.150*	0.150*
0.045*	0.045*
0.016	0.016
0.00142*	0.00142*
---	---

Run #20

0.095	0.095
0.086*	0.086*
0.050*	0.050*
0.027	0.027
0.010*	0.010*
0.0028*	0.0028*

Run #21

0.080	0.080
0.079*	0.079*
0.067*	0.067*
0.042	0.042
0.021*	0.021*
0.00663*	0.00663*

Run #22

0.114	0.114
0.079*	0.079*
0.052*	0.052*
0.030	0.030
0.014*	0.014*
0.005*	0.005*

Run #24

0.083	0.083
0.081*	0.081*
0.064*	0.064*
0.045	0.045
0.017*	0.017*
0.00886*	0.00886*

APPENDIX 2A

Calculation of the Spray Flux onto the Ship

For the purpose of this study, the stern trawler MT Zandberg has been divided into four components: a) the foredeck, b) the front of the wheel house, c) the top of the wheel house, and d) the mast. Each of these components is covered with a grid cell network. Since these four components have different geometries and orientations, the procedure for calculating the spray flux to each component is slightly different. The methodology is also different for cases with wind direction $\theta = 0°$ (head wind), and for cases with wind direction $0° < \theta \leq 90°$. We will limit our considerations to these wind directions since winds from the stern will not generally lead to waves from the bow, which is an important assumption implied in Equation 3.1.

2A.1 Wind direction $\theta = 0°$

(a) First component: the foredeck

Let us first assume that the foredeck is flat and that the origin of the coordinate system is located at the bow. The spray flux to a particular grid cell centred at (x',y',z') (Figure 2A.1.1) is to be calculated. The equation of motion (Equation 3.2.1) is used to calculate the trajectory which allows spray droplets, which are injected vertically at S, to arrive at the point (x',y',z'). The bisection method is used to determine the injection velocity which gives rise to a trajectory with the required end point. In this method, we begin by specifying (guessing) an injection velocity interval which encompasses the correct injection velocity. Since the calculations proceed from the bow towards the stern, the minimum injection velocity is that for the previous target cell (see Figure 2A.1.1). If the target is the first grid cell, the minimum injection velocity is set to 0 ms^{-1}. We obtain the maximum injection velocity by adding 20 ms^{-1} to this minimum value. Finally, using a bisection search, the correct injection velocity is obtained. In the present situation, with a grid cell length of less than 1 m, the correct injection velocity for all

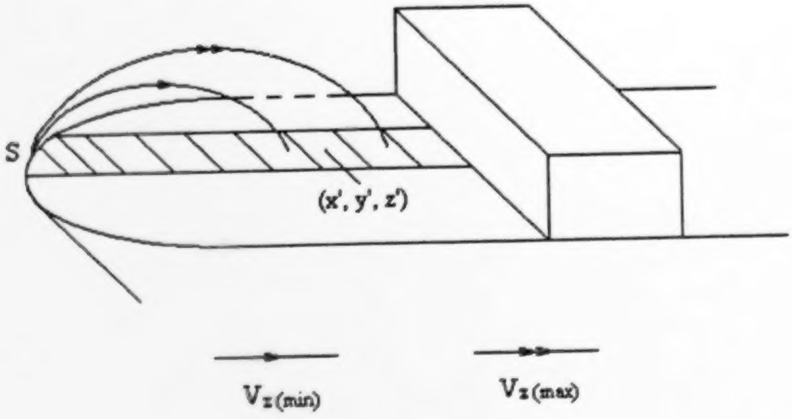

Figure 2A.1.1: Determination of the minimum and maximum injection velocities which gives rise to the two trajectories enclosing the target point (x′, y′, z′) in the bisection method.

cells on the ship falls within this velocity interval, except for very small wind and ship speeds. Should the bisection search fail, we simply increase the initial injection velocity interval by adding another 20 ms^{-1} to the maximum value until the bisection method succeeds in determining the required trajectory to the target. There must be an upper limit to the vertical injection velocity, however. Consequently, if the vertical injection velocity exceeds 120 ms^{-1}, and if the droplet still cannot reach the target, it is assumed that no spray impinges on this target cell. An injection velocity of 120 ms^{-1} allows droplets with a diameter of 1.75 mm to fly as high as 15 m. For most vessels, only a negligible amount of spray reaches such heights, so this limit seems appropriate.

After obtaining the correct vertical injection velocity V_{z0}, two trajectories with vertical injection velocities, $V_{zu} = V_{z0} + \Delta V_z$ and $V_{zl} = V_{z0} - \Delta V_z$, are launched from S to arrive at the points A' and B', respectively, which lie within the cell and enclose the centre point (Figure 2A.1.2a). These three trajectories characterize the spray zone over the grid cell. If the effect of wind and air drag is neglected, the three trajectories with initial vertical velocities V_{zl}, V_{z0}, and V_{zu} will arrive at A, O, B instead of A', O', B' (Figure 2A.1.2b). For a wind direction $\theta = 0°$, A, O, B, and A', O', B' all lie along the same longitudinal line. The situation shown in Figure 2A.1.2b is the conceptual basis for Equation 3.1. Hence, the spray flux, m(x',y',z'), at O'(x',y',z') can be calculated from Equation 3.2.5:

$$m(x',y',z') = m(x,y,z)\,\frac{\Delta x}{\Delta x'} \qquad (2A.1.1)$$

where

m(x',y',z'): the spray flux at O'(x',y',z') with the effect of wind and air drag included ($kgm^{-2}min^{-1}$).

m(x,y,z): the spray flux at O(x,y,z) under the hypothetical condition in which the wind drag is neglected ($kgm^{-2}min^{-1}$).

Δx': the distance between A' and B' in Figure 2A.1.2a (m).

Δx: the distance between A and B in Figure 2A.1.2b (m).

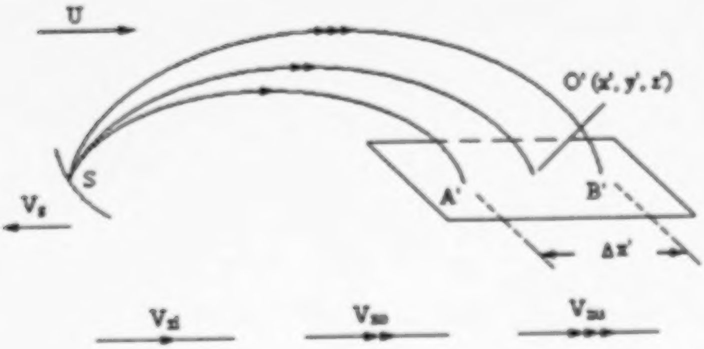

(a)

Figure 2A.1.2: Spray droplet trajectories, with the effect of wind drag, to various components under the situation with wind speed U, wind direction 0°, and ship speed V_s. (a) the deck, (c) the front of the wheelhouse, (e) the top of the wheelhouse, (f) the mast. Figures (b) and (d) show the trajectories under the hypothetical condition in which the wind drag is neglected, for the deck and the front of the wheelhouse respectively.

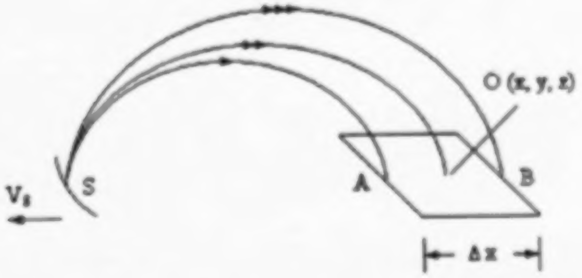

(b)

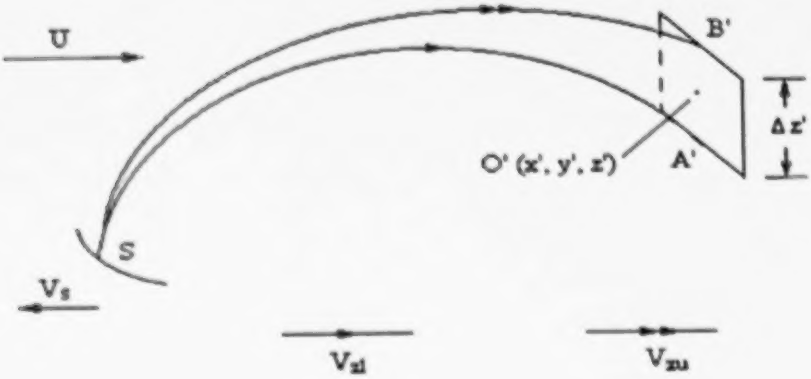
U
B'
Δz'
O' (x', y', z')
A'
S
V_s
V_{zl}
V_{zu}

(c)

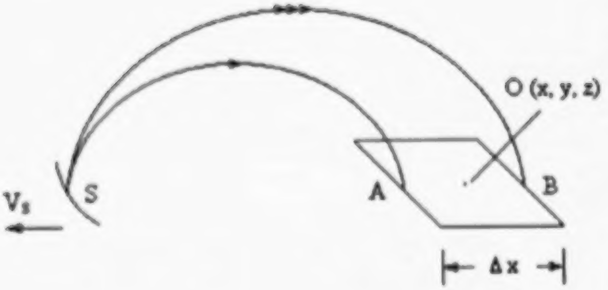
O (x, y, z)
S
A
B
V_s
Δx

(d)

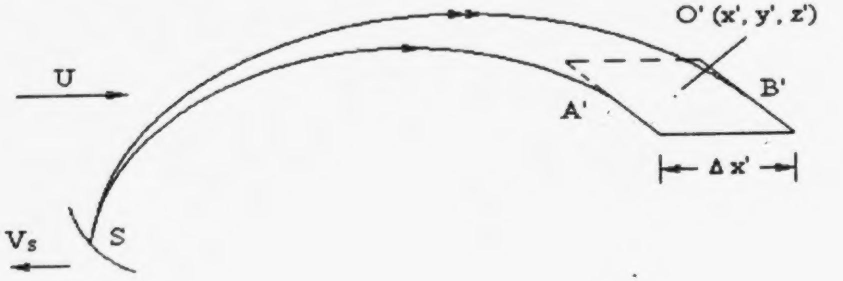

O' (x', y', z')
U
B'
A'
Δ x'
V_s
S

(e)

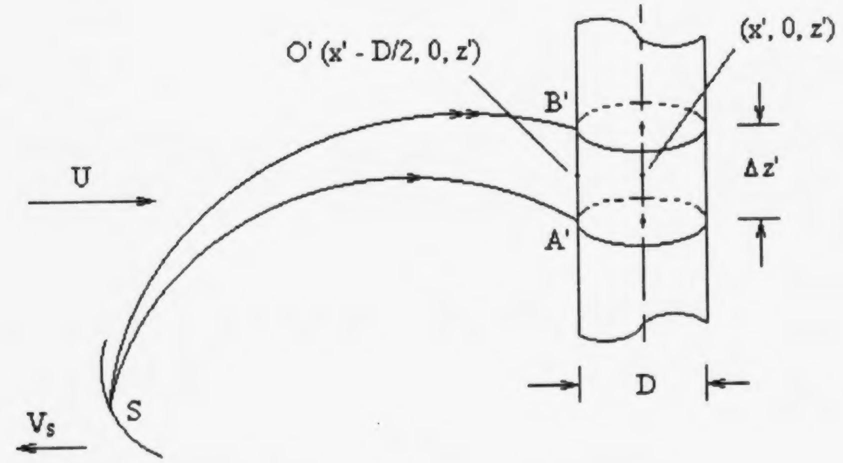

(x', 0, z')
O' (x' - D/2, 0, z')
B'
U
Δ z'
A'
D
S
V_s

(f)

Since the trajectories with no wind drag are ballistic, Δx can be calculated from:

$$\Delta x = \frac{2V_s(V_{zu} - V_{zl})}{g} \qquad (2A.1.2)$$

where

V_s: the ship speed (ms^{-1}).

$V_{zu} = V_{zo} + \Delta V_z$ (ms^{-1}).

$V_{zl} = V_{zo} - \Delta V_z$ (ms^{-1}).

It should be mentioned here that the calculation of the spray flux to a grid cell does not necessarily require three trajectories as described above. Two trajectories can also accomplish the same result, with one trajectory hitting the forward or lower boundary of the grid cell and the other hitting the aft or upper boundary. These two trajectories automatically enclose the centre of the cell. This method can be used for the deck behind the wheelhouse, since every grid cell has a fixed length of 1 m. However, on the foredeck, some of the grid cells have different lengths, and it is unnecessarily complicated to find the coordinates of the lower and the upper boundaries of each cell. Consequently, we use the three trajectory method for the foredeck.

(b) The front of the wheel house

Figure 2A.1.2c shows a grid cell on the front of the wheelhouse located at position O'(x',y',z'). The spray flux to this grid cell is to be calculated. Only two trajectories are needed in this case. The first, with initial vertical velocity V_{zl}, hits the lower boundary of the grid cell at A', and the second, with initial vertical velocity V_{zu}, hits the upper boundary of the grid cell at B' (Figure 2A.1.2c). Neglecting the effect of wind and air drag, and ignoring the superstructure, the two trajectories shown in Figure 2A.1.2c would arrive at their respective destinations on the deck at A and B, as shown in Figure 2A.1.2d. Since these two trajectories possess the same initial vertical velocities, V_{zl} and V_{zu}, the spray flux at O(x,y,z) can be estimated from:

$$m(x,y,z) = \frac{m(x,y,z)_A + m(x,y,z)_B}{2} \qquad (2A.1.3)$$

where $m(x,y,z)_A$ and $m(x,y,z)_B$ are the spray fluxes to A and B respectively. They are calculated using Equation 3.1. The spray flux to the point O'(x',y',z') is then calculated in a similar manner to case (a), that is:

$$m(x',y',z') = m(x,y,z)\left(\frac{\Delta x}{\Delta z'}\right) \qquad (2A.1.4)$$

where Δz' is the grid cell height and Δx is calculated using Equation 2A.1.2.

(c) The top of the wheelhouse

The method to calculate the spray flux to the top of the wheelhouse is the same as in case (b) except that the length of the grid in this case is Δx' instead of Δz'. Figures 2A.1.2e and 2A.1.2d show the spray trajectories for the situations with and without the effect of wind drag respectively. Therefore, the spray flux to O'(x',y',z') is:

$$m(x',y',z') = \left(\frac{m(x,y,z)_A + m(x,y,z)_B}{2}\right)\frac{\Delta x}{\Delta x'} \qquad (2A.1.5)$$

(d) The mast

The mast of the Zandberg has a non-circular cross-section whose area changes with height. However, to simplify the problem, it is assumed here that the mast is circular and that it has a diameter D which is calculated by averaging the equivalent circular diameters at the bottom and the top of the mast. This cylindrical mast is divided into 9 sections, each with diameter, D, and length, Δz', of 1 m. The spray flux to each section is calculated. Two simplifying assumptions are made:

i) Only the upstream semi-cylindrical surface which intercepts the oncoming spray is assumed to be wetted.

ii) The spray flux to this surface is uniformly distributed over it.

Figure 2A.1.2f shows two trajectories, with initial vertical velocities V_{zl} and V_{zu}, which impinge on the top and bottom of a particular cylindrical grid cell. Without the effect of wind drag, the trajectories are those shown in Figure 2A.1.2d. Thus, the spray flux to the mast can be calculated in a manner similar to that for cases (b) and (c). Hence,

$$m(x'-D/2,0,z') = \left(\frac{m(x,y,z)_A + m(x,y,z)_B}{2}\right)\frac{2\Delta x}{\pi\Delta z'} \qquad (2A.1.6)$$

2A.2 Wind direction 0° < θ ≤90°

(a) The deck

The calculation of the spray flux to a component becomes more complicated when the wind direction, θ, is no longer parallel (or more precisely, directly opposite) to the direction of the ship's course. If the wind makes an angle θ with the ship's course, the droplets move transversely as well as longitudinally over the ship. Consequently, stretching of the spray zone, under the effect of wind drag, will occur along both the x-axis and the y-axis. As a result, a spray source interval is used, instead of a spray source point, in order to calculate the spray flux to the grid cells. The method for choosing the size of the spray source interval has been described in Section 3.3.

To determine the location of the spray source interval located along the perimeter of the hull using the actual shape of the vessel would be very complicated and computationally time consuming. So, to simplify the problem, the hull perimeter is divided into twelve linear segments corresponding to the twelve columns of grid cells (see Figure 2A.2.1). Thus, each hull segment can be represented by a linear equation over the appropriate range of y. The actual hull perimeter is curved from R to P and then straight and parallel to the centreline from p aft. To assume that RP is a straight line could result in a large error in determining the coordinates of a spray source point because the length, RP, is large. In order to obviate this problem, we consider spray generation to occur only along the linear segment RQ. Spray generation beyond Q is

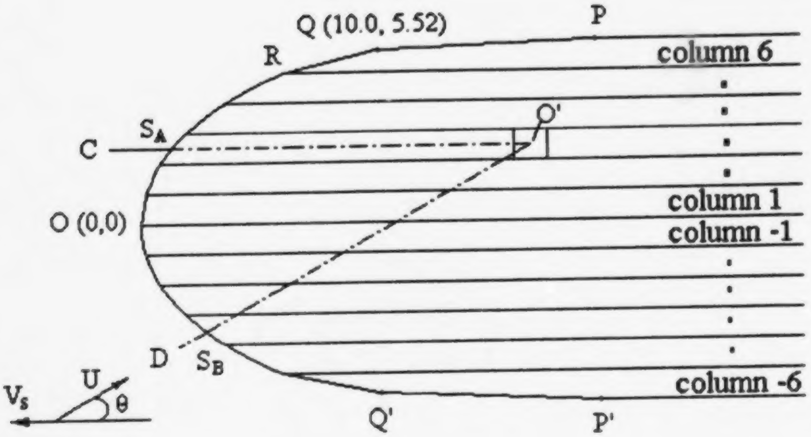
Q (10.0, 5.52)
P
R
column 6
S_A
O'
C
column 1
O (0,0)
column -1
D
S_B
column -6
U
V_s
θ
Q'
P'

Figure 2A.2.1: Ship hull perimeter segments used to determine spray source locations. The longitudinal strips along the deck are columns of grid cells (individual cells are not demarcated).

ignored. This assumption will not produce a significant error since QP is so far away from the centreline that the amount of spray generated is extremely small (Equation 3.1). Hence, the spray generation zone lies along Q'OQ (see Figure 2A.2.1). The coordinates of Q and Q' are designated somewhat subjectively to be (10.0 m, ±5.52 m).

With a wind direction, θ (Figure 2A.2.1), and the ship in forward motion, the spray source point for a target at O' must lie between S_A and S_B. S_A is the point of intersection of a line through O' parallel to the centreline and the segmented hull contour. S_B is the point of intersection of the segmented hull perimeter and a line through O' which makes an angle θ with the centreline. S_A and S_B can easily be found since the equations of each hull segment (within its range) and of the lines DO' and CO' are known. Knowing S_A and S_B, the bisection method is used to search for the spray source point. This method may be described as follows:

(1) We make a first estimate of the spray generation point S(x,y), by setting $y = (y_a + y_b)/2$ (Figure 2A.2.2). Knowing y, the hull segment to which S(x,y) belongs can be determined. Using the equation for that hull segment, x can then be calculated.

(2) Various droplet injection velocities are tried until the droplet trajectory terminates within the longitudinal strip bounded by the lines L1 and L2 (Figure 2A.2.2). The choice for the separation between L1 and L2 has been described in Section 3.3.

(3) Once (2) is satisfied, if the droplet trajectory also ends within the lateral strip bounded by H1 and H2, then the trajectory ends within a specified resolution box around the target point. When this happens, we conclude that S(x,y) is the correct spray source point. The choice for the separation between H1 and H2 has been described in Section 3.3.

(4) If condition (2) is satisfied, but the droplet trajectory terminates to the left of the line H1, the correct spray source point must lie between S(x,y) and $S_B(x_b,y_b)$. With these as end points, we estimate a new source point as described in (1). The whole process is repeated until both (2) and (3) are satisfied.

(5) If condition (2) is satisfied, but the droplet trajectory terminates to the right of the line H2, the correct spray source point must lie between S(x,y) and $S_A(x_a,y_a)$. With these as end points, we proceed as in (4).

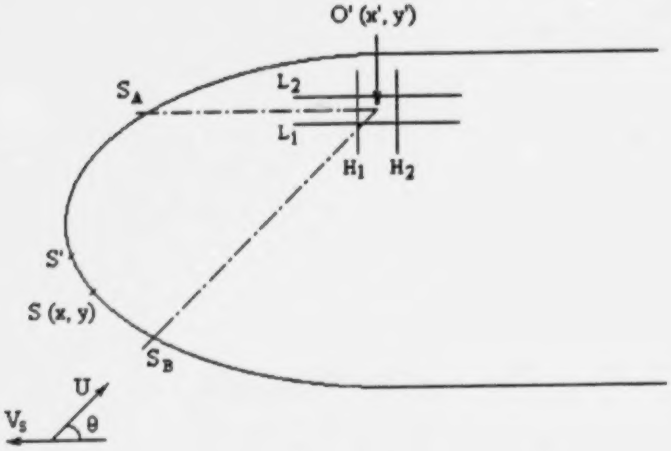
O' (x', y')
S_A
L_2
L_1
H_1
H_2
S'
S (x, y)
S_B
U
V_s
θ

Figure 2A.2.2: Determination of the spray source point using the bisection method.

It should be noted that different grid cells along the same longitudinal column have different spray source points. In step (2) of the bisection search method described above, the minimum injection velocity is zero and the maximum is the injection velocity for the previous target (along the same column) plus 20 ms^{-1}. This injection velocity interval should include the injection velocity for the required trajectory. Otherwise another 20 ms^{-1} will be added to the maximum injection velocity. The same principle applies to the other ship components in this searching process for the spray source points which correspond to specific targets.

To calculate the spray flux, two trajectories, with vertical velocities V_{zl} and V_{zu}, are injected at the point $S_1(x-\Delta x, y+\Delta y, 0)$ and the point $S_2(x+\Delta x, y-\Delta y, 0)$ respectively (see Figure 2A.2.3a). These four source points lead to four trajectories with four destination points, A', B', C', and D'. These four points form a spray zone quadrilateral enclosing the centre of the grid (Figure 2A.2.3a). If the effect of wind drag is neglected, the situation becomes that depicted in Figure 2A.2.3b. The five trajectories, which define the flux tube, possess the same initial vertical velocities as in the case with wind drag (Figure 2A.2.3a). The points A, B, C, D are thus the corners of the spray zone when wind drag is neglected. The spray flux, m(x,y,z), to the quadrilateral ABCD, centred at O(x,y,z) can be calculated using Equation 3.1. Then, by the conservation of spray mass and using the same initial vertical velocities with and without wind drag, the spray flux to the quadrilateral A'B'C'D' centred at point O'(x',y',z') is:

$$m(x',y',z') = m(x,y,z)\left(\frac{Area(ABCD)}{Area(A'B'C'D')}\right) \qquad (2A.2.1)$$

Now, ABCD is a parallelogram whose area is:

$$Area(ABCD) = \frac{2V_s(V_{zu} - V_{zl})}{g}(2\Delta y) \qquad (2A.2.2)$$

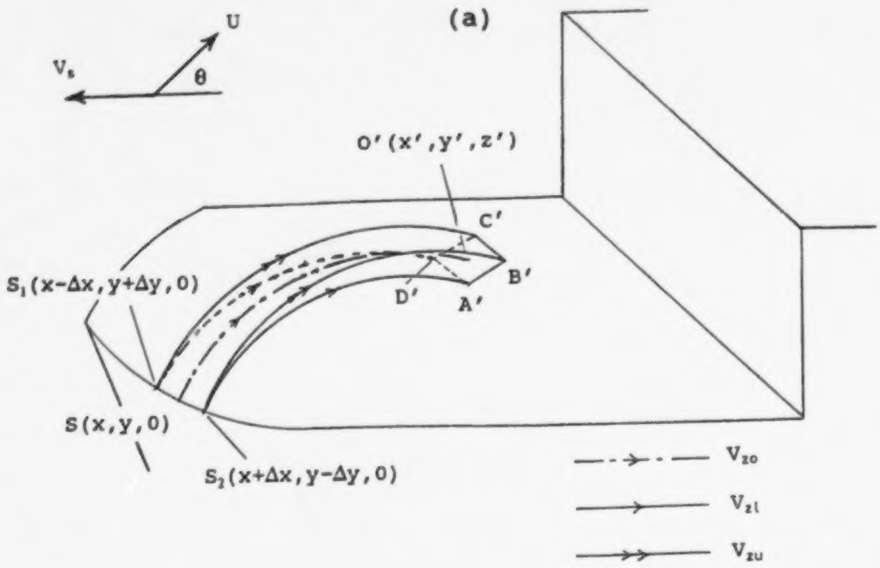
(a)
U
V_s
θ
O'(x',y',z')
C'
B'
D'
A'
S_1(x-Δx,y+Δy,0)
S(x,y,0)
S_2(x+Δx,y-Δy,0)
V_zo
V_zl
V_zu

Figure 2A.2.3: Spray droplet trajectories (with wind drag) to various components, for wind speed U, wind direction θ°, and ship speed Vs. (a) the ship's deck, (b) trajectories with wind drag neglected, (c) the front of the wheelhouse, (d) the top of the wheelhouse, (e) the mast, (f) plan view of the trajectories to the mast.

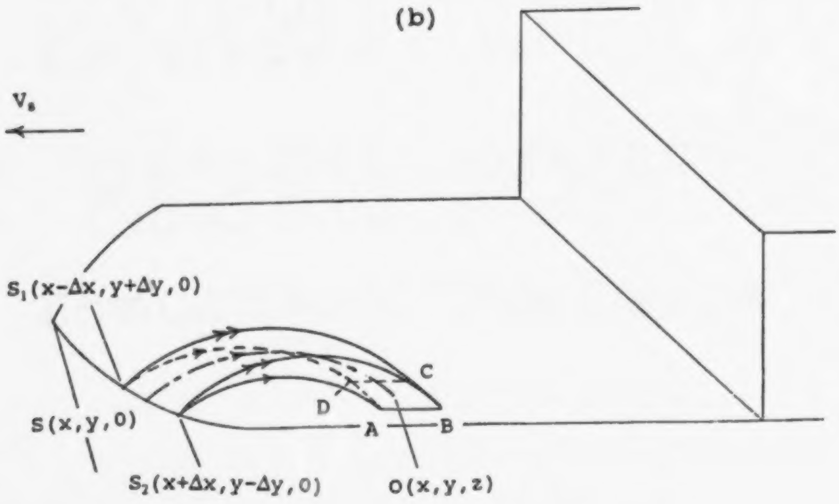
(b)
V_s
S_1(x-Δx,y+Δy,0)
S(x,y,0)
S_2(x+Δx,y-Δy,0)
C
D
A
B
O(x,y,z)

(c)

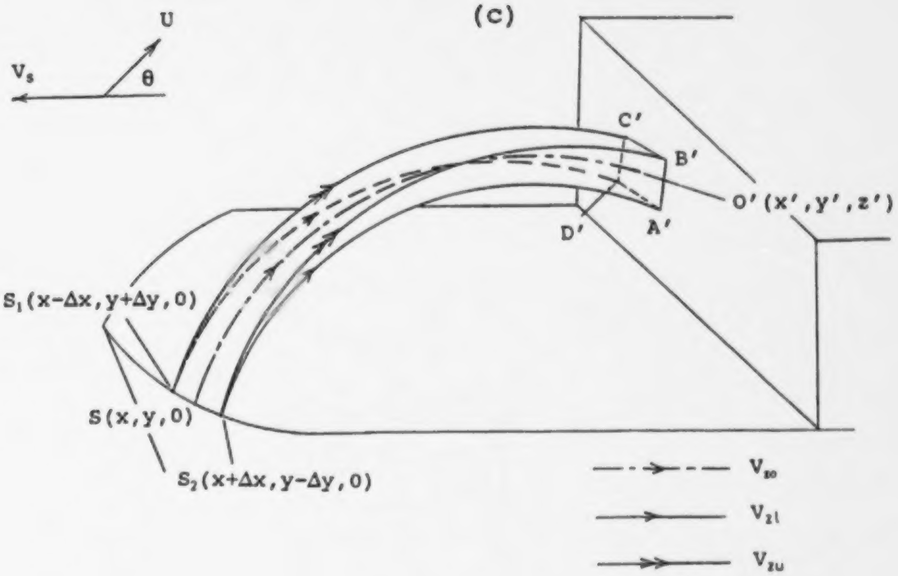
U
V_s
θ
C′
B′
O′(x′,y′,z′)
D′
A′
$S_1(x-\Delta x, y+\Delta y, 0)$
S(x,y,0)
$S_2(x+\Delta x, y-\Delta y, 0)$
V_{z0}
V_{zl}
V_{zu}

(d)

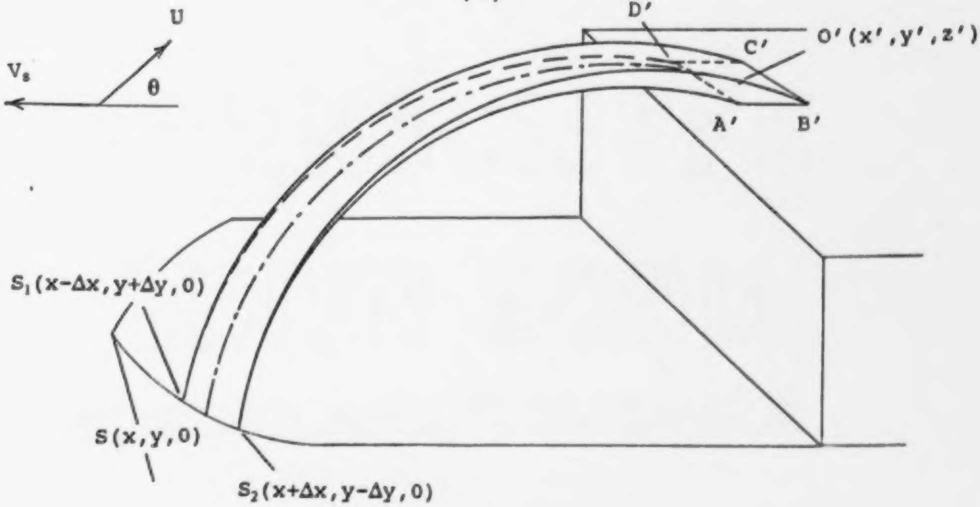
U
V_s
θ
D′
O′(x′,y′,z′)
C′
A′
B′
$S_1(x-\Delta x, y+\Delta y, 0)$
S(x,y,0)
$S_2(x+\Delta x, y-\Delta y, 0)$

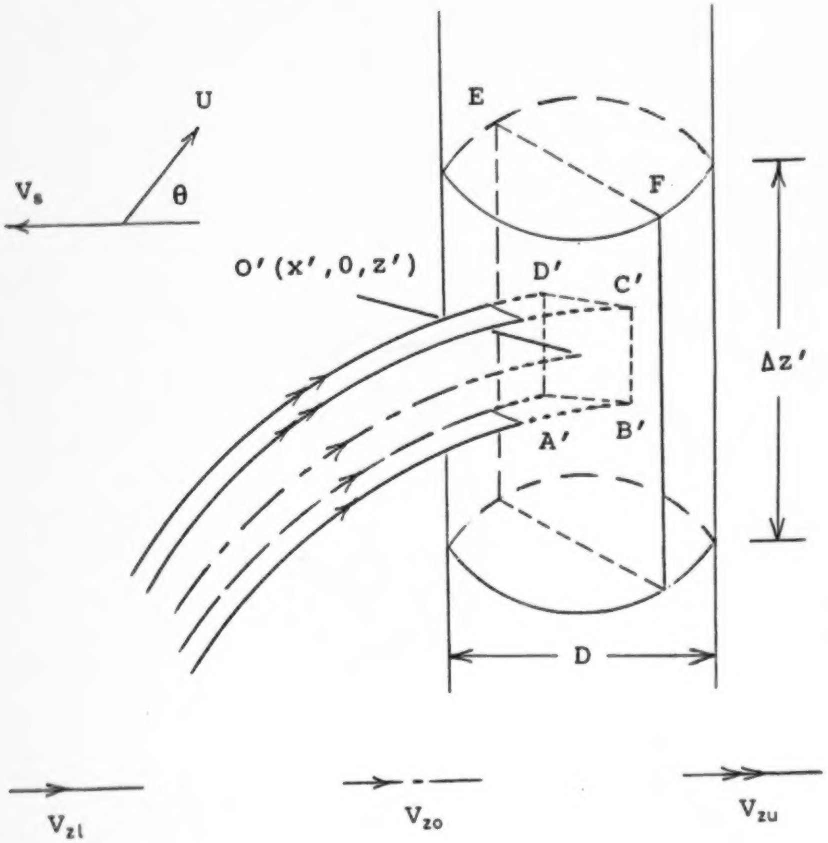
U
θ
V_s
E
F
O′(x′,0,z′)
D′
C′
Δz′
A′
B′
D
V_zl
V_zo
V_zu

(e)

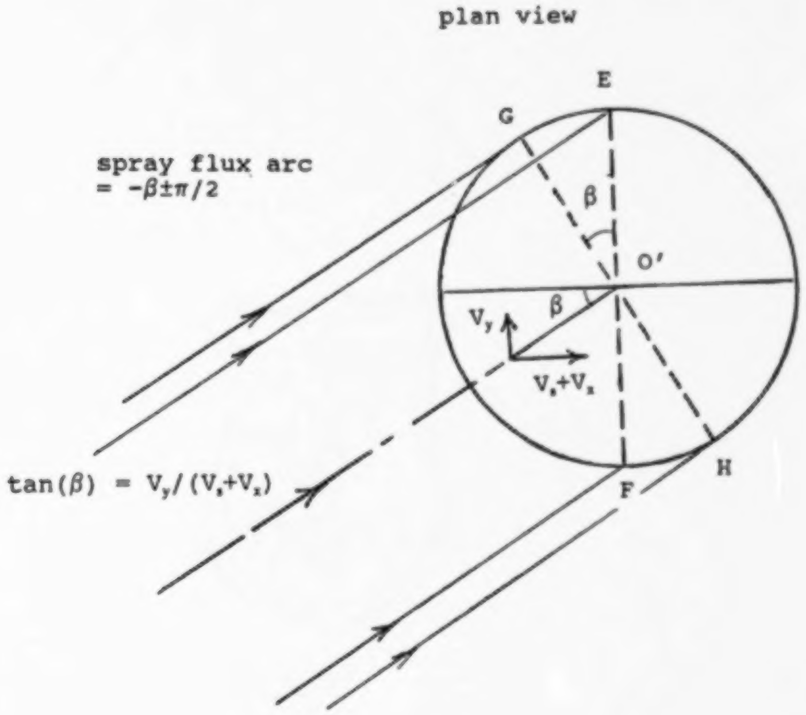
plan view
E
G
spray flux arc
$= -\beta \pm \pi/2$
β
O′
β
V_y
V_s+V_x
$\tan(\beta) = V_y/(V_s+V_x)$
F
H

(f)

where

$V_{su} = V_{so} + \Delta V_z$ (ms^{-1}).

$V_{sl} = V_{so} - \Delta V_z$ (ms^{-1}).

Since the points A'B'C'D' also lie on the deck, then A'B'C'D' is also a parallelogram whose area can be calculated by:

$$Area(A'B'C'D') = L_1 L_2 \sin(\theta_{12}) \qquad (2A.2.3)$$

Where L_1 and L_2 are the lengths of any 2 adjacent sides of the parallelogram, which can be calculated using the coordinates of the points A', B', C', and D'. θ_{12}, the angle between L_1 and L_2, can be computed by the vector dot product formula:

$$\cos(\theta_{12}) = \frac{\vec{L_1} \cdot \vec{L_2}}{L_1 L_2} \qquad (2A.2.4)$$

(b) The front of the wheelhouse

Figure 2A.2.3c shows five trajectories injected from the source points $S_1(x-\Delta x, y+\Delta y, 0)$, $S(x,y,0)$, and $S_2(x+\Delta x, y-\Delta y, 0)$. One of the trajectories hits the centre of the grid cell at $O'(x',y',z')$ and the other four hit the points A',B',C', and D'. Figure 2A.2.3b shows the equivalent trajectories when wind drag is neglected. The calculation of the spray flux to $O'(x',y',z')$ is similar to that for case (a) except that here A'B'C'D' is a rhombus, not a parallelogram, because these four points do not lie on the same horizontal level. The area of this rhombus can be calculated with the formula (Guo, 1985):

$$Area(A'B'C'D') = [(P-L_1)(P-L_2)(P-L_3)(P-L_4) - L_1 L_2 L_3 L_4 \cos^2(\phi)]^{1/2} \qquad (2A.2.5)$$

where L_1, L_2, L_3, and L_4 are the lengths of the four sides of the rhombus and P is:

$$P = \frac{(L_1 + L_2 + L_3 + L_4)}{2} \qquad (2A.2.6)$$

and the angle ϕ is:

$$\phi = \frac{(\theta_{12} + \theta_{34})}{2} \qquad (2A.2.7)$$

θ_{12} and θ_{34} are the angles between L_1 and L_2, L_3 and L_4 respectively. These two angles can be found using Equation 2A.2.4. Finally, by using Equations 3.1, 2A.2.1, 2A.2.2, and 2A.2.5, the spray flux, m(x',y',z'), to the grid cell centred at O'(x',y',z') can be calculated.

(c) The top of the wheelhouse

The spray source interval and the trajectories with wind drag are illustrated for this case in Figure 2A.2.3d. The corresponding trajectories without wind drag are shown in Figure 2A.2.3b. The calculation of the spray flux to the grid cell centred at O'(x',y',z') is the same as that for case (a).

(d) The mast

Let us first imagine that a vertical flat plate EF is inserted inside the mast. The plate width is D, the diameter of the mast, and its height is $\Delta z'$, the grid cell height of that cylindrical section (Figure 2A.2.3e). The plate EF is oriented perpendicular to the centreline of the deck (Figure 2A.2.3f). Four trajectories enclosing the geometric centre of this plate are shown. Without wind drag, these trajectories impinge on the deck, forming a parallelogram spray zone as shown in Figure 2A.2.3b. The spray flux to the plate EF is:

$$m_{EF}(x',y',z') = m(x,y,z)\left(\frac{Area(ABCD)}{Area(A'B'C'D')}\right) \qquad (2A.2.8)$$

m(x,y,z) may be calculated using Equation 3.1, and the Area(ABCD) with Equation 2A.2.2. A'B'C'D' is a rhombus whose area is calculated by Equations 2A.2.4, 2A.2.5, 2A.2.6, and 2A.2.7. We now wish to determine the spray flux to the semi-cylindrical surface which receives the oncoming spray. This may be done by means of some geometrical manipulation (Figure 2A.2.3f). Given the spray flux to the plate EF (Equation 2A.2.8), the spray flux to the plate GH (Figure 2A.2.3f), whose normal vector is parallel to the oncoming spray droplets, is given by:

$$m_{GH}(x',y',z') = \frac{m_{EF}(x',y',z')}{\cos(\beta)} \qquad (2A.2.9)$$

where

$m_{GH}(x',y',z')$: the spray flux to the plate GH ($kgm^{-2}min^{-1}$).

$m_{EF}(x',y',z')$: the spray flux to the plate EF ($kgm^{-2}min^{-1}$).

β: the droplet impact angle relative to the centreline of the ship.

The angle β may be calculated by:

$$\tan(\beta) = \frac{V_y}{V_s+V_x} \qquad (2A.2.10)$$

where

V_x: the x-component of the velocity of the spray droplets upon hitting the point O'(x',y',z') (ms^{-1}).

V_y: the y-component of the velocity of the spray droplets upon hitting the point O'(x',y',z') (ms^{-1}).

V_s: the magnitude ship velocity (ms^{-1}).

The sector of the cylindrical surface which receives spray is bounded by the angles $-\beta$

± π/2 (arc GH). Finally, then, the spray flux to the arc surface GH is:

$$m_{GH}(x', y', z')_{cyl} = m_{GH}(x', y', z')\left(\frac{2}{\pi}\right) \qquad (2A.2.11)$$

Thus, combining Equations 2A.2.8, 2A.2.9, and 2A.2.11, we have:

$$m_{GH}(x', y', z')_{cyl} = m(x, y, z)\left(\frac{Area(ABCD)}{Area(A'B'C'D')}\right)\frac{2}{\pi\cos(\beta)} \qquad (2A.2.12)$$

It should be mentioned here that the trajectory which hits the point O'(x',y',z') (Figure 2A.2.2e), does not actually hit the cylindrical grid cell surface at its geometrical centre. However, the difference will be small, and so Equation 2A.2.12 yields a good flux approximation.

APPENDIX 2B

Spray Flux Distributions over various components of the Zandberg for the Two Cases Studies described in Section 3.5.

2B.1 Low case

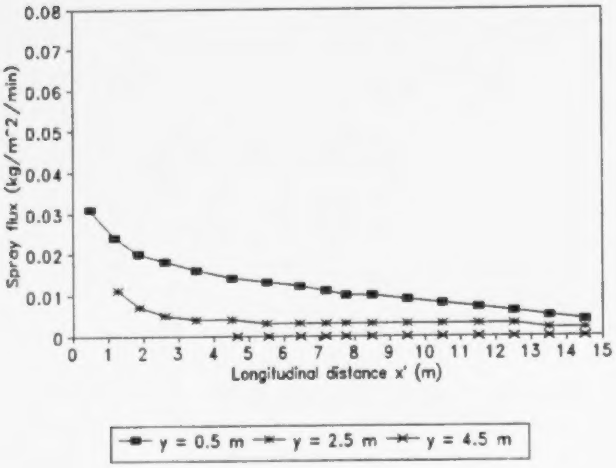

(a)

Figure 2B.1.1: Spray flux distribution over various components of the Zandberg under low conditions for a wind direction of 0°. a) the foredeck, b) the front of the wheelhouse, c) the top of the wheelhouse.

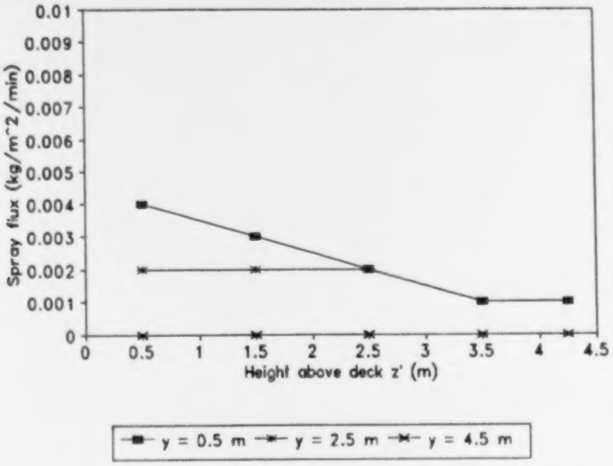

Spray flux (kg/m^2/min)
0.01
0.009
0.008
0.007
0.006
0.005
0.004
0.003
0.002
0.001
0
0
0.5
1
1.5
2
2.5
3
3.5
4
4.5
Height above deck z' (m)
y = 0.5 m
y = 2.5 m
y = 4.5 m

(b)

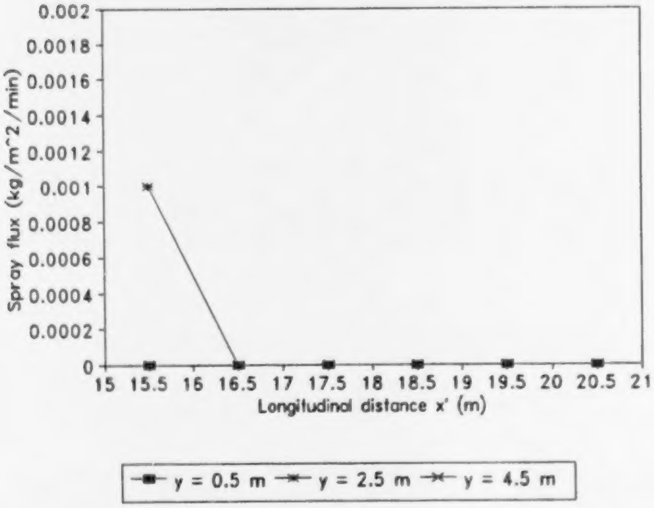

Spray flux (kg/m^2/min)
0.002
0.0018
0.0016
0.0014
0.0012
0.001
0.0008
0.0006
0.0004
0.0002
0
15
15.5
16
16.5
17
17.5
18
18.5
19
19.5
20
20.5
21
Longitudinal distance x' (m)
y = 0.5 m
y = 2.5 m
y = 4.5 m

(c)

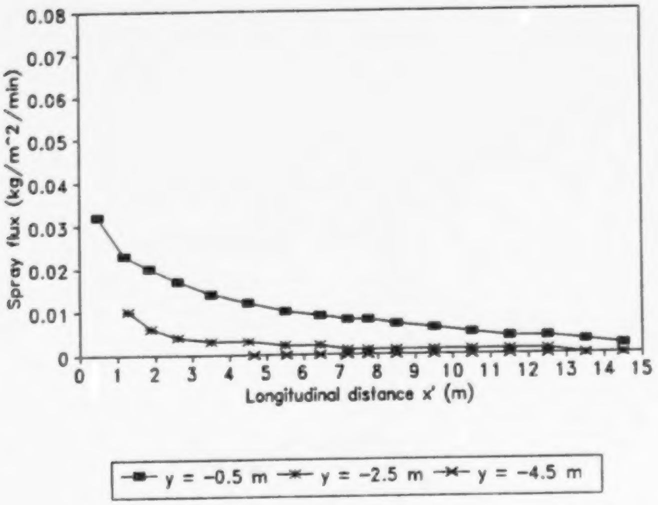

(a)

Figure 2B.1.2: Spray flux distribution over various components of the Zandberg under low conditions for a wind direction of 10°. a) the foredeck (port), b) the foredeck (starboard), c) the front of the wheelhouse (port), d) the front of the wheelhouse (starboard), e) the top of the wheelhouse (port), f) the top of the wheelhouse (starboard).

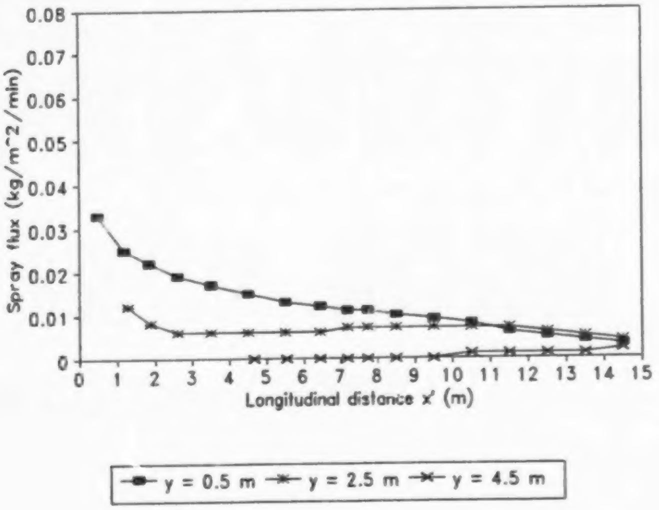

(b)

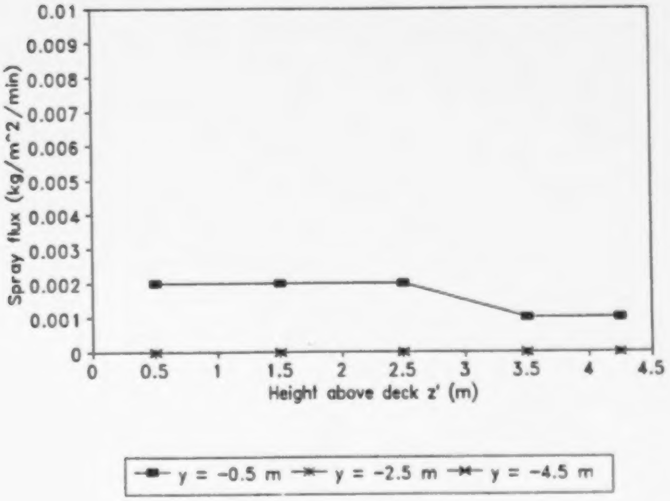

0.01
0.009
0.008
0.007
0.006
0.005
0.004
0.003
0.002
0.001
0
Spray flux (kg/m^2/min)
0
0.5
1
1.5
2
2.5
3
3.5
4
4.5
Height above deck z' (m)
y = -0.5 m
y = -2.5 m
y = -4.5 m

(c)

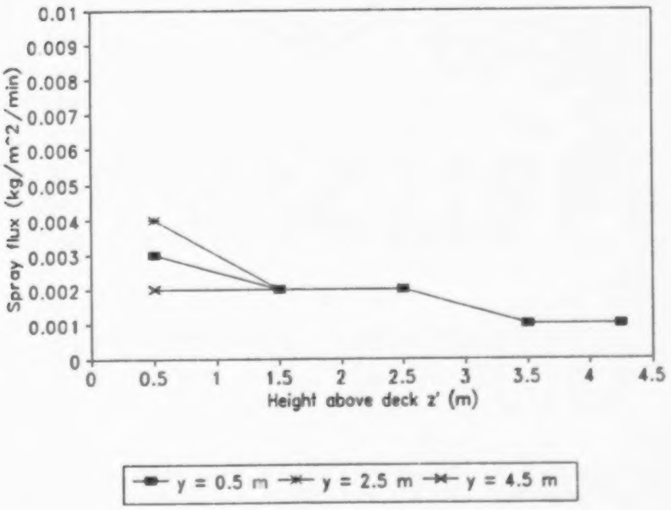

0.01
0.009
0.008
0.007
0.006
0.005
0.004
0.003
0.002
0.001
0
Spray flux (kg/m^2/min)
0
0.5
1
1.5
2
2.5
3
3.5
4
4.5
Height above deck z' (m)
y = 0.5 m
y = 2.5 m
y = 4.5 m

(d)

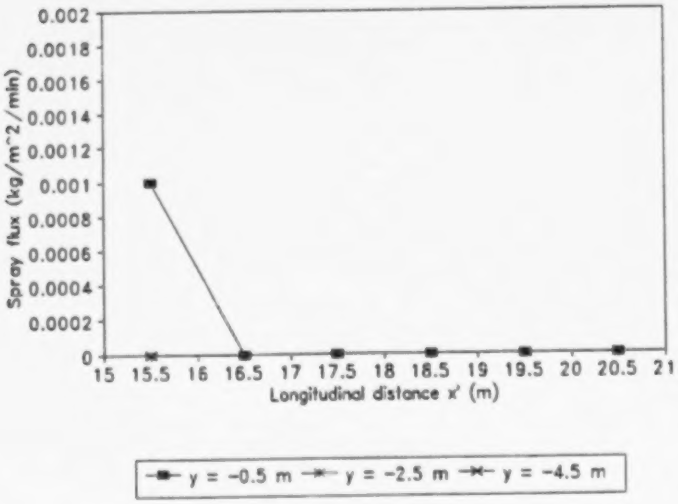
Spray flux (kg/m^2/min)
0.002
0.0018
0.0016
0.0014
0.0012
0.001
0.0008
0.0006
0.0004
0.0002
0
15 15.5 16 16.5 17 17.5 18 18.5 19 19.5 20 20.5 21
Longitudinal distance x' (m)
y = -0.5 m
y = -2.5 m
y = -4.5 m

(e)

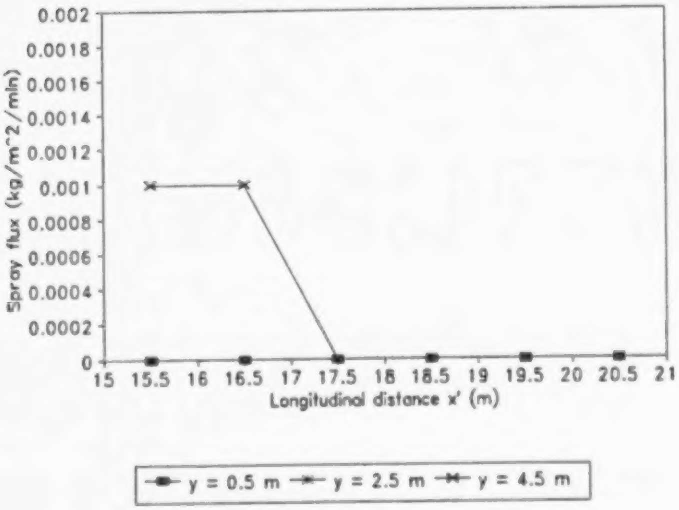
Spray flux (kg/m^2/min)
0.002
0.0018
0.0016
0.0014
0.0012
0.001
0.0008
0.0006
0.0004
0.0002
0
15 15.5 16 16.5 17 17.5 18 18.5 19 19.5 20 20.5 21
Longitudinal distance x' (m)
y = 0.5 m
y = 2.5 m
y = 4.5 m

(f)

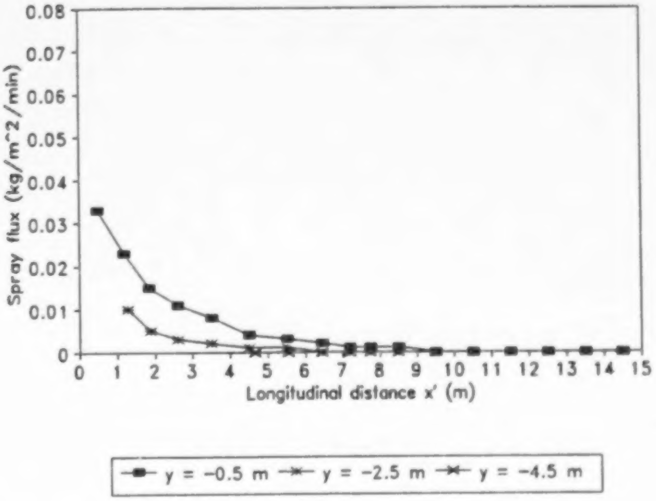

(a)

Figure 2B.1.3: Spray flux distribution over various components of the Zandberg under low conditions for a wind direction of 45°. a) the foredeck (port), b) the foredeck (starboard).

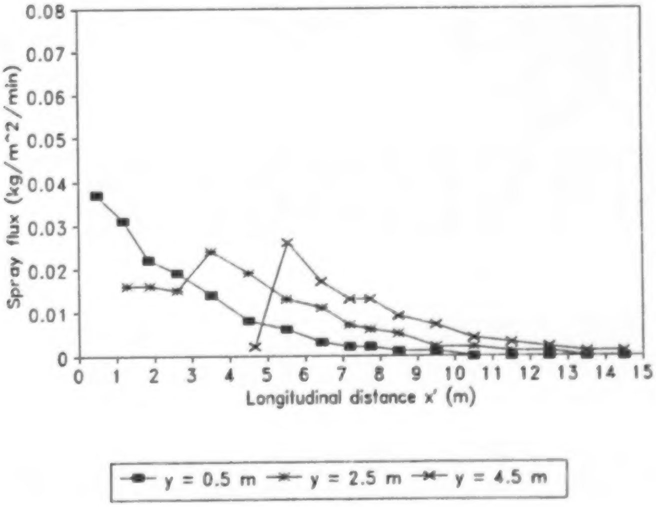

(b)

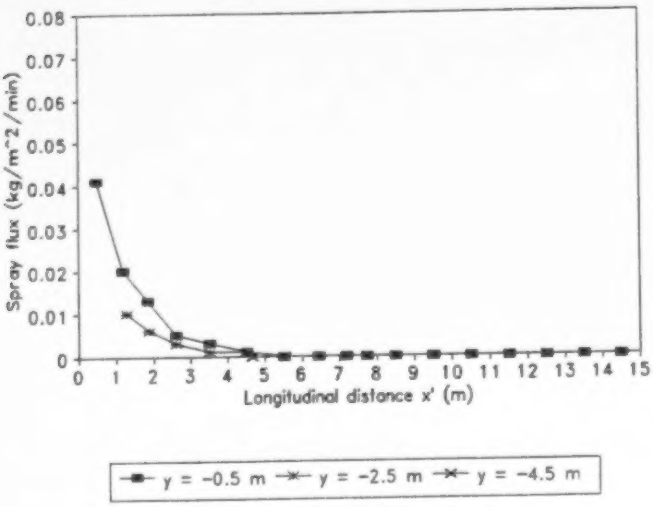

(a)

Figure 2B.1.4: Spray flux distribution over various components of the Zandberg under low conditions for a wind direction of 90°. a) the foredeck (port), b) the foredeck (starboard).

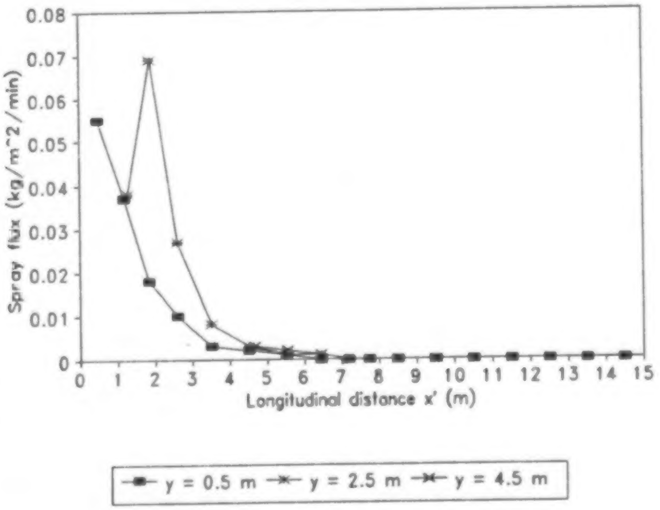

(b)

2B.2 Extreme case

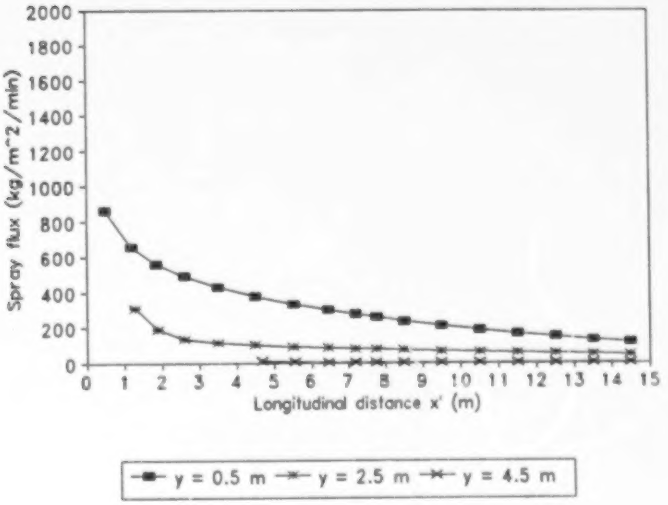

(a)

Figure 2B.2.1: Spray flux distribution over various components of the Zandberg under extreme conditions for a wind direction of 0°. a) the foredeck, b) the front of the wheelhouse, c) the top of the wheelhouse, d) the mast.

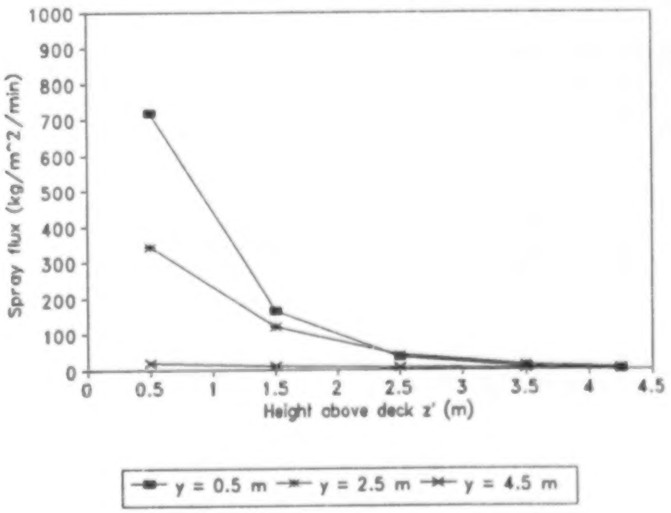

(b)

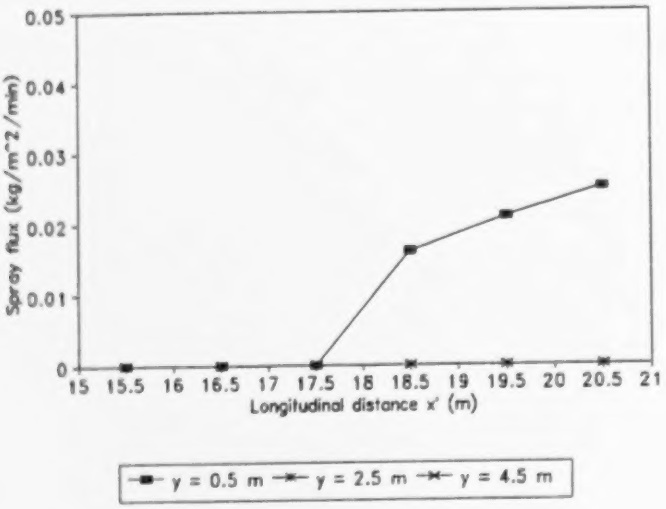
0.05
0.04
0.03
0.02
0.01
0
Spray flux (kg/m^2/min)
15
15.5
16
16.5
17
17.5
18
18.5
19
19.5
20
20.5
21
Longitudinal distance x' (m)
y = 0.5 m
y = 2.5 m
y = 4.5 m

(c)

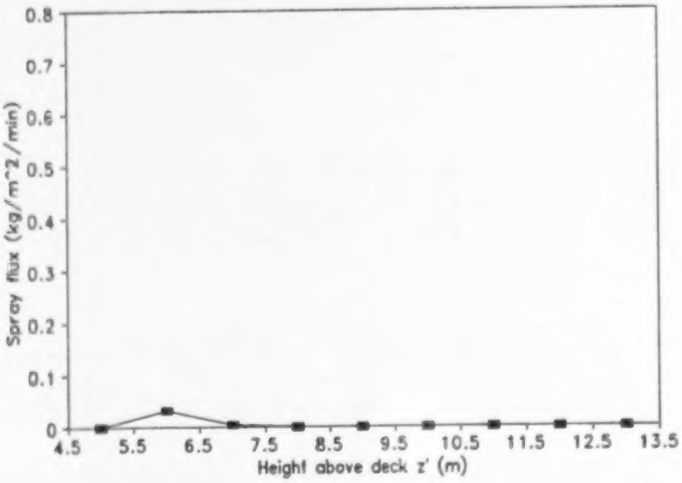
0.8
0.7
0.6
0.5
0.4
0.3
0.2
0.1
0
Spray flux (kg/m^2/min)
4.5
5.5
6.5
7.5
8.5
9.5
10.5
11.5
12.5
13.5
Height above deck z' (m)

(d)

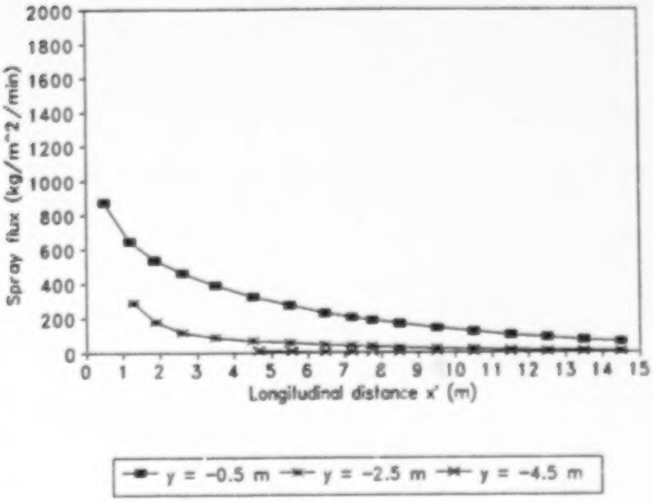

(a)

Figure 2B.2.2: Spray flux distribution over various components of the Zandberg under extreme conditions for a wind direction of 10°. a) the foredeck (port), b) the foredeck (starboard), c) the front of the wheelhouse (port), d) the front of the wheelhouse (starboard), e) the top of the wheelhouse (starboard), f) the mast.

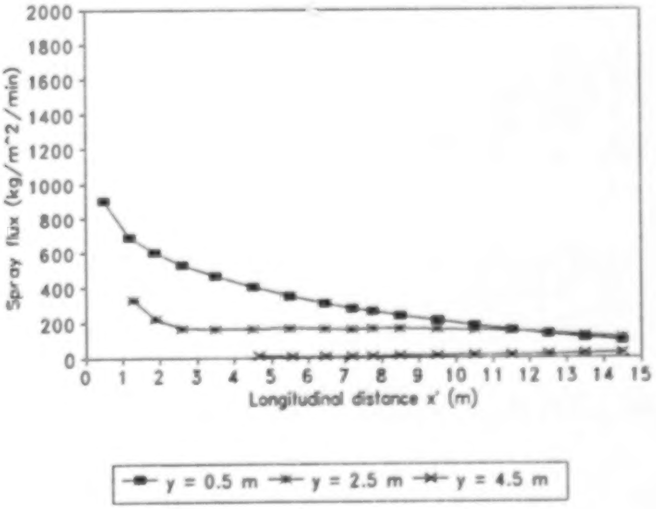

(b)

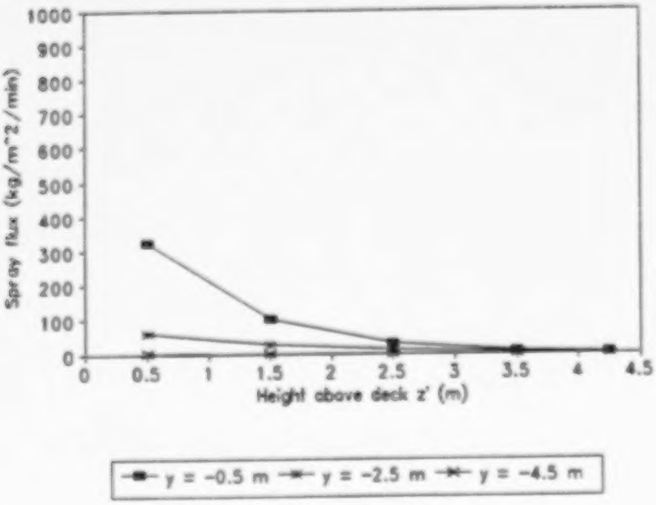
Spray flux (kg/m^2/min)
1000
900
800
700
600
500
400
300
200
100
0
0
0.5
1
1.5
2
2.5
3
3.5
4
4.5
Height above deck z' (m)
y = -0.5 m
y = -2.5 m
y = -4.5 m

(c)

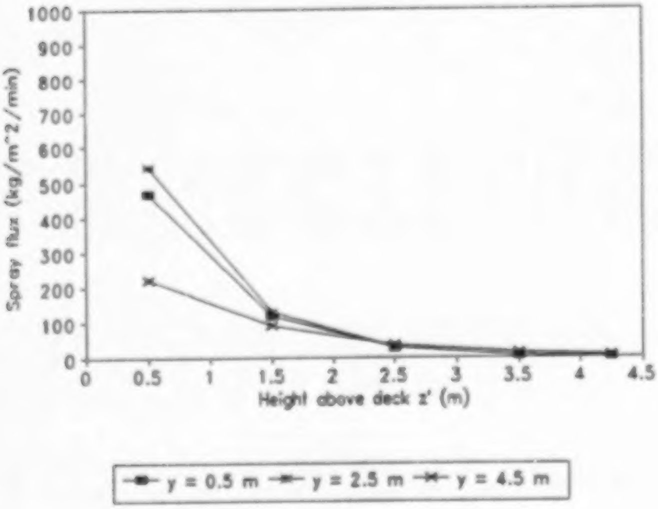
Spray flux (kg/m^2/min)
1000
900
800
700
600
500
400
300
200
100
0
0
0.5
1
1.5
2
2.5
3
3.5
4
4.5
Height above deck z' (m)
y = 0.5 m
y = 2.5 m
y = 4.5 m

(d)

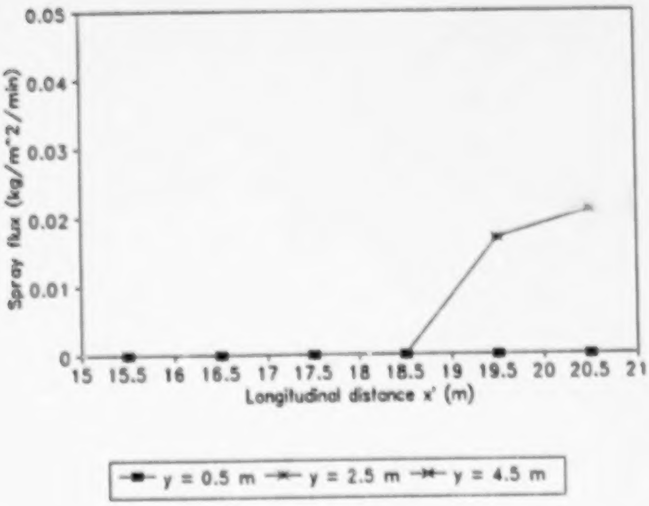
0.05
0.04
0.03
0.02
0.01
0
Spray flux (kg/m^2/min)
15
15.5
16
16.5
17
17.5
18
18.5
19
19.5
20
20.5
21
Longitudinal distance x' (m)
y = 0.5 m
y = 2.5 m
y = 4.5 m

(e)

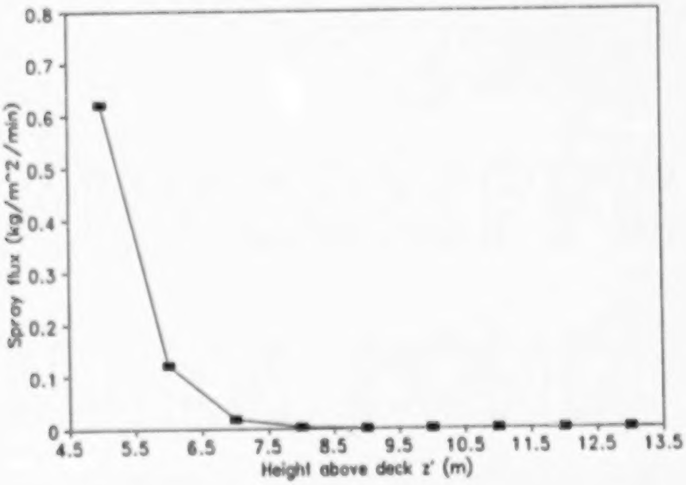
0.8
0.7
0.6
0.5
0.4
0.3
0.2
0.1
0
Spray flux (kg/m^2/min)
4.5
5.5
6.5
7.5
8.5
9.5
10.5
11.5
12.5
13.5
Height above deck z' (m)

(f)

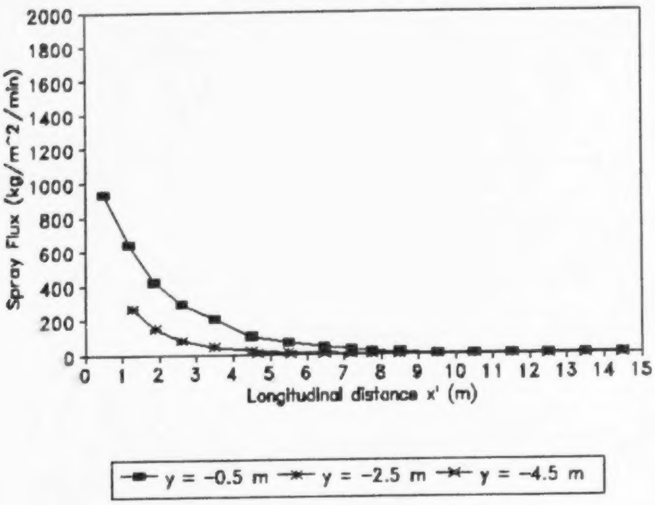

(a)

Figure 2B.2.3: Spray flux distribution over various components of the Zandberg under extreme conditions for a wind direction of 45°. a) the foredeck (port), b) the foredeck (starboard), c) the front of the wheelhouse (port), d) the front of the wheelhouse (starboard).

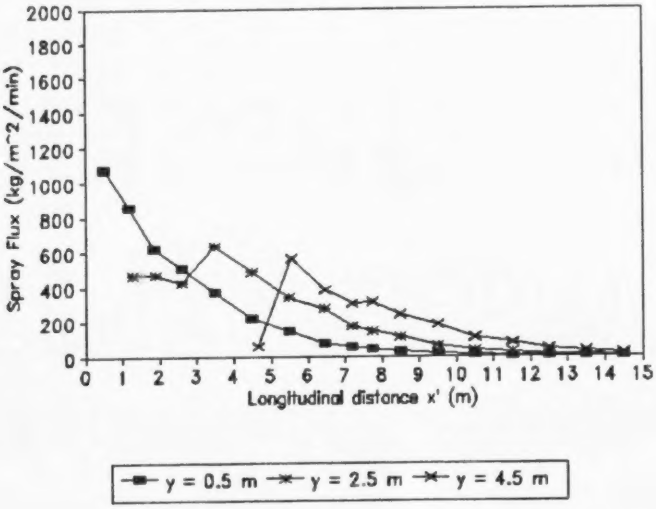

(b)

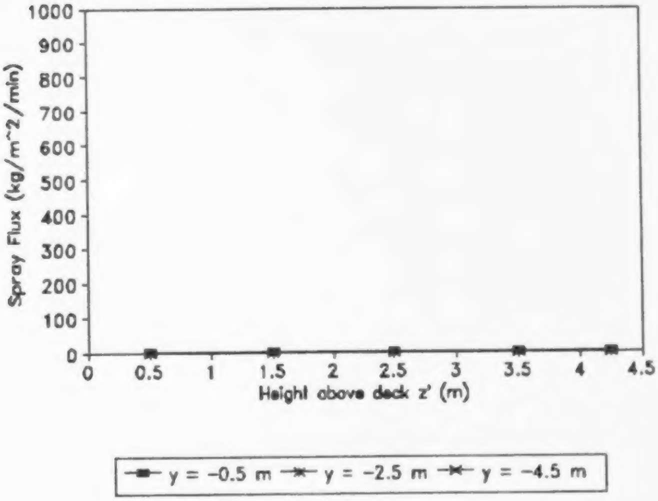
Spray Flux (kg/m^2/min)
1000
900
800
700
600
500
400
300
200
100
0
0
0.5
1
1.5
2
2.5
3
3.5
4
4.5
Height above deck z' (m)
y = -0.5 m
y = -2.5 m
y = -4.5 m

(c)

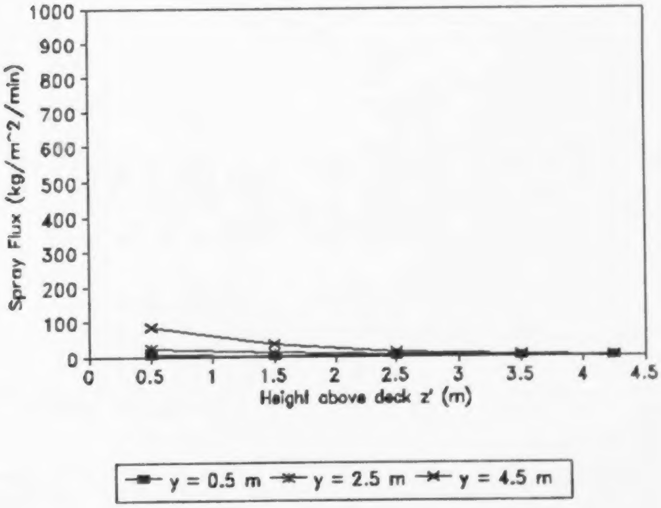
Spray Flux (kg/m^2/min)
1000
900
800
700
600
500
400
300
200
100
0
0
0.5
1
1.5
2
2.5
3
3.5
4
4.5
Height above deck z' (m)
y = 0.5 m
y = 2.5 m
y = 4.5 m

(d)

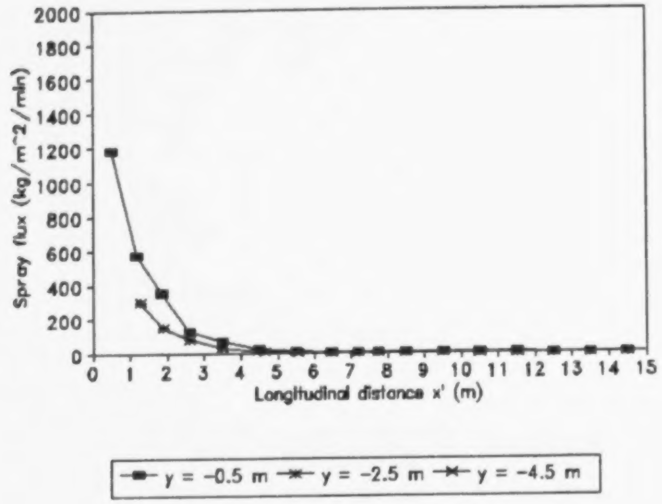

(a)

Figure 2B.2.4: Spray flux distribution over various components of the Zandberg under extreme conditions for a wind direction of 90°. a) the foredeck (port), b) the foredeck (starboard).

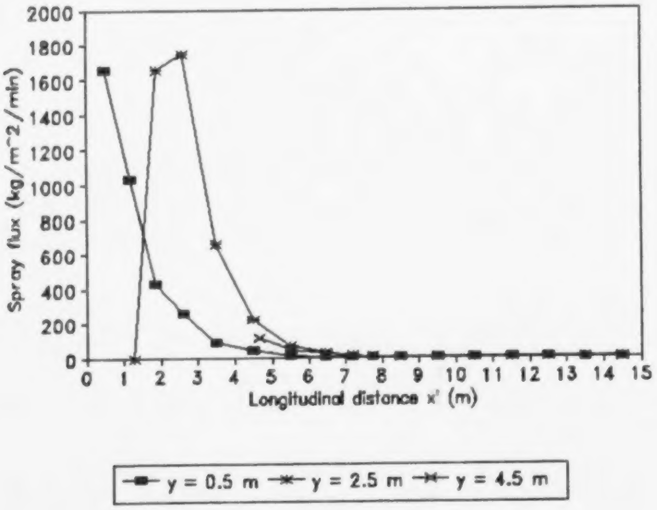

(b)

APPENDIX 3A

A Comparison between Predictions of the Zandberg Icing Model and Those of the Comiskey Icing Nomogram

The Wise and Comiskey (1980) nomogram was derived directly from the Mertins' nomogram (Mertins, 1968). Based on ship icing reports from ship of around 1000 tonnes displacement travelling at low speed in the North Sea, Mertins proposed an icing nomogram which correlates a categorical icing rate with wind speed, air and sea-surface temperatures. As mentioned in Section 4.8II, the Wise and Comiskey nomogram was further modified by Comiskey et al. (1984) by doubling the icing rate (in thickness) in each icing category. There are five icing categories in the nomogram: light, moderate, heavy, very heavy, and extreme (see Figure 3A.1). By comparing the results from the Zandberg icing model with the nomogram, we can obtain a qualitative evaluation of the model performance.

In order to evaluate the performance of the present icing model, various environmental conditions corresponding to the various icing categories of the nomogram (indicated by black dots in Figure 3A.1) are used as inputs to the Zandberg icing model and the resulting icing rates calculated. The results from the model are then compared with the nomogram's prediction.

However, the model's prediction is quantitative while the nomogram's prediction is rather qualitative (in terms of categorical icing rate as shown in Figure 3A.1). This makes the comparison difficult to present. Therefore, in order to quantify the comparison, each black dot in each icing category (see Figure 3A.1) is ranked in an orderly way according to its relative location to the upper and lower boundaries. Dots nearer the upper boundary mean a higher icing rate, while dots nearer the lower boundary mean a lower icing rate. In each icing category, there is a specific range of icing rate (see Figure 3A.1). Consequently, a value of icing rate is assigned to each dot according to its rank. Also, the value is assigned in a such way that the entire range of icing rate in each category is covered evenly. Since there are no lower and upper

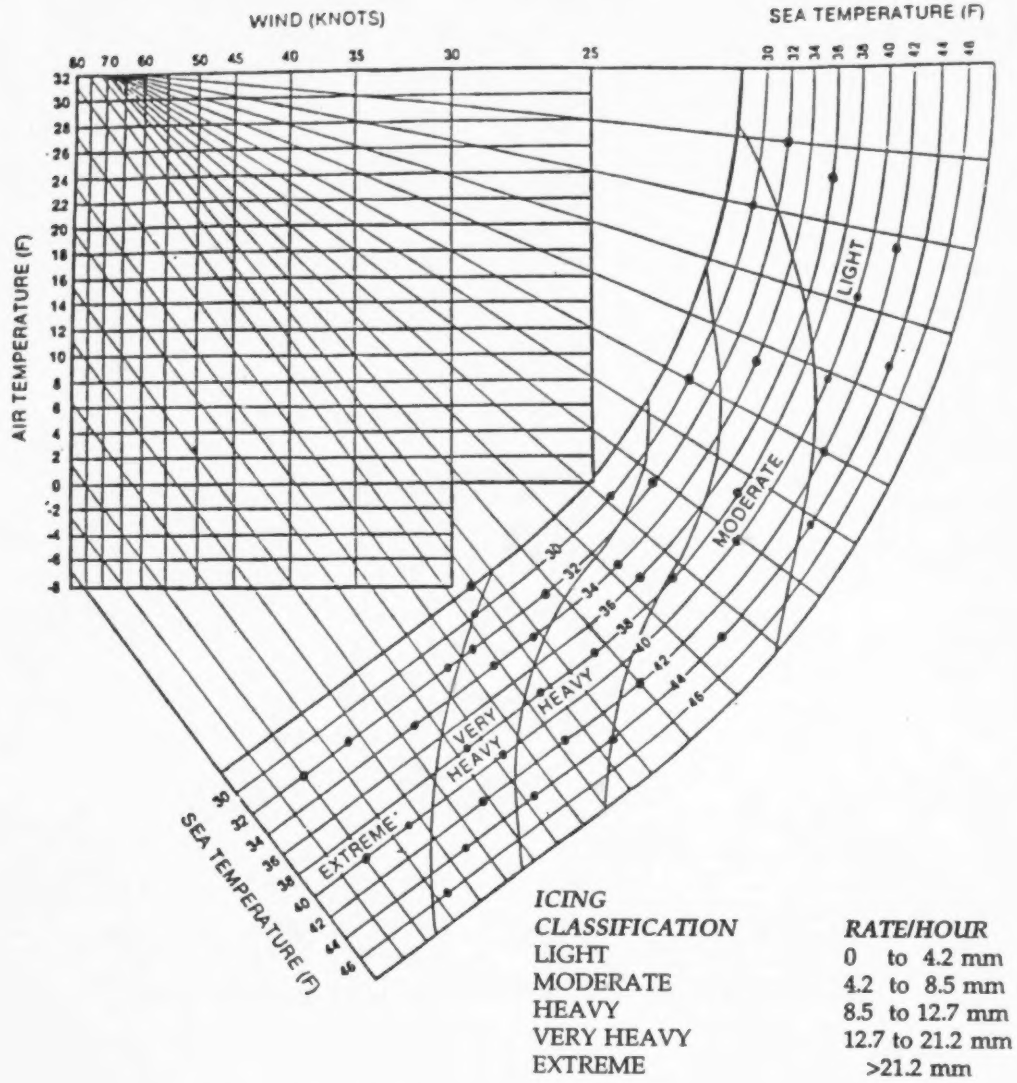

ICING CLASSIFICATION	*RATE/HOUR*
LIGHT	0 to 4.2 mm
MODERATE	4.2 to 8.5 mm
HEAVY	8.5 to 12.7 mm
VERY HEAVY	12.7 to 21.2 mm
EXTREME	>21.2 mm

Figure 3A.1: The modified version of Wise and Comiskey's nomogram (1980). Black dots indicate the environmental conditions which are used as inputs to the present icing model. For each input of wind speed, air and sea-surface temperature, the model generates three icing rates on three locations on the foredeck (x = 0.49 m, 7.75 m, and 14.50 m) along the longitudinal line y = 0.5 m. These icing rates are shown as triangles in Figure 3A.2.

boundaries for the light and extreme categories, a value of zero icing rate is used as the lower limit for the light category and a value of 30 mmhr^{1} as the upper limit for the extreme category. This procedure of ranking and quantifying the nomogram is rather arbitrary; nevertheless it is reasonable and it simplifies the comparison and makes it easier to comprehend.

The nomogram requires only air temperature, wind speed, and sea-surface temperature as inputs, but the Zandberg icing model requires additional inputs. Consequently, it is assumed in the model simulation that P_a = 1000 mb, RH = 75 %, $\theta = 0°$, F = 200 n.m., and V_s = 3 ms^{-1}. It has already been shown in Section 4.7 that wind direction, fetch, and ship speed can have significant effects on icing rate. As a result, the choice of the above constant values may cause some inaccuracies in the comparison. In the nomogram method, the location on the vessel where the icing rate is valid is not specified. Consequently, in the icing model, the icing rates are computed at three locations on the foredeck (x = 0.49 m, 7.75 m, and 14.50 m) along the longitudinal line y = 0.5 m. The results are plotted in Figure 3A.2. The results indicate that the model and nomogram are in good agreement for light, moderate, and heavy icing categories. For the very heavy and extreme icing categories, however, the model underestimates the icing rate relative to the nomogram. It should be noted that there are six data points which fall into the extreme icing category with icing rates greater than 30 mm/hr. For economy of space, these have not been plotted.

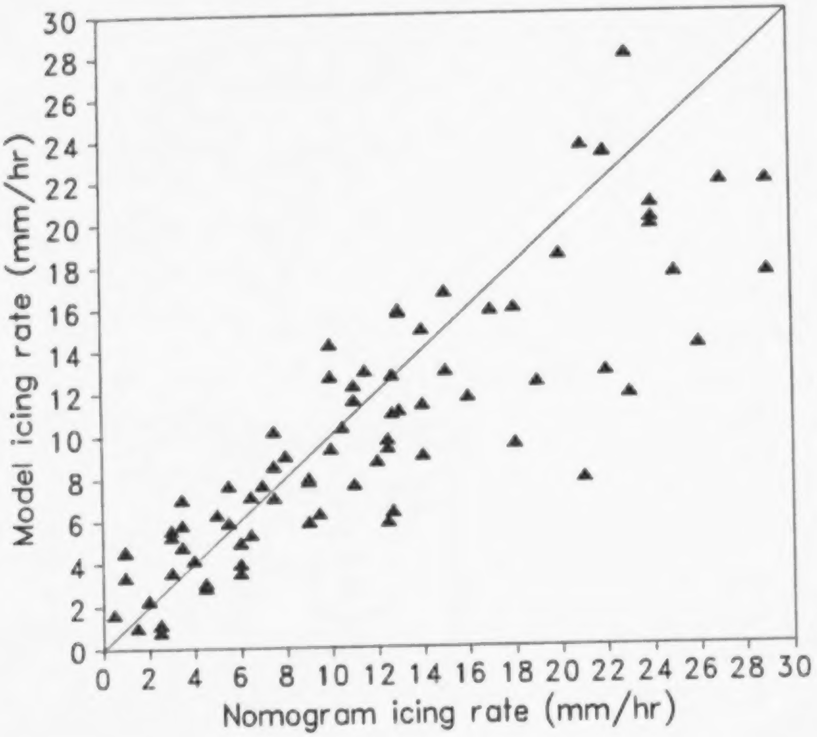

Figure 3A.2: A comparison between the model's results and the modified nomogram's prediction. The horizontal axis shows the quantified nomogram icing rates. The vertical axis shows the model predicted icing rates.

APPENDIX 3B: NOAA Icing Data Collected in Alaskan Waters

Case #	Length (m)	T_a (°C)	RH (%)	T_{sea} (°C)	U (ms^{-1})	heading (°)	V_s (ms^{-1})	H (m)	Obs. icing rate (tonnes/hr)
15	40	-2.8	70	2.5	14	160	5.1	3.1	0.497
29	32	-13.3	81	3.5	26	170	4.1	5.5	2.607
30	32	-3.3	70	4.4	7	165	4.1	1.2	0.497
34	39	-4.4	41	1.6	13	165	4.1	2.4	0.621
46	66	-2.8	50	3.3	13	175	2.6	2.4	0.248
63	29	-15	54	5.0	23	145	7.7	3.7	4.47
68	64	-3.9	71	3.2	17	175	2.0	7.5	1.987
69	115	-8.3	59	3.5	23	145	5.7	4.0	0.993
72	89	-7.8	75	2.0	12	155	6.2	3.7	3.104
75	66	-7.2	77	2.2	13	180	2.0	3.8	2.483
77	50	-9.4	75	4.5	15	145	6.2	2.9	5.008
78	50	-2.8	59	4.0	11	140	6.2	2.4	2.607
80	50	-15.0	51	3.0	26	150	5.7	6.1	11.009
85	70	-12.2	75	1.0	13	160	3.1	3.7	4.966

APPENDIX 3C: Soviet Icing Data Collected by Soviet Fishing Vessels

Case #	Length (m)	T_a (°C)	T_{sea} (°C)	U (ms^{-1})	heading (°)	V_s (ms^{-1})	H (m)	Spraying freq. (min^{-1})	Obs. icing rate (tonnes/hr)
10	39.2	-11.2	1.6	12.2	150	2.1	3.01*	7.06*	2.1
11	39.2	-11.0	0.8	17.5	150	2.1	5.01*	5.34*	6.1
23	38.5	-4.0	-1.0	14.5	150	2.1	3.86*	6.19*	0.3
24	38.5	-12.0	-1.8	11.0	150	2.1	2.58*	7.62*	2.8
39	39.0	-10.0	5.0	13.0	175	2.6	3.31*	6.96*	0.15
70	43-45	-22.0	-2.0	10.0	180	5.1	2.23*	9.68*	2.5
72	54	-13.8	-0.1	15.0	153	4.6	4.0	4.0	2.6
89	54	-5.3	2.5	18.0	165	1.6	5.0	3.5	0.3
90	54	-5.6	2.4	18.0	175	1.6	5.0	3.5	0.5
91	54	-6.6	2.2	18.0	175	1.6	5.5	3.5	0.7
92	54	-8.6	1.4	17.0	175	0.5	5.0	3.5	0.8
93	54	-10.1	1.2	14.0	165	0.5	5.5	3.5	2.9
94	54	-11.1	1.1	13.0	175	1.0	5.0	2.5	1.6
95	54	-11.6	1.0	13.0	175	2.1	4.0	2.5	1.2
96	54	-11.7	0.6	13.0	155	2.1	4.0	2.5	1.2

Case #	Length (m)	T_a (°C)	T_{sea} (°C)	U (ms^{-1})	heading (°)	V_s (ms^{-1})	H (m)	Spraying freq. (min^{-1})	Obs. icing rate (tonnes/hr)
97	54	-10.3	0.6	13.0	150	3.1	3.5	1.5	1.2
98	54	-15.0	-1.6	16.0	160	4.1	3.5	0.5	6.6
103	39.5	-9.5	0.0	14.0	170	4.6	3.68*	7.38*	3.37
104	39.5	-13.2	0.9	19.5	160	4.1	5.79*	5.51*	2.1
105	39.5	-14.1	0.9	17.0	170	4.1	4.82*	6.17*	3.3
106	39.5	-10.2	0.5	16.0	170	4.6	4.43*	6.65*	1.6

* The wave height and frequency of spraying are not given in the data set. They are calculated based on the given wind speed and a fetch of 200 n.m.

APPENDIX 4

Listing of Programs

One input data file and three Fortran programs have been created in order to accomplish the analysis of ship icing and stability in this dessertation. The three Fortran programs are written with detailed documentation and comment statements in the code so that the logic of programming may easily be followed. Complete descriptions of the functions of the input data file and the three Fortran programs are given in the main text. However, the purposes of the data file and the programs are summarized below.

1. GRDCM4 is the input data file which provides the following grid cell data: coordinates of the geometric centroid of the cell, the longitudinal distance of the centroid from the perimeter of the hull, the surface area of the cell, and the unit normal vector to the surface of the cell. This is an input file for the main program SPYICE.

2. SPYICE is the program which is used to calculate the icing rate on each grid cell. This program uses four subroutines: SPRAYA, TSPY1, SPRAYB, and TSPY2. The functions of these four subroutines are summarized as follows:

   a) SPRAYA calculates local spray flux to the grid cell located at (x, y, z) for a wind direction of 0° (head wind).

   b) SPRAYB calculates local spray flux to the grid cell located at (x, y, z) for a wind direction between 10° and 90°.

   c) TSPY1 calculates the droplet impingement temperature for a wind direction of 0° (head wind).

   d) TSPY2 calculates the droplet impingement temperature for a wind direction between 10° and 90°.

3. SHGEOM is the program which is used to calculate the centre of mass and moments of inertia of the ship under icing conditions. Inputs to this program are the centre of mass

and moments of inertia of the uniced ship, and the icing data generated from the icing program SPYICE.

4. FTRANS is the program used to calculate the power spectrum of a time series of ship motions.

The source files described above are stored in the root directory on the attached floppy diskette. The input data file GRDCM4 is stored in the file "GRDCM4". The program SPYICE is stored in the file "SPYICE.FOR", SHGEOM in the file "SHGEOM.FOR", and FTRANS in the file "FTRANS.FOR".

Figures 4A.1a to 4A.1d are simplified flowcharts which illustrate the algorithms of the above computer programs and the ship dynamics model. They also show how they are linked together in the calculation of the icing and ship stability.

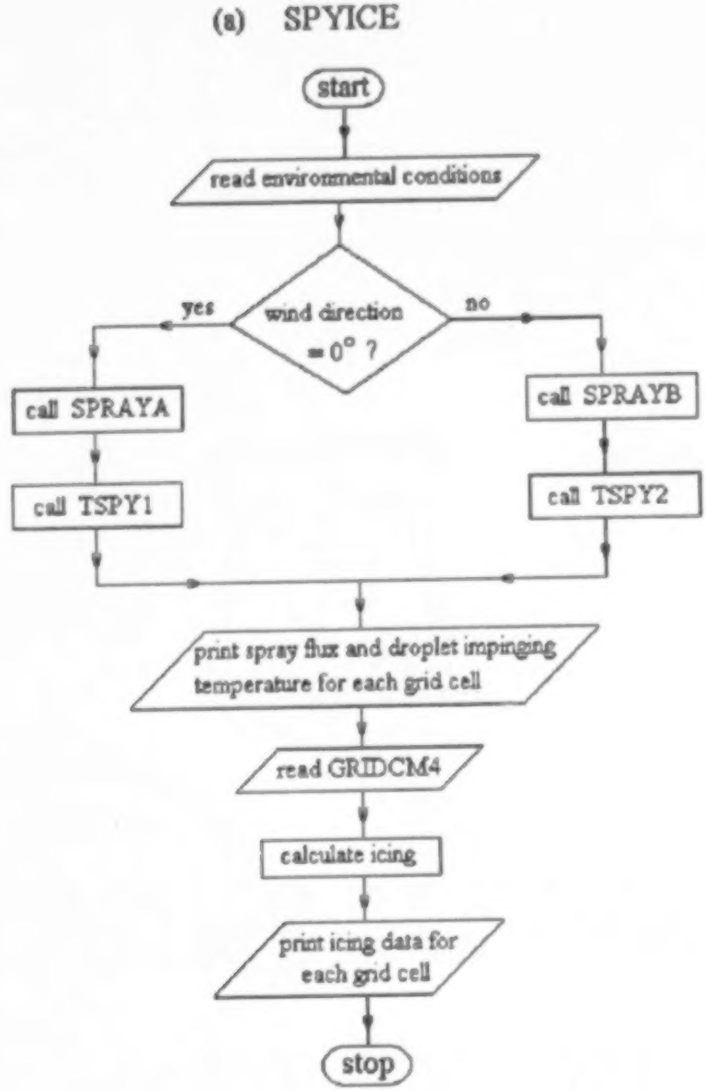
(a) SPYICE
start
read environmental conditions
wind direction
= 0° ?
yes
no
call SPRAYA
call TSPY1
call SPRAYB
call TSPY2
print spray flux and droplet impinging temperature for each grid cell
read GRIDCM4
calculate icing
print icing data for each grid cell
stop

Figure 4A.1: Four simplified flowcharts showing the processing flow of the computer programs developed to study ship icing and stability. (a) a flowchart for the program SPYICE, (b) a flowchart for the program SHGEOM, (c) a flowchart for the ship dynamics program (developed by Pawlowski and Bass, 1991), and (d) a flowchart for the program FTRANS.

(b) SHGEOM

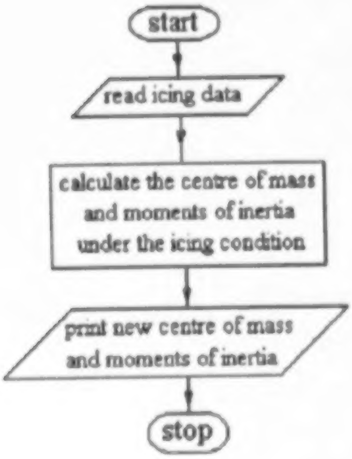
start
read icing data
calculate the centre of mass and moments of inertia under the icing condition
print new centre of mass and moments of inertia
stop

(c) SHIP DYNAMICS

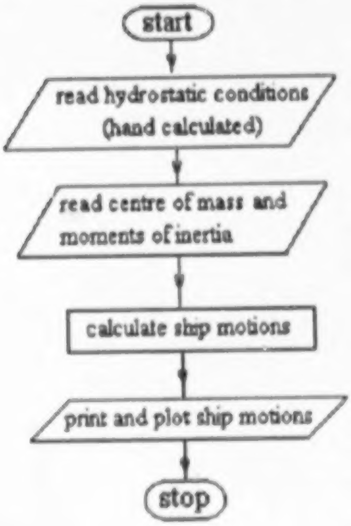
start
read hydrostatic conditions (hand calculated)
read centre of mass and moments of inertia
calculate ship motions
print and plot ship motions
stop

(d) FTRANS

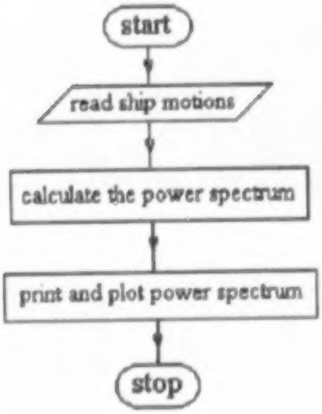
start
read ship motions
calculate the power spectrum
print and plot power spectrum
stop